Plasma Physics Reports, Vol. 28, No. 2, 2002, pp. 103–110. Translated from Fizika Plazmy, Vol. 28, No. 2, 2002, pp. 119–127.

TOKAMAKS

Study of Plasma Fluctuations in the TUMAN-3M Tokamak during Various Types of L–H Transitions

L. G. Askinazi*, V. V. Bulanin, V. V. D'yachenko*, S. V. Lebedev*, L. S. Levin*, V. S. Roitershtein**, and O. N. Shcherbinin***

**Ioffe Physicotechnical Institute, Russian Academy of Sciences, Politekhnicheskaya ul. 26, St. Petersburg, 194021 Russia*
***St. Petersburg State Technical University, Politekhnicheskaya ul. 29, St. Petersburg, 195251 Russia*
Received June 14, 2001; in final form, September 18, 2001

Abstract—The reflectometer method is used to comparatively study plasma fluctuations in the edge plasma of the TUMAN-3M tokamak during L–H transitions initiated by different methods. It is shown that the width of the spectrum of backscattered microwave radiation is the most representative parameter when comparing the results obtained in different confinement regimes. The following methods for affecting the edge plasma were applied: gas puffing, a fast current ramp-up, a rapid increase in the toroidal magnetic field, and ion cyclotron heating. The studies were performed at different positions of the cutoff of O- and X-mode probing waves. A similar behavior of the spectral width was observed during transitions triggered by the fast current ramp-up and the rapid increase in the toroidal field. This provides evidence that the mechanism for transition to the H-mode is the same in both cases in spite of the different character of the evolution of the current density profiles. The fastest and strongest narrowing of the spectra was observed during the transition triggered by ion cyclotron heating. Possible reasons for similarities and differences in the behavior of the spectra during the transitions to the improved confinement regime are discussed. © *2002 MAIK "Nauka/Interperiodica".*

1. INTRODUCTION

Among the processes associated with a transition to the improved confinement mode in a tokamak plasma, the occurrence of an edge transport barrier in the H-mode is the most extensively studied phenomenon, both in divertor and limiter discharges. It is commonly accepted that the improved confinement in the H-mode is ensured by the drift in the radial electric field, which results in the sheared poloidal rotation. The sheared rotation causes the decorrelation of fluctuations and decreases the rate of turbulent transport processes [1]. Although the nature of the occurrence and maintenance of a plasma state with improved confinement is basically the same for different types of L–H transitions, the mechanisms for generating the radial electric field can differ widely. They are determined by specific methods for triggering the H-mode. In recent experiments in the TUMAN-3M tokamak, a transition to the H-mode was achieved by different methods [2]; this made it possible to carry out a comparative study of L–H transitions. The study included an analysis of the behavior of plasma fluctuations. According to theoretical models, the suppression of plasma turbulence is related to the sheared rotation; hence, the study of fluctuations can provide indirect evidence of the generation of the radial electric field, which is necessary for the L–H transition. The rate and degree of the suppression of fluctuations were estimated from the scattering of probing microwave radiation under conditions of strong refraction; i.e., the measurements were carried out in the reflectometer version of the experiment. In this paper, we present phenomenological data demonstrating that the change in the spectral width of the reflected signal is related to the change in transport processes in the edge plasma and is the most representative parameter in comparative studies using different scenarios of the L–H transition. In Sections 3 and 4, we present the results from a comparison of the time evolution of the spectral width of the reflected signal obtained in different scenarios of the L–H transition for different cutoff positions of the incident microwaves. In Section 5, based on the results obtained, we discuss possible primary mechanisms giving rise to the electric field, which is a key factor for the suppression of turbulence and transition to the H-mode in the TUMAN-3M tokamak.

2. METHOD FOR ESTIMATING THE SPECTRAL WIDTH OF THE BACKSCATTERED MICROWAVE SIGNAL

The TUMAN-3M backscattering microwave diagnostics is based on a single-antenna reflectometer scheme, which allows probing by O- and X-mode microwaves [3]. The frequency of the probing microwaves could vary in the range F = 17–25 GHz from shot to shot. At such frequencies, the cutoff is at the plasma edge, where the transport barrier arises during the transition to the H-mode. The probing radiation was launched from the low-field side with the help of a conical antenna 4 cm in diameter and 8 cm in length. The scheme is designed to observe backscattered radiation for various angles of incidence of the probing micro-

1063-780X/02/2802-0103$22.00

wave beam (see [3]). However, in the described experiments, most of the measurements were performed with an antenna placed in the equatorial plane of the torus, when the probing radiation was normally incident onto the flux surface. The reflected radiation was detected by the microwave two-homodyne receiver technique (quadrature detection), which is described in detail in [4]. This method allowed us to obtain the spectra in the blue and red frequency ranges by means of the Fourier transform of the complex signal $\dot{U}(t) = U_{\cos}(t) + iU_{\sin}(t)$ (where $U_{\cos}(t)$ and $U_{\sin}(t)$ are the signals from two homodyne channels in which the phases of reference radiation are shifted by $\pi/2$ with respect to each other). In the course of experiments, we obtained statistically averaged estimates for the power spectrum of the complex signal $\dot{U}(t)$. These spectral estimates were then used to determine how the width of the spectrum and the root mean square (RMS) values of $\dot{U}(t)$ in different frequency ranges varied during the discharge. The spectra were analyzed in the frequency band ± 0.5 or ± 1 MHz.

3. COMPARISON OF THE TIME EVOLUTION OF THE BACKSCATTERED SPECTRA DURING DIFFERENT TYPES OF TRANSITIONS TO THE H-MODE

Experimental studies of turbulence were carried out in the TUMAN-3M tokamak ($a = 0.22$ m, $R = 0.53$ m, and $B_T \leq 1.2$ T) after the boronization of the vessel at relatively high discharge currents ($I_p > 140$ kA) in a deuterium plasma. A traditional method for triggering the H-mode in the TUMAN-3M tokamak is gas puffing [5]. In recent years, new methods for triggering the transition to improved confinement have been sought with the purpose of investigating the generation mechanisms for the radial electric field. As a result, transitions to the H-mode triggered by perturbing the current profile during a rapid increase in the toroidal field (magnetic compression) or a fast current ramp-up have been found and investigated. In addition, a specific L–H transition triggered by an RF pulse in the ion cyclotron resonance (ICR) frequency range was obtained. The occurrence of a transport barrier at the plasma edge was usually identified by an increase in the average plasma density accompanied by a decrease in the D_α emission, which was detected in several sections of the torus. It was natural to suggest that the transitions observed in the TUMAN-3M tokamak were accompanied by an increase in the energy confinement time. This fact was confirmed for the case when a transition to the H-mode of an ohmically heated plasma was triggered by gas puffing [5].

With the above methods for triggering the H-mode, transitions to improved confinement were always accompanied by a decrease in the level of the reflectometer signal in the high-frequency (>100 kHz) range. Such a decrease in the oscillation level was observed in many reflectometer experiments in tokamaks during transitions to the H-mode and is now interpreted as the suppression of plasma fluctuations (see review [1]). However, the TUMAN-3M experiments showed that the change in the level of the fluctuation signal of the reflectometer did not necessarily correlate with the achievement of improved confinement or its degradation. As an example, Fig. 1 shows how the RMS value of the output signal in the band 0.5–1 MHz varies during the fast plasma current ramp-up or ramp-down. The fast current ramp-up triggers a transition to the H-mode, which is seen, e.g., in the increase in the average plasma density (Fig. 1c). In contrast, the decrease in the current is not accompanied by an L–H transition (Fig. 1a). Nevertheless, a decrease in the level of the output U_{RMS} signal was observed in both cases. This experimental result can be explained by the fact that variations in the level of the reflectometer signal at a fixed probing frequency can be attributed to both the variations in the level of plasma fluctuations and the change in the conditions for detecting backscattered radiation, e.g., the shift of the cutoff and/or the change of the fluctuation scale.

In our opinion, the change in the level of scattering plasma fluctuations is more adequately represented by the spectral width of the output signal δf. This spectral characteristic was determined as $\delta f = \int S(f)df/S(0)$, where $S(f)$ is the averaged power spectrum of the complex signal $\dot{U}(t)$. As is seen in Fig. 1b, the spectral width δf in a discharge with a current ramp-down only fluctuates about a certain mean level. In contrast, when a transition to the H-mode is triggered by a fast current ramp-up, the spectral width drops and remains at a low level throughout the entire phase of improved confinement (Fig. 1d). It should be noted that, in many experiments carried out in the TUMAN-3M tokamak, the narrowing of the spectrum of the output signal always correlates with the increase in the plasma density and the decrease in the intensity of the D_α line, i.e., with the suppression of the charged particle transport at the plasma edge. In contrast, the degradation of confinement was always accompanied by a broadening of the spectrum. Another example of such correlation between the spectral width and plasma confinement is illustrated in Fig. 2, which shows the discharge phase in which radiation at the ICR frequency was launched in the plasma. It is seen that the RF pulse results in a short period of improved confinement, which manifests itself by an increase in the density and a decrease in the D_α emission. This phase (from 35 to 38 ms) is characterized by a sharp narrowing of the spectrum. However, the density then stops growing and the D_α emission increases. This change in the confinement correlates with an increase in the spectral width. A spontaneous transition to the H-mode in the ohmically heated plasma occurs at 47 ms. This appears in the narrowing

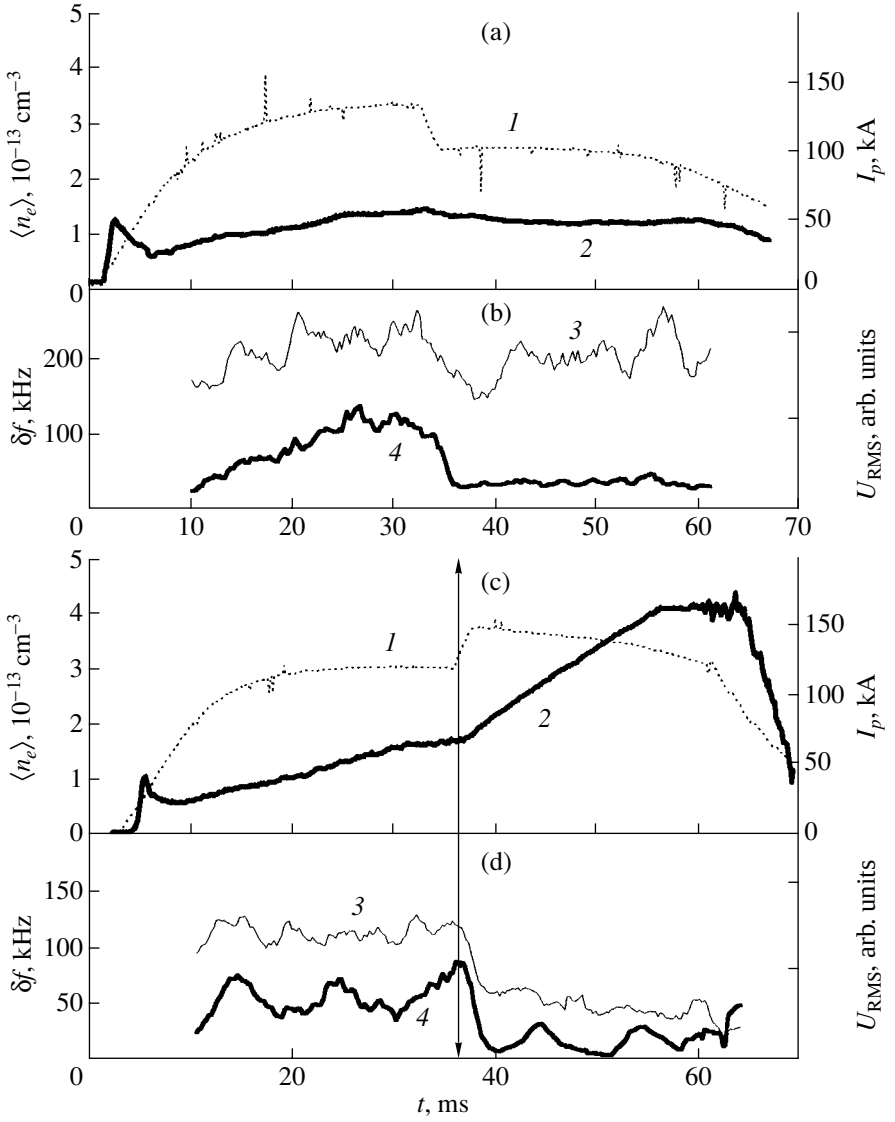

Fig. 1. Comparison of the RMS values U_{RMS} and the spectral width δf of the output complex reflectometer signal in discharges with a fast plasma current (a, b) ramp-down and (c, d) ramp-up: (*1*) plasma current I_p, (*2*) line-averaged electron density $\langle n_e \rangle$, (*3*) δf, and (*4*) U_{RMS}. The vertical line marks the instant of transition to the H-mode during a fast current ramp-up. The probing O-mode frequency is F = (b) 20 and (d) 18 GHz.

of the spectrum and also in the characteristic increase in the plasma density and decrease in the D_α emission.

The possible mechanisms for the broadening of the spectrum under the experimental conditions of the TUMAN-3M tokamak were discussed in detail in [3]. It was shown that the observed spectral width could not be attributed to the Doppler broadening due to a finite width of the antenna directivity diagram in the presence of the poloidal rotation. The broadening of the spectrum by the Doppler mechanism because of the presence of the rotation shear (i.e., because of the spread in the poloidal velocities in the scattering volume) is also of less importance. It is well known that the shear of the poloidal rotation should increase during the transition to the H-mode [1] and should also result in an increase in the spectral width. However, in our experiments, the spectral width decreased. The observed correlation between the change in the spectral width of the backscattered signal and the change in the rates of anomalous transport allows us to assume that the spectral width is determined primarily by a chaotic displacement of scattering fluctuations in the strongly nonlinear stage of instability. In this case, we may expect a correlation between the anomalous transport and the spectral width. This correlation is qualitatively confirmed by the theory of small-angle scattering of laser radiation [6]. According to [6], if the characteristic size of scattering fluctuations is larger than the correlation length of the velocity of chaotic plasma density perturbations, then

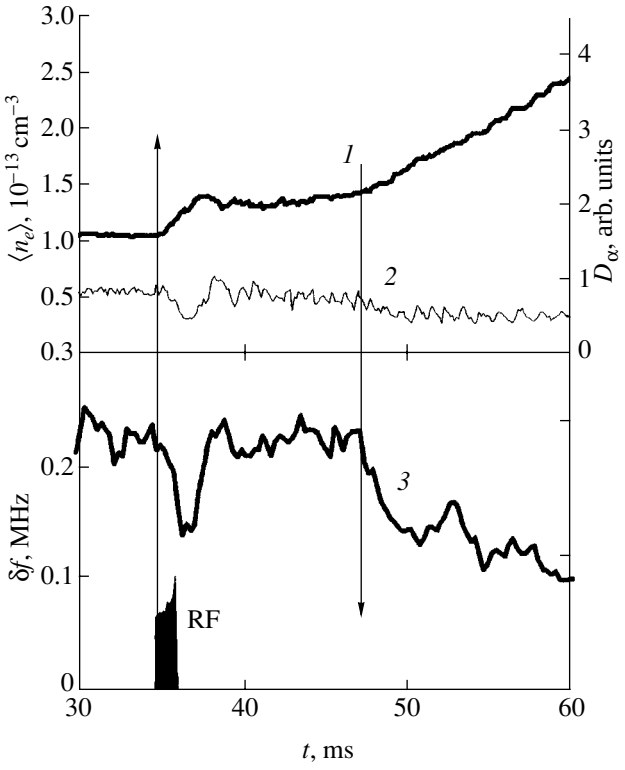

Fig. 2. Time dependence of the spectral width δf in the discharge with a short RF pulse at the ICR frequency: (*1*) $\langle n_e \rangle$, (*2*) D_α emission, and (*3*) δf. Two vertical lines mark the front of the RF pulse and the instant of spontaneous transition to the H-mode. The probing O-mode frequency is F = 19 GHz.

the spectral width is proportional to the turbulent diffusion coefficient. Under conditions of strong refraction of the incident and scattered waves (i.e., under conditions of reflectometry measurements), such correlation has not yet been verified theoretically. Nevertheless, the above phenomenological facts allow us to consider the spectral width to be the most representative parameter when comparing the results obtained using different methods for triggering the H-mode.

Figure 3 shows a comparison of such results in the case when the L–H-transition was triggered by the perturbation of the current profile caused by the magnetic compression (Figs. 3a, 3b) or the plasma current ramp-up (Figs. 3c, 3d). The current I_p increased by 15–20% of its initial value [7]. The rapid increase in the toroidal magnetic field B_T corresponded to a low compression ratio of 1.15 [8]. The transition times are marked in Fig. 3 by vertical lines. In Fig. 3, we can see the fast phases of the transitions, i.e., the short time intervals (shorter than 1 ms) in which the growth rate of the average plasma density increases and the slope of the time dependences of the D_α emission and the spectral width δf vary. The subsequent growth of the average density and the drop of the spectral width apparently indicate that a transport barrier increases and extends in space. As is seen in Fig. 3, the relative variations in the spectral width during the transitions ($\delta f_{OH}/\delta f_H \approx 2$), the characteristic time of spectrum narrowing τ ($\tau = [(1/\delta f_{OH}) d\delta f/dt]^{-1} \approx$ 4–5 ms), and the behavior of the line-averaged density and the D_α emission are close for both scenarios of the transition to the H-mode. Here, δf_{OH} and δf_H are the spectral widths before and after the transition, respectively. All of this apparently indicates that the mechanism for the occurrence and further evolution of the transport barrier is the same in both cases. It is particularly remarkable that similar dependences were observed when the variations in the current-density profile $j(r)$ at the plasma edge (and, correspondingly, in the q profile) were opposite in character. When the magnetic field increases, the current profile should sharpen; in contrast, when the current increases, the profile $j(r)$ should flatten [7].

The variations in the spectral width and the average plasma parameters for the other two scenarios of the transition to the H-mode are compared in Fig. 4. In these discharges, the H-mode was triggered by gas puffing or by launching RF radiation at the cyclotron resonance frequency for hydrogen minority. The triggering of the H-mode in an ohmically heated plasma in TUMAN-3M by means of an additional gas puffing is described in many papers (see, e.g., [5]). A specific transition to improved confinement triggered by an RF pulse was revealed in experiments on ICR heating. The RF power with a power of 100 kW and a frequency of 12 MHz was launched from the low-field side with the use of a single-loop antenna coated with boron nitride. It is well known from divertor experiments in large tokamaks that the L–H transition occurs spontaneously during ICR heating (see, e.g., [9]). Unlike this type of transition, the drop in the D_α emission and the increase in the average plasma density (i.e., the processes associated with the L–H transition in TUMAN-3M) were observed immediately after the RF generator was switched on (Fig. 4c). Over this period, we observed a sharp narrowing of the spectrum of the reflectometer output signal. We should note that, with this method for triggering the H-mode, the relative change of the spectral width $\delta f_{OH}/\delta f_H \approx 3.2$ and the time during which the spectral width δf decreased (τ = 2 ms) were maximum as compared to the other scenarios for achieving improved confinement. In contrast, with gas puffing, we observed a slow variation in the measured values (Fig. 4a), which clearly indicates that the mechanisms for the generation of an edge transport barrier are different in these two cases.

4. MEASUREMENTS OF THE SPECTRAL WIDTH AT DIFFERENT POSITIONS OF THE MICROWAVE CUTOFF

Since the experimental facts indicate that the change in the spectral width δf is related to the rates of anomalous transport processes, it is interesting to estimate the

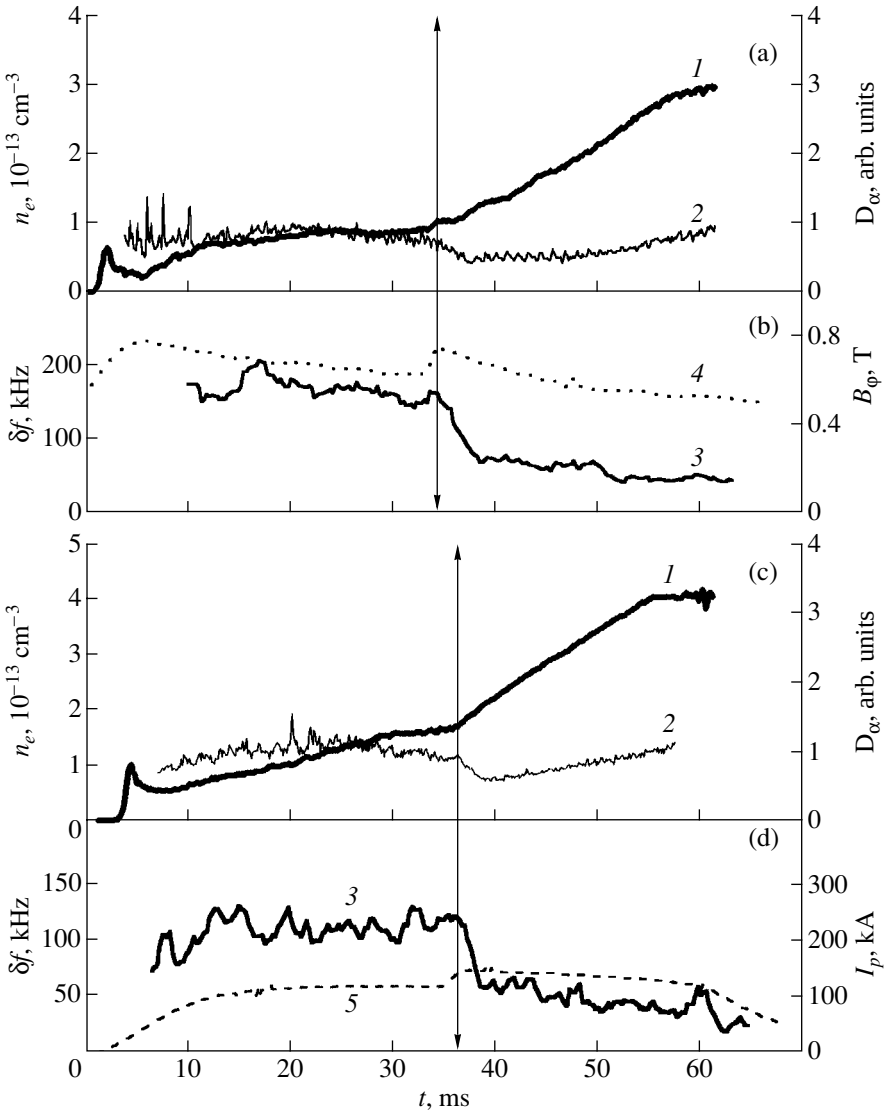

Fig. 3. Comparison of the time dependences of the spectral widths δf for the triggering of the H-mode by (a, b) a rapid increase in the magnetic field B_T and (c, d) a fast plasma current ramp-up: (*1*) $\langle n_e \rangle$, (*2*) D_α emission, (*3*) δf, (*4*) B_T, and (*5*) I_p. The instants of transition to the H-mode are marked by vertical lines. The probing O-mode frequency is F = (b) 17.5 and (d) 18 GHz.

spatial region in which, for different transitions, the suppression of fluctuations, resulting in the narrowing of the observed spectra, occurs. For this purpose, measurements were performed at different positions of the cutoff of the O-mode probing wave, i.e., at different microwave frequencies from 17.5 to 25 GHz. The probing radiation frequency F was varied from shot to shot. We could select a relatively small number of shots with identical signals of monitor diagnostics for different frequencies F. It is these measurements that were used for a comparative analysis. In Fig. 5, the measurements of the spectral width for transitions triggered by the current ramp-up (Figs. 5a, 5b) are compared with those triggered by an RF pulse at the ICR frequency (Figs. 5c, 5d). The results are presented for two probing frequencies 17.5 (curve *1*) and 25 GHz (curve *2*), corresponding to the cutoff electron densities of 3.5×10^{12} and 7.5×10^{12} cm^{-3}, respectively. Figure 5 shows the positions r_c of the probing wave cutoffs estimated from the data of multichord interferometer measurements. In spite of the relatively low accuracy of the determination of r_c, the estimates clearly demonstrate the different penetration depth of incident radiation in the plasma at the given frequencies F.

It is seen in Figs. 5a and 5b that, during a transition triggered by a fast current ramp-up, the narrowing of the spectrum is first observed only when the cutoff is located at the edge, near the last closed flux surface ($r_c \approx 22$–23 cm). It is interesting to note that the values of the spectral width at the instants of transition are different for different probing frequencies. This difference

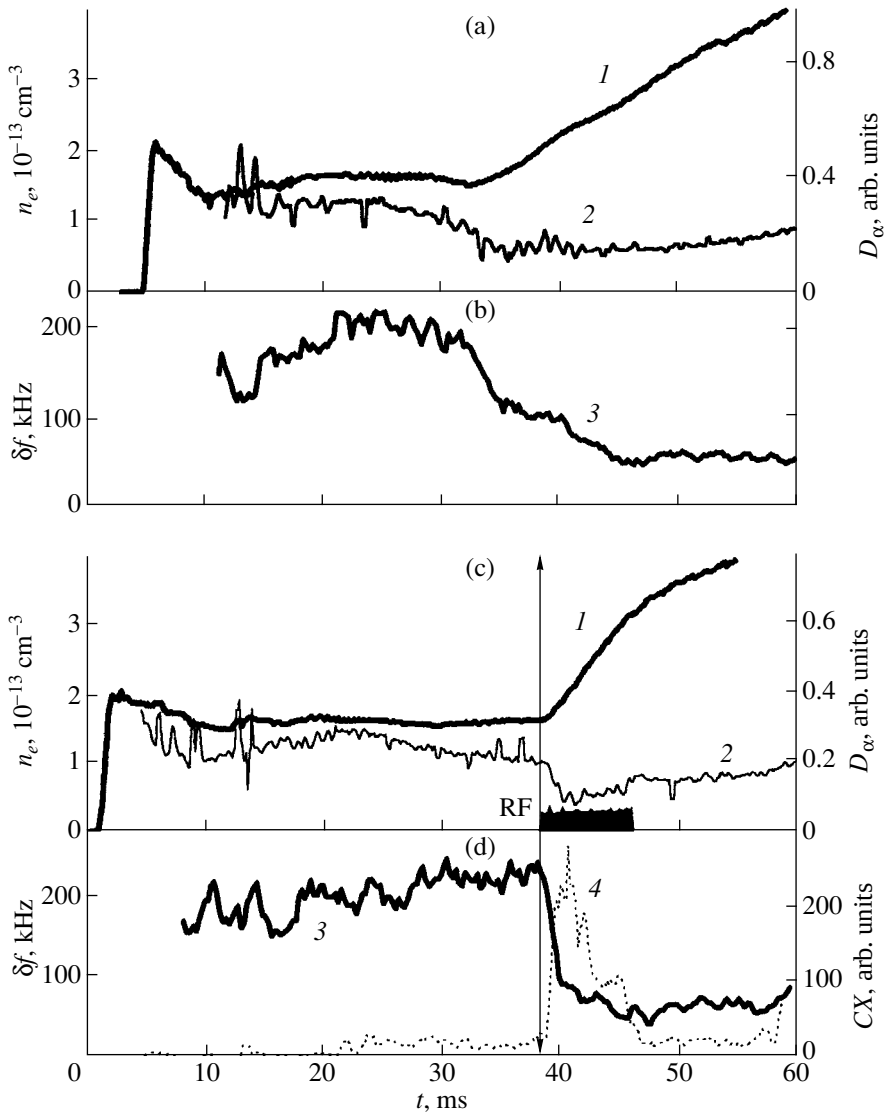

Fig. 4. Comparison of the time dependences of the spectral width δf for the triggering of the H-mode by (a, b) gas puffing and (c, d) an ICR pulse: (*1*) $\langle n_e \rangle$, (*2*) D_α emission, (*3*) δf, and (*4*) charge-exchange (CX) flux of neutral hydrogen with an energy of 1.01 keV. The instants of transition to the H-mode are marked by vertical lines. The probing O-mode frequency is F = (b) 18.5 and (d) 19 GHz.

apparently points to the local character of the method of microwave backscattering, i.e., to the fact that the scattered signal comes dominantly from the cutoff region. On the other hand, assuming that the spectral width is related to the transport coefficient, we can conclude that, during this transition, the transport suppression first occurs at the edge of the plasma and then expands gradually into deeper plasma regions. It follows from the presented dependences that, in this case, the narrowing of the spectrum during the discharge is more pronounced at the edge.

A radically different behavior of the spectral width was observed during transitions triggered by an RF pulse. After RF radiation was input into the plasma, the narrowing of the spectrum was observed simultaneously for every cutoff position (see the time interval 35–38 ms in Figs. 5c, 5d). After the end of the RF pulse, the spectral width measured for deeper cutoff positions was restored rapidly to its value measured before the transition. In contrast, when the cutoff was located at the edge, the narrowed spectrum was observed up to the end of the discharge, which probably indicates that the transport barrier is formed near the plasma edge.

5. DISCUSSION OF RESULTS

The similar behavior of the width of the signal spectrum during both a fast current ramp-up and magnetic compression (Fig. 3) is evidence that the mechanism for the suppression of plasma turbulence and anoma-

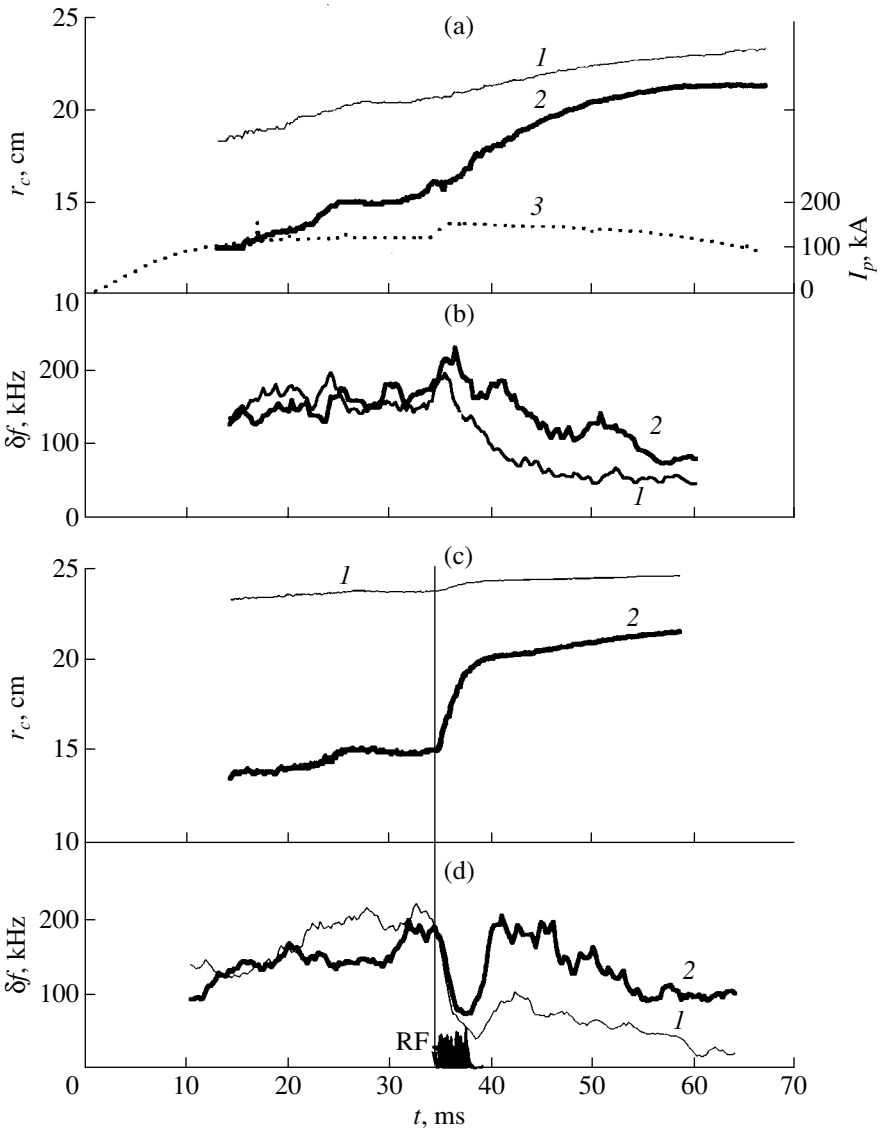

Fig. 5. Time dependences of the spectral width δf for two positions r_c of the cutoff of the probing O-mode radiation during transitions triggered by (a, b) a fast current ramp-up and (c, d) an ICR pulse: (*1*) r_c (F = 17.5 GHz), (*2*) r_c (F = 25 GHz), and (*3*) I_p.

lous transport is the same in both cases. According to the recently proposed concept of an L–H transition triggered by a perturbation of the current profile (see [7, 8]), the primary cause of the transition in both cases is the generation of an inhomogeneous toroidal electric field E_φ at the periphery of the discharge. The Ware drift in the field E_φ turns out to be uncompensated for electrons and ions under the TUMAN-3M conditions. This eventually results in the generation of a negative radial electric field E_r. As was previously established [7], the negative electric field is favorable for the L–H transition. In contrast, according to the same mechanism, the current ramp-down is accompanied by the formation of a positive field E_r at the edge. In this case, the transport barrier does not form and the narrowing of the spectrum is not observed in the experiment (Figs. 1a, 1b). It is obvious that a finite time is required for the expansion of the positive radial field and the transport barrier. This time should be on the order of the diffusion time. This circumstance can probably explain the character of the behavior of the spectral width δf measured at different positions of the incident radiation cutoff. As was expected, δf first decreases at the plasma edge (Figs. 5a, 5b). The delay times observed for the spectrum narrowing at cutoff positions spaced by nearly 3 cm amounts to 8–10 ms, which coincides with the delay time of the expansion of the negative field E_r that was obtained in numerical simulations [10].

A different mechanism for the generation of a negative electric field takes place when the H-mode is initiated by gas puffing. This is evidenced by a slow narrowing of the spectrum and, accordingly, a slow increase in

the plasma density and a slow decrease in the D_α emission (Figs. 3a, 3b). The most probable cause of an increase in the radial electric field in this case is the formation of a pedestal in the plasma pressure during an additional pulsed injection of the neutral gas. Model calculations [11] confirm this mechanism for the generation of the radial electric field. The energy source for such an evolution of the plasma pressure in TUMAN-3M is ohmic heating. In this context, it is interesting to note that the time interval in which the narrowed spectrum was observed increased just after the boronization of the chamber, when the ohmic heating power was reduced [12].

The strong narrowing of the spectrum of the backscattered signal when the H-mode is triggered by an ICR heating pulse allows us to conclude that there is another mechanism for the formation of the transport barrier, different from those governing the transition to the H-mode in the previous scenarios. We note that the transition to the H-mode is not related to heating of the main ion component, because the transition occurs immediately after the RF pulse is switched on and its occurrence depends weakly on the concentration of the resonant hydrogen minority. The primary mechanism for the H-mode initiation in this case may be the rapid generation of high-energy ions in the RF wave field; leaving the plasma, these ions can give rise to a negative electric field. This mechanism for the generation of the radial electric field related to the loss of ions moving along banana orbits was studied theoretically for tokamaks with divertors [13]. The generation of fast ions in the TUMAN-3M tokamak is indirectly confirmed by the data on charge-exchange neutral fluxes. For example, Fig. 4d demonstrates the flux of neutral hydrogen with an energy of 1.01 keV (the temperature of the main ion component is $\approx$0.2 keV). As is seen, the growth time of this flux is close to the characteristic time of spectrum narrowing. Note that, during the RF pulse, the region in which the spectrum narrowing was detected spans to $r = (2/3)a$. However, after the RF pulse, the narrowed spectrum was observed only when the cutoff was located at the edge (Fig. 5d). This means that, during the suppression of turbulent transport, an appreciable pressure gradient responsible for sustaining the radial electric field after the RF pulse occurs only at the plasma edge. Obviously, a certain time is needed for this pressure gradient to form. Actually, when the RF pulse duration was decreased to 3–4 ms, the narrowed spectrum and all characteristic signs of transport suppression were observed only for a short time (Fig. 2); then, the discharge was restored to the regime with a low energy confinement time.

Hence, a comparative study of plasma turbulence confirms that, in the cases when the H-mode is triggered by magnetic compression or by the plasma current ramp-up, the mechanism for the formation of a negative radial field at the plasma edge is basically the same. A fast transition to the H-mode is revealed during an RF pulse at the ICR frequency. In this case, the primary process starting the sequence of phenomena resulting in improved confinement may be the loss of fast ions. A remarkable fact is that the transition to the H-mode in the TUMAN-3M tokamak occurs immediately after the RF pulse is switched on.

ACKNOWLEDGMENTS

We thank V.A. Rozhansky for fruitful discussions. This work was supported in part by the Russian Foundation for Basic Research (project no. 01-02-17992), INTAS (grant no. 97-11018), and the Ministry of Education of the Russian Federation (grant no. TO-7.4-2797).

REFERENCES

1. K. L. Burrell, Phys. Plasmas **4**, 1499 (1997).
2. S. V. Lebedev, M. V. Andreiko, L. G. Askinazi, *et al.*, in *Proceedings of the 18th IAEA Fusion Energy Conference, Sorento, Italy, 2000*, Paper no. EXP5/18.
3. V. V. Bulanin, S. V. Lebedev, L. S. Levin, and V. S. Roitershtein, Fiz. Plazmy **26**, 867 (2000) [Plasma Phys. Rep. **26**, 813 (2000)].
4. V. V. Bulanin and D. O. Korneev, Fiz. Plazmy **20**, 20 (1994) [Plasma Phys. Rep. **20**, 14 (1994)].
5. S. V. Lebedev, M. V. Andreiko, L. G. Askinazi, *et al.*, Plasma Phys. Controlled Fusion **36**, B289 (1994).
6. D. Gresillon, B. Cabrit, J. P. Villain, *et al.*, Plasma Phys. Controlled Fusion **34**, 1985 (1992).
7. L. G. Askinazi, V. E. Golant, V. A. Kornev, *et al.*, in *Proceedings of the 27th European Conference on Controlled Fusion and Plasma Physics, Budapest, 2000*, p. 520; ECA **24B**, 520 (2000).
8. S. V. Lebedev, M. V. Andreiko, L. G. Askinazi, *et al.*, in *Proceedings of the 27th European Conference on Controlled Fusion and Plasma Physics, Budapest, 2000*, p. 524; ECA **24B**, 524 (2000).
9. K. Steinmetz, J. M. Noterdaeme, F. Wagner, *et al.*, Phys. Rev. Lett. **58**, 124 (1987).
10. V. A. Rozhansky, S. P. Voskoboynikov, and A. Yu. Popov, Fiz. Plazmy **27**, 219 (2001) [Plasma Phys. Rep. **27**, 205 (2001)].
11. V. Rozhansky, M. Tendler, and S. Voskoboynikov, in *Proceedings of 23rd EPS Conference on Controlled Fusion and Plasma Physics, Kiev, 1996*, p. 444; ECA **20C**, 444 (1996).
12. S. V. Lebedev, M. V. Andreiko, K. G. Askinazi, *et al.*, Plasma Phys. Controlled Fusion **38**, 1103 (1996).
13. S.-I. Itoh and K. Itoh, Phys. Rev. Lett. **60**, 2276 (1988).

Translated by N. Larionova

Plasma Physics Reports, Vol. 28, No. 2, 2002, pp. 111–124. Translated from Fizika Plazmy, Vol. 28, No. 2, 2002, pp. 128–143.

TURBULENCE AND CHAOS

New Approach to the Probabilistic–Statistical Analysis of Turbulent Transport Processes in Plasma

G. M. Batanov*, V. E. Bening, V. Yu. Korolev**, A. E. Petrov*, K. A. Sarksyan*, N. N. Skvortsova*, and N. K. Kharchev***

**Institute of General Physics, Russian Academy of Sciences, ul. Vavilova 38, Moscow, 119991 Russia*

***Moscow State University, Vorob'evy gory, Moscow, 119899 Russia*

Received September 27, 2001

Abstract—It is proposed to apply the statistical analysis of the increments of fluctuating particle fluxes to examine the probability characteristics of turbulent transport processes in plasma. Such an approach makes it possible to pass over to the analysis of the dynamical probability characteristics of the process under study. It is shown that, in the plasmas of the L-2M stellarator and the TAU-1 linear device, the increments of local fluctuating particle fluxes are stochastic in character and their distributions are scale mixtures of Gaussians. In particular, in TAU-1, the increments obey a Laplacian distribution (which is a scale mixture of Gaussians with an exponential mixing distribution). A mathematical model is proposed to explain such distributions. Possible physical mechanisms responsible for the random character of the increments of fluctuating particle fluxes are discussed.

1. INTRODUCTION

It is clear that heat transport in the edge plasma of toroidal magnetic confinement systems is largely governed by turbulent fluctuations in the charged particle density and the electric and magnetic fields [1, 2]. The correlation between transport processes and turbulent fluctuations manifests itself most clearly during transitions to the improved confinement mode (H-mode) and the generation of transport barriers both at the plasma edge and in the plasma core [3, 4]. A general feature of such transitions is the change in the gradients of the plasma parameters and the shear of the poloidal rotation velocity, as well as variations in the local characteristics of turbulent fluctuations. A transition from one plasma confinement mode to another can be induced in different ways, in particular, by varying the plasma heating power or the particle flux from the toroidal chamber wall [5–7]. However, both of the mechanisms by which local turbulent fluctuations affect the plasma as a whole and the influence of these fluctuations on the features of the processes occurring in plasma still remain unclear.

In some respects, the development of the experimental research on plasma turbulence resembles the evolution of the experimental research on hydrodynamic turbulence. Let us quote here an excerpt from the book by Belotserkovskiĭ and Oparin [8]: "During the first years, these phenomena were interpreted to be completely stochastic processes (determined by the distributions of fluctuating quantities). However, to date, a radical revolution has occurred in the understanding of these phenomena. It was found that turbulence also includes the ordered motion of almost coherent structures, and the interrelation between determinate and chaotic sources is being actively studied now." Indeed, a similar revolution in the study of plasma turbulence has occurred over the last few years: a mixed determinate–chaotic state was observed in plasma turbulence. Moreover, structural plasma turbulence seems to be peculiar to all plasmas. In such turbulence, the formation of structures is random in character and the role of rare events increases (in [9], such a state was called rigid turbulence). That is why the probabilistic–statistical approach to the analysis of turbulent plasma fluctuations has been developed in recent years [10, 11]. Strong structural plasma turbulence was observed in several plasma experiments in which random ensembles of stochastic plasma structures were revealed. For example, it was shown that strong structural turbulence is characteristic of the plasma of the L-2M stellarator: at the edge, it is produced by ensembles of MHD structures, whereas, in the plasma core, it is produced by ensembles of vortex drift structures [12, 13]. Ensembles of nonlinear ion-acoustic solitons were observed in ion-acoustic structural turbulence in a low-temperature plasma [14]. At present, all of the methods of spectral analysis of the experimental data can be applied to examining the turbulence characteristics. However, we believe that the use of the above probabilistic–statistical analysis is more adequate for studying such turbulence, because this method makes it possible to obtain additional information on the turbulent process. The method implies the calculation and analysis of the correlation coefficients between the amplitudes of plasma fluctuations, the means and variances of the ensembles of plasma processes, and the probability distribution functions (PDFs). To date, a great deal of experimental

1063-780X/02/2802-0111$22.00

data from PDF measurements has been accumulated in experiments performed in different devices. The quantities measured in experiments on structural plasma turbulence usually have non-Gaussian PDFs. In this context, the problem of the deviation of the PDF from Gaussian arises, because, until now, all theories of plasma turbulence operated with Gaussian distributions of the fluctuation amplitudes. The conclusion that the PDF differs from Gaussian is usually deduced from the shape of a histogram constructed from the amplitudes of fluctuating quantities at equidistant times. The construction of the PDF in this way is not quite adequate. In fact, it can be easily shown that, even for a discrete time sequence constructed for classical Brownian motion, this approach gives an excess value of $M_4 \approx 4$, whereas, for a Gaussian distribution, we have $M_4 = 3$.[1] The problem is that the amplitude values taken at equidistant times do not constitute a homogeneous independent sample; as a result, it is difficult to make decisive conclusions about the probabilistic properties of the process under study.

In this paper, we will consider the problem of correct (from the standpoint of mathematical statistics) processing of the experimental data on turbulent plasma fluctuations using as an example the measured local turbulent fluxes in the L-2M stellarator and the TAU-1 linear device and will discuss in more detail the resultant statistical characteristics of the turbulent processes under study.

We will mainly consider the PDF of amplitudes of the radial local turbulent particle flux (which will be referred to below as a local flux).[2] The PDF measurements of local fluxes have been carried out in many devices (linear devices, tokamaks, and stellarators [15, 16]). The measured PDFs usually differ from Gaussians by a higher peakedness and more slowly decreasing tails. Such features of the amplitude distribution of the local flux indicate the important role of rare events in transport processes. However, until recently, the mechanisms responsible for the difference of the local flux PDF from Gaussian were not discussed. Only recently [17, 18] have attempts been made to relate the statistical probability characteristics to nonlinear wave processes in plasma.

The paper is organized as follows. Section 2 gives a brief mathematical description of PDFs with tails decreasing more slowly than in Gaussian distributions. Section 3 is devoted to the processing of the measured local fluxes. In Section 4, the results obtained are discussed, and Section 5 presents a brief summary.

[1] Proof of this assertion is given in the Appendix.

[2] Below, we consider the so-called one-point radial fluctuating particle flux defined as $\tilde{\Gamma} = \frac{c}{\mathbf{B}} n_{\sim} \mathbf{E}_{\sim}$.

2. HEAVY-TAILED DISTRIBUTIONS IN PHYSICS

During the last few decades, non-Gaussian probability models have attracted considerable interest in various fields of science. Now, it is generally accepted that normal distributions (which are applied to the modeling of many physical phenomena) fail to adequately describe experimental data. The observed empirical distributions possess considerably larger excesses, higher peakedness, and heavier tails (i.e., tails decreasing more slowly as compared to normal distributions). This means that, for such processes, the number of observations of very small and very large values (i.e., values substantially different from the standard deviation) exceeds the number of similar observations for a normal process. This phenomenon is almost universal and is observed, e.g., in turbulent plasma and stock price fluctuations.

There have been many attempts to explain the observed departure from the normal distribution. Historically, the first models were stable distribution models that appeared as limit laws in the limit theorems for the sums of independent random variables (see, e.g., [19, 20]). These models possess two drawbacks. The first is that only a few stable distributions can be expressed via elementary or special functions; for this reason, the statistical analysis of stable models is not a simple matter because it is often impossible to deal directly with the probability functions. The second drawback is the assumption that elementary summands have infinite variances is very far from being realistic.

Recently, alternative models have been proposed to describe heavy-tailed distributions. These models have the form of scale mixtures of normal laws. Such distributions appear as limit distributions in the limit theorems for the sums of a random number of random variables with finite variances (see, e.g., [21, 22]). In these models, the observed high peakedness of sample distributions can be explained as follows. Each observation in the sample has the normal distribution (there are many reasons for this assumption; the entropy approach and the approach based on the central limit theorem of probability theory both lead to this conclusion). However, being influenced by some global factor (or several factors), each observation has its own values of the location and scale parameters of the normal distribution. In other words, the sample can be regarded as nonhomogeneous. As a result, we naturally arrive at the representation of the sample as an ensemble of many homogeneous subsamples. This actually means that the total sample distribution is a mixture of normal distributions of homogeneous subsamples. In this case, the problem of determining the mixing distribution is of great importance. This distribution corresponds to the distribution of global factors.

In other words, if the system under consideration is closed, then the observed distribution is normal. However, in open systems influenced by some external fac-

tors, this is not the case, and, instead of a normal distribution, we have a mixture of normals with mixing distributions determined by external factors.

Formally, if the standard normal distribution $\Phi(x)$ is defined as

$$\Phi(x) = \frac{1}{\sqrt{2\pi}}\int_{-\infty}^{x} e^{-u^2/2}du, \quad x \in \mathbf{R},$$

then, in the general case, the total sample distribution can be written in the form

$$F(x) = \int_{-\infty}^{\infty}\int_{0}^{\infty}\Phi\left(\frac{x-\nu}{u}\right)dQ(u,\nu), \quad x \in \mathbf{R}, \qquad (1)$$

where $Q(u, \nu)$ is the two-dimensional distribution function. Therefore, the problem of fitting the sample by a model distribution reduces to the problem of finding $Q(u, \nu)$. Unfortunately, in the general case, the latter problem appears to be ill-posed. Its solution is not unique. There are two ways of regularizing this problem.

(i) A simplification of the model by replacing distribution (1) by simpler representations. One of them is

$$F(x) = \int_{-\infty}^{\infty}\Phi\left(\frac{x-\nu}{u}\right)dQ_1(\nu), \quad x \in \mathbf{R} \qquad (2)$$

with an unknown parameter u and unknown one-dimensional distribution function $Q_1(\nu)$. Formula (2) represents $F(x)$ as a location mixture of normals. The second simpler representation of $F(x)$ is

$$F(x) = \int_{0}^{\infty}\Phi\left(\frac{x-\nu}{u}\right)dQ_2(u), \quad x \in \mathbf{R} \qquad (3)$$

with an unknown parameter ν and unknown one-dimensional distribution function $Q_2(u)$. Expression (3) represents $F(x)$ as a scale mixture of normal distributions.

(ii) Replacing $Q(u, \nu)$ with its discrete approximation $Q_n(u, \nu)$. In this case, instead of the integral representation (1), we obtain

$$F(x) = \sum_{j=1}^{n} p_j\Phi\left(\frac{x-\nu_j}{u_j}\right), \quad x \in \mathbf{R} \qquad (4)$$

with $3n - 1$ parameters $p_1, \ldots, p_n, u_1, \ldots, u_n, \nu_1, \ldots, \nu_n$ ($p_1 + \ldots + p_n = 1$).

All of the reduced problems are well posed and can be solved by either parametrical techniques (i.e., using a special parametric representation for $Q_1(\nu)$ and $Q_2(u)$; for example, $Q_2(u)$ may be regarded as a gamma distribution or a universal Gaussian distribution with unknown parameters whose estimates should be found statistically) or nonparametric techniques (the so-called "separation of mixtures").

3. EXPERIMENTAL RESULTS

In this paper, we study the probability characteristics of fluctuating particle fluxes measured in the plasmas of the L-2M stellarator and the TAU-1 model device. The parameters of the devices and the plasma are presented in [13, 14]. The L-2M stellarator has two helical windings of different polarity ($l = 2$). The major radius of the torus is $R = 100$ cm, and the mean minor plasma radius is $\langle r\rangle = 11.5$ cm. The plasma was produced and heated by ECR heating at the second harmonic of the electron gyrofrequency. The magnetic field at the axis of the plasma column was $B = 1.3$–1.4 T, the gyrotron power was $P_0 = 150$–200 kW, and the microwave pulse duration was 10–12 ms. Measurements were performed at the mean plasma density $\langle n\rangle = (1.3–1.8) \times 10^{13}$ cm^{-3}. The central electron temperature was in the range $T_e(0) = 0.6$–1.0 keV. The working gas was hydrogen. In the edge plasma at the radius $r/r_s = 0.9$ (where r_s is the separatrix radius), the density was at a level of $n(r) = (1–2) \times 10^{12}$ cm^{-3} and the electron temperature was $T_e(r) = 30$–40 eV. The relative level of density fluctuations was $(\delta n/n)_{\text{out}} = 0.2$–$0.25$ in the outer plasma region and $(\delta n/n)_{\text{in}} = 0.1$ in the inner plasma region. In the TAU-1 device, a cylindrical argon plasma column 4 cm in diameter and 100 cm in length was produced in a uniform magnetic field with an induction of $\leq$800 G by a steady low-energy electron beam with an energy of $E_b = 60$–150 eV at an argon pressure of $p = (2–4) \times 10^{-4}$ torr. The plasma density was maintained at a level of $n = (0.9–1.2) \times 10^{10}$ cm^{-3}. The electron temperature was 5–7 eV, and the ion temperature was $T_i \approx 0.1T_e$. The main differences between these devices are the magnetic field topology (the L-2M field is toroidal and the TAU-1 field is uniform) and the plasma temperature ($T_e(0) = 0.6$–1.0 keV in L-2M and $T_e = 5$–7 eV in TAU-1). On the other hand, as was observed in previous experiments [23], the spectral and statistical characteristics of plasma turbulence in both devices are very similar (broadband continuous frequency spectra, autocorrelation functions with nonvanishing oscillating tails, etc.).

In our measurements, the local fluctuating particle flux was defined as $\tilde{\Gamma} = (\delta n_e \delta v_r)$ [10, 11], where δn_e is the plasma density fluctuation, $\delta v_r = c\delta E_\Theta/B$ is the radial velocity fluctuation, $\delta E_\Theta = (\delta\varphi_1 - \delta\varphi_2)/\Delta\Theta r$ is the fluctuation of the poloidal electric field, $\delta\varphi$ is the fluctuation of the plasma floating potential, Θ is the poloidal angular coordinate, and r is the mean radius of the magnetic surface. Obviously, the local flux is governed by turbulence resulting from a variety of instabilities existing in the plasmas of these devices. The description of the local flux is simplified if its origin is associated with a limited set of plasma instabilities. In exper-

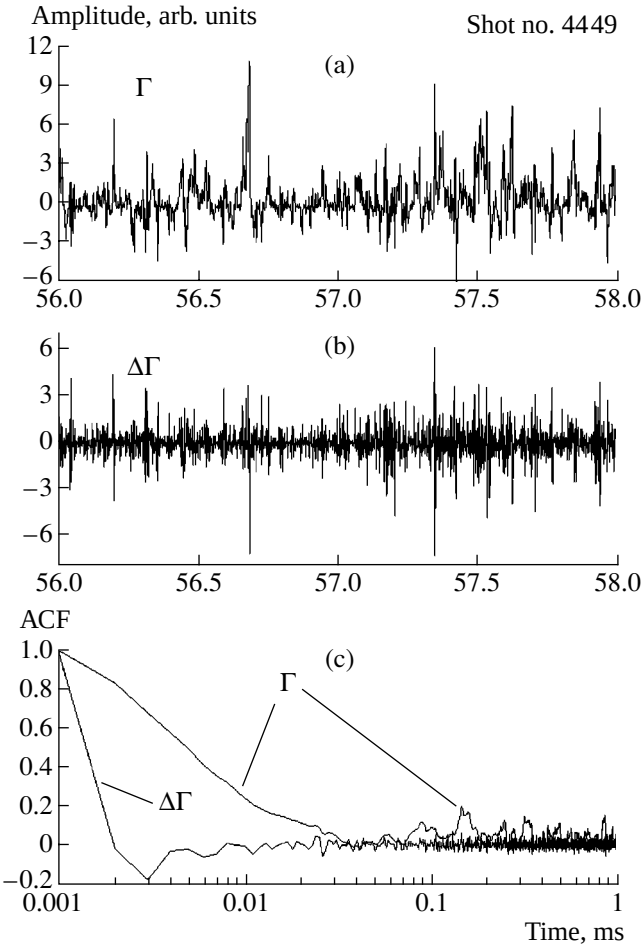

Fig. 1. Time behavior of (a) the local particle flux $\tilde{\Gamma}$ and (b) its increments $\Delta\tilde{\Gamma}$ and (c) the ACFs of $\tilde{\Gamma}$ and $\Delta\tilde{\Gamma}$ in the L-2M stellarator. The signal sampling rate is 1 MHz.

iments carried out in the TAU-1 device, the local flux is governed by the drift-dissipative instability [24]. In the L-2M stellarator, the interchange resistive ballooning instability is dominant in the edge plasma [11], whereas the drift-dissipative instability prevails in the plasma core [13]. For TAU-1, the frequencies of turbulent fluctuation spectra are in the range from several kilohertz to one-hundred kilohertz ($\Delta f/f|_{\text{TAU-1}} \approx 0.3$). The frequency spectrum of turbulence resulting from the resistive ballooning instability in the stellarator is broader and extends over several hundreds of kilohertz ($\Delta f/f|_{\text{[L-2M]}} \approx 1$). In this paper, we analyze the local fluxes measured in the edge plasma of the L-2M stellarator and in the low-temperature plasma of TAU-1. In these relatively simple cases, we can introduce the effective growth rate, $\gamma^{\text{eff}} = f(\gamma, \chi)$ (where $\gamma = \gamma_1, \ldots, \gamma_k$ and $\chi = \chi_1, \ldots, \chi_l$), in order to describe variations in the local flux. Even if only one type of instability develops, the effective growth rate includes not only the linear growth rate of the instability but also the characteristic nonlinear growth rates related to the limitation of the amplitudes of unsteady motions, the appearance of plasma structures in the nonlinear stage of the instability, and the interaction between plasma structures: $\gamma = \gamma_1, \ldots, \gamma_k$, where k is the number of linear and nonlinear mechanisms responsible for the growth of fluctuations. It is reasonable that all of the linear and nonlinear damping rates $\chi = \chi_1, \ldots, \chi_l$ (where l is the number of linear and nonlinear mechanisms responsible for the damping of fluctuations) also must be included in the effective growth rate of the local flux. The variation in the local flux is determined by variations in δn_e and δv_r with respect to the thermal noise level. In our experiments, variations in the local fluxes were measured with probe arrays, each consisting of three individual cylindrical probes. The probes measured the plasma density fluctuations δn (in the regime in which the ion saturation current I_s is measured, $\delta I_s \sim \delta n$) and floating potential fluctuations $\delta\varphi$. These measurements were then used to calculate the radial fluctuating particle flux. The sampling rate (i.e., the reciprocal of the time interval between successive points) was up to 5 MHz, and the realization length was up to 128 kB. The sampling rates are given in the figure captions.

Figure 1a shows typical signals of the local flux $\tilde{\Gamma}$ (Fig. 1a) and its increment $\Delta\tilde{\Gamma} = \tilde{\Gamma}_j(t_j) - \tilde{\Gamma}_{j-1}(t_{j-1})$ (Fig. 1b) for edge plasma of the L-2M stellarator. It is seen that both signals are intermittent and bursty. Figure 1c shows the autocorrelation functions (ACF) of the flux and its increment for the same signals. It is seen that, within the given time window, the ACF of $\tilde{\Gamma}$ does not approach the noise level, whereas the ACF of $\Delta\tilde{\Gamma}$ approaches this level in several microseconds. The slow variation of the ACF of the local flux in the edge plasma demonstrates that the flux amplitudes does not represent a homogeneous independent sample, whereas the rapid drop in the ACF of $\Delta\tilde{\Gamma}$ indicates the random and independent character of the increments. Figure 2 illustrates the time dependence of the local flux (Fig. 2a) and its increments (Fig. 2b) in the TAU-1 plasma and their autocorrelation functions (Fig. 2c). The autocorrelation function of the local flux $\tilde{\Gamma}$ associated with drift instability in the low-temperature plasma approaches the noise level more rapidly than the local flux in the stellarator, but the ACF of its increment $\Delta\tilde{\Gamma}$ approaches the noise level even more rapidly. Hence, the amplitudes of the local flux in TAU-1 do not represent a homogeneous independent sample; in contrast, the increments of the local flux constitute a homogeneous independent sample. Hence, when applying the conventional methods of probability analysis, it is more correct to use the increments of the fluctuating flux instead of the flux amplitudes themselves.

We describe the local particle flux determined by plasma fluctuations in the following form: $\tilde{\Gamma} = \tilde{\Gamma}(t_j) =$

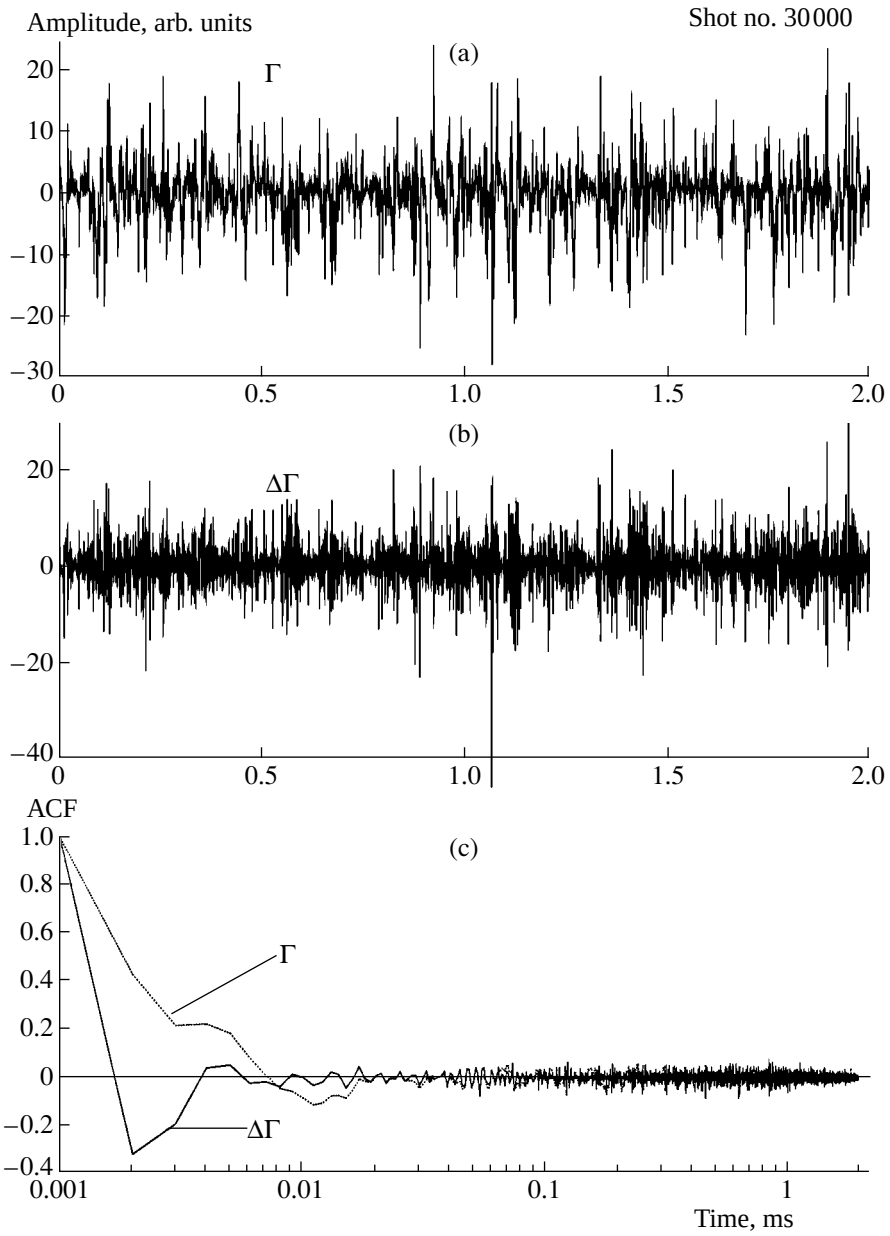

Fig. 2. Time behavior of (a) the local particle flux $\tilde{\Gamma}$ and (b) its increments $\Delta\tilde{\Gamma}$ and (c) the ACFs of $\tilde{\Gamma}$ and $\Delta\tilde{\Gamma}$ in the TAU-1 device. The signal sampling rate is 1 MHz.

$\tilde{\Gamma}_j^0(t_j)e^{\gamma^{\text{eff}}}t_j$, where $\tilde{\Gamma}_j^0$ is a quantity slowly varying in time. Then, we can consider a mathematical model of the dynamic characteristics of the process $\tilde{\Gamma}$ (namely, $\gamma^{\text{eff}} = \gamma_j^{\text{eff}}(t_j)$ dependent on the random time t_j and constituting the set of random values γ_j^{eff}). Such a representation corresponds to the shape of the ACF of the local flux increments shown in Figs. 1c and 2c. As was mentioned above, for unstable plasma fluctuations, the parameter γ^{eff} depends on all of the linear and nonlinear growth and damping rates that can occur under our experimental conditions. We can suggest that the physical mechanisms responsible for the random character of the parameter γ^{eff} will determine the characteristic features of local fluctuation transport.

Figure 3 shows the PDFs for the processes of a local fluctuating flux and its increments in L-2M (Figs. 3a, 3c) and TAU-1 (Figs. 3b, 3d). The asymmetry coefficient M_3 and the excess M_4 of the corresponding PDFs are also shown. The PDF of the time sample of the local flux $\tilde{\Gamma}$ (Figs. 3a, 3c) differs substantially from Gaussian. Note that the measured PDFs of the density fluctu-

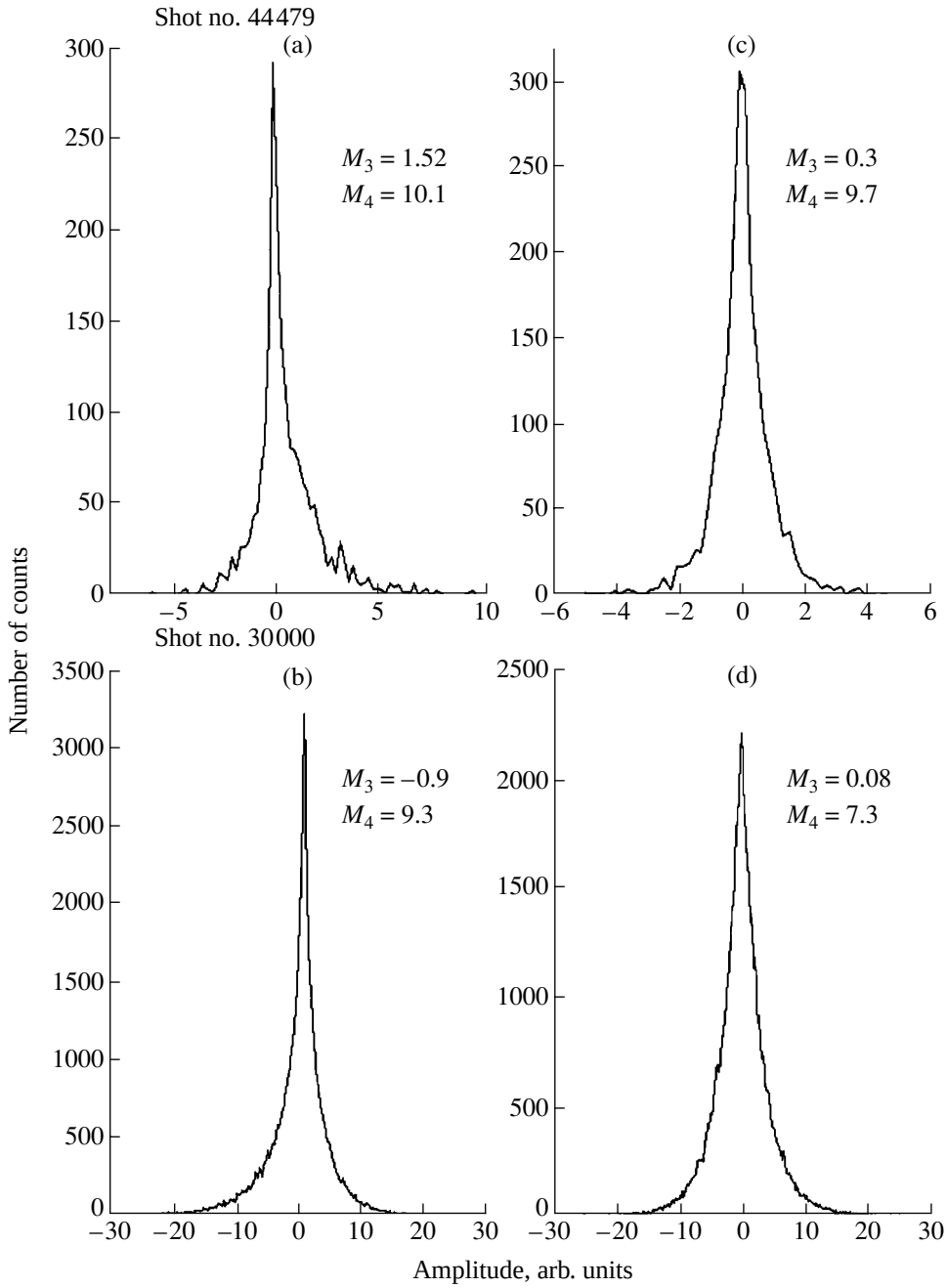

Fig. 3. PDF for the local particle flux $\tilde{\Gamma}$ and its increments $\Delta\tilde{\Gamma}$: (a) PDF of $\tilde{\Gamma}$ for L-2M, (b) PDF of $\tilde{\Gamma}$ for TAU-1, (c) PDF of $\Delta\tilde{\Gamma}$ for L-2M, and (d) PDF of $\Delta\tilde{\Gamma}$ for TAU-1.

ations δn_e and the poloidal electric field δE_Θ in L-2M and TAU-1 are usually Gaussian. Even if the data from the time sample of $\tilde{\Gamma}$ were independent and homogeneous, the PDF of the local flux $\tilde{\Gamma}$ obtained by multiplying two Gaussian fluctuating variables (δn_e and δE_Θ) would differ from Gaussian by having a heavier tail and sharper vertex (the proof of this assertion is given in the Appendix). In our case, when there are no homogeneous and independent data in the time sample of the local flux $\tilde{\Gamma}$, such a non-Gaussian PDF of the local flux is difficult to analyze. Hence, it is more interesting to consider the deviation of the increments of the local flux $\Delta\tilde{\Gamma}$ from the Gaussian PDF, because, as was noted above, the time sample for the flux increments consists of statistically homogeneous and independent values. Characteristically, the PDF of the process $\Delta\tilde{\Gamma}$ is sym-

metric, which indicates a dynamic symmetry of the flux increments. The asymmetry coefficient and excess of the PDF of the process $\Delta\tilde{\Gamma}$ in L-2M are $M_3 = 0.9$ and $M_4 = 9.3$; for TAU-1, they are $M_3 = 0.08$ and $M_4 = 7.3$. The values of the moments of the discrete process of increments of the local flux in TAU-1 are very close to the moments of the continuous process of a random variable with the Laplacian PDF: $M_3 = 0$ and $M_4 = 6$ (the difference between the excess values may be attributed to the procedure of the signal discretization). Figure 4a shows a histogram of the amplitudes of the increments of the local flux in TAU-1 (see Fig. 3d) and its approximation by a Laplacian distribution (the Gaussian distribution is also shown in the figure). In Fig. 4b, we can see that the Gaussian distribution is inappropriate for describing the heavy tail in the histogram of the amplitudes of the local flux increments. Note that the time sample of the local flux increments contains 64 kB points. The two curves differ by only several percent, and the peakedness of the PDF is described better by the Laplacian process than by the Gaussian distribution. This example is more interesting because the corresponding histogram agrees well with the Laplacian PDF. The Laplacian PDF (accurate to the scale parameter) can be represented as a scale mixture of Gaussians with an exponential[3] mixing distribution. Thus, if $L(x)$ is a Laplacian PDF,

$$L(x) = \frac{1}{\sqrt{2}}\int_{-\infty}^{x} e^{-\sqrt{2}|x|}dx = \left\{\begin{array}{ll} \frac{1}{2}e^{\sqrt{2}x}, & x < 0 \\ 1 - \frac{1}{2}e^{-\sqrt{2}x}, & x \geq 0 \end{array}\right\}, \quad (5)$$

and $\Phi(x)$ is the standard normal distribution function,

$$\Phi(x) = \frac{1}{\sqrt{2\pi}}\int_{-\infty}^{x} e^{-u^2/2}du, \quad (6)$$

then we have

$$L(x) = \int_0^\infty \Phi\left(\frac{x}{\sqrt{\sigma}}\right)e^{-\sigma}d\sigma, \quad x \in R \quad (7)$$

(see, e.g., [25]). From here, we can conclude that each increment $\Delta\tilde{\Gamma} = \tilde{\Gamma}_j - \tilde{\Gamma}_{j-1}$ is a result of classical (Brownian) diffusion from the point $\tilde{\Gamma}_{j-1}$ to the point $\tilde{\Gamma}_j$ occurring with its own diffusion coefficient σ_j. This means that the random process of the local flux increments can be described by the diffusion law in which the coefficient σ_j varies randomly on successive sampling intervals (when varying j). Hence, in this diffusion law for the process of the local flux increments, the diffusion coefficients σ_j ($j \geq 1$) are random values that obey the exponential distribution [see Eqs. (1)–(3)]. In this connection, we note that the Gaussian distribution has the highest entropy among all the laws with a finite second moment and corresponds to steady states in closed systems. The exponential distribution has the highest entropy among the laws with a finite first moment that are concentrated on the positive semiaxis; this distribution corresponds to stable states in open systems. Naturally, both plasma devices are open systems for which the duration of dynamic equilibrium with respect to macroscopic plasma parameters substantially exceeds the characteristic fluctuation times. It turns out that the measured distribution of the local flux increments in the TAU-1 device corresponds to the most stable steady-state process for an open plasma system. The PDF for the local flux increments is the Laplacian distribution (the distribution with the highest entropy) only if the sampling interval is as short as 1–5 μs; as the time interval increases, the PDF of the increments departs from Laplacian (the shape of the

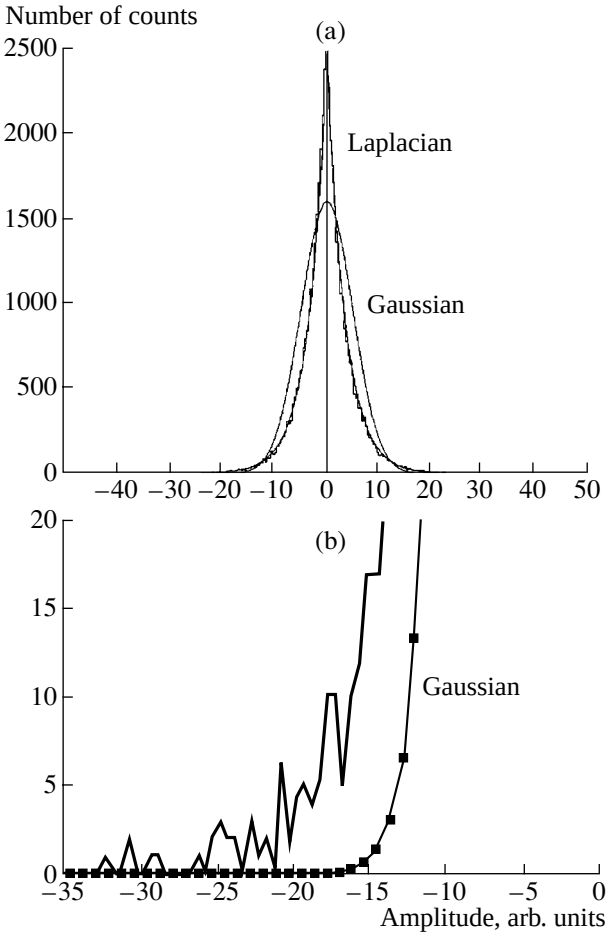

Fig. 4. (a) Approximation of the histogram of the increments $\Delta\tilde{\Gamma}$ of the local flux in TAU-1 by a Laplacian distribution, and (b) the comparison of a Gaussian distribution with the tail of the histogram of the increments. The signal sampling rate is 1 MHz.

[3] In the case of drift oscillations in TAU-1, the PDFs of the increments of fluctuations of the floating potential and the saturation ion current are described by normal distributions.

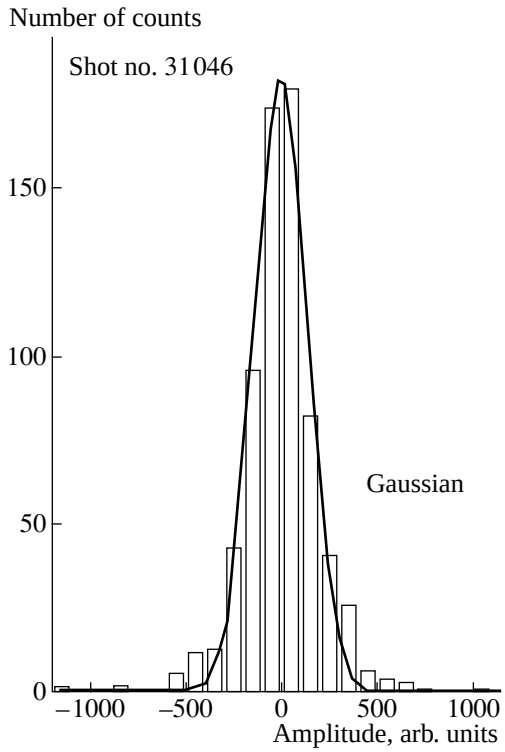

Fig. 5. Histogram of the increments of the local flux measured at a sampling rate of 10 kHz in TAU-1 (M_3 = 0.1, M_4 = 7).

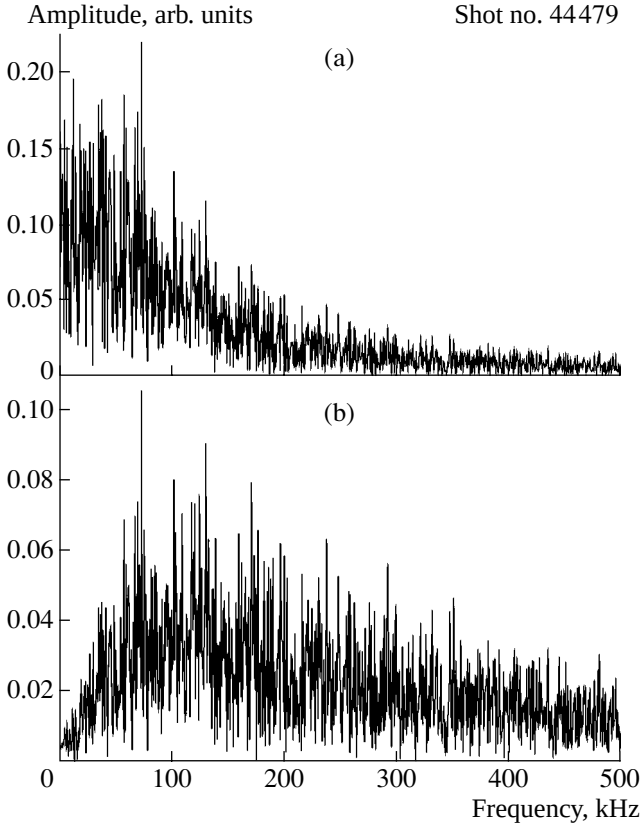

Fig. 6. Fourier spectra of (a) the local flux and (b) its increments in the edge plasma of the L-2M stellarator.

PDF in this case will be examined below). This time interval (1–5 μs) is characteristic of a local flux associated with the drift-dissipative instability. Previously, we measured the oscillation periods, the linear growth rates, the saturation times, the autocorrelation times of turbulent fluctuations, etc., for drift motions driven by the drift-dissipative instability under the TAU-1 experimental conditions. It turns out that the variations in the local particle flux determined by drift motions occur on a time scale (we have already mentioned that this time is characteristic of the local flux) more than one order of magnitude shorter than those drift-motion times.

We can also assume that, in the general case, the fluctuating particle flux $\tilde{\Gamma}$ is a doubly stochastic diffusion process (or, in other terms, the diffusion process with random time). Mathematically, such a process results from the passage to the limit in the generalized Cox process[4] [21]. In this case, the incremental distributions of individual processes can be represented as scale mixtures of Gaussians, which is confirmed in our case by the statistical analysis of $\Delta\tilde{\Gamma}$. The Laplacian distribution obtained for the drift flux increments is one of the important cases of such distributions. The probability for large (larger than three standard deviations[5]) variations in the local flux increments distributed by the Laplacian law is many times higher than that for the Gaussian law. In other words, the probability of the experimental observations of ultrafast[6] increments of the local flux increases (Fig. 4b). Figure 5 shows a histogram of the increments of the drift particle flux in the TAU-1 device for the case when the time interval between observations is 100 times longer than for the initial distribution presented in Fig. 2d (the longer the sampling time, the lower the contribution to the PDF from the processes determined by the influencing functions). The PDF for $\Delta\tilde{\Gamma}$ approaches the normal (Gaussian) distribution, which corresponds to the asymptotic of the generalized Cox processes [22].

The spectral characteristics of the local flux increments apparently differ from the spectral characteristics of the fluxes themselves. This is illustrated in Fig. 6 by the Fourier spectra of the local fluxes (Fig. 6a) and their increments (Fig. 6b) in the edge plasma of the L-2M stellarator. The broadband ($\Delta\omega > \omega$) spectra of the local flux increments have a typical noise shape, and the frequency values for $\Delta\tilde{\Gamma}$ are higher than those

[4] This is a doubly stochastic Poisson process $N^{(k)}(t) = N_1(\Lambda_k(t))$, where N_1 is a homogeneous Poisson process with unit intensity and Λ_k are random processes independent of N_1. In [21], arguments are also presented in favor of using generalized Cox processes as mathematical models for inhomogeneous chaotic physical processes.

[5] In probability theory, this estimate is known as the three-sigma rule.

[6] In principle, the probability of the observation of slow (ultraslow) events also increases; however, the contribution from these events to the transport processes is insignificant (Fig. 4a).

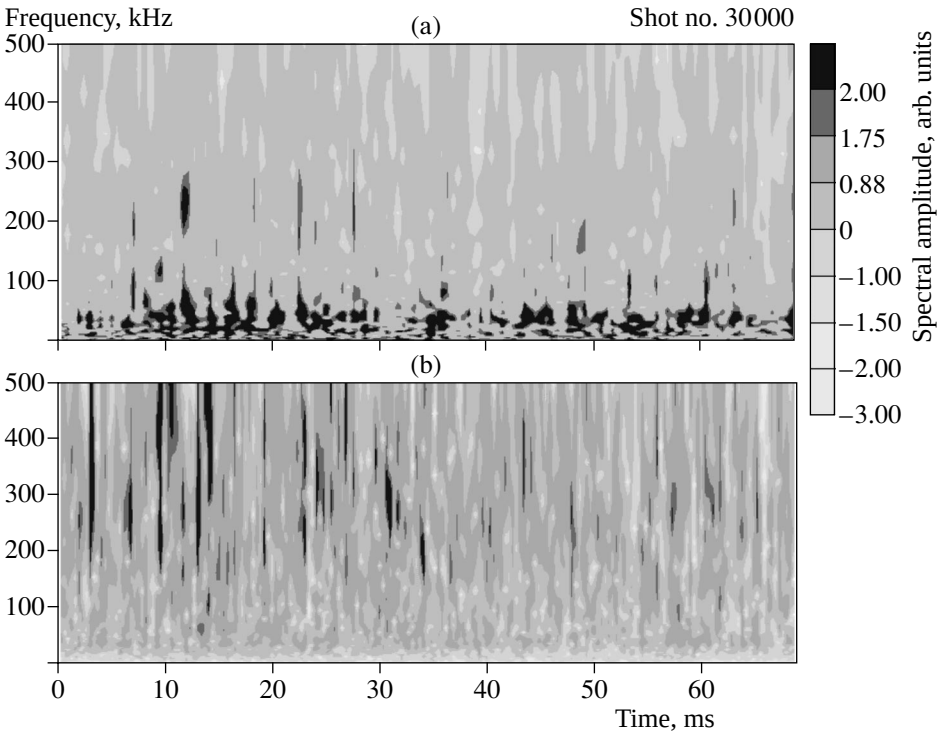

Fig. 7. Time behavior of the wavelet spectra of (a) the local flux and (b) its increments in the TAU-1 device.

for $\tilde{\Gamma}$. Similar to the local flux increments in the TAU-1 device, the characteristic times of the local flux increments in the edge plasma of the L-2M stellarator turn out to be much shorter than the previously known periods and autocorrelation times for the edge turbulence driven by the resistive ballooning instability.

We have already pointed to the intermittent character of the signals $\tilde{\Gamma}$ and $\Delta\tilde{\Gamma}$ (see the time dependences shown in Figs. 1a and 2a). We believe that the random character of the local flux and its increments is more clearly demonstrated in the time dependence of the wavelet spectra of these quantities, when the signal is represented not as a superposition of harmonic functions (as in the conventional Fourier analysis), but as a superposition of another base functions, the so-called wavelets [14]. Wavelet analysis allowed us to trace the time evolution of the flux events and their emergence and disappearance in the spectrum. The frequency spectrum was constructed in successive time intervals using the formula

$$W_f(a,\tau) = \int_T x(t)\Psi_a(t-\tau)dt. \qquad (8)$$

We used wavelets of the same form $\Psi_a(t) = a^{-1/2}\exp[i2\pi t/a - (t/a)^2/2]$ as in [14]. Figure 7 shows the time evolution of the wavelet spectra of both the flux driven by the drift instability and the flux increments. These time-dependent spectra are compiled from 100 spectra computed for successive 200-μs time intervals. The amplitude of spectral components is shown by shades of gray. The frequency corresponding to the wavelet duration is plotted on the abscissa, and the time is plotted on the ordinate. The spectra of $\tilde{\Gamma}$ and $\Delta\tilde{\Gamma}$ vary substantially with time, whereas the macroscopic plasma parameters do not change. It is seen that the local flux in TAU-1 and the increments of this flux are intermittent and exist as extending events with pauses between them. In Fig. 7, these events correspond to intense random dark zones that represent the wavelet harmonics. The characteristic duration of the local flux events is ~1 ms, and the pauses between them are shorter. The individual flux events do not resemble each other; their spectra and amplitudes are also different (e.g., the flux events at times 12 and 14.5 ms are quite different). The characteristic flux frequency related to the wavelet duration as $\omega = 2\pi/a$ indicates a longer duration of the local flux events (the low-frequency region in Fig. 7a) as compared to the characteristic time of the local flux increments (the high-frequency region in the spectra of flux increments in Fig. 7b). The local flux in the L-2M stellarator also occurs in the form of individual events; the duration of individual events exceeds the incremental times for these events. The time behavior of the wavelet spectra of the local flux and the local flux increments in the stellarator is identical to that in the TAU-1 device. Hence, the measured steady-state local flux in the plasma can be represented as an ensemble of individual flux events. Figures 1 and

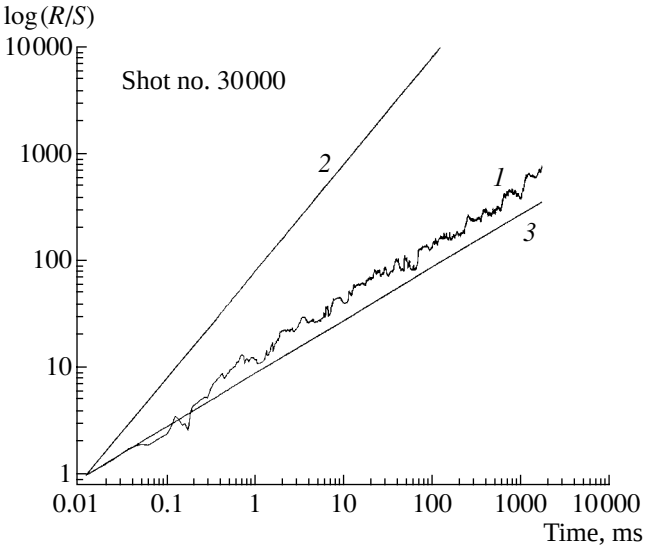

Fig. 8. Time dependences of the function log(*R*/*S*) for (*1*) the local flux in the TAU-1 device, (*2*) a regular signal, and (*3*) a Gaussian signal.

2 show that, as the delay time increases, the value of the correlation coefficient for the events of the local flux increments decreases more rapidly than that for the events of the local flux. We can attribute this independence of the events to the random nature of the correlation coefficients between the fluctuations of the density and poloidal field in each individual flux event. For very long arrays of flux events in the TAU-1 device, it is possible to estimate how these events are related in time or whether the next flux event remembers the preceding one.

To answer this question, we can determine the Herst parameter [26] for the local flux. In the present paper, we found this parameter only for the steady-state flux in TAU-1, because this parameter can only be determined from long arrays of steady-state experimental data. The method for evaluating the Herst parameter is based on the so-called *R*/*S* analysis [27]. The Herst parameter *H* characterizes the relation between events on long time intervals and is convenient to use when analyzing experimental data. We can use the following criteria: $H = 1$ for regular processes, $H = 0.5$ for random Gaussian processes, $H > 0.5$ for self-similar processes with a positive correlation, and $H < 0.5$ for self-similar processes with a negative correlation. In Fig. 8, the value of log(*R*/*S*) (where *R*/*S* is the range of accumulation divided by the standard deviation for a certain time interval [27]) calculated for the local flux in TAU-1 is shown as a function of the logarithm of time (the length of a data file is 128 kB). Two lines obtained from the *R*/*S* analysis for a regular ($H = 1$) and a Gaussian ($H = 0.5$) process are also presented in the figure. The shape of the function log(*R*/*S*) for the local flux in TAU-1 is very close to that for a random process. Strikingly, the self-similarity Herst parameter ($H = 0.58$) turned out to be equal (accurate to the second digit) to the Herst parameter for the local flux in the edge plasma of the W7-AS stellarator [18]. Note that the W7-AS stellarator and the TAU-1 device belong to different classes of plasma devices and the plasma characteristics in these devices are very different, whereas the memory characteristics between the flux events coincide. Such a small departure of the local flux from a random process may be attributed to the existence of a certain weak influence function, which we plan to analyze in our future studies.[7]

4. DISCUSSION OF RESULTS AND CONCLUSIONS

Now, we attempt to clarify the physical mechanisms responsible for the random character of the dynamical characteristics of the local flux (such as the growth and damping rates) and, correspondingly, the values of the local flux increments. We will try to identify some physical mechanisms whose influence on the formation of the process of random increments is confirmed by the experimental data. It is clear that the measured incremental times for local fluxes are shorter than the reciprocals of the growth rates of the above-mentioned instabilities, which are related to the poloidal field and plasma density fluctuations. We recall that the local flux is determined not only by the amplitudes of the density and poloidal field fluctuations, but also the cross-correlation coefficient between these amplitudes at a certain time. The characteristic times of the local flux variations can be related to the characteristic times of variations in the cross-correlation coefficient between the fluctuation events. The variations in the cross-correlation coefficient may be very sensitive to the collisional damping of oscillations, the nonlinear mechanisms governing the growth of oscillations, the limitation of their amplitude, and the suppression of unstable oscillations; other mechanisms are also possible. For example, for the beam–plasma and parametric instabilities, the process determining variations in the value of the cross-correlation coefficient between the density and poloidal field fluctuations may be Langmuir collapse. For the drift-dissipative instability responsible for the local flux in TAU-1, the growth of fluctuations can be limited by stochastic ion heating, which increases plasma diffusion [24]. The additional ion heating not only changes the conditions for the onset of the drift-dissipative instability, but also causes its aperiodic suppression. It is obvious that, when the instability is suppressed, the associated flux must decay, in which case the cross-correlation coefficient between the density and field fluctuations changes rapidly. Note that the mechanisms for the instability suppression due to stochastic ion heating and convection are nonlinear, because they depend on the amplitude of the growing

[7] We believe that the *R*/*S* analysis can be widely used to analyze the processes with memory that are determined by strong structural turbulence.

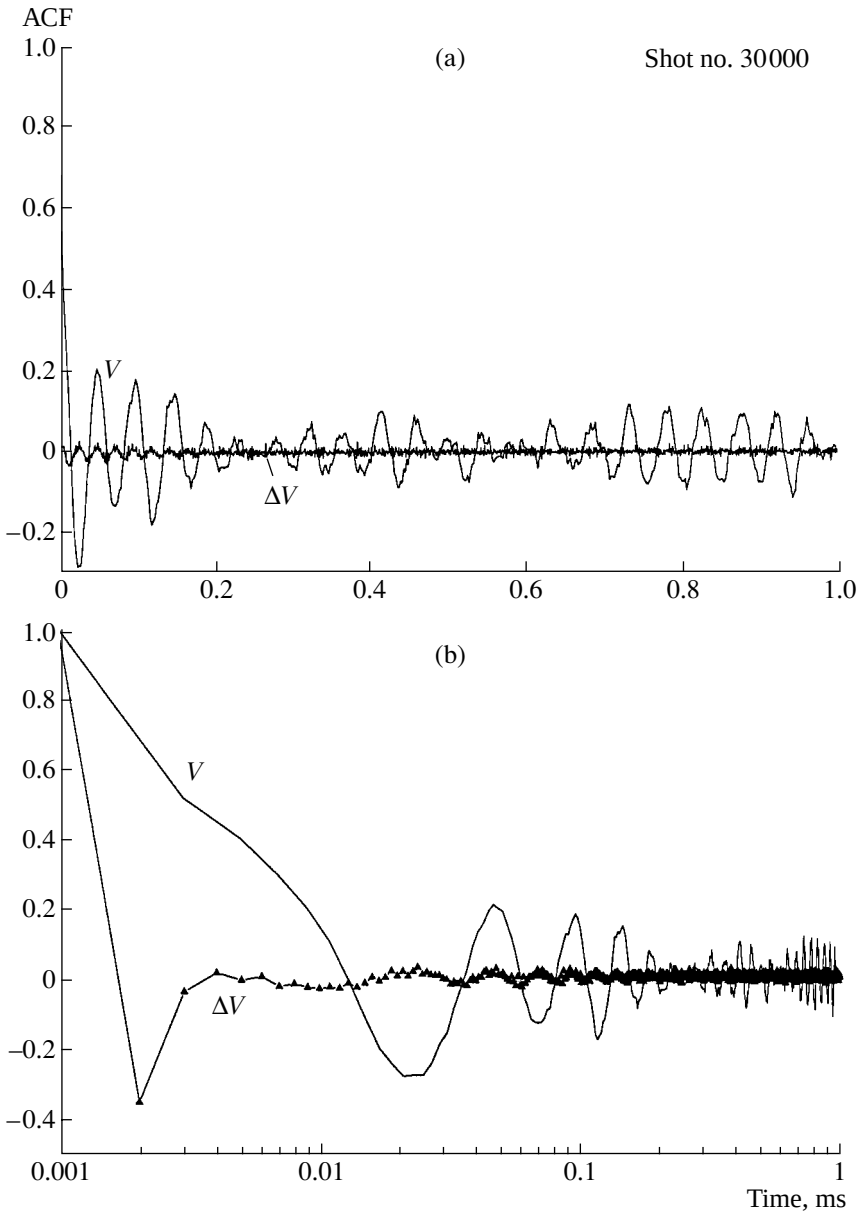

Fig. 9. Autocorrelation functions of drift-dissipative fluctuations of the floating potential V in the TAU-1 device and the increments ΔV represented on (a) the linear and (b) logarithmic time scales.

oscillations. Such a mechanism may be one of the possible mechanisms responsible for the random change of the cross-correlation coefficient between the density and poloidal field fluctuations, which determine an individual fluctuation of the local flux.

Another mechanism responsible for the random character of the flux increments $\Delta\tilde{\Gamma}$ and, accordingly, the parameter γ^{eff} may be the generation of nonlinear structures in the turbulent plasma. Previously, turbulent plasma states were described as states of strong structural turbulence, when a random ensemble of plasma structures is superimposed on strong plasma turbulence. In low-frequency turbulence in the edge plasma of the L-2M stellarator, we observed extended poloidal structures; it was also found that vortex drift structures can form in the plasma core [12, 13]. In the TAU-1 device, we observed ion-acoustic solitons in the low-frequency structural ion-acoustic turbulence [14, 27]; the solitons moved with velocities exceeding the ion-acoustic velocity. The plasma turbulent structures arise and decay randomly in time; the characteristic times of their appearance/disappearance at a given point can be much shorter than the plasma oscillation period. They can significantly contribute to the local flux.[8] Hence, the growth and decay of plasma structures is an addi-

[8] For example, up to 10–15% of the energy of turbulent fluctuations in the edge plasma of the L-2M stellarator is contained in MHD structures; in the structural ion-acoustic turbulence in the TAU-1 device, up to 30% of the fluctuation energy is contained in ion-acoustic nonlinear solitons.

tional factor provoking the random change in the characteristic times of the growth and damping of individual events in the local flux and the change in $\Delta\tilde{\Gamma}$.

The incremental method is useful for analyzing the original fluctuations in structural plasma turbulence, because it provides an opportunity to determine the characteristic time scales on which nonlinear structures evolve. From this standpoint, it is important to note that the characteristic time of the turbulent process can be deduced from the ACF of the increments of fluctuating quantities (such as the ion saturation current, the floating potential, and the local flux). As is seen in Fig. 1, this time is ~1 μs for the flux increments $\Delta\tilde{\Gamma}$ in the edge plasma of the L-2M stellarator. An analysis of the ACF of the increments of fluctuations in the floating potential and the ion saturation current of original signals in the edge plasma of the stellarator gives a time of 2 μs. The same value was also obtained for the characteristic time of the increments of microwave gyrotron radiation scattered by plasma density fluctuations in the plasma core [28]. Since, in the latter case, we measured the scattered signal averaged over a rather large volume near the plasma column axis, we can assume that the dynamic time of the local flux is the characteristic dynamic time of certain plasma processes occurring in the stellarator. For instance, this time may be the characteristic time of the growth and decay of nonlinear structures in the stellarator plasma. Similar results were obtained for the characteristic time of the increments of the local flux (Fig. 2), floating potential, and ion saturation current in the case of the drift-dissipative instability in the TAU-1 plasma. To illustrate the importance of determining the increments of various fluctuating quantities (not only fluxes), Fig. 9 shows the ACFs of the floating potential and the increments of the floating potential in the case of drift-dissipative oscillations in TAU-1. Here again, the characteristic time of increments deduced from the ACF amounts to several microseconds. Such a short characteristic time of the increments of the floating potential may be attributed to the short time of the appearance and disappearance of drift wavelets, which, in aggregate, determine a steady state in the drift frequency range [29].

We draw attention to the fact that, in both the edge plasma and the plasma core, the characteristic (dynamic) time is nearly one order of magnitude shorter than the correlation time defined as a characteristic time of fluctuating quantities. Hence, the growth and decay of a nonlinear structure occur nonadiabatically (they may be characterized as the abrupt misphasing of particle motion). To estimate the diffusion coefficient, one must know the characteristic decorrelation time τ_{decorr} and the characteristic spatial length Δl of the process:

$$D \sim \frac{(\Delta l)^2}{\tau_{\text{decorr}}}. \tag{9}$$

The problem is to estimate the quantities involved. We assume that the decorrelation time is a time scale on which the cross-correlation coefficient between fluctuations in the plasma density and the poloidal field and, consequently, the flux evolve. The characteristic spatial scale length can be chosen as the maximum scale length of the process (the scale length of nonlinear structures). Thus, we can conclude that the dynamic time and the spatial scale length of nonlinear structures determine the characteristic velocity of plasma transport across the magnetic field. Let us estimate this velocity for the L-2M stellarator. For the characteristic scale length of fluctuations $\Delta l \sim 0.2$–1 cm [6] and the dynamic time $\tau_{\text{decorr}} \sim 1$–2 μs, we obtain a characteristic transport velocity of $(1–5) \times 10^5$ cm/s, which agrees with the results of probe measurements in the edge plasma [3].

5. CONCLUSIONS

The results obtained can be summarized as follows:

(i) It is shown that a correct statistical analysis of the characteristics of fluctuating particle fluxes in plasma should be carried out with an equidistant sample of the process, namely, the sample of incremental amplitudes of this process.

(ii) It is shown that the increments of the local fluxes in the L-2M and TAU-1 devices are stochastic in character and the PDFs of increments are scale mixtures of Gaussians. The PDF of increments corresponds to a Laplacian distribution in the case of the drift turbulence and a more complicated distribution in the case of edge plasma turbulence.

(iii) A correct statistical analysis of the local flux fluctuations carried out with an equidistant sample of the local flux increments provides an opportunity to determine the characteristic (dynamic) time of a process of the local flux in the L-2M and TAU-1 plasmas. In both cases, this time turns out to be one order of magnitude shorter than the characteristic correlation time.

(iv) The measured steady-state local flux in a plasma can be represented as an ensemble of random individual flux events that arise spontaneously in time.

(v) Possible physical mechanisms responsible for the random character of the time-dependent parameters of the local flux in a plasma are as follows: nonlinear processes suppressing the growth of unstable oscillations, Langmuir collapse, stochastic particle heating, and the formation of nonlinear structures.

Taking into account the above said, we can formulate several questions to be answered in future investigations. Do the PDF and the corresponding characteristic correlation time of the increments vary when one plasma state transforms into another? What are the characteristics of the local turbulence in transport barriers in toroidal confinement systems? Do the turbulent plasma states under study belong to systems with dynamic chaos? Can the transitions in such systems be controlled with the help of weak regular waves? Note

that, in [30], a weak signal was successfully used to affect the transition from a state with a broad drift spectrum to a single-mode state with a suppressed noise spectrum. In this case, it turns out that the controlling signal should be appropriately phased. Finally, we note that, although we have considered the processes of particle diffusion, the approach proposed may be used to analyze heat transport processes in toroidal confinement systems.

ACKNOWLEDGMENTS

We are grateful to L.M. Kovrizhnykh and S.V. Shchepetov (Institute of General Physics, Moscow) for discussing the experimental results. This work was supported in part by the Russian Foundation for Basic Research (project nos. 00-02-17507 and 01-02-16527) and the Federal Program "Support of Scientific Schools" (project no. 00-15-96676).

APPENDIX

For a random variable Y with $EY < \infty$, the excess coefficient $\vartheta(Y)$ (which is referred to as M_4 in the text) is defined as $\vartheta(Y) = E\left(\frac{Y - EY}{\sqrt{DY}}\right)^4$. If $P(X < x) = \Phi(x)$, then we have $\vartheta(Y) = 3$. Here, E is the mathematical expectation of a random variable and P is the PDF. For PDFs with higher peakedness (and, accordingly, heavier tails), we have $\vartheta(Y) > 3$. For flatter PDFs, we have $\vartheta(Y) < 3$. The PDF of the random flux amplitude $\tilde{\Gamma}$ is equal to the product of the two fluctuating variables, δn_e and δE_Θ, whose PDFs are Gaussian.

Lemma 1. Let X and U be independent random variables with finite fourth moments. We also assume that $EX = 0$ and $P(U \geq 0) = 1$. Then, $\vartheta(XU) \geq \vartheta(X)$. Furthermore, $\vartheta(XU) = \vartheta(X)$ if and only if $P(U = \text{const}) = 1$.

Proof. The independence of X and U implies that

$$\vartheta(XU) = E\left(\frac{XU - EXU}{\sqrt{DXU}}\right)^4 = \frac{E(XU - EXU)^4}{(E(XU - EXU)^2)^2}$$

$$= \frac{E(XU - EXEU)^4}{(E(XU - EXEU)^2)^2} = \frac{EX^4EU^4}{(EX^2)^2(EU^2)^2} \qquad \text{(A.1)}$$

$$= \vartheta(X)\frac{EU^4}{(EU^2)^2}.$$

According to Jensen's inequality, we obtain $EU^4 \geq (EU^2)^2$. Hence, the right-hand side of formula (A.1) always is greater than or equal to $\vartheta(X)$. Furthermore, it is equal to $\vartheta(X)$ if and only if $EU^4 = (EU^2)^2$, which is obviously possible only if $P(U = \text{const}) = 1$. Thus, the lemma is proved.

Using Jensen's inequality, we can easily obtain another inequality directly related to the tails of the normal distribution.

Lemma 2. We assume that the random variable U satisfies the normalization condition $EU^1 = 1$. Then, $1 - E\Phi(x/U) \geq 1 - \Phi(x)$ $(x > 0)$. The proof is elementary and, therefore, is omitted.

Thus, scale mixtures of normal distributions are always more leptokurtic and have heavier tails than the normal distribution.

Let us consider an effect observed when analyzing inhomogeneous samples. As is known, Brownian motion is well modeled by the Wiener processes. Let $W(t)$, where $t \in [0, 1]$, be a Wiener process; i.e., $W(t)$ is a homogeneous Gaussian stochastic process with independent increments such that $W(0) = 0$, $EW(t) = at$, and $DW(t) = \sigma^2 t$ for some $a \in \mathbf{R}$ and $\sigma^2 > 0$. For simplicity, we assume that $a = 0$ and $\sigma^2 = 1$. Let $n > 1$ be an integer. We assume that $W(t)$ is observed at equidistant times $t_i = i/n$, where $i = 1, \ldots,$ and n, so that we have the sample $W_1, W_2, \ldots,$ and W_n with $W_i = W(t_i)$. Note that all W_i are independent and have different distributions. Namely,

$$P(W_i < x) = \Phi(x\sqrt{n/i}), \quad x \in \mathbf{R}.$$

If the sample $W_1, W_2, \ldots,$ and W_n is independent, then each W_i is assumed to be the observation of a random variable W with the probability

$$P(W < x) = \frac{1}{n}\sum_{i=1}^{n} P(W_i < x) = \frac{1}{n}\sum_{i=1}^{n} \Phi(x\sqrt{n/i}),$$

so that, for large n, we have

$$P(W < x) \approx \int_0^1 \Phi(x/\sqrt{s})ds.$$

However, the latter expression is the distribution function of the product of the random variable X with the standard normal distribution and the random variable $\sqrt{S}$, where S is distributed uniformly over [0,1] and is independent of X; i.e.,

$$P(W < x) \approx P(X\sqrt{S} < x).$$

From Lemma 1, it follows that

$$\vartheta(X\sqrt{S}) = \vartheta(X)\frac{ES^2}{(ES)^2}.$$

It is easy to see that

$$\vartheta(X) = 3, \quad ES^2 = \int_0^1 s^2 ds = \frac{1}{3}, \quad ES = \int_0^1 s ds = \frac{1}{2}.$$

Finally, we obtain

$$\vartheta(W) \approx \vartheta(X\sqrt{S}) = 4 \neq 3.$$

REFERENCES

1. J. W. Connor, P. Burraffi, J. G. Cordey, *et al.*, Plasma Phys. Controlled Fusion **41**, 639 (1999).
2. A. Yoshozawa, S.-I. Itoh, K. Itoh, and N. Yokoi, Plasma Phys. Controlled Fusion **43**, R1 (2001).
3. U. Stroth, K. Itoh, S.-I. Itoh, *et al.*, Phys. Rev. Lett. **86**, 5910 (2001).
4. A. Fujisawa, H. Iguchi, T. Minami, *et al.*, Phys. Rev. Lett. **82**, 2669 (1999).
5. G. M. Batanov, L. V. Kolik, A. E. Petrov, *et al.*, Pis'ma Zh. Éksp. Teor. Fiz. **68**, 560 (1998) [JETP Lett. **68**, 585 (1998)].
6. E. J. Synakowski, Plasma Phys. Controlled Fusion **40**, 581 (1998).
7. V. V. Alikaev, A. A. Borshchegovskiĭ, V. A. Vershkov, *et al.*, Fiz. Plazmy **26**, 979 (2000) [Plasma Phys. Rep. **26**, 917 (2000)].
8. O. M. Belotserkovskiĭ and A. M. Oparin, *Numerical Experiment in Turbulence: From Order to Chaos* (Nauka, Moscow, 2000).
9. G. G. Malinetskiĭ and A. B. Potapov, *Modern Problems of Nonlinear Dynamics* (Éditorial URSS, Moscow, 2000).
10. M. A. Pedrosa, M. A. Ochando, J. A. Jiménez, *et al.*, Plasma Phys. Controlled Fusion **38**, 365 (1996).
11. G. M. Batanov, O. I. Fedyanin, N. K. Kharchev, *et al.*, Plasma Phys. Controlled Fusion **40**, 1241 (1998).
12. G. M. Batanov, A. E. Petrov, K. A. Sarksyan, *et al.*, Pis'ma Zh. Éksp. Teor. Fiz. **67**, 634 (1998) [JETP Lett. **67**, 662 (1998)].
13. G. M. Batanov, K. M. Likin, K. A. Sarksyan, and M. G. Shats, Fiz. Plazmy **7**, 1199 (1993) [Plasma Phys. Rep. **7**, 628 (1993)].
14. K. A. Sarksyan, N. N. Skvortsova, N. K. Kharchev, and B. F. van Milligen, Fiz. Plazmy **25**, 346 (1999) [Plasma Phys. Rep. **25**, 312 (1999)].
15. C. Hidalgo, Plasma Phys. Controlled Fusion **37**, A53 (1995).
16. I. U. Stroth, K. Itoh, S.-I. Itoh, *et al.*, Phys. Rev. Lett. **86**, 5910 (2001).
17. G. M. Zaslavsky, M. Edelman, H. Weiltzner, *et al.*, Plasma Phys. **7**, 3691 (2000).
18. B. A. Carreras, B. van Milligen, C. Hidalgo, *et al.*, Phys. Rev. Lett. **83**, 3653 (1999).
19. V. M. Zolotarev, *One-Dimensional Stable Distributions* (American Mathematical Society, New York, 1986).
20. V. V. Uchaikin and V. M. Zolotarev, *Chance and Stability: Stable Distributions and Their Applications* (VSP, Utrecht, 1999).
21. B. V. Gnedenko and V. Yu. Korolev, *Random Summation: Limit Theorems and Applications* (CRC, Boca Raton, 1996).
22. V. M. Kruglov and V. Yu. Korolev, *Limit Theorems for Random Sums* (Moscow Univ. Publ. House, Moscow, 1990).
23. N. K. Kharchev, N. N. Skvortsova, and K. A. Sarksyan, J. Math. Sci. **106** (1), 2691 (2001).
24. F. F. Asadullin, G. M. Batanov, L. V. Kolik, *et al.*, Fiz. Plazmy **7**, 414 (1981) [Sov. J. Plasma Phys. **7**, 226 (1981)].
25. I. S. Gradshteyn and I. M. Ryzhik, *Table of Integrals, Series, and Products* (Fizmatgiz, Moscow, 1962; Academic, New York, 1980).
26. F. R. Hampel, E. M. Ronchetti, P. J. Rousseeuw, and W. A. Stahel, *Robust Statistics: The Approach Based on Influence Functions* (Wiley, New York, 1986).
27. N. N. Skvortsova, K. A. Sarksyan, and N. K. Kharchev, Pis'ma Zh. Éksp. Teor. Fiz. **70**, 203 (1999) [JETP Lett. **70**, 201 (1999)].
28. G. M. Batanov, K. A. Sarksyan, N. K. Kharchev, *et al.*, Pis'ma Zh. Éksp. Teor. Fiz. **72**, 250 (2000) [JETP Lett. **72**, 174 (2000)].
29. A. E. Petrov, K. A. Sarksyan, N. N. Skvortsova, and N. K. Kharchev, Fiz. Plazmy **27**, 58 (2001) [Plasma Phys. Rep. **27**, 56 (2001)].
30. A. E. Petrov, K. A. Sarksyan, N. N. Skvortsova, *et al.*, Fiz. Plazmy **23**, 654 (1997) [Plasma Phys. Rep. **23**, 606 (1997)].

Translated by N. Larionova

Plasma Physics Reports, Vol. 28, No. 2, 2002, pp. 125–140. Translated from Fizika Plazmy, Vol. 28, No. 2, 2002, pp. 144–160.

PARTICLE ACCELERATION IN PLASMA

Charged Particle Acceleration by an Intense Ultrashort Electromagnetic Pulse Excited in a Plasma by Laser Radiation or by Relativistic Electron Bunches

V. A. Balakirev, V. I. Karas', and I. V. Karas'

National Science Center Kharkov Institute of Physics and Technology, ul. Akademicheskaya 1, Kharkov, 310108 Ukraine
e-mail: karas@kipt.kharkov.ua

Received September 27, 2001

Abstract—A review is given of theoretical and experimental investigations and numerical simulations of the generation of intense electromagnetic fields in accelerators based on collective methods of charged particle acceleration at rates two or three orders of magnitude higher than those in classical resonance accelerators. The conditions are studied under which the excitation of accelerating fields by relativistic electron bunches or intense laser radiation in a plasma is most efficient. Such factors as parametric and modulational processes, the generation of a quasistatic magnetic field, and the acceleration of plasma electrons and ions are investigated in order to determine the optimum conditions for the most efficient acceleration of the driven charged-particle bunches. © *2002 MAIK "Nauka/Interperiodica".*

1. INTRODUCTION

One of the most promising methods for collective acceleration [1–9] is a plasma-based scheme for particle acceleration by space-charge waves [3]. There are many papers devoted to the development of such schemes [10–77]. The most important of these are the following: paper [3], in which this method was first proposed by Fainberg; paper [4], in which Tajima and Dawson suggested new efficient methods for exciting plasma waves by laser light [plasma beat-wave accelerator (PBWA) and laser wake-field accelerator (LWFA) schemes] and analyzed some important relevant problems of particle acceleration; and paper [10] by Chen *et al.*, who proposed to excite plasma waves by a short electron bunch or a periodic train of electron bunches [plasma wake-field accelerator (PWFA)]. An important point here is that it was suggested to accelerate particles by wake plasma waves. Note that the question of the excitation of an electromagnetic field by an electron bunch in a plasma has already been discussed in the literature [69–74]. The self-consistent dynamics of rectangular electron bunches in a plasma has been examined in many papers (see, e.g., [14, 36, 78] and the literature cited therein). Theoretical investigations [15–18] and experimental works [19–22] (see also [48]) have also substantially contributed to the development of acceleration schemes based on laser-driven plasma waves, and papers [12, 13, 79–82] made significant contributions to research on the excitation of wake plasma waves by electron bunches in PWFA schemes. In recent years, the wake-field acceleration method has been substantially modified: a new version—Self-Modulated Wake-Field Acceleration (SMWFA), which is based on the self-modulation of a laser pulse—was proposed in [15–20, 83–85] (see also [52]). The most impressive results on plasma acceleration of charged particles were obtained in experimental studies on LWFA [19–22], in which the accelerating fields at short distances were as strong as $1.5–20 \times 10^8$ V/cm and particles were accelerated to energies of 100–300 MeV over distances of about 1 cm. Thus, the method of laser acceleration in a plasma is now being actively developed. The results achieved in the acceleration method based on relativistic electron bunch–driven wake plasma waves are not as significant: the accelerating fields are about 50 kV/cm, the bunch charge being about 4 nC. Recent progress in producing short dense electron bunches raises the hope that very strong accelerating fields will also be achieved in PWFA research [13, 80].[1]

2. NEW POSSIBILITIES OF INCREASING THE ACCELERATING FIELD STRENGTH IN A PLASMA

In this section, we discuss new possibilities of further increasing the accelerating field. Recall that the maximum electric field of a relativistic space-charge wave in a plasma is $E_{\max} = \frac{\tilde{n}_p}{n_0}\sqrt{4\pi n_0 mc^2\gamma}$, where $\tilde{n}_p$ is the maximum density in the space-charge wave [24]. The ratio $\frac{\tilde{n}_p}{n_0}$ is governed by the way in which the space-charge wave is initiated. In experiments on laser excitation, this ratio is less than 15% (LWFA), and, in exper-

[1] The reviews and descriptions of the theoretical and experimental results on this subject can be found in, e.g., [55, 56].

1063-780X/02/2802-0125$22.00

iments on the generation of plasma waves by electron bunches, it is about 3% (PWFA). According to [15–19, 48], for LWFA, we have $\frac{\tilde{n}_p}{n_0} = \frac{a^2}{\sqrt{1+a^2}}$, where $a = \frac{eE\lambda}{2\pi mc^2}$, E is the electric field, and $\lambda = \frac{2\pi}{\omega}$ is the laser wavelength. For the excitation of wake plasma waves by electron bunches (PWFA), this ratio is known to be approximately equal to $\frac{\tilde{n}_p}{n_0} \sim \frac{n_b}{n_0}$ [13], where n_b is the beam density. Consequently, the maximum electric field in a plasma wave can be increased by increasing the laser field and/or laser wavelength as well as the density of the electron bunch exciting the plasma wave (or by searching for new ways of generating plasma waves). Comparing the ratios $\frac{\tilde{n}_p}{n_0}$ for LWFA and PWFA gives [9]

$$\left(\frac{eE\lambda}{2\pi mc^2}\right)^2 \approx \frac{n_b}{n_0}, \quad (1)$$

thereby determining the electron density in the bunch n_b that is required to excite a plasma wave with the same maximum electric field as that of a laser-driven plasma wave. This relationship implies that, in order to generate such a plasma wave in PWFA, it is necessary to make the ratio n_b/n_0 as large as possible. Note that the case $n_b/n_0 \sim 1$ is not considered here, because it goes beyond the applicability range of the above expression for $E_{\max}$ in LWFA, which was derived under the assumption $a \ll 1$.

2.1. Excitation of Wake Fields by Laser Pulses in a Solid-State Plasma

Another way of increasing $E_{\max}$ is to initiate waves in higher density plasmas, in particular, in a solid-state plasma. This possibility can be realized, in particular, in semiconductor plasmas. However, the plasma density in semiconductors ($n_0 \sim 10^{14}$–10^{18} cm^{-3}) is lower than the gas plasma density that has already been achieved in experiments on LWFA (~10^{19} cm^{-3}). Consequently, in developing plasma-based charged particle accelerators, it seems natural to turn to the plasma of metals, in which the density of free electrons is as high as 10^{22}–10^{23} cm^{-3}. Chen *et al.* [59, 60] proposed a very daring but somewhat exotic[2] idea of implementing LWFA, which, however, involves solving the following challenging problems [9]:

(i) launching laser light into a metal,

(ii) exciting space-charge waves in a metal plasma by laser light,

(iii) weakening the effect of multiple scattering of a beam of accelerated particles by the plasma electrons that occur between the channeling planes, and

(iv) solving a very important problem of preventing the destruction of crystals affected by extremely powerful laser radiation via utilizing very short (~ω_{pe}^{-1}) laser pulses.

According to the Chen and Nable's estimates [59], the energy density required to generate accelerating fields of about 100 GeV/cm should be as high as 3×10^7 J/cm^3.

Recall that the electric field of a space-charge wave is governed to a large extent by the way in which it is generated. The authors of [59, 60] proposed to excite a plasma wave by laser light via either the method used in LWFA or the method suggested by Katsouleas *et al.* [56], which involves the interaction between laser radiation and a plasma whose density is made periodically nonuniform in space by an acoustic wave or with the help of a diffraction grating. The latter method is based on the three-wave interaction involving a laser wave, an ion acoustic wave, and a Langmuir plasma wave. The wave interaction can give rise to a plasma wave with the frequency ω_{pe} and wavenumber k_p only under the following conditions: $\omega \approx \omega_{pe}$, $\omega_s \ll \omega_{pe}$, the wavenumber of a laser wave in a plasma is close to zero, and the wavenumber of an ion acoustic wave is equal to k_p. The phase velocity $v_{ph} = \omega_{pe}/k_p$ of the excited plasma wave is close to c.

Another method suggested by the authors of [60] is the generation of wake plasma waves by short laser pulses (as is done in the LWFA scheme), in which case the condition $\omega \gg \omega_{pe}$ should be satisfied. Since $\omega_{pe} \approx 10^{16}$ s^{-1} in both methods, it is necessary to develop and create extrapowerful UV lasers. It is suggested that a plasma density of about ~10^{23} cm^{-3} will be achieved by ionizing the atoms of a solid body by the same UV laser. In this way, however, the fact that laser light will be strongly damped because of the strong absorption should also be taken into account. To answer the question of whether or not the very daring and interesting ideas expounded in [59, 60] can be implemented in practice, it is necessary to investigate the issue of how deep intense UV laser light can penetrate into a metal with allowance for the losses from ionization and photoeffect. Keeping in mind the fact that even very short laser pulses of enormous power will destroy a solid body, the authors of those two papers proposed to accelerate charged particles in optical fibers or thin metal films, in which case laser radiation may become easier to launch into a crystal. They are justified in sug-

[2] Note that our views regarding exotic things may soon undergo a radical revision. The methods of collective acceleration (in particular, the scheme for accelerating charged particles by charge-density waves in a plasma), which were proposed in 1956, also seemed to be very exotic at that time.

gesting that preliminary experiments in this direction can be performed with semiconductors in which the electron density is as high as ~10^{18} cm^{-3}. In this connection, we must point out the very interesting work by Kitson *et al.* [64], in which the phenomenon of anomalous penetration of visible laser pulses into a semiconductor was predicted theoretically and discovered experimentally. In the opinion of the authors of [66, 67], this anomaly can be attributed to the excitation of surface plasma waves.

Note that the maximum possible electric field strength in a steady-state space-charge wave in a plasma is limited by the condition that the velocity v_e acquired by the plasma electrons in the field of this wave is equal to the wave phase velocity v_{ph}, so that we have

$$E_{\max} = \sqrt{4\pi n_0 mc^2(2\gamma - 1)}. \quad (2)$$

Another idea (of no less importance) presented in [59, 60] is that of utilizing not only solid-state crystal bodies in order to raise the electric fields of laser-driven plasma waves but also of using the crystalline properties of solid bodies in order to generate high-brightness beams of accelerated particles through the channeling effect. In fact, under the channeling conditions, strong accelerating fields and the very high rates at which accelerated particles acquire energy can substantially lower the emittance of a beam of accelerated particles; however, it is necessary to take into account the fact that the channeling angle is approximately equal to $\psi \approx \sqrt{eU_b/\varepsilon_p}$, where eU_b is the depth of the potential well (or the height of the potential barrier that forms between the lattice planes of the crystal). For very high energies ε_p, this angle is very small. That is why the possibility of substantially reducing the emittance of a beam of charged particles accelerated to extremely high energies in crystals requires more detailed theoretical and experimental investigations. It may be that the ideas developed by the authors of [59, 60] will not be implemented in full measure in the near future. However, some aspects of the acceleration methods proposed in those papers can be used to create very-high-energy (about 10^{13}–10^{18} eV) particle accelerators.

A different scheme for charged-particle acceleration in crystals was proposed by Tajima *et al.* [62, 63] and was further developed in subsequent works. This scheme is based on the analogy with particle acceleration in microwave waveguides with periodically spaced metal or dielectric disks and implies acceleration via hard X radiation, for which a periodic crystalline structure plays the same role that periodically spaced disks play for microwave radiation in waveguides. The use of crystals for particle acceleration via hard X radiation on the basis of the Borman effect [62] eliminates the problems of launching laser radiation into a crystal and of guiding laser pulses over relatively large distances in a crystal. Tajima and Covenago [62] proposed to channel accelerated charged particles in a crystal in order to reduce their scattering. They also noted that Hofstadter had already originated analogous ideas in his unpublished paper. At this point, we should say a few words about the history of research on charged-particle acceleration in solids. Grishaev and Nasonov [61] suggested to accelerate charged particles by longitudinal polarization waves of an optically active matter that are driven by the beating of two electromagnetic waves and noted that the channeling effect can serve to reduce the divergence of a beam of accelerated particles due to their multiple scattering. Tajima and Covenago [62] proposed to accelerate charged particles in crystals by hard X radiation and to lower the divergence of a beam of accelerated particles by channeling them. They also studied some other aspects of this acceleration method. Examining the prospects for the new concept of accelerating charged particles by laser radiation in a solid body, Tajima and Covenago determined the electric field of a plasma wave in a metal from the relationship that was obtained for the maximum field of a nonlinear wave propagating in a plasma by solving the problem of natural waves. However, it is clear that the electric field should be estimated by solving the problem of induced oscillations and waves. Since the electric field of the plasma wave is very sensitive to the way in which the wave is excited, we think that deriving the final expression for the electric field requires solving the problem of the excitation of the plasma wave in the case at hand. In the wake-field acceleration scheme proposed in the rather interesting paper by Rosenzweig *et al.* [14], a high-energy electron beam is used to excite extremely nonlinear plasma oscillations in which acceleration occurs preferentially in the transverse direction.

Balakirev *et al.* [42] proposed a method for substantially increasing relativistic electron bunch–driven wake fields owing to the self-modulation of a long pulsed electron bunch in a plasma. The field excited by the bunch front affects the motion of the bunch electrons in such a way as to modulate the bunch density, or, in other words, to break the bunch into microbunches. Since the bunch is modulated at the plasma frequency, the wake fields generated by microbunches are coherent, so that the amplitude of the excited wake fields can increase substantially. However, the results of 2.5-dimensional simulations carried out by Batishchev *et al.* [34] show that, because of the unsteady dynamics of the self-consistent fields of a relativistic electron bunch with dimensions comparable to the skin depth, the wake field amplitude along the train of microbunches increases more gradually than in the case of a "rigid" bunch.

2.2. PWFA Experiments

Experimental investigations on PWFA were begun at the Argonne National Laboratory (ANL) [13, 14, 79–82, 86] and then were continued at the University of Tokyo [87]. The first experiments at ANL were carried out with 24.1-MeV beams (the electric charge of the

driving bunch was 4 nC, the bunch dimensions being about 1 mm) and 16.6-MeV beams (the accelerated and diagnosed bunches had the same dimensions). The bunches were injected into a plasma whose density was varied from 10^{11} to 10^{13} cm^{-3}. The amplitude of the excited wake fields was measured to be about 6 MeV/m, which could only be explained by invoking the plasma and bunch nonlinearities. The corresponding simulations performed at this time were all one-dimensional (see, e.g., [13, 14]), and only some estimates were obtained with allowance for two- and three-dimensional effects. It was pointed out that three-dimensional effects should be systematically taken into account in investigating the role of the nonlinear behavior of the plasma and bunch particles. At the University of Tokyo, PWFA experiments were carried out with trains of six 500-MeV bunches. The plasma density was varied approximately within the same range as in the experiments at ANL. It was found that the amplitude of the excited wake field depends linearly on the plasma density in the range from 10^{11} to 10^{12} cm^{-3} [87]. The insufficiently high excitation rates of the wake fields and large radial displacements of the succeeding bunches in the train were not adequately explained at the theoretical level (these questions were mostly answered in our investigations). Further PWFA research is aimed at developing wake-field acceleration schemes for future linear colliders. At present, the PWFA scheme is being investigated most actively at ANL, the University of California at Los Angeles (UCLA), and the University of Southern California (USC) in collaboration with the Stanford Linear Accelerator Center (SLAC) on the 30-GeV linear accelerator at Stanford. Preliminary results from these very important experiments were reported at the annual meeting of the American Physical Society in October 2000. However, since these promising results were presented as abstracts of papers and have not yet been published in scientific journals, we cannot discuss them here. The photocathode in an accelerator created at ANL [79–82] is capable of ensuring the following bunch parameters: an electron energy of 200 MeV, a bunch charge of 100 nC, and a bunch duration of 20 ps. The photocathode is struck by light from a laser with a wavelength of 248 nm, a pulse duration of 2 ns, and an input energy of 8 mJ. This project is aimed at achieving acceleration rates of about 100 MeV/m.

2.3. Excitation of Wake Fields by Laser Pulses

Another promising method for exciting wake fields in a plasma makes use of short (picosecond and femtosecond) laser pulses with intensities of 10^{16} to 10^{19} W/cm^2. The results of recent PBWA experiments at UCLA are presented in [88–90] (recall that the acceleration scheme based on the beating between electromagnetic beam pulses was first proposed by Litvak [91]). In those experiments, relativistic plasma waves were resonantly excited in a plasma by the beating between two collinear beams from CO_2 lasers operating simultaneously at two different wavelengths. The acceleration of test electrons in a plasma was investigated using electron beams with a peak current of 200 mA, an electron energy of 2 MeV, and a pulse duration of 1 ns in order to measure the longitudinal wake fields, which themselves had a large relativistic factor equal to 34 (the relativistic factor of the excited wake field is large because of the large ratio of the laser frequency to the electron plasma frequency, $\gamma = \omega/\omega_{pe}$). The energy spectrum of the accelerated electrons was recorded using a special-purpose multisector magnet and a surface-barrier detector. The electrons were accelerated to an energy of 20 MeV over a distance of 1 cm, the acceleration rate being higher than 1.8 GeV/m. Clayton *et al.* [90] experimentally demonstrated the acceleration of electrons by relativistic plasma waves generated by stimulated Raman forward scattering of a short single-frequency laser pulse with a wavelength of 1.053 μm, a duration of 6×10^{-13} s, and a peak power of 8×10^{17} W/cm^2. The density of the plasma created by an auxiliary laser was varied in the range $(1–2.5) \times 10^{15}$ cm^{-3}, and the plasma itself was homogeneous over a length of 0.8 mm. Electron acceleration was observed to correlate with the generation of the first anti-Stokes satellite in the radiation spectrum. The calculations carried out in [90] showed that, by increasing the interaction length to 1.3 mm, it is possible to achieve acceleration rates as high as 1 GeV/cm. Beginning with the pioneering paper [4] by Tajima and Dawson, the PBWA method has been actively investigated not only theoretically and experimentally but also numerically [21, 88]. These investigations showed that the PBWA method works most efficiently with the theoretically predicted lengths of the laser pulses [92] because of the detuning of the plasma frequency from the difference between the laser frequencies. Numerical simulations showed that short acceleration lengths stem not from the plasma inhomogeneity but rather from the effect of the diffractive spreading of laser pulses on the Rayleigh length, in which case only about 2% of the injected particles are accelerated. The progress achieved in theoretical and numerical studies on plasma-based laser accelerators was reported in [57, 88], where the possibility of guiding laser pulses in plasma channels was also discussed in the context of preventing their radial spreading. The question of whether or not it is expedient to use plasma channels has already been discussed by Tajima and Dawson [4]. At present, it is proposed to use channels preformed in a special manner rather than rectangular channels. Since the most serious obstacle to acceleration is the diffractive spreading of the pulse, it is by the appropriate choice of the channel parameters that the acceleration length was significantly increased to

$$l_{\text{acc}} = \lambda_{pe}\frac{\omega^2}{\omega_{pe}^2}\left[1 + \left(\frac{c}{V_{\text{osc}}}\right)^2\right], \qquad (3)$$

where $V_{\rm osc} = \dfrac{eE}{m\omega}$ is the electron oscillatory velocity in the laser field. In this case, the growth rate of the Raman instability is equal to

$$\gamma_{RS} = 2^{-3/2}\frac{V_{\rm osc}}{c}\frac{\omega_{pe}^2}{\omega}\sqrt{1-\left(\frac{4p\lambda_{pe}}{2\pi}\right)^2}, \qquad (4)$$

where $p^2 + h^2 = \left(\dfrac{2\pi}{\lambda_{pe}}\right)^2$, $p = h\tanh a_0$, and a_0 is the characteristic channel radius.

The guiding of intense laser pulses by plasma channels preformed in a special way was investigated in [57, 93]. It was shown that, in an empty channel, the growth rate of the Raman forward scattering instability decreases if $\pi a_0 < 0.13\lambda_{pe}$.

2.4. SMWFA Method

This method for charged particle acceleration has already been discussed above. Here, we analyze recent results on this subject. The SMWFA scheme is of considerable physical interest because the self-modulation of a laser pulse and the self-modulation of a relativistic electron bunch have much in common. As will be seen below, the self-modulation of a relativistic electron bunch is one of the most promising methods for exciting intense accelerating fields in a plasma. Moore *et al.* [94] carried out a detailed experimental investigation of the self-modulation of intense laser pulses with a power of 2 TW, a duration of 400 fs, an energy of 1 J, a wavelength of 1.054 nm, and an intensity of 5×10^{18} W/cm^2, the radius of the initial focal spot being 6 μm. In a plasma with a density of 1.4×10^{19} cm^{-3}, they succeeded in accelerating 10^8 plasma electrons to an energy of 30 MeV. The plasma wave was generated over a distance of 20 Rayleigh lengths. It was established that electron acceleration correlates with the generation of harmonics in the radiation spectrum. When the laser power was decreased by one-half or the plasma density was lowered, no high-energy electrons were observed. In the experiments of [95, 96], intense (10^{18} W/cm^2) laser pulses in the plasma were found to undergo self-channeling over a distance of 20 Rayleigh lengths. Papers [97, 98] were devoted to an experimental and theoretical study of the acceleration of the injected 3-MeV electrons by an intense wake wave, such that the accelerating electric field strength was 1.5–15 GV/m. The wake wave was excited by a 5-J laser pulse with a duration of 0.4–7 ps, which was guided in a preformed plasma channel with a density of 10^{19} cm^{-3}. It was shown that, in such plasma channels, long laser pulses (such that the laser power is low in comparison with the critical power for self-focusing) propagated a distance of three Rayleigh lengths. The self-modulation of a laser pulse led to the excitation of a plasma wave with a density variation of 6%. Since the amplitude of this plasma wave was far below the wave-breaking amplitude, the electrons could not be accelerated to megaelectronvolt energies. High-power laser pulses were observed to interact with a plasma in a strongly nonlinear fashion, giving rise to the filamentation instability. The pulses underwent self-focusing and self-modulation without generating high-energy resonant plasma electrons. The acceleration of a large number of plasma electrons to megaelectronvolt energies was observed with laser pulses whose power was 28 times higher than the relativistic self-focusing threshold. The radial structure of a wake wave excited during the self-modulation of a laser pulse in a homogeneous subcritical plasma was studied in detail by Andreev *et al.* [99]. The generation of an electron beam in the SMWFA scheme was thoroughly investigated by Chen *et al.* [100] both experimentally and by three-dimensional numerical simulations. They showed that the emittance of the generated 2-MeV electron beams is extremely small (0.06π mm mrad), in which case the main role is played not by the space-charge forces in the beam but by the nonlinearity of the plasma wave and the magnetic field of the wave (rather than the quasistatic magnetic field, as was asserted in many papers; see, e.g., [101, 102]). The interaction of short laser pulses with a transversely inhomogeneous plasma, relativistic filamentation, and field ionization were studied in [103–107]. The self-focusing of an intense ultrashort laser pulse and the accompanying processes (such as the generation and acceleration of ions, electron cavitation, the formation of channels, and the magnetic field generation) were investigated in detail in [101, 102, 108, 109].

2.5. PWFA Scheme with a Plasma Channel of Depressed Density

The PWFA research program proposed by Barov and Rosenzweig [81] relies on the use of plasma channels with a depressed electron density. The authors of [81] presented previous results obtained on the interaction of intense relativistic electron beams with plasmas in weak magnetic fields and suggestions for future work. This PWFA method deals with electron beams of density $n_b > n_p$. In such a situation, the plasma electrons escape from the propagating beam, thereby giving rise to an ion channel (the so-called ion focus regime). The PWFA experimental research program is being implemented in the accelerator at ANL. In recent papers [81, 110], it was proposed to use the so-called blow-out regime, which ensures that an electron beam propagates through a plasma with minimum distortions and losses. The model developed in those papers describes a nearly equilibrium electron beam propagating in such a manner through an underdense plasma, in particular, in the presence of an external magnetic field. The numerical results were obtained by solving the Vlasov–Maxwell equations for beam electrons and the hydrodynamic equations for plasma particles. A comparison

between the results obtained from the equilibrium model and from the related simulations based on the macroparticle method showed that, under the conditions of collisional damping, the beam keeps its equilibrium. In addition, the possibility of using a relativistic electron bunch as an adiabatic lens was discussed. The blow-out regime, which has been recently proposed for the PWFA scheme [81, 110] and in which the plasma electrons are completely blown out from the beam region, has a number of advantages. When an intense electron beam with a sufficiently long duration propagates through a low-density ($n_0 < n_b$) plasma, the blow-out of all plasma electrons from the beam region gives rise to an ion channel. This regime was called the ion focus regime. The magnetic self-focusing forces cause the beam to propagate in the ion channel. The radius R_{eq} of the equilibrium beam propagating in a fully formed ion channel is equal to

$$R_{eq} = \frac{\varepsilon_n}{\sqrt{2\pi r_e n_0 \gamma_b}}, \quad (5)$$

where ε_n is the normalized beam emittance and r_e is the classical radius of an electron. It is possible to single out three qualitatively different regions of the beam. The leading part of the beam (the beam head) is not focused by the plasma and therefore expands. The body of a beam propagating in the ion channel experiences the strongest focusing force. The transition region between the head of the beam and its body cannot be described in the linear-optics approximation because of the presence of plasma electrons. For a laser pulse of sufficiently short length L_0 ($2\pi L_0 \le \lambda_{pe}$), the evolution of both the beam head and the transition region has a substantial impact on the efficiency with which the beam is transported over long distances. The head of an ultrarelativistic beam expands freely in accordance with the value of the emittance, in which case the blow-out rate of the plasma electrons becomes slower. As a result, the succeeding parts of the beam experience a weaker focusing force, so that the beam is distorted to a significant extent. A simple one-dimensional model shows that, after a certain period of initial expansion, the beam is distorted at a very slow rate. It was also shown that the beam continues to expand until the plasma electrons are completely blown out from the beam region; in other words, the beam slowly evolves to a pinching regime and acquires an equilibrium structure. Barov *et al.* [110] proposed to use the blow-out regime in order to generate accelerating fields of 80–150 MeV/m by electron bunches with a charge of 90 nC. Below, we will describe the results from investigations of the formation of an ion channel due to the ion motion in self-consistent electromagnetic fields excited by a relativistic electron bunch.

3. 2.5-DIMENSIONAL NUMERICAL SIMULATION OF THE EXCITATION OF WAKE FIELDS BY A TRAIN OF RELATIVISTIC ELECTRON BUNCHES IN LOW- AND HIGH-DENSITY PLASMAS

The excitation of a steady-state nonlinear wake wave by a periodic train of relativistic electron bunches in a plasma was studied by Amatuni *et al.* [12], who showed that, when the plasma and bunch densities are comparable, the wave electric field increases with the relativistic factor of the train. Investigations of the nonlinear regime in PWFA experiments made clear the importance of three-dimensional effects [13, 14]. There are two different mechanisms that can produce strong wake fields and thus can be exploited in the physics of plasma-based accelerators. On the one hand, a short wide first bunch can excite large-amplitude wake waves capable of accelerating the succeeding bunches. On the other hand, a long narrow electron bunch can be well focused by its own magnetic field, provided that its space charge is completely neutralized by the plasma. The wake-field excitation is studied with COMPASS, a modified two-coordinate three-velocity axisymmetric, truly relativistic electromagnetic code [30–32]. Previously, this code was used to model inductive plasma accelerators [32], to simulate the interaction of relativistic beams with plasmas [33], and to investigate the propagation of a solitary relativistic electron bunch or a train of such bunches through both high-density and low-density plasmas [34]. Note that, in the experiments of [13, 14], the density of relativistic electron bunches was $n_b \le n_0/2$, in which case the transverse and longitudinal dimensions of the bunch, R_0 and L_0, were small in comparison with the skin depth c/ω_{pe}. Computer simulations [34, 35] showed that the transverse dimension of the bunch may change substantially as it propagates through the plasma. This results in significant changes in both the bunch density (by more than one order of magnitude) and the excited wake fields. It was shown that the amplitudes of the transverse and longitudinal fields increase as each next relativistic electron bunch is injected, but, unlike in the case of rigid bunches, their increase is not proportional to the number of injected bunches. A new electron accelerator created at the Kharkov Institute of Physics and Technology [69] is expected to be used in future experimental research on the acceleration of charged particles in intense wake fields. The operating parameters of the accelerator are as follows: the electron energy is W = 18–20 MeV, the number of electrons in a bunch is $N \approx 10^{10}$, the number of bunches is up to 20, and the modulation frequency of the bunches is 2797.16 MHz. It is proposed that, in experiments, relativistic electron bunches with dimensions comparable to the skin depth will be injected into a plasma whose density will be varied over a very wide range (by more than four orders of magnitude). The plasma is to be homogeneous to within several percent,

so that the homogeneous plasma approximation is quite adequate for describing the experiment.

Since it is anticipated that no instabilities giving rise to the azimuthal plasma inhomogeneity would occur under the planned experimental conditions, a theoretical description can be based on the azimuthally symmetric mathematical model involving the injection of particles into the computation region and their escape from it. Under the conditions that are expected to prevail in experiments with the new accelerator, relativistic electron bunches will be injected into a plasma column with the length $L = 100$ cm, the radius $R = 10$ cm, the density in the range $n_0 = 10^{10}$–10^{14} cm^{-3}, and a minimum longitudinal density gradient. The numerical results presented below were obtained precisely for this experimental situation.

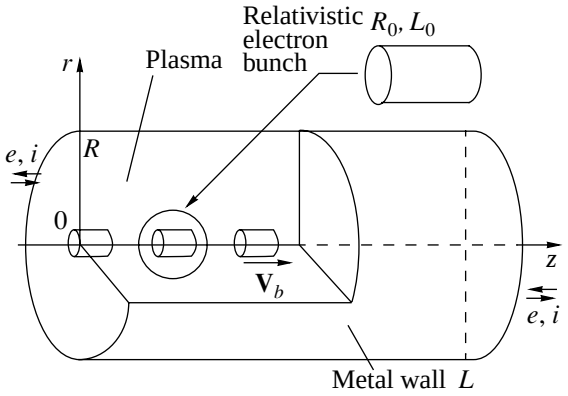

Fig. 1. Schematic of the model plasma–bunch system.

3.1. Mathematical Model

We describe the dynamics of a relativistic electron bunch by the relativistic Vlasov equations (the Belyaev–Budker equations) for the distribution functions of each of the plasma components and by the set of Maxwell's equations for the self-consistent electric (**E**) and magnetic (**B**) fields. The plasma–bunch system to be modeled is shown schematically in Fig. 1. At the initial instant, a two-component ($m_i/m_e = 1840$, where m_i and m_e are the ion and electron masses) cold plasma fills the entire computation region $[0, L] \times [0, R]$. In simulations, we usually set L and R equal to 100 and 10 cm, respectively. A finite number of relativistic electron bunches with the electron density

$$n(r, z) = n_b\theta(R_0 - r)\theta(v_b t - z + (n-1)\lambda_p) \times \theta(z - v_p t + L_0 + (n-1)\lambda_p)$$

are injected into a plasma through the $z = 0$ plane. Here, $\theta(z)$ is the Heaviside step function; n is the order number of the injected bunch; $V_b = c\sqrt{1 - 1/\gamma_b^2}$ is the bunch velocity; the initial bunch dimensions L_0 and R_0 are equal to 0.4 and 0.5 cm, respectively; $\lambda_p = 2\pi c/\omega_{pe}$; and n_b is the mean bunch density. The bunch electrons and plasma particles can escape from the computation region through the boundary surfaces $z = 0$ and $z = L$. The plasma particles can also enter the computation region. The boundary conditions at the inner surface of the computation region assume a metal surface $r = R$ and a free escape of electromagnetic waves through the front and back surfaces. In our calculations, we use an explicit difference scheme. The excitation of wake fields by a train of bunches in a plasma was investigated in four series of simulations aimed at analyzing the dependences of the excited field on the number N_b of bunches injected into the plasma, on the bunch-to-plasma density ratio, on the repetition rate of the bunches, and on the ratio of the bunch radius R_0 to the skin depth c/ω_{pe}. The parameters of these four series are presented in the table.

The mass of the model particle is a function of its radial positions. In a lesser perturbed region (which is farther from the symmetry axis), the plasma is modeled by a relatively small number of particles. The total number of macroparticles is about 10^6. Note that all simulations were carried out with an advanced particle-in-cell (PIC) method implemented on a Pentium-133 PC.

3.2. Numerical Results and Discussion

Computer modeling showed that, as a relativistic electron bunch with $R_0 < c/\omega_{pe}$ and $L_0 < c/\omega_{pe}$ propagates in a plasma, its radius changes substantially. In contrast to the frequently used conditions $L_0 \gg c/\omega_{pe} > R_0$ or $R_0 \gg c/\omega_{pe} > L_0$, we simulated bunches with the initial dimensions $L_0 \approx R_0 < c/\omega_{pe}$ or $L_0 \approx R_0 \approx c/\omega_{pe}$, which correspond to those in the experiments of [13, 14]. In this case, the plasma and bunches are essentially nonlinear. The numerical results obtained in [36] showed

Parameters of the plasma and the bunches

Calculation version	Bunch density n_b, cm^{-3}	Plasma density n_0, cm^{-3}	Plasma frequency ω_{pe}, s^{-1}	Skin depth c/ω_{pe}, cm	Number of electrons in a bunch N
1	2×10^{10}	4×10^{10}	1.13×10^{10}	2.66	6.28×10^9
2	2×10^{10}	4×10^{11}	3.57×10^{10}	0.84	6.28×10^9
3	4.86×10^{10}	9.72×10^{10}	1.76×10^{10}	1.71	1.53×10^{10}
4	4.86×10^{10}	8.75×10^{11}	5.27×10^{10}	0.57	1.53×10^{10}

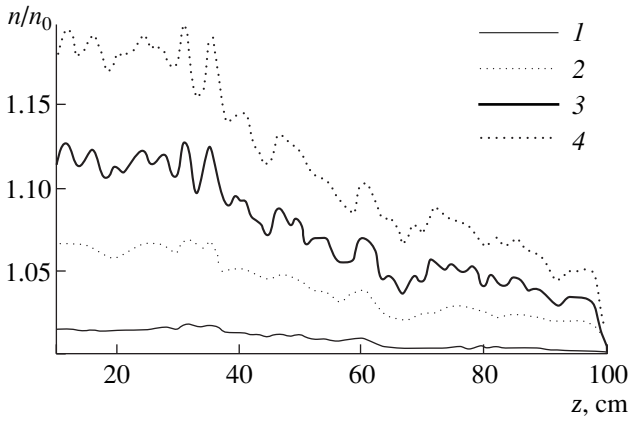

Fig. 2. Longitudinal profiles of the ion density obtained in calculation version 1 at the radius r = 0.5 cm at the times $t\omega_{pe}$ = (*1*) 70, (*2*) 120, (*3*) 150, and (*4*) 180.

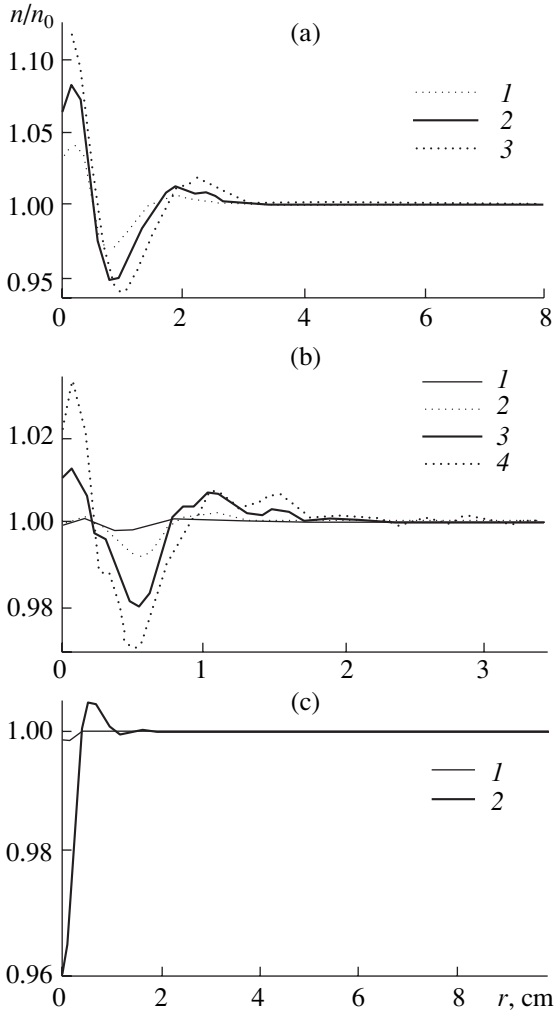

Fig. 3. Radial profiles of the ion density obtained (a) in calculation version 1 at the times $t\omega_{pe}$ = (*1*) 70, (*2*) 120, and (*3*) 150; (b) in calculation version 4 at the times $t\omega_{pe}$ = (*1*) 100, (*2*) 200, (*3*) 260, and (*4*) 330; and (c) in calculation version 3 at the times $t\omega_{pe}$ = (*1*) 100 and (*2*) 300.

that the propagation of a relativistic electron bunch in a plasma is greatly affected by the ion motion. The time evolution of the longitudinal profile of the ion density n_i is illustrated in Fig. 2, which was obtained in calculation version 1 (see table). The time evolutions of the dependence of the ion density on the radial coordinate r are illustrated in Figs. 3a, 3b, and 3c, which were obtained in calculation versions 1, 4, and 3, respectively. From Figs. 2 and 3, we can see that the formation of an ion channel stems from the radial ion motion in self-consistent fields. At the axis of the system, the ion density is elevated and increases in the direction opposite to the propagation direction of the bunches. The elevated central density is higher than the unperturbed ion density by more than 15%. The characteristic time scales on which the ion channel forms are about a hundred inverse electron Langmuir frequencies; in other words, as may be expected from illustrative physical considerations, these scales are governed by the inverse ion Langmuir frequencies. The channel parameters are determined by the plasma-to-bunch density ratio and the ratio of the initial bunch radius R_0 to the skin depth c/ω_{pe}.

The amplitude of the ion density oscillations is seen to be substantially smaller than the averaged density. For comparison with the longitudinal profile of the ion density, Fig. 4 shows the longitudinal profile of the electron density. The electron density is seen to undergo only strong oscillations driven by the excited wake wave, and its averaged value remains essentially unchanged. In wake fields, the electrons oscillate without any significant change in their equilibrium positions. As a result, the electric field of the unneutralized positive ion charge accumulating at the system axis stabilizes the propagating electron bunches.

Figures 5 and 6 show longitudinal profiles of the longitudinal (E_z) and radial (E_r) electric fields at two times. One can see that the amplitudes E_r and E_z increase as each next bunch is injected, but, unlike in the case of rigid bunches, their increase is not proportional to the number of injected bunches. This dependence stems from the fact that, because of the charge and current neutralization processes, the bunch electrons undergo transverse oscillations in self-consistent fields. We can see that, owing to neutralization of the bunch space charge by a dense plasma, the azimuthal magnetic field is not fully canceled and thus drives the bunch electrons into radial motion, leading to a significant distortion of the bunch shape and a charge density redistribution within the bunches. As a result, the wake fields are excited in an unsteady fashion, which is unfavorable for charged particle acceleration. The shape of the envelope of the bunches is seen to deviate substantially from the Bennett equilibrium shape. The electromagnetic fields generated by the bunches propagating in a plasma redistribute the ion plasma density and give rise to the averaged electric field, which promotes the focusing of the bunch electrons. Hence, the radial expansion of the bunches is prevented to a large extent

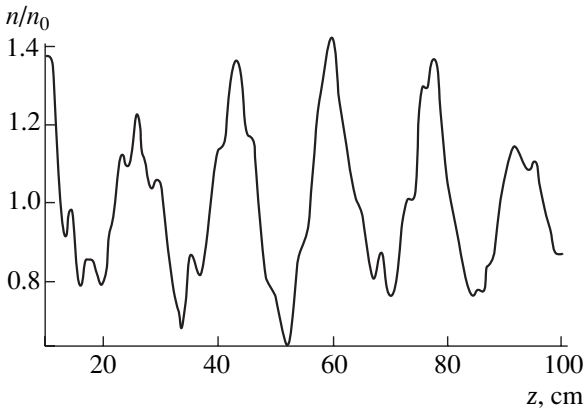

Fig. 4. Longitudinal profile of the electron density obtained in calculation version 1 at the radius $r = 0.5$ cm at the time $t\omega_{pe} = 180$.

by the formation of the plasma channel due to the radial motion of the plasma ions. A train of bunches propagating in a stable and steady-state fashion in the fully developed ion channel excites steady-state wake fields suitable for accelerating the injected electrons. We can thus conclude that the nonlinear processes analyzed in this section have a beneficial effect on the bunch propagation and, accordingly, on the excitation of the accelerating fields by the bunches. The investigation of the three-dimensional nonlinear behavior of the beam–plasma system was undertaken in order to provide a better insight into the fundamental physics governing the acceleration and focusing of charged particles by the wake waves. Numerical experiments show that the ion motion in the self-consistent fields excited by a train of relativistic electron bunches gives rise to an ion channel at the symmetry axis of the system; in turn, the ion channel makes the bunch propagation more stable, so that the accelerating fields excited by the bunches are stronger.

4. 2.5-DIMENSIONAL NUMERICAL SIMULATION OF THE EXCITATION OF WAKE FIELDS DURING THE SELF-MODULATION OF A LONG RELATIVISTIC ELECTRON BUNCH

In this section, we describe the results of numerical modeling of the wake-field excitation by a relativistic electron bunch in a dense plasma. The results presented were obtained using a two-coordinate three-velocity model in which the complete set of equations for the bunch–plasma interaction consists of the relativistic Vlasov equations for the bunch electrons, the nonlinear Vlasov equations for each of the plasma components, and nonlinear Maxwell's equations for the self-consistent electromagnetic fields. Our computer modeling showed that the nonlinear dynamics of the plasma and bunch particles leads to a significant self-modulation of the density of a long bunch, in which case the amplitude of the excited wake fields substantially increases.

4.1. 2.5-Dimensional Numerical Modeling of the Wake-Field Excitation by a Long Relativistic Electron Bunch

The physics of plasma accelerators usually deals with two regimes of the bunch–plasma interaction accompanied by the generation of large-amplitude wake plasma waves. In the first regime, a large-amplitude wake field excited by a short wide first bunch can accelerate the succeeding bunches in the train. In the second regime, a long narrow relativistic electron bunch can be strongly focused by its own magnetic field, provided that its space charge is completely neutralized by the plasma. In a wake electric field, the bunch electrons experience not only transverse forces but also strong longitudinal forces. Longitudinal wake fields give rise to a longitudinal modulation (with the period $\lambda_p = 2\pi c/\omega_{pe} = 3.36 \times 10^6/\sqrt{n_0}$ cm) of the origi-

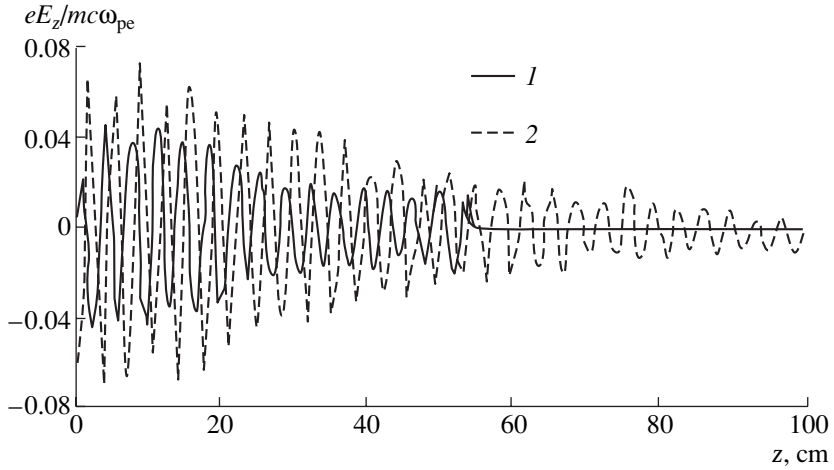

Fig. 5. Profiles of the longitudinal electric field E_z along the z-axis obtained in calculation version 4 at the radius $r = R_0 = 0.5$ cm at the times (*1*) $t = 100\,\omega_{pe}^{-1}$ and (*2*) $t = 200\,\omega_{pe}^{-1}$.

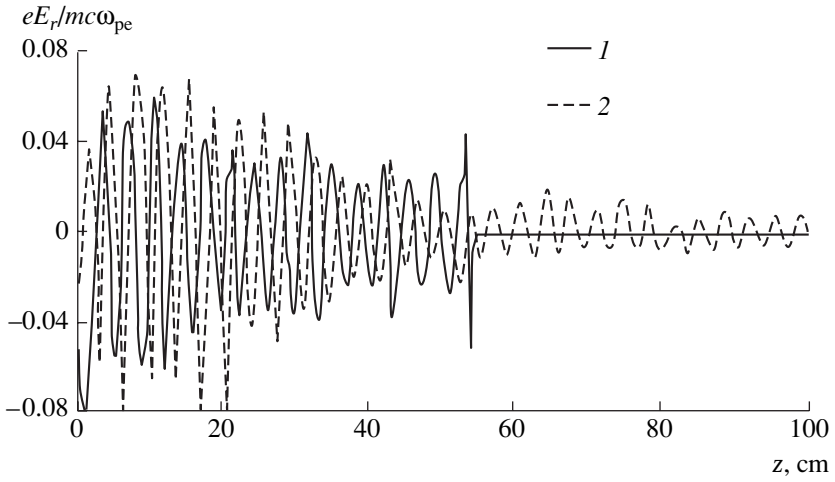

Fig. 6. Profiles of the radial electric field E_r along the z-axis obtained in calculation version 4 at the radius $r = R_0 = 0.5$ cm at the times (*1*) $t = 100\,\omega_{pe}^{-1}$ and (*2*) $t = 260\,\omega_{pe}^{-1}$.

nally uniform electron bunch, thereby breaking it into microbunches. In particular, in a plasma with a particle density of 10^{16} cm^{-3}, the modulation period is 0.3 mm. The effect of the longitudinal modulation of relativistic electron bunches by the wake fields can be used to develop plasma modulators of high-density electron beams. Now, we should say a few words about another aspect of the modulation phenomenon. Since the modulation frequency coincides with the plasma frequency, the wake fields of the microbunches are coherent. Consequently, the modulation of an electron bunch leads to an increase in the wake-field amplitude behind the bunch. This effect makes it possible to use long relativistic electron bunches to generate intense wake fields in a plasma. It is important to note that long laser pulses can also undergo longitudinal modulation at the plasma frequency [28]. The modulation of long electron bunches by longitudinal wake fields in a plasma was investigated theoretically by Balakirev *et al.* [42]. The results of one-dimensional numerical modeling of the nonlinear dynamics of the bunch modulation showed that the modulation of a long electron bunch propagating in a plasma increases the amplitude of the excited wake wave. This effect is explained as being due to the coherence of the wake fields generated by microbunches resulting from the modulation of a long bunch at the plasma frequency. The one-dimensional approximation applies only to relativistic electron bunches with a sufficiently large radius ($2\pi R_0/\lambda_p \gg 1$).

The results presented in this section were obtained from 2.5-dimensional numerical modeling of the wake-field excitation by long relativistic electron bunches [38–41] with the COMPASS code [30–32].

4.2. Mathematical Model and Parameter Choice

The dynamics of a relativistic electron bunch is described by the relativistic Vlasov equations (the Belyaev–Budker equations)

$$\frac{\partial f_\alpha}{\partial t} + \mathbf{V}_\alpha \cdot \frac{\partial f_\alpha}{\partial \mathbf{r}} + eZ_\alpha\left(\mathbf{E} + \frac{1}{c}\mathbf{V}_\alpha \times \mathbf{B}\right) \cdot \frac{\partial f_\alpha}{\partial \mathbf{p}} = 0$$

for the distribution functions $f_\alpha(\mathbf{r}, \mathbf{p})$ of each plasma component and by Maxwell's equations for the self-consistent electric and magnetic fields. At the initial instant, a two-component ($m_i/m_e = 1840$) cold plasma fills the entire computation region $[0, L] \times [0, R]$ with the length $L = 100$ cm and radius $R = 10$ cm. A cold relativistic electron bunch is injected into the plasma through the $z = 0$ plane. The bunch velocity is $V_b = c\sqrt{1 - 1/\gamma_b^2}$, and the initial bunch radius is $R_0 = 4c/\omega_{pe}$. The plasma and bunch particles can escape freely from the computation region through the two boundary surfaces $z = 0$ and $z = L$ and are elastically reflected from the $r = R$ surface. Cold plasma electrons and ions can also return to the computation region from the buffer zones $z < 0$ and $z > L$. The boundary conditions for the electromagnetic fields imply the existence of a metal wall at the cylindrical surface $r = R$ and free emission of electromagnetic waves from the right and left boundaries. In calculations, we used an explicit scheme. The mass of the model particle is a function of the radial coordinate, and the total particle number is about 10^6. Like the calculations described in Section 3, all simulations were carried out with a Pentium-133 PC using an advanced PIC algorithm. Our simulations showed that, for $\gamma_b = 5$, the bunch-to-plasma density ratio n_b/n_0 increases from the initial value 0.018 to 0.04 already at

$t = 60\,\omega_{pe}^{-1}$. At the time $t = 100\,\omega_{pe}^{-1}$, the maximum electron density in the bunch becomes comparable to the plasma density, thereby indicating a very strong bunch modulation. In this case, the electron plasma density n_e also becomes modulated very strongly. The spatial distributions of n_e at the times $t = 60\,\omega_{pe}^{-1}$ and $t = 100\,\omega_{pe}^{-1}$ are shown in Figs. 7a and 7b, respectively. We can see that, at the time $t = 100\,\omega_{pe}^{-1}$, the maximum amplitude of n_e is larger than the initial amplitude by a factor of 4.5. The spatial distributions of the longitudinal (E_z) and radial (E_r) electric fields computed for the same times as in Fig. 7 are shown in Figs. 8 and 9, respectively.

4.3. Discussions and Conclusions

The numerical experiments described above show that the nonlinear dynamics of both the bunch electrons and the electron and ion plasma components lead to the following effects. The radii of the bunches vary over a very wide range. The self-modulation of a long bunch gives rise to a very strong modulation of the bunch and plasma densities, thereby substantially increasing the amplitude of the excited wake electric fields. However, it is necessary that the bunch length be optimum, because the self-modulation of longer bunches does not increase the amplitude of the excited electric fields. The results of numerical modeling show that even a very low-density relativistic electron bunch can perturb the plasma so strongly that the density perturbation ampli-

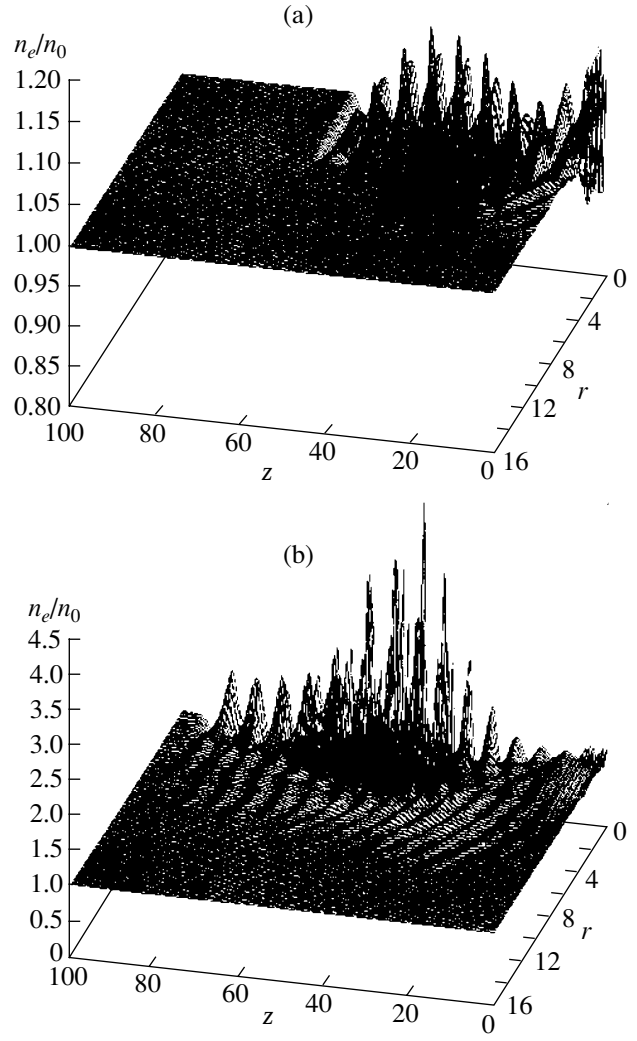

Fig. 7. Spatial distributions of the electron plasma density at the times (a) $t = 60\,\omega_{pe}^{-1}$ and (b) $t = 100\,\omega_{pe}^{-1}$. The coordinates are normalized to the skin depth c/ω_{pe}.

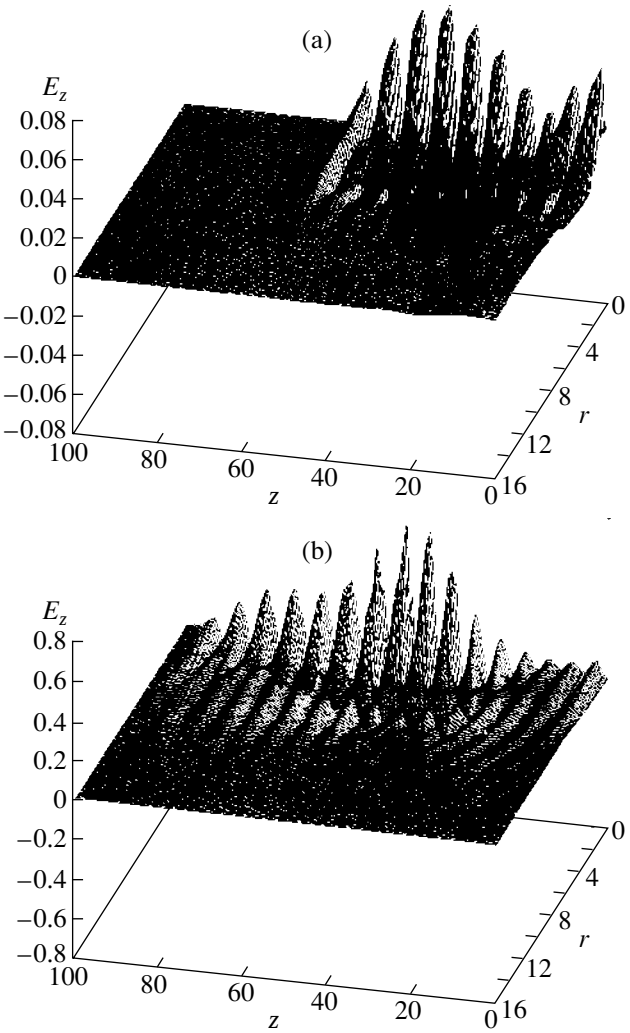

Fig. 8. Spatial distributions of the longitudinal electric field E_z (in units of $m_e\omega_{pe}c/e$) at the times (a) $t = 60\,\omega_{pe}^{-1}$ and (b) $t = 100\,\omega_{pe}^{-1}$. The coordinates are normalized to the skin depth c/ω_{pe}.

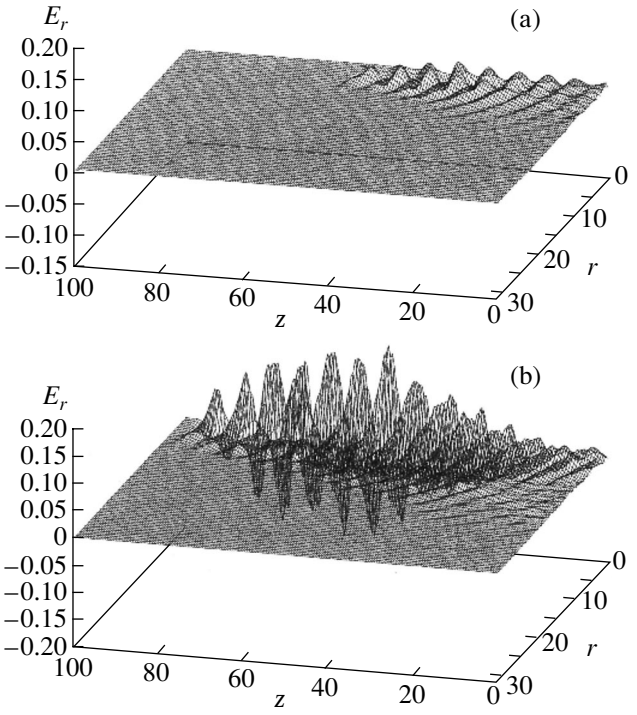

Fig. 9. Spatial distributions of the radial electric field E_r (in units of $m_e\omega_{pe}c/e$) at the times (a) $t = 60\,\omega_{pe}^{-1}$ and (b) $t = 100\,\omega_{pe}^{-1}$. The coordinates are normalized to the skin depth c/ω_{pe}.

tude will become comparable with the initial particle density of the plasma. This conclusion indicates that the plasma electrons cannot be described in the linear approximation. The results obtained show that both the effect of the self-modulation of long relativistic electron bunches and the use of a train of bunches hold promise for the generation of accelerating fields that would be far stronger than those achievable in conventional accelerators. Further investigations in this direction will provide the physical basis for the development and creation of a new generation of devices capable of accelerating charged particles at higher rates.

5. EXCITATION OF WAKE FIELDS BY A RELATIVISTIC ELECTRON BUNCH IN A MAGNETIZED PLASMA

Another promising way of accelerating charged particles is to excite wake fields by a relativistic electron bunch in a magnetized plasma [25–27]. Here, we present the main results obtained on the excitation of wake fields by an individual bunch in a magnetized plasma. In our opinion, this scheme is the most advantageous: because of the nonresonant character of the wake field excitation, it is only slightly sensitive to longitudinal density variations peculiar to a real plasma. Additionally, in order to prevent the development of electromagnetic filamentation or the onset of slipping instabilities, as well as other kinds of instabilities (see, e.g., [28]), it is worthwhile to apply a stabilizing external longitudinal magnetic field. As will be seen below, the stabilizing field not only serves to suppress instabilities but also gives rise to a large number of new wave branches, thereby substantially expanding the possibilities of the wake field acceleration scheme. In this section, we determine the wake field generated by an axisymmetric relativistic electron bunch propagating along the *z*-axis in a magnetized plasma, assuming that the ions are immobile and neglecting the electron thermal motion. The expression for the longitudinal component of the electric field excited by an annular relativistic electron bunch in an unbounded magnetized plasma was obtained in [25]:

$$E_z = \frac{2Q_0\omega_{pe}^2}{V_b^2\gamma_b^2}\frac{\tau}{(\tau^2+\mu^2)^{3/2}} \times \left(\sqrt{\mu^2+\tau^2}\sin\sqrt{\tau^2+\mu^2}+\cos\sqrt{\tau^2+\mu^2}\right),$$

where $\tau = \omega_{pe}\left(t - \frac{z}{V_b}\right)$; $\mu = \frac{\omega_{pe}R_0}{V_b\gamma_b}$; ω_{pe} is the Langmuir frequency of the plasma electrons; and V_b, R_0, and Q_0 are the velocity, radius, and electric charge of the bunch, respectively.

Far behind the bunch, the wake field falls off as $\tau^{-3/2}$, because the group velocity of plasma oscillations in a sufficiently strong magnetic field is finite. Because of the emission of plasma waves from the axial region, the wake field decreases in the longitudinal direction.

We consider a waveguide partially filled with a plasma, i.e., a waveguide with a vacuum gap between the plasma surface $r = a$ and the perfectly conducting wall $r = b$, and assume that the waveguide is placed in an external magnetic field.

The field distribution over the waveguide cross section is governed by the transverse wavenumbers. The ranges $\lambda_{1,2}^2 > 0$ and $\lambda_{1,2}^2 < 0$ correspond to the spatial and surface modes, respectively. The complex values of $\lambda_{1,2}^2$ refer to a hybrid mode. The boundaries of the region where $\lambda_{1,2}^2$ are complex are determined by the inequalities $\omega_1 > \omega > \omega_2$, where

$$\omega_{1,2} = kc\frac{2\omega_{pe}^2+\omega_{He}^2 \pm (\omega_{pe}^4+\omega_{He}^2\omega_{pe}^2-\omega_{He}^2k^2c^2)^{1/2}}{\omega_{He}^2+4k^2c^2},$$

ω_{He} is the gyrofrequency of the plasma electrons, and k is the longitudinal wavenumber.

In order for a relativistic electron bunch to excite a hybrid mode, the relativistic factor of the bunch should satisfy the condition $\gamma_b > \frac{\omega_{He}}{2\omega_{pe}}$.

The electromagnetic field distribution and the frequency of a hybrid mode that synchronously accompanies the bunch were obtained numerically for the following parameters of the plasma waveguide: $\frac{\omega_{He}}{\omega_{pe}} = 6.3$, $\frac{\omega_{pe}a}{c} = 23.3$, $\frac{b}{a} = 2.4$, and $\gamma_b = 4.6$, in which case the frequency of the wake hybrid mode is equal to $0.35\omega_{pe}$. It was found that, at the radius $\frac{r}{a} = 0.8$, the absolute value of the longitudinal component of the electric field has a pronounced maximum, which corresponds to an energy conversion factor equal to $R_E = \left|\frac{E_{z\max}}{E_z(r=0)}\right| = 37$.

Recall that the energy conversion factor is defined as the ratio of the amplitude of the electric field accelerating a driven bunch to the amplitude of the electric field decelerating a driving bunch (the bunch exciting the wake field). Such a large value of R_E indicates that the maximum energy the driven bunch can gain during acceleration is significantly higher (by a factor of R_E) than the initial energy of the driving bunch.

Hence, it is shown that, for a certain relation among the parameters of the plasma–bunch–magnetic field system, the hybrid nature of the wake waves, which are excited by a relativistic electron bunch in a magnetized plasma and are a superposition of the surface and spatial modes, makes it possible to accelerate the driven bunch to the maximum energy

$$\varepsilon_{\max} = mc^2(R_E\gamma_b - 1),$$

which is many times higher than the initial energy of the driving bunch (even when the bunch is initially unmodulated in the longitudinal direction).

6. CONCLUSION

We have reviewed the results from theoretical and experimental investigations as well as from mathematical modeling of the wake-field generation by both charged-particle bunches and laser radiation in a plasma and have analyzed the wake-field acceleration of charged particles. A new, substantially modified version of the PBWA scheme has recently been proposed—a version based on the self-modulation of a laser pulse. The most impressive results on plasma methods of charged particle acceleration were obtained in the LWFA experiments [19–22], in which the accelerating fields at short distances were as strong as (1.5–20) $\times 10^8$ V/cm and the particles were accelerated to energies of 100–300 MeV over distances of about 1 cm. An interesting fact has been established: for a certain relation among the parameters of the plasma–bunch–magnetic field system, the hybrid nature of the wake waves (which are excited by a relativistic electron bunch in a magnetized plasma and are a superposition of the surface and spatial modes) makes it possible to accelerate the driven bunch to an energy $\varepsilon_{\max}$ that is many times higher than the initial energy of the driving bunch (even when the bunch is initially unmodulated in the longitudinal direction). We have discussed the formation of an ion channel as a result of the radial ion motion in self-consistent electromagnetic fields excited by a train of relativistic electron bunches. The parameters of the fully developed channel are determined by the plasma-to-bunch density ratio and the ratio of the bunch radius to the skin depth. The effective dimensions of the channel and its "depth" (i.e., the elevated ion density at the channel axis) increase monotonically both in time and in the direction opposite to the propagation direction of the bunches. The formed ion channel stabilizes the propagation of relativistic electron bunches, which thus generate stronger accelerating fields. The results of 2.5-dimensional numerical modeling of the wake-field excitation during the self-modulation of a long relativistic electron bunch showed that the maximum electron density in the bunch becomes comparable to the plasma density and the amplitude of the plasma density perturbations becomes larger than the initial plasma density by a factor of 4.5. This indicates a very strong modulation of both the bunch density and the plasma density. That is why, even in the above case of a low-density bunch (in which the unperturbed electron density is about two orders of magnitude lower than the plasma density), it is incorrect to describe the plasma in the linear approximation. The amplitude of the longitudinal field is about 0.8 of the maximum electric field that can be generated in the plasma, and the amplitude of the radial field is about 0.4 of the maximum possible field. An important point is that the field amplitude increases only over a short distance along a relativistic electron bunch; hence, it would be of no use to operate with bunches whose length exceeds the distance over which the longitudinal field amplitude is maximum, because doing so would provide no additional increase in the excited wake field. The results obtained with allowance for all possible nonlinearities give a better insight into the three-dimensional behavior of relativistic electron bunches in a plasma and may help to ensure the optimum conditions for the wake-field generation during the dynamic self-modulation of the bunches. The results of investigations of the excitation of accelerating fields by an individual relativistic electron bunch or by a train of such bunches in a plasma (in particular, in the presence of an external magnetic field) make it possible to evaluate the potentialities of the wake-field acceleration method and to analyze whether it can serve as a basis for creating a new generation of devices capable of accelerating charged par-

ticles at substantially higher (by two to three orders of magnitude) rates in comparison with those achievable in classical linear resonance accelerators.

REFERENCES

1. G. I. Budker, in *Proceedings of the CERN Symposium on High Energy Accelerators and Pion Physics, Geneva, 1956*, Vol. 1, p. 68.
2. V. I. Veksler, in *Proceedings of the CERN Symposium on High Energy Accelerators and Pion Physics, Geneva, 1956*, Vol. 1, p. 80.
3. Ya. B. Fainberg, in *Proceedings of the CERN Symposium on High Energy Accelerators and Pion Physics, Geneva, 1956*, Vol. 1, p. 84.
4. T. Tajima and J. M. Dawson, Phys. Rev. Lett. **43**, 267 (1979).
5. Ya. B. Fainberg, Usp. Fiz. Nauk **93**, 617 (1967) [Sov. Phys. Usp. **10**, 750 (1968)].
6. Ya. B. Fainberg, Fiz. Plazmy **13**, 607 (1987) [Sov. J. Plasma Phys. **13**, 350 (1987)].
7. Ya. B. Fainberg, Fiz. Plazmy **20**, 613 (1994) [Plasma Phys. Rep. **20**, 549 (1994)].
8. Ya. B. Fainberg, Fiz. Plazmy **23**, 275 (1997) [Plasma Phys. Rep. **23**, 251 (1997)].
9. Ya. B. Fainberg, Fiz. Plazmy **26**, 362 (2000) [Plasma Phys. Rep. **26**, 335 (2000)].
10. P. Chen, J. M. Dawson, R. W. Huff, and T. Katsouleas, Phys. Rev. Lett. **54**, 693 (1985).
11. T. Katsouleas, Phys. Rev. A **33**, 2056 (1986).
12. A. Ts. Amatuni, M. R. Magomedov, E. V. Sekhposyan, and S. S. Elbakyan, Fiz. Plazmy **5**, 85 (1979) [Sov. J. Plasma Phys. **5**, 49 (1979)].
13. J. B. Rosenzweig, Preprint No. 90/40 (FERMILAB, Batavia, 1990).
14. J. B. Rosenzweig, B. N. Breizman, T. Katsouleas, and J. J. Su, Phys. Rev. A **44**, R6189 (1991).
15. N. E. Andreev, L. M. Gorbunov, V. I. Kirsanov, *et al.*, Pis'ma Zh. Éksp. Teor. Fiz. **55**, 551 (1992) [JETP Lett. **55**, 571 (1992)].
16. J. Krall, A. Ting, E. Esarey, and P. Sprangle, Phys. Rev. E **48**, 2157 (1993).
17. T. M. Antonsen and P. Mora, Phys. Rev. Lett. **69**, 2204 (1992).
18. P. Sprangle, E. Esarey, J. Krall, and G. Joyce, Phys. Rev. Lett. **69**, 2200 (1992).
19. K. Nakajima, T. Kawakubo, H. Nakanishi, *et al.*, in *Proceedings of the Conference on Advanced Accelerator Concepts, Fontana, 1994*, p. 145; AIP Conf. Proc. **335**, 145 (1995).
20. A. Modena, Z. Najimidin, A. E. Dangor, *et al.*, Nature (London) **337**, 806 (1995).
21. D. Umstadter, J. K. Kim, and E. Dodd, Phys. Rev. Lett. **76**, 2073 (1996).
22. A. Ogata, H. Nakanishi, T. Kawakubo, *et al.*, in *Proceedings of the Conference on Advanced Accelerator Concepts, Fontana, 1994*, p. 501; AIP Conf. Proc. **335**, 501 (1995).
23. S. V. Bulanov and A. S. Sakharov, Fiz. Plazmy **26**, 1074 (2000) [Plasma Phys. Rep. **26**, 1005 (2000)].
24. A. I. Akhiezer and R. V. Polovin, Zh. Éksp. Teor. Fiz. **30**, 915 (1956) [Sov. Phys. JETP **3**, 696 (1956)].
25. V. A. Balakirev, V. I. Karas', I. V. Karas', and G. V. Sotnikov, Vopr. At. Nauki Tekh., Ser.: Plazm. Élektron. Novye Metody Uskoreniya **1** (2), 113 (2000).
26. V. A. Balakirev, V. I. Karas', I. V. Karas', and Ya. B. Fainberg, in *Proceedings of the XXVII Zvenigorod Conference on Plasma Physics and Controlled Nuclear Fusion, Zvenigorod, 2000*, p. 180.
27. V. A. Balakirev, I. V. Karas', and G. V. Sotnikov, Fiz. Plazmy **26**, 948 (2000) [Plasma Phys. Rep. **26**, 889 (2000)].
28. C. Joshi, T. Katsouleas, J. M. Dawson, *et al.*, IEEE J. Quantum Electron. **QE-23**, 1571 (1987).
29. V. A. Balakirev, G. V. Sotnikov, and Ya. B. Fainberg, Fiz. Plazmy **22**, 634 (1996) [Plasma Phys. Rep. **22**, 573 (1996)].
30. O. V. Batishev, I. V. Karas', O. N. Shulika, *et al.*, Bull. Am. Phys. Soc. **45** (7), 72 (2000).
31. O. V. Batishchev, V. I. Karas', V. D. Levchenko, *et al.*, Fiz. Plazmy **20**, 654 (1994) [Plasma Phys. Rep. **20**, 587 (1994)].
32. V. I. Karas', O. V. Batishchev, Yu. S. Sigov, and Ya. B. Fainberg, Part. Accel. **37–38**, 281 (1992).
33. O. V. Batishchev, V. B. Krasovitskiĭ, Yu. S. Sigov, *et al.*, Fiz. Plazmy **19**, 738 (1993) [Plasma Phys. Rep. **19**, 379 (1993)].
34. O. V. Batishchev, V. I. Karas', Yu. S. Sigov, and Ya. B. Fainberg, Fiz. Plazmy **20**, 650 (1994) [Plasma Phys. Rep. **20**, 583 (1994)].
35. V. I. Karas', Ya. B. Fainberg, V. D. Levchenko, and Yu. S. Sigov, in *Proceedings of the Particle Accelerator Conference and International Conference on High-Energy Accelerators, Dallas, 1995*, Vol. 2, p. 1233.
36. V. I. Karas', I. V. Karas', V. D. Levchenko, *et al.*, Fiz. Plazmy **23**, 311 (1997) [Plasma Phys. Rep. **23**, 285 (1997)].
37. N. I. Aĭzatskiĭ, V. A. Balakirev, A. N. Dovbnya, *et al.*, in *Proceedings of the XXVII Zvenigorod Conference on Plasma Physics and Controlled Nuclear Fusion, Zvenigorod, 2000*, p. 156.
38. V. A. Balakirev, V. I. Karas', Ya. B. Fainberg, *et al.*, in *Proceedings of the 12th International Conference on High-Power Particle Beams, Haifa, 1998*, Vol. 2, p. 392.
39. V. I. Karas', V. A. Balakirev, Ya. B. Fainberg, *et al.*, in *Proceedings of XVIII International Symposium on Discharges and Electrical Insulation in Vacuum, Eindhoven, 1998*, Vol. 2, p. 781.
40. V. I. Karas', V. A. Balakirev, Ya. B. Fainberg, *et al.*, Vopr. At. Nauki Tekh., Ser.: Plazm. Élektron. Novye Metody Uskoreniya **1** (2), 122 (2000).
41. V. I. Karas', V. A. Balakirev, Ya. B. Fainberg, *et al.*, J. Tech. Phys. **41** (1), 293 (2000).
42. V. A. Balakirev, G. V. Sotnikov, and Ya. B. Fainberg, Fiz. Plazmy **22**, 165 (1996) [Plasma Phys. Rep. **22**, 151 (1996)].
43. R. Keinigs and M. E. Jones, Phys. Fluids **30**, 252 (1987).

44. A. Ts. Amatuni, E. V. Sekhposyan, A. G. Khachatryan, and S. S. Elbakyan, Fiz. Plazmy **21**, 1000 (1995) [Plasma Phys. Rep. **21**, 945 (1995)].
45. E. Esarey, J. Krall, and P. Sprangle, Phys. Rev. E **48**, 2157 (1993).
46. D. Umstadter, E. Esarey, and J. Kim, Phys. Rev. Lett. **69**, 2204 (1992).
47. P. Sprangle and E. Esarey, Phys. Rev. Lett. **67**, 2021 (1991).
48. V. A. Balakirev, A. O. Ostrovskiĭ, and Yu. V. Tkach, Vopr. At. Nauki Tekh., Ser.: Tekh. Fiz. Éksp. **6**, 168 (1990).
49. A. Ting, C. I. Moore, K. Krushelnik, *et al.*, IEEE Trans. Plasma Sci. **PS-26**, 611 (1998).
50. K. Nakajma and A. Ogata, in *Proceedings of the 11th Symposium on Accelerator Science and Technology, Harima, 1997*, p. 36.
51. R. Assmann, P. Chen, F. Decker, *et al.*, in *Proceedings of the 1999 Particle Accelerator Conference, New York, 1999*, p. 330.
52. S. V. Bulanov, V. A. Vshivkov, G. I. Dudnikova, *et al.*, Fiz. Plazmy **23**, 284 (1997) [Plasma Phys. Rep. **23**, 259 (1997)].
53. N. E. Andreev, L. M. Gorbunov, and A. A. Frolov, Fiz. Plazmy **24**, 888 (1998) [Plasma Phys. Rep. **24**, 825 (1998)].
54. V. A. Balakirev, V. I. Karas', A. P. Tolstoluzhskiĭ, and Ya. B. Fainberg, Fiz. Plazmy **23**, 316 (1997) [Plasma Phys. Rep. **23**, 290 (1997)].
55. J. Krall and G. Joyce, Phys. Plasmas **2**, 1326 (1995).
56. T. Katsouleas, J. M. Dawson, D. Sultana, and Y. Yan, IEEE Trans. Nucl. Sci. **32**, 3554 (1985).
57. P. Sprangle, B. Hafizi, J. R. Penano, *et al.*, Phys. Rev. Lett. **85**, 5110 (2000).
58. L. M. Gorbunov and V. I. Kirsanov, Zh. Éksp. Teor. Fiz. **93**, 509 (1987) [Sov. Phys. JETP **66**, 290 (1987)].
59. P. Chen and R. Nable, in *Advanced Acceleration Concepts*, Ed. by S. Chattopadhyay, S. McCullough, and P. Dahl (American Inst. of Physics, New York, 1997), p. 273.
60. P. Chen, Z. Huang, and R. Ruth, in *Proceedings of the 4th Tamura Symposium on Accelerator Physics*, Ed. by T. Tajima (American Inst. of Physics, New York, 1995), p. 95; AIP Conf. Proc. **356**, 95 (1995).
61. I. A. Grishaev and N. N. Nasonov, Pis'ma Zh. Tekh. Fiz. **3**, 1084 (1977) [Sov. Tech. Phys. Lett. **3**, 446 (1977)].
62. T. Tajima and M. Covenago, Phys. Rev. Lett. **59**, 1440 (1987).
63. T. Tajima and B. S. Newberger, Phys. Rev. A **40**, 6897 (1989).
64. S. C. Kitson, W. L. Barnes, and J. R. Sambles, Phys. Rev. Lett. **77**, 2670 (1996).
65. *Discrete Simulation of Plasma*, Ed. by Yu. S. Sigov (Inst. Prikl. Mat. im. M. V. Keldysha Akad. Nauk SSSR, Moscow, 1990).
66. O. V. Batishchev, V. I. Karas', V. D. Levchenko, and Yu. S. Sigov, Fiz. Plazmy **20**, 654 (1994) [Plasma Phys. Rep. **20**, 587 (1994)].
67. O. V. Batishchev, Preprint No. 4, IPM im. M.V. Keldysha AN SSSR (Keldysh Institute of Applied Mathematics, Academy of Sciences of USSR, Moscow, 1986).
68. O. V. Batishchev and Yu. S. Sigov, Preprint No. 87, IPM im. M.V. Keldysha AN SSSR (Keldysh Institute of Applied Mathematics, Academy of Sciences of USSR, Moscow, 1988).
69. N. I. Aĭzatskiĭ, E. Z. Biller, V. N. Boriskin, *et al.*, Fiz. Plazmy **20**, 671 (1994) [Plasma Phys. Rep. **20**, 603 (1994)].
70. *Theory and Computation of Linear Accelerators: Collection of Articles* (Gosatomizdat, Moscow, 1962).
71. B. M. Bolotovskiĭ and S. N. Stolyarov, *Einsteinian Collection, 1978–1979*, Ed. by V. L. Ginzburg *et al.* (Nauka, Moscow, 1983), p. 173.
72. V. P. Kovalenko, V. M. Pergamenshchik, and V. I. Starkov, Fiz. Plazmy **11**, 417 (1985) [Sov. J. Plasma Phys. **11**, 241 (1985)].
73. V. M. Kuklin, Ukr. Fiz. Zh. **31**, 853 (1986).
74. A. Ts. Amatuni, E. V. Sekhposyan, and S. S. Elbakyan, Fiz. Plazmy **12**, 1145 (1986) [Sov. J. Plasma Phys. **12**, 662 (1986)].
75. V. A. Balakirev, Yu. P. Bliokh, I. N. Onishchenko, and Ya. B. Fainberg, Fiz. Plazmy **14**, 218 (1988) [Sov. J. Plasma Phys. **14**, 123 (1988)].
76. S. V. Bulanov, L. M. Kovrizhnykh, and A. S. Sakharov, Phys. Rep. **186**, 1 (1990).
77. A. V. Kuznetsov, T. Zh. Esirkepov, F. F. Kamenets, and S. V. Bulanov, Fiz. Plazmy **27**, 225 (2001) [Plasma Phys. Rep. **27**, 211 (2001)].
78. I. V. Karas', Author's Abstract of Candidate's Dissertation in Physics and Mathematics (NNTs KhFTI, Kharkov, 2001).
79. J. B. Rosenzweig, Phys. Rev. A **38**, 3634 (1988).
80. P. Schoessow, E. Chojnacki, W. Gai, *et al.*, in *Proceedings of the 1993 Particle Accelerator Conference, Washington, 1993*, Vol. 4, p. 2596.
81. N. Barov and J. Rosenzweig, in *Proceedings of the 1995 Particle Accelerator Conference, Dallas, 1995*, Vol. 2, p. 976.
82. N. Barow, M. Conde, J. B. Rosenzweig, *et al.*, in *Proceedings of the 1995 Particle Accelerator Conference, Dallas, 1995*, Vol. 2, p. 631.
83. M. I. K. Santala, Z. Najmudin, E. L. Clark, *et al.*, Phys. Rev. Lett. **86**, 1227 (2001).
84. C. Coverdale, C. B. Darrow, C. D. Decker, *et al.*, in *Proceedings of the 1995 Particle Accelerator Conference, Dallas, 1995*, Vol. 2, p. 758.
85. R. Wagner, S.-Y. Chen, A. Maksimchuk, and D. Umstadter, Phys. Rev. Lett. **78**, 3125 (1997).
86. J. Rosenzweig, D. Cline, B. Cole, *et al.*, Phys. Rev. Lett. **61**, 98 (1988).
87. A. Ogata, in *Proceedings of the Congress on Advanced Accelerator Concepts, Port Jefferson, 1992*, Ed. by J. Wurtele (American Inst. of Physics, New York, 1993), p. 420; AIP Conf. Proc. **279**, 420 (1993).
88. J. M. Dawson, Phys. Plasmas **6**, 4436 (1999).
89. C. E. Clayton, K. A. Marsh, M. Everett, *et al.*, Phys. Rev. Lett. **70**, 37 (1993).

90. C. E. Clayton, K. A. Marsh, M. Everett, *et al.*, in *Proceedings of 1993 Particle Accelerator Conference, Washington, 1993*, Vol. 4, p. 2551.
91. A. G. Litvak, Izv. Vyssh. Uchebn. Zaved., Radiofiz. **7**, 562 (1964).
92. M. N. Rosenbluth and C. S. Liu, Phys. Rev. Lett. **29**, 701 (1972).
93. G. Shvets and J. S. Wurtele, Phys. Rev. Lett. **73**, 3540 (1994).
94. C. I. Moore, A. Ting, K. Krushelnick, *et al.*, Phys. Rev. Lett. **79**, 3909 (1997).
95. K. Krushelnik, A. Ting, C. I. Moore, *et al.*, Phys. Rev. Lett. **78**, 4047 (1997).
96. C. E. Clayton, K.-C. Tzeng, D. Gordon, *et al.*, Phys. Rev. Lett. **81**, 100 (1998).
97. F. Dorchies, F. Amiranoff, V. Malka, *et al.*, Phys. Plasmas **6**, 2903 (1999).
98. F. Amiranoff, S. Baton, D. Bernard, *et al.*, Phys. Rev. Lett. **81**, 995 (1998).
99. N. E. Andreev, V. I. Kirsanov, and A. S. Sakharov, Fiz. Plazmy **26**, 416 (2000) [Plasma Phys. Rep. **26**, 388 (2000)].
100. S. Y. Chen, M. Krishnan, A. Maksimchuk, *et al.*, Phys. Plasmas **6**, 4739 (1999).
101. V. Malka, N. Renard-Le Galloudec, S. Huller, *et al.*, Phys. Plasmas **7**, 4259 (2000).
102. G. S. Sarkisov, V. Y. Bychenkov, V. N. Novikov, *et al.*, Phys. Rev. E **59**, 7042 (1999).
103. J. Faure, V. Malka, J.-R. Marques, *et al.*, Phys. Plasmas **7**, 3009 (2000).
104. P. E. Young and P. R. Bolton, Phys. Rev. Lett. **77**, 4556 (1996).
105. B. Ritchie and P. R. Bolton, Phys. Rev. E **58**, 6460 (1998).
106. M. Tatarakis, J. R. Davies, P. Lee, *et al.*, Phys. Rev. Lett. **81**, 999 (1998).
107. M. Borghesi, A. J. MacKinnon, A. R. Bell, *et al.*, Phys. Rev. Lett. **81**, 112 (1998).
108. G.-Z. Sun, E. Ott, Y. C. Lee, and P. Guzdar, Phys. Fluids **30**, 526 (1987).
109. N. E. Andreev and L. M. Gorbunov, Usp. Fiz. Nauk **169**, 53 (1999).
110. N. Barov, M. Conde, W. Gai, and J. B. Rosenzweig, IEEE Trans. Plasma Sci. **PS-26**, 627 (1998).

Translated by O. Khadin

Plasma Physics Reports, Vol. 28, No. 2, 2002, pp. 141–157. From Fizika Plazmy, Vol. 28, No. 2, 2002, pp. 161–179.

CHARGED PLASMA

l = 1 Diocotron Instability of Single Charged Plasmas[1]

A. V. Arefiev*, I. A. Kotelnikov, M. Romé***, and R. Pozzoli*****

**University of Texas at Austin, Austin, TX, USA*

***Budker Institute of Nuclear Physics, Siberian Division, Russian Academy of Sciences, pr. Akademika Lavrent'eva 11, Novosibirsk, 630090 Russia*

e-mail: Kotelnikov@inp.nsk.su

****Istituto Nazionale di Fisica della Materia, U.d.R. Milano, and Dipartimento di Fisica, Università degli Studi di Milano, Italy*

e-mail: Massimiliano.Rome@mi.infn.it; e-mail: Roberto.Pozzoli@mi.infn.it

Received August 24, 2001

Abstract—The linear stability analysis of the $l = 1$ diocotron perturbations in a low density single charged plasma confined in a cylindrical Penning trap is critically revisited. Particular attention is devoted to the instability due to the presence of one or more stationary points in the radial profile of the azimuthal rotation frequency. The asymptotic analysis of Smith and Rosenbluth for the case of a single-bounded plasma column (algebraic instability proportional to $t^{1/2}$) is generalized in a few respects. In particular, the existence of unperturbed density profiles that give rise to $l = 1$ algebraic instabilities growing with time proportionally to $t^{1-1/m}$, $m \geq 3$ being the order of a stationary point in the rotation frequency profile, and even proportionally to t, is pointed out. It is also shown that smoothing the density jumps of a multistep density profile can convert algebraically growing perturbations into exponentially decaying modes. The relevant damping rates are computed. The asymptotic analysis ($t \longrightarrow \infty$) of the fundamental diocotron perturbations is then generalized to the case of a cylindrical Penning trap with an additional coaxial inner conductor. It is shown that the algebraic instability found in the case of a single-bounded plasma column becomes exponential at longer times. The relevant linear growth rate is computed by a suitable inverse Laplace transform (contour integral in the complex plane). In the particular case of an uncharged inner conductor of radius a, the growth rate is shown to scale as $a^{4/3}$ for $a \longrightarrow 0$. The theoretical results are compared with the numerical solution of the linearized two-dimensional drift Poisson equations. © *2002 MAIK "Nauka/Interperiodica".*

1. INTRODUCTION

It is known that nonneutral plasmas consisting of an ensemble of single species charged particles have some unique properties. In particular, a single charged plasma can approach a state of global (though localized in space) state of thermodynamic equilibrium, where the plasma is contained in a cylindrical Penning trap by means of static electric and magnetic fields for up to a few hours, without visible degradation of confinement [1]. The existence of a state of global thermodynamic equilibrium in a cylindrical Penning trap (see Fig. 1a) has been known for more than 20 years [2–6]. Recently, it was observed that a thermodynamic equilibrium is also possible for a hollow plasma cloud confined in a cylindrical trap with a coaxial inner conductor [7] (see Fig. 1b).

A cloud of single charged particles with an arbitrary radial density profile (i.e., in general, not consistent with a thermodynamic equilibrium) can be unstable against small azimuthal and axial perturbations. The linear stability of a single charged plasma column was studied in detail in the literature [8, 9]. In this paper, we are interested in the case of purely azimuthal diocotron perturbations (i.e., $k_z = 0$, k_z being the axial wavenumber of the perturbation). In this case, using a model with a radial step density profile (Fig. 2a), Levy [10] showed that an infinitely long plasma column radially bounded by two cylindrical conductors held at fixed potential is neutrally stable when it is in contact with one or both conductors or if the charge on the inner conductor has a large enough (positive or negative) value. If the central conductor is absent, the $l = 1$ diocotron mode is neutrally stable, while lower $l \geq 2$ modes can be unstable. The effect of the central conductor on the stability of a hollow plasma column has also been studied experimentally [11].

In general, the number of eigenmodes in a plasma with a multistep density profile for a given azimuthal number l is equal to the number of density jumps [10, 12]. A smooth density profile yields a continuum spectrum, while neutrally stable modes become exponentially decaying modes [13–16], except for the case $l = 1$, for which neutrally stable modes exist for an arbitrary density profile [13, 17]. The continuum spectrum decays as some power of time [13–16, 18–20], so that neutrally stable eigenmodes can be hidden in the time evolution.

[1] This article was submitted by the authors in English.

1063-780X/02/2802-0141$22.00 © 2002 MAIK "Nauka/Interperiodica"

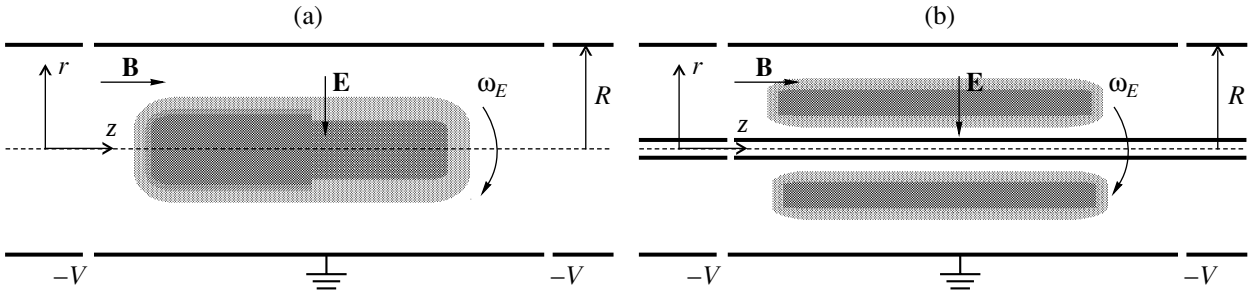

Fig. 1. Scheme of a cylindrical Penning trap (a) without a central conductor and (b) with a central conductor.

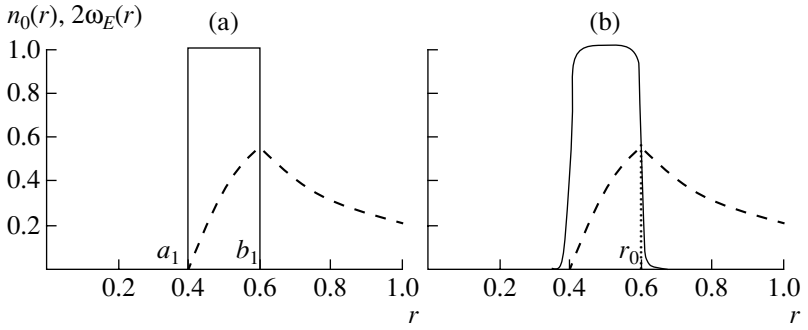

Fig. 2. Plasma density and electric drift frequency vs. radius: (a) a plasma column with a step density profile and (b) more realistic profile. When the density jump at $r = 0.6$ is smoothed, a stationary point of the electric drift frequency $r_0 \approx 0.6$ appears, where $\omega_E' = 0$, which gives rise to an algebraic SR instability. When an inner conductor is included, the algebraic instability is converted into an exponential one at late times, with the real part of frequency close to $\omega_E(r_0)$.

Earlier theories were recently critically reviewed, because the results of experiments showed an exponential growth of the $l = 1$ diocotron mode [21]. The explicit solution to the initial value problem obtained by Smith and Rosenbluth [22] for the special case $l = 1$, but for an arbitrary density profile, reveals an algebraic instability of a hollow electron column with the perturbation growing as $\sqrt{t}$. In the following, this instability will be referred to as the Smith–Rosenbluth (SR) instability. In [23, 24], it was shown that finite-Larmor-radius (FLR) effects can lead to an exponentially growing instability, but with a growth rate much smaller than that experimentally observed. Smith [25] showed that shifts in the azimuthal rotation frequency due to the finite plasma length can lead to exponential growth rates comparable to those of the experiments, but the shifts were adjusted *ad hoc*, making a quantitative comparison with the experiments difficult. More recently, Finn *et al.* [26] included the effect of a finite plasma length in a quasi-two-dimensional model, allowing a direct test of the theory. The instability mechanism involves compression of the plasma parallel to the magnetic field, with conservation of its line-integrated density. This mechanism has recently been tested experimentally by Kabantsev and Driscoll [27]. A more general treatment of this case was presented very recently in [28]. An analysis of finite-length diocotron modes, which includes kinetic effects, was also reported in [29]. For completeness, we also note that the nonlinear theory of the $l = 1$ diocotron modes was developed in [30, 31]. The nonlinear stage was investigated experimentally in [32]. It was found that a steplike electron cloud persists in a stationary state for a long time. In this case, the center of rotation of the cloud is displaced away from the axis of the trap and drifts around it.

In the present paper, the linear stability analysis of the $l = 1$ diocotron perturbations is critically revisited. Finite-length and FLR effects are neglected here. Particular attention is devoted to the instability due to the presence of one or more stationary points in the radial profile of the azimuthal rotation frequency. The asymptotic analysis of Smith and Rosenbluth [22] for the case of a single-bounded plasma column (algebraic instability proportional to $t^{1/2}$) is generalized to include density profiles that give rise to algebraic instabilities growing as $t^{1-1/m}$, $m \geq 3$ being the order of a stationary point in the rotation frequency profile, and even proportionally to t.

Moreover, the asymptotic analysis is generalized to the case of a Penning trap with a coaxial inner conduc-

tor. It is shown that the algebraic instability found in the case of a single-bounded plasma column becomes exponential at longer times. The relevant linear growth rate is computed using a suitable inverse Laplace transformation. The theoretical results are compared with the numerical solution of the linearized two-dimensional drift Poisson equations.

The paper is organized as follows. In Section 2, the SR solution of the initial-value problem is extended to the case of a Penning trap with a central conductor. In Section 3, the stability of a single charged plasma with a general density profile is analyzed. It is shown that an inflection point in the density profile yields an algebraic instability that grows proportionally to $t^{2/3}$. An example is also given of a density profile that exhibits an instability growing proportional to t. It is also shown how the asymptotic behavior of an initial density perturbation changes as the sharp edges of a multistep density profile are smoothed. The relevant computations are presented in Appendix A, in which an alternative derivation of the algebraic growth rate for the SR instability is also presented. Section 4 is devoted to an analysis of the plasma stability in a cylindrical Penning trap with a central conductor. The discussion is based on the calculations performed in Appendix B, which extend the derivation of the SR instability reported in Appendix A. The conclusions are drawn in Section 5.

2. BASIC EQUATIONS

In the model considered here, the evolution of the two-dimensional plasma density $n(r, \theta, t)$ and the electrostatic potential $\varphi(r, \theta, t)$ are governed by the equations [8, 9]

$$\frac{\partial n}{\partial t} + \frac{c}{B}(\nabla\varphi \times \nabla n)\cdot \mathbf{z} = 0, \tag{1a}$$

$$\Delta\varphi = -4\pi e n. \tag{1b}$$

Eqs. (1) are known as drift Poisson equations (or 2D MHD equations) and are written here for the guiding center of particles with charge e. The charged plasma is assumed to be contained in an infinitely long grounded cylindrical conductor of radius R. The system is immersed in a static and uniform magnetic field $\mathbf{B} = B\mathbf{z}$, directed along the axis of the cylinder.

The unperturbed equilibrium situation is described by a plasma density $n_0(r)$, depending only on the radial coordinate. The density $n_0(r)$ and the corresponding potential $\varphi_0(r)$, where $(1/r)(d/dr)r(d/dr)\varphi_0 = -4\pi e n_0$, obviously satisfy Eqs. (1). In the unperturbed state, the plasma is convected azimuthally with the local $\mathbf{E}\times\mathbf{B}$ velocity. The corresponding angular frequency is given by

$$\omega_E(r) = \frac{c}{B}\frac{1}{r}\frac{d\varphi_0}{dr} = \frac{4\pi e^2}{m\Omega r^2}\int_a^r n_0(r) r dr + \frac{2Qe}{m\Omega r^2}, \tag{2}$$

where Q denotes the charge per unit length on the inner conductor; a is its radius; and $\Omega = -eB/mc$ is the cyclotron frequency, assumed conventionally to be positive for negatively charged particles. The other notation is standard. The frequency ω_E is sometimes referred to as the electric drift frequency; we will follow this terminology. The drift Poisson Eqs. (1) are valid as long as the plasma frequency $\omega_p = \sqrt{4\pi n e^2/m}$ is small compared to the cyclotron frequency $|\Omega|$. Note that, due to the inequality $\omega_p \ll |\Omega|$, the drift frequency is also small, $|\omega_E| \ll \omega_p$.

In the following, dimensionless quantities are used. The density is normalized to an arbitrary reference density $\hat{n}$ (usually the maximum value of the density $\hat{n} = \max[n(r)]$ will be chosen unless the opposite is indicated). The lengths are normalized to the radius of the outer cylindrical conductor $\hat{r} = R$, while the normalization factors for the other relevant quantities are as follows: $\hat{\varphi} = 4\pi e\hat{n}\hat{r}^2$ for the potential, $\hat{\omega} = 4\pi e^2\hat{n}/m\Omega$ for frequencies, and $\hat{Q} = \pi e\hat{n}\hat{r}^2$ for the electric charge per unit length on the central conductor. Note that the normalization factors of φ and Q explicitly contain the particle charge e and, therefore, its sign. The normalization factor for the frequency also depends on the sign of e because it contains Ω.

The same notation is used in the following for dimensionless quantities, so that, e.g., Eq. (2) takes the form

$$\omega_E(r) = \frac{1}{r^2}\int_a^r n_0(r) r dr + \frac{Q}{2r^2}. \tag{3}$$

Note, in particular, the useful relations

$$n_0(r) = \frac{1}{r}\frac{d}{dr}[r^2\omega_E(r)], \quad Q = 2a^2\omega_E(a).$$

Linearizing the set of equations (1) for the perturbations $\delta\varphi = \phi_l(r, t)e^{il\theta}$, $\delta n = n_l(r, t)e^{il\theta}$ with a given azimuthal number l yields the following second-order differential equation for the potential amplitude ϕ_l (see, e.g., [8]):

$$\left[\frac{\partial}{\partial t} + il\omega_E(r)\right]\left[\frac{1}{r}\frac{\partial}{\partial r}r\frac{\partial}{\partial r} - \frac{l^2}{r^2}\right]\phi_l - \frac{il}{r}n_0'(r)\phi_l = 0, \tag{4}$$

where the prime stands for the derivative over r.

Equation (4) should be supplemented with the boundary conditions $\phi_l = 0$ at $r = a$ and $r = R$ (though $R = 1$ in dimensionless units, we will maintain an explicit notation for R).

In the following, we restrict our analysis to the case $l = 1$. A neutrally stable linear $l = 1$ mode is known to survive for an arbitrary density profile $n_0(r)$ of a single-

bounded plasma column [13, 17]. In addition, for a step density profile, the $l = 1$ mode can become exponentially unstable in the presence of an inner conductor [17]. These results will be generalized in a few respects. At the end, we will be able to track the transitions between neutrally stable, algebraically unstable, and exponentially unstable regimes for a general plasma density profile, with or without a central conductor.

Applying the Laplace transformation to Eq. (4), we obtain an ordinary differential equation:

$$[p + i\omega_E(r)]\left[\frac{1}{r}\frac{\partial}{\partial r}r\frac{\partial}{\partial r} - \frac{1}{r^2}\right]\phi_p - i\frac{1}{r}n_0'(r)\phi_p = -n_1(r, 0). \quad (5)$$

As was noted in [22], the left-hand side of Eq. (5) can be written in the form

$$\frac{1}{r^2}\frac{\partial}{\partial r}r^3[p + i\omega_E(r)]^2\frac{\partial}{\partial r}\frac{\phi_p}{r[p + i\omega_E(r)]}. \quad (6)$$

It is possible to integrate Eq. (5) for an arbitrary density profile. Introducing the dimensionless functions

$$h(r) = \int_a^r x^2 n_1(x, 0)dx, \quad (6a)$$

$$\bar{h}(p) = \int_a^R \frac{h(x)dx}{x^3[p + i\omega_E(x)]^2}\Bigg/\int_a^R \frac{dx}{x^3[p + i\omega_E(x)]^2}, \quad (6b)$$

which depend on the initial perturbed plasma density $n_1(r, 0)$, we obtain the Laplace transforms for the perturbed potential and density,

$$\phi_p(r) = r[p + i\omega_E(r)]\int_r^R \frac{h(x) - \bar{h}(p)}{x^3[p + i\omega_E(x)]^2}dx, \quad (7a)$$

$$n_p(r) = \frac{n_1(r, 0)}{p + i\omega_E(r)} - in_0'(r)\int_r^R \frac{h(x) - \bar{h}(p)}{x^3[p + i\omega_E(x)]^2}dx. \quad (7b)$$

Note that the solution for the $l = -1$ mode can be obtained from Eq. (7) by reversing the sign of the drift frequency, $\omega_E \longrightarrow -\omega_E$. The inversion of the Laplace transform,

$$\phi_1(r, t) = \int_{Br}\frac{dp}{2\pi i}\phi_p(r)e^{pt}, \quad (8a)$$

$$n_1(r, t) = \int_{Br}\frac{dp}{2\pi i}n_p(r)e^{pt}, \quad (8b)$$

involves an integration in the complex plane along a Bromwich contour *Br*, which lies to the right of all the transform's singular points and branch cuts.

3. STABILITY IN THE CASE WITHOUT A CENTRAL CONDUCTOR

The inverse Laplace transformation (8) can be performed in a closed form if $a = 0$ and $Q = 0$. Taking into account that $\bar{h}(p) = 0$ in this case, it is possible to recover the result of [22] (corrected from missprints):

$$\phi_1(r, t) = r\int_r^R [h(x)/x^3][1 + i\omega_E(r)t - i\omega_E(x)t]e^{-i\omega_E(x)t}dx, \quad (9a)$$

$$n_1(r, t) = n_1(r, 0)e^{-i\omega_E(r)t} - itn_0'(r)\int_r^R [h(x)/x^3]e^{-i\omega_E(x)t}dx. \quad (9b)$$

The first term on the right-hand side of Eq. (9b) describes the unperturbed azimuthal rotation of the initial perturbation. The differential rotation produces a phase mixing (similar to the case of Landau damping), which transforms the first term to a fast oscillating function of r as $t \longrightarrow \infty$. Growing disturbances are latent in the second term only, which contains the explicit factor t. It is readily seen that an unstable perturbation cannot grow faster than the first power of t, because the integrals in Eq. (9) are decreasing functions of time. Similar terms appear in Eq. (9a). An asymptotically nondecaying solution can originate from the two ends of the integration interval in Eq. (9) or from stationary points inside the same interval.

3.1. End Points

As long as $\omega_E(r)$ is a monotonically decreasing function of r, the main contribution to Eq. (9) comes from the upper limit of integration, $r = R$. This yields an oscillatory solution with the frequency $\omega = \omega_E(R)$:[2]

$$\phi_1 \approx -\frac{rh(R)}{\omega_E'(R)R^3}[\omega_E(r) - \omega_E(R)]e^{-i\omega_E(R)t} + \mathbb{O}\left(\frac{1}{t}\right). \quad (10)$$

This is the neutrally stable Levy's mode for $l = 1$, which is found in [17].

3.2. Contribution of Nondegenerate Stationary Points

If the plasma density is a nonmonotonic function of r, then the electric drift frequency $\omega_E(r)$ can also be nonmonotonic with the extremum points of the function $\omega_E(r)$ being the points of the stationary phase for the integrand functions in Eqs. (9). Suppose that $r = r_0$ is a nondegenerate stationary point for ω_E, i.e.,

[2] In the corresponding Eq. (5) in [22], a factor $-\omega_E'(R)$ is missing in the denominator of the right-hand side.

$\omega_E'(r_0) = 0$, while $\omega_E''(r_0) \neq 0$. Then, the main contribution to the asymptotic behavior of the integral in Eq. (9a) comes from the neighborhood of the point r_0,

$$\phi_1 \approx \frac{i\sqrt{2\pi} r h(r_0)}{\sqrt{|\omega_E''(r_0)|}\, r_0^3} [\omega_E(r) - \omega_E(r_0)] H(r_0 - r) \sqrt{t} \times \exp\left[- i\omega_E(r_0) t - \frac{i\pi}{4} \mathrm{sgn}(\omega_E'') \right], \quad (11)$$

where $H(x)$ is the Heaviside step function. The perturbation grows in this case proportionally to $\sqrt{t}$ [22]. In particular, if $r_0 = R$, then an additional factor 1/2 appears in Eq. (11), which was not taken into account in [22]. To distinguish this kind of instability from other cases where the perturbation always grows algebraically but with a different power of t, we refer to Eq. (11) as the SR instability. An example of the density profile that gives rise to the SR instability and the corresponding time behavior of the complex amplitude of the potential perturbation are shown in Figs. 3 and 4, respectively.

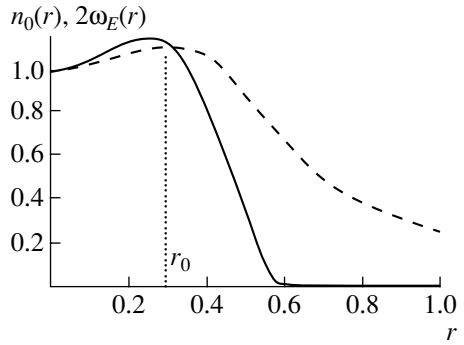

Fig. 3. Example of the density (solid line) and corresponding electric drift frequency $\omega_E(r)$ (dashed line) profiles, which determine an SR algebraic instability as is shown in Fig. 4. The density profile is borrowed from [22] and is given by $n_0 = [1 + (r/r_p)^2/\Delta][1 - (r/r_p)^2]^2$ for $r < r_p$ and $n_0 = 0$ for $r > r_p$ with $\Delta = 0.25$ and $r_p = 0.6$.

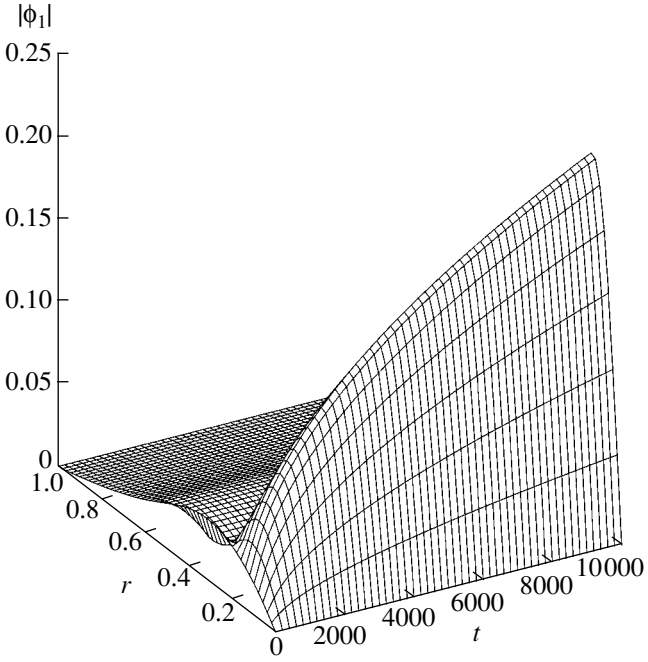

Fig. 4. Amplitude of the perturbed potential $|\phi_1|$ vs. r and t for the density profile shown in Fig. 3. Here, and in subsequent figures, the initial density perturbation is assumed to be given by $\delta n(r, \theta, t = 0) = \epsilon n_0(r) \cos\theta$. Since ϵ can be included in the normalization factors of the perturbed quantities, we set $\epsilon = 1$.

3.3. Density Jumps

Suppose that a density jump occurs at $r = r_s$. This gives rise to a jump in the derivative of the electric drift frequency $\omega_E'(r)$ at the same radius. If the density jump carries a surface charge σ as well, then the function $h(r)$ is also discontinuous at $r = r_s$, with the jump given by $h(r_s + 0) - h(r_s - 0) = \sigma/r_s$. The asymptotic contribution of the density jump to ϕ_1,

$$\phi_1 \approx r[\omega_E(r) - \omega_E(r_s)] H(r_s - r) \times e^{-i\omega_E(r_s)t} \left\{ \frac{h/r^3}{\omega_E'} \right\}_{r_s - 0}^{r_s + 0}, \quad (12)$$

describes a neutrally stable eigenmode with the eigenfrequency equal to $\omega_E(r_s)$. This eigenmode was first discussed by Levy [10]. Note in particular that the perturbation fades outside the density jump; i.e., $\phi_1 \equiv 0$ for $r > r_s$.

3.4. Fast Algebraic Instability

A charged plasma column with a multistep density profile, where layers of constant density are alternated with empty gaps, is known to have eigenmodes for an arbitrary azimuthal number l, with eigenfrequencies being either real or complex conjugated by pairs [13]. In the former case, the modes are neutrally stable; in the latter case, one of the two conjugated modes is exponentially damping, while the other is exponentially growing. The exact solution described by Eq. (9) reveals that an $l = 1$ exponentially growing mode cannot exist,[3] since in this case, the perturbation cannot grow faster than the first power of t.

A linear growth of the amplitude of an initial perturbation is found if there is some interval where $\omega_E(r)$ is constant and if this interval does not comprise the

[3] To avoid possible misunderstandings, recall that both the present and previous statements are valid in the framework of the 2D electron magnetohydrodynamics [see Eqs. (1)] and for a single-bounded plasma only.

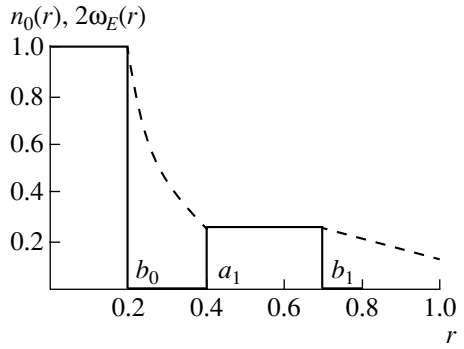

Fig. 5. Density (solid line) and electric drift frequency $\omega_E(r)$ (dashed line) profiles that give rise to a linear growth of initial perturbations, as is shown in Fig. 6. The densities of the internal ($r < b_0$) and external ($a_1 < r < b_1$) columns are related by $n_0(b_0)b_0^2 = n_0(a_1)a_1^2$.

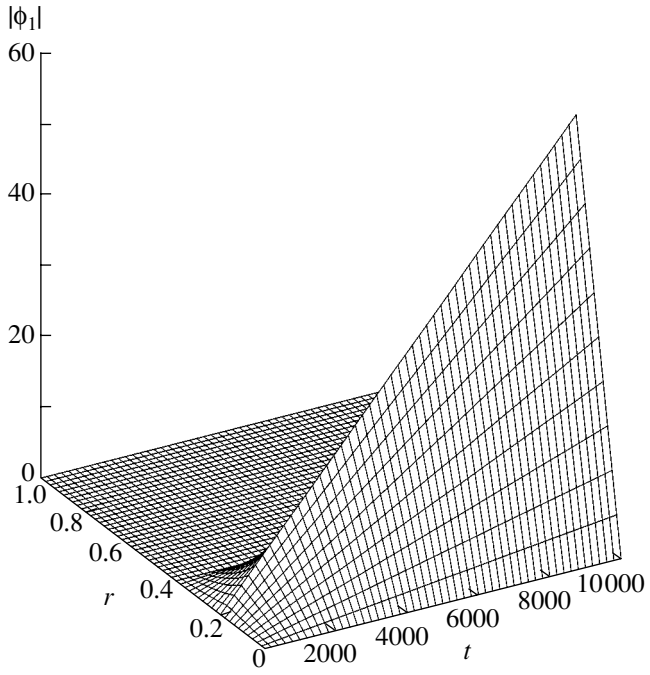

Fig. 6. Amplitude of the perturbed potential $|\phi_1|$ vs. r and t for the density profile shown in Fig. 5.

whole plasma column. In Fig. 5, this is the interval between a_1 and b_1. The frequency ω_E is constant inside that interval, if the plasma density is also constant and equal to the average density inside the inner boundary of the same interval. The perturbed potential ϕ_1 turns out to be nonzero only within the inner boundary ($r < a_1$) as $t \longrightarrow \infty$,

$$\phi_1(r) \approx itr[\omega_E(r) - \omega_E(a_1)]H(a_1 - r) \times e^{-i\omega_E(a_1)t}\int_{a_1}^{b_1}[h(x)/x^3]dx. \quad (13)$$

This behavior is confirmed by the numerical evaluation of Eq. (4), as is shown in Fig. 6.

The oscillations that grow algebraically in time are not eigenmodes. We will show in the next section that smoothing the density jumps leads to an exponential decay of these oscillations at late times. Note also that the instability of a plasma with a radial density profile similar to that shown in Fig. 5 is not in contradiction with the stability in a state of global thermodynamic equilibrium [7]. Namely, although each of the two coaxial columns in Fig. 5 fits an equilibrium profile (in the limit $\lambda_D \longrightarrow 0$), they do not form together a thermodynamic equilibrium, because they have different azimuthal drift frequencies.

3.5. Merging Extremum Points

A real density profile can only be very roughly approximated with a set of steps that have sharp edges. It is useful to track how the asymptotic behavior of ϕ_1 changes as the idealized multistep density profile shown in Fig. 2a is transformed into the smoother profile shown in Fig. 2b. The density profile in Fig. 2a has two neutrally stable eigenmodes. The first mode, described by Eq. (10), has the eigenfrequency $\omega_E(R)$. This is independent of the length over which the density decays to zero. The second mode, described by Eq. (12), has the frequency $\omega_E(b_1)$. As the sharp edge at $r = b_1$ becomes smoother, the extremum point $r = r_0$ appears near the endpoint $r = b_1$, and this mode is transformed into an algebraically unstable mode that grows as $\sqrt{t}$. The amplitude of the unstable mode is roughly proportional to the decay length of the density, because the right-hand side of Eq. (11) contains the factor $|\omega_E''|^{-\frac{1}{2}}$.

Smoothing the density profile further, it is possible to produce algebraic instabilities that grow faster than $\sqrt{t}$, as one can deduce from the example of Section 3.4. This increase of the instability occurs through a merging of the extremum points considered in Section 3.2. Let us consider the two close extremum points r_+ and r_- shown in Fig. 7a. Turning to a progressively smoothing density profile, the extremum points merge at the inflection point r_*, where the equality $\omega_E'' = 0$ holds (Fig. 7b). As smoothing progresses, the extremum points r_+ and r_- disappear, while the inflection point $r = r_*$ exists both before and after merging. The neighborhood of the point r_* overwhelmingly contributes to the integral on the right-hand side of Eq. (9a), thus determining the asymptotic behavior of the initial perturbation. Inside this neighborhood, we can expand the electric drift frequency as

$$\omega_E(r) \approx \omega_E(r_*) + \omega_E'(r_*)x + \omega_E'''(r_*)x^3/6, \quad (14)$$

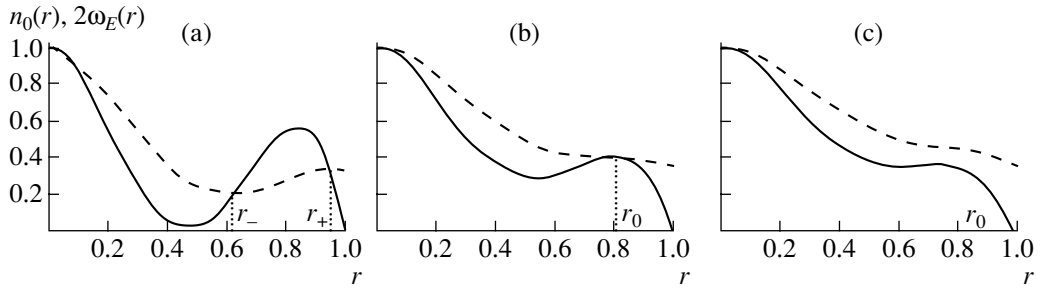

Fig. 7. Density profiles (solid lines) and corresponding electric drift frequency profiles (dashed lines) for different evolution scenarios of initial linear perturbations: (a) growth proportional to $\sqrt{t}$ (see Fig. 8), (b) growth proportional to $t^{2/3}$ (see Fig. 10), and (c) exponential damping (see Fig. 11). In all cases, the density profiles are described by the fourth-order polynomial $n_0(r) = (1 - r)(1 + r + ar^2 + br^3)$, where $a = [36\alpha + 3(3 - 20\alpha)r_* - 20r_*^2]/[r_*(9 - 20r_* + 12r_*^2)]$ and $b = [3(12\alpha r_* - 5\alpha + 3r_*^2)]/[r_*^2(9 - 20r_* + 12r_*^2)]$ are expressed through the coordinate r_* of the inflection point, $\omega_E''(r_*) = 0$, and the corresponding value of ω_E' ($\alpha = \omega_E'(r_*)$). The parameter $r_* = 0.8$ is the same for all cases, while α = (a) 0.3, (b) 0, and (c) –0.1. In case (a), two extrema are located at $r_- = 0.626539$ and $r_+ = 0.942552$ and the corresponding values of ω_E are 0.108805 and 0.171385, respectively. In case (b), the two extrema coalesce in the inflection point at $r_* = 0.8$ ($\omega_E(r_*) = 0.198824$). The parameter Γ, which characterizes the separation of the two extrema, is equal to (a) $i0.0308593$, (b) 0, and (c) 0.00923489, respectively.

where $x = r - r_*$ and $\omega_E''(r_*)$ plays the role of a smallness parameter.

If $\omega_E'(r_*)/\omega_E'''(r_*) < 0$, the function $\omega_E(r)$ has two extrema at $r_\pm = r_* \pm \sqrt{-2\omega_E'/\omega_E'''}$ (see Fig. 7a). At large times, $t \gg |\Gamma|^{-1}$, with $\Gamma = \sqrt{8\omega_E'^3/9\omega_E'''}$, these extrema contribute separately. Therefore, the perturbed potential is the sum of two asymptotic contributions [see Eq. (11)] coming from r_+ and r_-, so that the initial perturbation grows as $\sqrt{t}$. Figure 8 clearly exhibits two modes localized in the regions $r < r_+ \approx 0.94$ and $r < r_- \approx 0.59$. A spectral analysis supports the prediction of the analytic theory, which gives the following values for the mode frequencies: $\omega_E(r_-) = 0.0500865$ and $\omega_E(r_+) = 0.120887$. These modes produce a beating effect in the inner radial region, $r < r_-$, with the period $T = 2\pi/|\omega_E(r_+) - \omega_E(r_+)| \approx 88.74$. However, this period is too short to be resolved on the time scale of Fig. 8. The actual wave beating is evidenced in Fig. 9. Note in particular that the beating period increases as $\omega_E(r_*)$ becomes smaller and the extremum points $r_\pm$ become closer to each other.

At smaller times, $t \ll |\Gamma|^{-1}$, we can set $\omega_E'(r_*) = 0$.

If $\omega_E'(r_*) = 0$ and the stationary points merge at $r = r_*$, which, in this particular case, appears to be the extremum of the density profile $n_0(r)$, then the perturbation grows proportionally to $t^{2/3}$ (see Figs. 7b, 10):

$$\phi_1 \approx \frac{i2^{1/3}\Gamma(1/3)rh(r_*)}{3^{1/6}|\omega_E'''|^{1/3}r_*^3}[\omega_E(r) - \omega_E(r_*)] \times H(r_* - r)t^{2/3}e^{-i\omega_E t}. \quad (15)$$

Finally, if $\omega_E'(r_*)/\omega_E'''(r_*) > 0$ (see Fig. 7c), the extremum points move into the complex plane x, while ϕ_1 grows algebraically according to Eq. (15) in the initial time evolution, $t \ll |\Gamma|^{-1}$ (see Fig. 11) and then decays exponentially at late times,

$$\phi_1 \approx \frac{i\sqrt{2\pi}rh(r_*)}{(2\omega_E'\omega_E''')^{1/4}r_*^3}[\omega_E(r) - \omega_E(r_*)] \times H(r_* - r)\sqrt{t}\exp[-i\omega_E t - \Gamma t]. \quad (16)$$

Figure 11 shows a sort of saturation. A spectral analysis shows that the "saturated" mode has the frequency $\omega_E(R)$ and, hence, is nothing but the neutrally stable Levy's mode [see Eq. (10)].

Using Eq. (14), it is possible to derive a more general formula which combines all the cases discussed above:

$$\phi_1 \approx \frac{i\sqrt{3}rh(r_*)}{r_*^3\omega_E'(r_*)}[\omega_E(r) - \omega_E(r_*)] \times H(r_* - r)e^{-i\omega_E(r_*)t}\tau K_{1/3}(\tau). \quad (17)$$

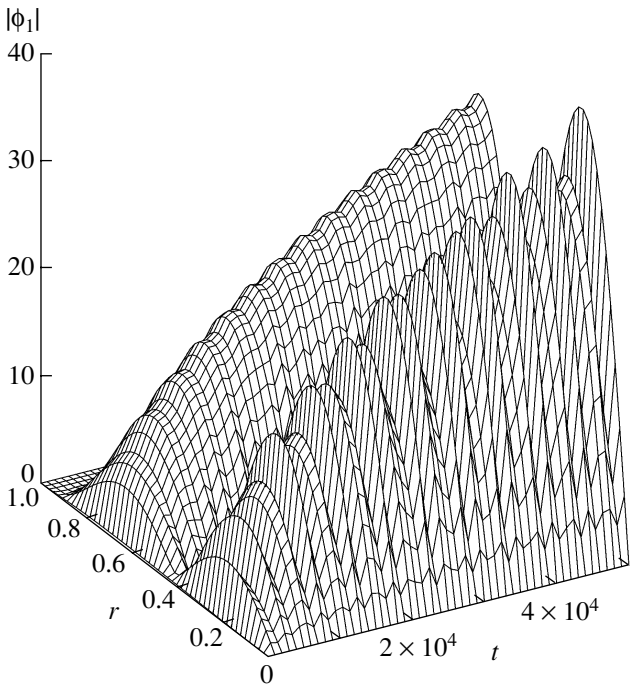

Fig. 8. Amplitude of the perturbed potential $|\phi_1|$ vs. r and t for the density profile shown in Fig. 7a.

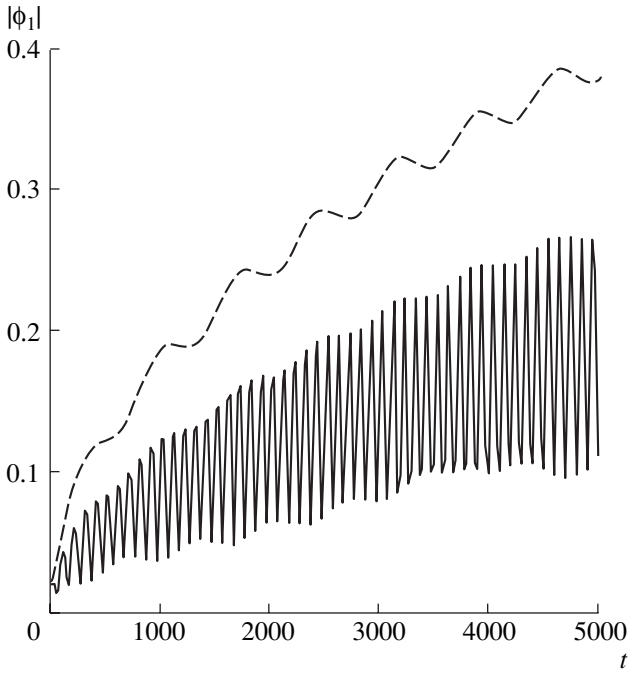

Fig. 9. Time evolution of the amplitude of the perturbed potential $|\phi_1|$ for $r = 0.4$ (solid line, the beating effect is evident) and $r = 0.7$ (dashed line, oscillations without beating) for the density profile shown in Fig. 7a.

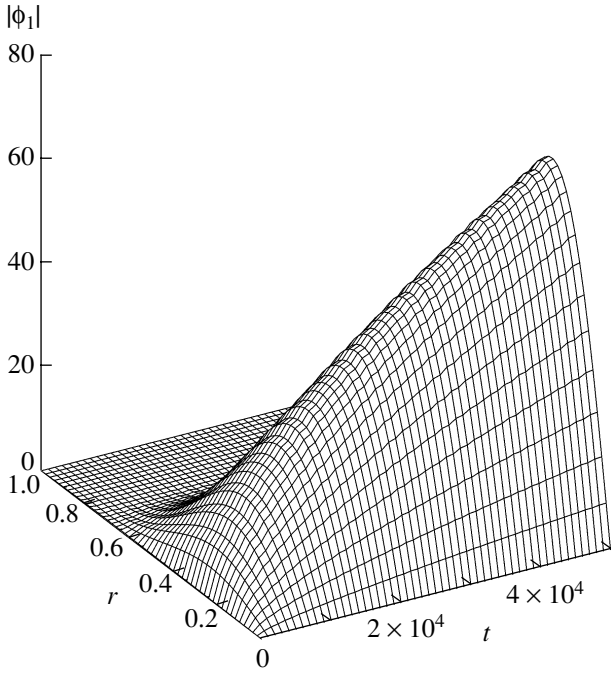

Fig. 10. Amplitude of the perturbed potential $|\phi_1|$ vs. r and t for the density profile shown in Fig. 7b.

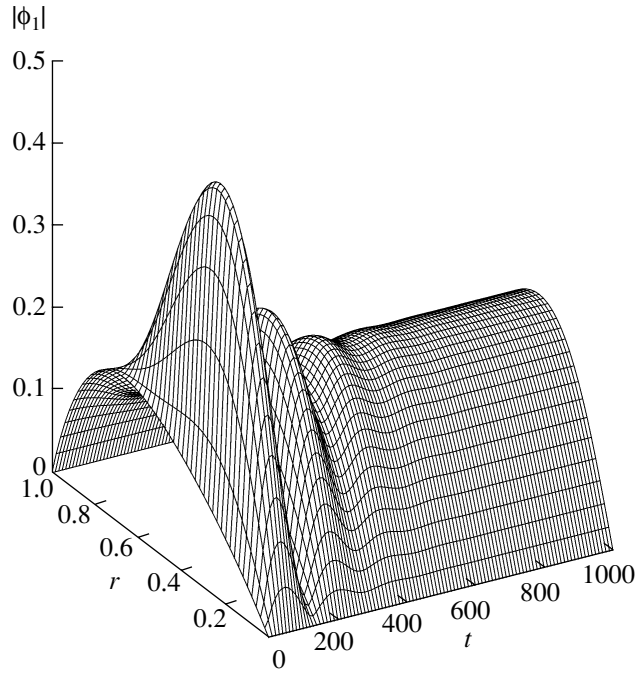

Fig. 11. Amplitude of the perturbed potential $|\phi_1|$ vs. r and t for the density profile shown in Fig. 7c. The initial stage exhibits a growth proportional to $\sqrt{t}$. A sort of "saturation" is reached in a relatively short time, which is nothing but the Levy's mode.

Here, $\tau = \Gamma t$, and $K_{1/3}(\tau)$ is the McDonald's function of order 1/3.

3.6. Higher Order Stationary Points

If the ω_E profile has, for the sake of simplicity, only one stationary point r_* of order m (i.e., $\omega_E^{(j)}(r_*) = 0$ for all derivatives with $j < m$ and $\omega_E^{(m)}(r_*) \neq 0$), then we can repeat the computation of the asymptotic behavior of the perturbed potential to obtain

$$\phi_1 \approx it^{1-1/m} r[\omega_E(r) - \omega_E(r_*)]H(r_* - r)$$
$$\times e^{-i\omega_E(r_*)t} \frac{h(r_*)}{r_*^3} \frac{2}{m} \left| \frac{m!}{\omega_E^{(m)}(r_*)} \right|^{1/m} \Gamma\left(\frac{1}{m}\right) \tag{18}$$
$$\times \left\{ \cos\left(\frac{\pi}{2m}\right) + i\left[\frac{(-1)^{m-1} - 1}{2}\right] \mathrm{sgn}(\omega_E^{(m)}(r_*)) \sin\left(\frac{\pi}{2m}\right) \right\},$$

which is valid for all integers $m > 1$. For $m = 2$, this formula gives Eq. (11), and, for $m = 3$, it gives Eq. (15).

4. TRAP WITH A CENTRAL CONDUCTOR

We now turn to the analysis of the stability of $l = 1$ diocotron perturbations in a cylindrical Penning trap with a coaxial inner conductor. It is shown how the presence of the central conductor transforms the algebraic SR instability into a weakly exponential one at longer times, while the algebraic growth survives in the initial stage of the evolution.

Contrary to the previous case with no central conductor, the inversion of the Laplace transform [see Eq. (8)] cannot be performed in a closed form. In any case, an asymptotic analysis is still possible. To this aim, Appendix A contains an alternative derivation of Eq. (11) by an explicit contour integration in the complex plane of Eq. (8a). This derivation is extended here and in Appendix B to the case where an additional inner conductor is present in the trap configuration. In this section, we present the results obtained by the method described in Appendix B.

As was shown in Section 3.2, the SR instability comes from the neighborhood of a nondegenerate stationary point r_0 where $\omega_E' = 0$. Appendix A interprets this instability as the contribution of the branching point $p = -i\omega_E(r_0)$ in the complex p-plane. The major difference from the case considered in Appendix A is of course the presence of a nonzero function $\bar{h}(p)$.

Near the branching point $p = -i\omega_E(r_0)$, the integrals over r that enter the definition of $\bar{h}(p)$ [see Eq. (6b)] are mainly determined by the neighborhoods of the points $r = r_0$ and $r = a$. Near the central conductor, $r \longrightarrow a$, the frequency ω_E can be expanded as $\omega_E(r) \approx \omega_E(a) + \Delta\omega_E[1 - a^2/r^2]$, where $\Delta\omega_E = n_0(a)/2$ and $\omega_E(a) = Q/2a^2$. Near the stationary point, $r \longrightarrow r_0$, we can write $\omega_E(r) \approx \omega_E(r_0) + \omega_E''(r - r_0)^2/2$, where ω_E'' stands for $\omega_E''(r_0)$. Using these expansions, we obtain

$$\bar{h}(p) = \frac{\mathcal{J}(p + i\omega_E(r_0))/r_0^3}{\mathcal{J}(p + i\omega_E(r_0))/r_0^3 + \beta(p)} h(r_0), \tag{19}$$

where

$$\mathcal{J}(\sigma) = \frac{\pi e^{-i\pi \mathrm{sgn}[\omega_E'']/4}}{\sqrt{|2\omega_E''|}\sigma^{3/2}},$$

$$\beta(p) = \frac{1}{2a^2[p + i\Delta\omega_E][p + i\omega_E(a)]}$$

come from points r_0 and a, respectively. The function $\mathcal{J}(\sigma)$ is two-valued, because it contains the rational power 3/2 of $\sigma = p + i\omega_E(r_0)$. As is explained in Appendix A, one should choose the "physical" sheet ($\arg\sigma \in (-\pi, \pi)$) of the Riemann surface, which corresponds to the complex σ-plane with the branch cut $\sigma \in (-\infty, 0)$ along the negative part of the $\mathrm{Re}\,\sigma$ axis.

For a rough estimate of the integral in Eq. (8a), we can evaluate σ as t^{-1}. This shows that the effect of the central conductor is negligible ($\bar{h} \ll h(r_0)$) at small times, $t \ll T \approx |\omega_E''|^{1/3} \omega_E^{-4/3} r_0^2 a^{-4/3}$. At larger times, $t \gg T$, the value of $\bar{h}(p)$ tends to $h(r_0)$ at the branching point $p = -i\omega_E(r_0)$, so that two terms, $h(x)$ and $\bar{h}(p)$, in the integrand of expressions (7) cancel each other and the algebraic SR instability disappears. This conclusion might seem to be a paradox. If the inner conductor is very thin and is not charged, the spatial structure of the perturbed potential is changed only in the small vicinity of the central conductor itself. It is therefore puzzling how such a small modification is able to change the time evolution of the perturbation so strongly. Note, however, that the thinner the internal conductor, the longer is the initial stage $t < T$ of the algebraic growth.

A careful analysis reveals that $\bar{h}(p)$ has poles close to the branching point. They can be found from the equation

$$\mathcal{J}(p + i\omega_E(r_0))/r_0^3 = -\beta, \tag{20}$$

where $\beta \approx \beta(-i\omega_E(r_0))$ is real,

$$\beta(p) \approx \frac{1}{2a^2[\Delta\omega_E - \omega_E(r_0)][\omega_E(a) - \omega_E(r_0)]}.$$

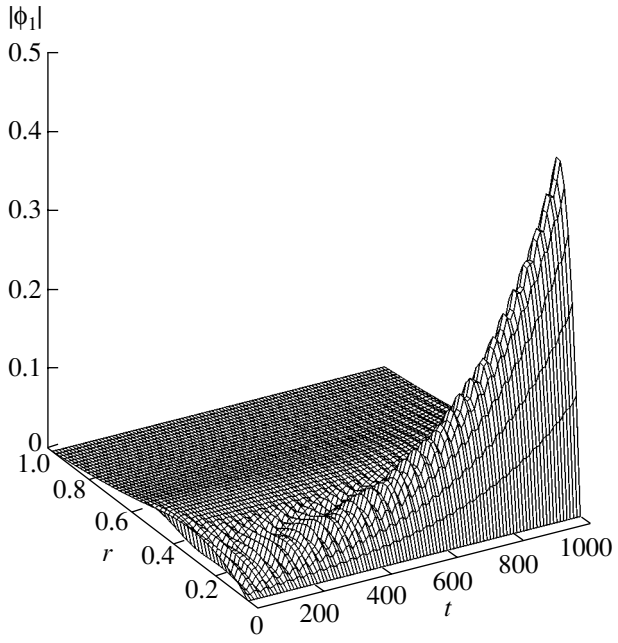

Fig. 12. Amplitude of the perturbed potential $|\phi_1|$ vs. r and t for the density profile shown in Fig. 3, truncated at the radius $a = 0.05$ of the central conductor. The value of Q on the central conductor corresponds to the total charge of the particles within $r = 0.05$ in the case of Fig. 3.

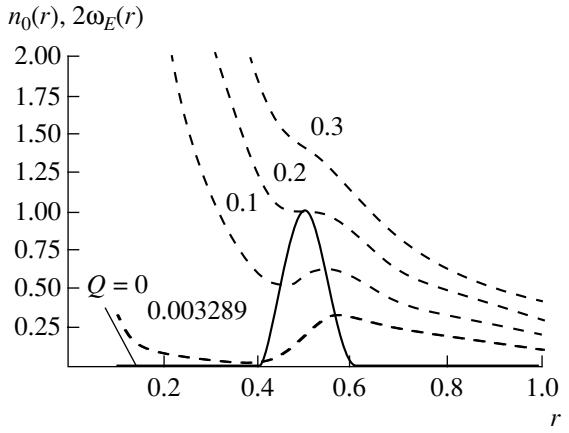

Fig. 13. Generalized parabolic density profile (solid line) and electric drift frequency (dotted lines). The density profile is given by $n_e = [1 - (r - r_c)^2/r_p^2]^2$ for $|r - r_c| < r_p$ and $n_e = 0$, otherwise, with the parameters $r_c = 0.5$ and $r_p = 0.1$. Frequency profiles are calculated for $a = 0.1$ and different values of Q, indicated directly on the plot.

Squaring both sides of Eq. (20), we obtain three different roots,

$$p_n = -i\omega_E(r_0) + i\sqrt[3]{\frac{\pi^2}{2\omega_E'' r_0^6 \beta^2}}\, e^{-2\pi i n/3}, \qquad (21)$$

where n is an integer. However, it is worth emphasizing that not all of them belong to the physical sheet. Depending on the sign of β, only one or two of the roots satisfy the condition $\arg[p_n + i\omega_E(r_0)] \in (-\pi, \pi)$. The other roots belong to adjacent sheets.

The inverse Laplace transform can be performed, at least asymptotically for $t \longrightarrow \infty$, by means of a suitable deformation of the inversion (Bromwich) contour inside the physical sheet. The deformed contour wraps around the poles of the Laplace transform (7) and its branch cuts. The contribution of the poles can be computed with the theory of residues. Poles on adjacent sheets are not wrapped around and, hence, do not contribute to the asymptotic behavior of the perturbed quantities. Such poles are sometimes associated with the so called quasi-modes [15, 16, 33], but the fact that they do not contribute to the asymptotic behavior of the perturbation is not well elucidated in the existing literature. Appendix B provides more details about this issue.

For the sake of clarity, we assume that the cubic root in Eq. (21) has a real positive value if $\omega_E'' > 0$ and a real negative value if $\omega_E'' < 0$. The condition $\arg[p + i\omega_E(r_0)] \in (-\pi, \pi)$ then selects $n = 0, +1, +2$ for $\omega_E'' > 0$ and $n = 0, -1, -2$ for $\omega_E'' < 0$.

The first root, p_0, is purely real. The second root, $p_{\pm 1}$ (i.e., p_{+1} for $\omega_E'' > 0$ and p_{-1} for $\omega_E'' < 0$), has a positive real part, $\mathrm{Re}\, p_{\pm 1} > 0$. The third root has a negative real part, $\mathrm{Re}\, p_{\pm 2}\, 1 < 0$. In terms of the frequency $\omega = ip$, the second and third roots form a complex conjugate pair of eigenfrequencies.

The function $\mathcal{J}(p + i\omega_E(r_0))$ has a real negative value at $p = p_0$ and $p = p_{\pm 2}$, while it is positive at $p = p_{\pm 1}$. This simply means that the number of roots on the "physical" sheet depends on the sign of β. If $\beta > 0$, Eq. (20) has two roots: p_0 and $p_{\pm 2}$. If $\beta < 0$, only the roots $p_{\pm 1}$ belong to the "physical" sheet. Observing that only $p_{\pm 1}$ has a positive imaginary part, we conclude that an exponential instability exists if $\beta < 0$, or

$$[\omega_E(r_0) - \Delta\omega_E][\omega_E(r_0) - \omega_E(a)] > 0. \qquad (22)$$

The growth rate is given by

$$\gamma = \frac{3^{1/2}\pi^{2/3} a^{4/3}}{2^{2/3} r_0^2 \left|\omega_E''\right|^{1/3}} [\omega_E(r_0) - \omega_E(a)]^{2/3} \times [\omega_E(r_0) - \Delta\omega_E]^{2/3}. \qquad (23)$$

If inequality (22) breaks, the algebraic SR instability saturates at $t > T$.

The destabilizing effect of the central conductor is confirmed by the simulations relevant to the density profile shown in Fig. 3. If the central conductor is

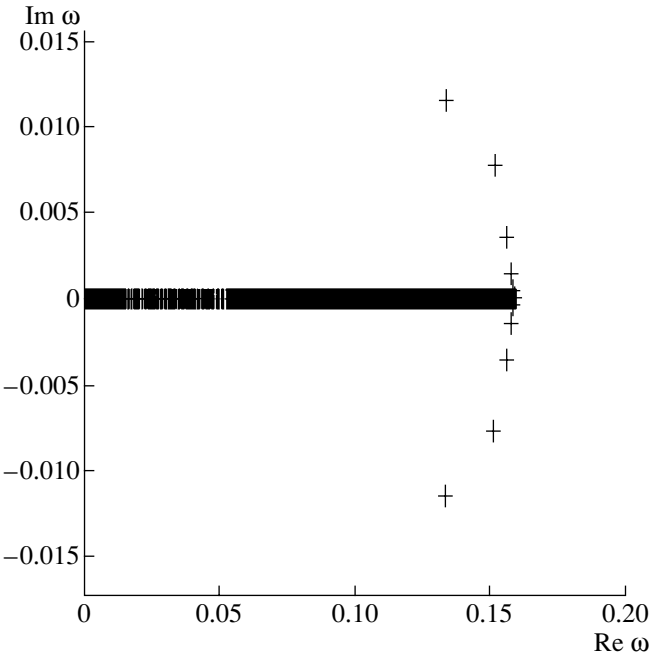

Fig. 14. Frequency spectrum for the density profile shown in Fig. 13, $Q = 0$, and different values of a: 0.2, 0.1, 0.05, 0.025, and 0.001 (the closest to the $\mathrm{Re}\,\omega$ axis). The solutions are indicated by dots. The continuum spectrum lies on the $\mathrm{Re}\,\omega$ axis from 0 to $\omega_E(r_0)$. For a given a, there are two complex conjugate discrete frequencies. As $a \longrightarrow 0$, they converge to $\omega_E(r_0)$ at the upper end of the continuum spectrum. Stable solutions ($\mathrm{Im}\,\omega < 0$) do not belong to the "physical" sheet of the Riemann surface.

absent, this case exhibits an algebraic SR instability, as is shown in Fig. 4. We have repeated the simulation for the same density profile with an inner conductor of radius $a = 0.05$ and electric charge per unit length $Q = 2\int_0^a n_0(x)xdx$, which exactly compensates the charge of the removed particles, so that the radial profile of ω_E is not changed outside the inner conductor. Figure 12 clearly shows that the perturbed potential evolves in a qualitatively different fashion than that in Fig. 4.

For a further comparison, we have used the generalized parabolic profile shown in Fig. 13. This profile provides a more realistic approximation of the experimental conditions, because the plasma density vanishes close to the central conductor. The growth rates were estimated numerically by solving the eigenvalue equation by the finite difference method. The agreement between the theoretical and numerical γ values is typically within 10% for sufficiently low values of the inner conductor radius ($a \le 0.05$) and a spatial grid of 800 points in the interval $r \in [a, R]$. The agreement improves by increasing the number of grid points.

The frequency spectrum computed numerically is drawn in Fig. 14 for a set of a values. The number of solutions with $\mathrm{Im}\,\omega = 0$ increases with the number of radial grid points, indicating that these solutions correspond to the continuous spectrum. The range of $\mathrm{Re}\,\omega$ corresponds (as it must for the case $l = 1$) to the interval of values of $\omega_E(r)$.

These results, in particular the existence of an unstable solution, are also confirmed by the numerical solution of the linearized drift Poisson system. In the numerical code, $\omega_E(r)$ and $n_0'(r)$ are assigned as inputs. The solution is then found on a grid that is radially uniform between a and R. At every time step, the radial Helmholtz equation for the $l = 1$ harmonic of the perturbed potential is solved with the boundary conditions $\phi_1 = 0$ for $r = a$ and $r = R$.

The eigenfunction relevant to the unstable mode for the $l = 1$ perturbation of the density profile shown in Fig. 13 is plotted in Fig. 15. Note in particular that this extends over the whole interval $r \in [a, R]$. On the contrary, neutrally stable eigenmodes (which exist, e.g., in the case of a multistep density profile treated in Section 3.3)

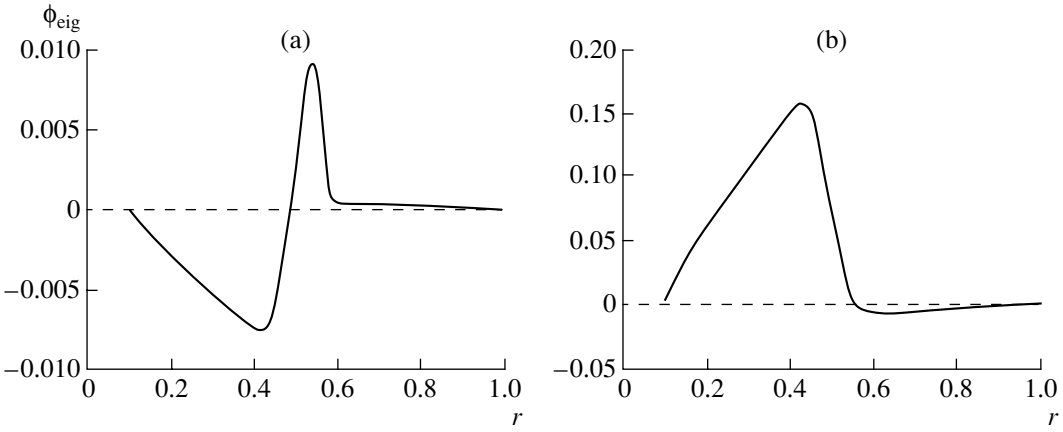

Fig. 15. Eigenfunction $\phi_{eig}(r)$ (in arbitrary units) for the discrete unstable mode for the generalized parabolic density profile shown in Fig. 13, $Q = 0$, and $a = 0.1$: (a) real part and (b) imaginary part. The stable mode with the complex conjugate eigenfrequency ω^* has the complex conjugate eigenfunction $\phi_{eig}^*(r)$. The stable mode does not belong to the physical sheet of the Riemann surface.

are localized inside the resonant radius, as is deduced from Eq. (12). An eigenfunction of the continuum spectrum is discontinuous at its resonant radius, where $\omega = \omega_E(r)$ [33]. It is interesting to compare these results with those obtained for a step density profile. In this case, we can compute the discrete spectrum analytically (see, e.g., [8–10]). In particular, for a step density profile located between $r = 0.4$ and 0.6 ($n_0 = 1$) and the inner conductor at $a = 0.1$, the discrete spectrum for $Q = 0$ has two neutrally stable modes, $\omega_1 \simeq 0.10$ and $\omega_2 \simeq 0.26$. The first exponentially unstable solution appears for $Q \simeq 0.0176$, and this becomes more and more unstable (i.e, its growth rate increases) as Q increases.

5. CONCLUSIONS

We have shown that for an infinitely long charged plasma column with radial density gaps, algebraic instabilities growing with time proportionally to $t^{1-1/m}$, $m \geq 3$ being the order of a stationary point in the rotation frequency profile, and even proportionally to t can be found. All these instabilities grow faster than what is called the SR instability, already known in the literature.

We have then observed that smoothing the density jumps in a single-bounded plasma converts algebraically growing perturbations into exponentially decaying modes at late times, and we have computed the damping rate of these modes.

We have also shown that the presence of an additional inner conductor (even very thin and uncharged) can transform the algebraic SR instability into an exponential one at late times (while the algebraic character of the instability persists in the initial time evolution). In particular, we have obtained a criterion for the exponential instability to occur and we have computed the growth rate analytically in a limiting case. These results have been confirmed by the numerical solution of the linearized drift Poisson equations (1).

Finally, we note that the analytic theory developed here successfully handles the problem of the presence of an inflection point in a stratified flow. This allowed us to trace the above-mentioned mode transformations. Explicit results related to this particular problem are very rare, if any, in the literature. Qualitative predictions of a slow instability near the inflection point can be found in the review paper by Timofeev [14]. Our results confirm the predictions of that work.

APPENDIX A

SMITH–ROSENBLUTH INSTABILITY

Here, we explicitly perform the integration in Eq. (8a) to invert the Laplace transform (7a). The result will be the same as that described by Eq. (11), derived by another method in Section 3.2. The method presented here will be used, with small amendments, in Appendix B to study the asymptotic time evolution of linear perturbations in a cylindrical Penning trap with an inner conductor. The notion of the physical sheet of the Riemann surface used in Section 4 to derive the stability criterion is also introduced here.

Our goal is to calculate integral (8a)

$$\phi_1(r, t) = \int_{-i\infty+\sigma}^{+i\infty+\sigma} \frac{dp}{2\pi i}\phi_p(r)e^{pt}, \qquad (A.1)$$

where σ is a positive real number and $\phi_p(r)$ is the usual Laplace transform defined by

$$\phi_p(r) = \int_0^\infty \phi_1(r, t)e^{-pt}dt. \qquad (A.2)$$

We will refer to the integration path in Eq. (A.1) as the Bromwich, or the inversion, contour. The solution for $\phi_p(r)$ can be obtained from Eq. (7a) with $\bar{h}(p) \equiv 0$:

$$\phi_p(r) = r[p + i\omega_E(r)]\int_r^R \frac{h(x)dx}{x^3[p + i\omega_E(x)]^2}. \qquad (A.3)$$

The integration contour in Eq. (A.3) will be referred to as the *r*-contour to distinguish it from the inversion contour in the complex *p*-plane. The initial, or undeformed, *r*-contour belongs to the Re x axis, $x \in [r, R]$ (see Fig. 16).

To be definite, we consider an $\omega_E(r)$ profile such that $\omega_E''(r)$ is negative in a stationary point r_0 where $\omega_E' = 0$. The final result will be written in a form valid for any sign of $\omega_E''(r_0)$. Reversing the sign of ω_E can be accomplished by reflecting all the figures in this appendix around the horizontal (real) axis.

The Laplace transform (A.3) is an analytic function of p in the right half of the p-plane. This statement follows from the discussion of Eq. (9) in the beginning of Section 3.2, where it is emphasized that any initial perturbation cannot grow faster than t. Namely, recall that a singularity in the p-plane in a point with $\mathrm{Re}\,p > 0$ would mean an exponential instability.

It is worth emphasizing that the Laplace transform (A.3) is a multivalued function of p. To prove this, we consider a path in the p-plane for which p passes through the imaginary axis Imp (see Fig. 17a). The dashed line in Fig. 17a denotes the branch cut, which is the projection $p(x) \equiv -i\omega_E(x)$ of the *r*-contour of integration, $x \in [r, R]$, in Eq. (A.3) onto the p-plane. The integrand function in Eq. (A.3) becomes singular as p tends to the branch cut. Consider now a path in the p-plane starting somewhere in the right half-plane. The starting point can be thought of as belonging to the inversion contour. If the path meets the branch cut, as path *1* in Fig. 17a does, the branch cut should wrap around the final point of the path in order to avoid any singularity in the integrand. Consequently, the *r*-con-

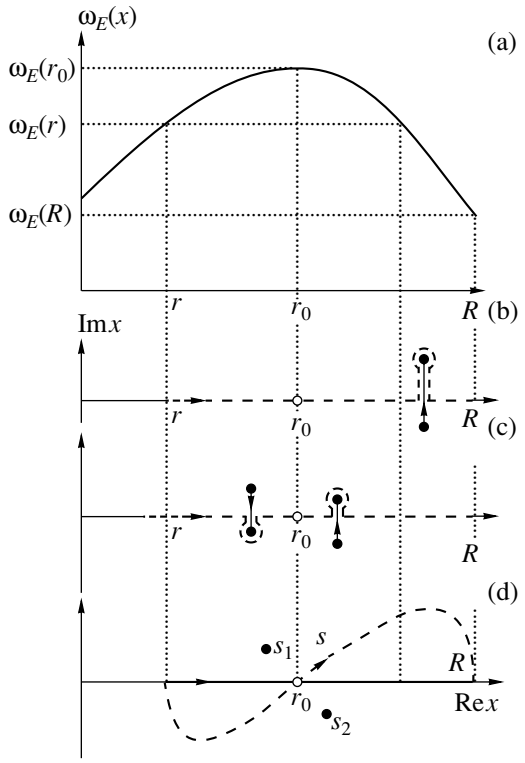

Fig. 16. A sketch of the drift frequency profile $\omega_E(x)$ with an inflection point and the r-contours of integration in the complex x-plane in Eq. (A.3). If the inflection point r_0 occurs inside the interval of integration, then $\omega_E(x)$ is a nonmonotonic function of x on the interval [plot (a)]. The original r-contour goes along the Rex axis [plots (b)–(d), dashed lines]. The contour encompasses the image x_p of the Laplace variable p defined by $p = -i\omega_E(x_p)$ as x_p approaches the r-contour [plot (b)]. Two images exist if $\omega_E(r) < \omega_E(x_p) < \omega_E(r_0)$ close to the Rex axis, because $\omega_E(x)$ assumes two times any value between $\omega_E(r)$ and $\omega_E(r_0)$ along the r-contour on the Rex axis [plot (c)]. The transformed r-contour suitable to uncover the asymptotic behavior of the inverse Laplace transform crosses the Rex axis in the inflection point r_0 at an angle of +45° in the case $\omega_E'' < 0$ [plot (d)]. Reversing the sign of the frequency, $\omega_E \longrightarrow -\omega_E$, reflects the transformed contour vertically around the Rex axis (not shown).

tour should wrap around the pole $x = x_p$ in the x-plane, where $p = -i\omega_E(x_p)$, as is shown in Fig. 16b. We denote the value assumed by the Laplace transform in the final point of the path in the left half of the p-plane as $\phi_p^{(1)}(r)$. If one arrives at the same final point, encompassing the branch cut along, e.g., path *0*, then the Laplace transform assumes a different value $\phi_p^{(0)}(r)$. The two values differ by the residue at the pole $x = x_p$; the residue is namely just integral (A3) along a small contour that detours the pole.

Moving along path *2* in the p-plane, which meets the branch cut between the points $p = -i\omega_E(r)$ and $p = -i\omega_E(r_0)$, we obtain, generally speaking, a third value $\phi_p^{(2)}(r)$, because the r-contour wraps around two projections x_p of the point p onto the complex x-plane, because $\omega_E(x)$ assumes two times any value between $\omega_E(r)$ and $\omega_E(r_0)$ along the unperturbed r-contour (see Fig. 16c).

It is readily seen that the function described by Eq. (A.3) is a multivalued function in the right half of the p-plane as well. This follows from the fact that paths *0* and *1* (or *2*) combine in a close contour any point of which can be treated as starting/final point in the above treatment. It is clear that the points $-i\omega_E(R)$, $-i\omega_E(r)$, and $-i\omega_E(r_0)$ in the complex p-plane play a special role. We will refer to them as branching points.

Any additional turn around any branching point adds one or more residue values. Hence, the branches $\bar{\phi}_1(r)$ of the Laplace transform are related to the fundamental branch $\phi_1^{(0)}(r)$ by the equation

$$\bar{\phi}_1(r) = \phi_1^{(0)}(r) + r[p + i\omega_E(r)]\sum_s n_s \operatorname{res}_{x_{p,s}}\left[\frac{h(x)}{x^3[p + i\omega_E(x)]^2}\right],$$

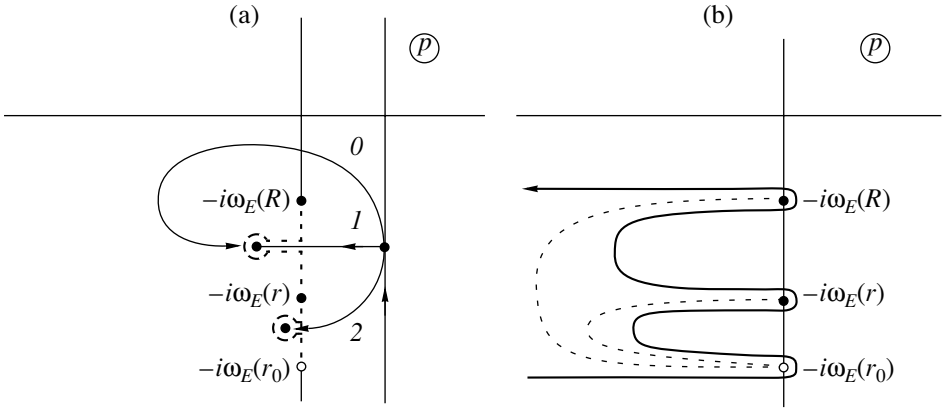

Fig. 17. Contour of integration in the complex p-plane: (a) initial contour and (b) transformed contour. The branch cut (dotted line) goes along the projection $p(x) = -i\omega_E(x)$ of the integration contour in the x-plane shown in Fig. 16.

where n_s is an integer and the summation goes over all poles. The number of branches is generally infinite. An important exception of the last statement is represented by a multistep density profile. In that case, all the residues in the above equation are equal to zero and the Laplace transform is a single-valued function of p. Note that any numerical simulations are, in fact, performed for a multistep density profile.

To proceed further, we need to fix the branch of the Laplace transform (A.3) to be substituted into the inverse Laplace transform (A.1). The desired branch is fixed by the condition that the integration contour in Eq. (A.3) goes exactly along the Rex axis for any p such that Re$p > 0$. This is in fact a general feature of the solution to an initial-value problem with the use of the Laplace transform. Indeed, the integral in Eq. (A.2) must, at least, converge, which requires the real part of p to be positive and sufficiently large. This also explains why the inversion contour must go to the right of all the integrand's singular and branch points in Eq. (A.1).

The inversion contour in the p-plane is shown in Fig. 17a as a solid line parallel to the Imp axis. Shifting it to the left as far as possible, it is a standard matter to find out the asymptotic behavior of Eq. (A.1) at $t \longrightarrow \infty$. Namely, the parts of the inversion contour that remain the farthest right yield the most significant contribution to the integral in Eq. (A.1), because the integrand function contains the factor e^{pt}. Being shifted, the inversion contour wraps around the branch cuts and, possibly, around other singularities of the Laplace transform in the left half of p-plane.

To characterize the asymptotic behavior, the branch cut should also be shifted to the left as far as possible. Shifting the branch cut requires the r-contour in the x-plane to be deformed as is shown in Fig. 16. The end points of the branch cut, $p = -i\omega_E(r)$ and $p = -i\omega_E(R)$, cannot be moved away from the Imp axis because they correspond to the actual point r and the boundary conditions imposed on the outer conducting cylinder, respectively. An additional point, $p = -i\omega_E(r_0)$, which also cannot be moved, corresponds to the stationary point r_0 in the x-plane, where $\omega_E' = 0$. Shifting the point from the Rex axis in any direction would even increase Re$p(x)$. Thus, the farthest left parts of the inversion contour in the p-plane wrap around these branch points. Other points that have to be wrapped around are the poles of the Laplace transform $\phi_p(r)$. However, as is explained above, no such poles exist to the left of the Imp axis.

In the following, we restrict ourselves to the contribution of the stationary point r_0. Expanding $\omega_E(x)$ in the denominator of Eq. (A.3) over a small distance $s = x - r_0$, we obtain from Eq. (A.1)

$$\phi_1(r, t) = r[h(r_0)/r_0^3]\int\limits_{Br}\frac{dpe^{pt}}{2\pi i}[p + i\omega_E(r)] \times \int\limits_{r-r_0}^{\infty} ds[p + i\omega_E(r_0) + i\omega_E''s^2/2]^{-2}, \tag{A.4}$$

where, again, Br denotes the inversion contour and ω_E'' stands for $\omega_E''(r_0)$. Since we are interested in the asymptotic behavior at long times (so that $|\omega_E''|(r - r_0)^2 t \gg 1$), it is possible to substitute the lower limit $r - r_0$ of the inner integral in Eq. (A.4) with $+\infty$ or $-\infty$, depending on the sign of $r - r_0$. This yields

$$\phi_1(r, t) = r[h(r_0)/r_0^3]H(r_0 - r) \times \int\limits_{Br}\frac{dp}{2\pi i}e^{pt}[p + i\omega_E(r)]\mathcal{J}(p + i\omega_E(r_0)), \tag{A.5}$$

where

$$\mathcal{J}(\sigma) = \int\limits_{-\infty}^{\infty}\frac{ds}{[\sigma + i\omega_E''s^2/2]^2}. \tag{A.6}$$

The function $\mathcal{J}(\sigma)$ has two branches corresponding to two poles $s_{1,2} = \pm\sqrt{2i\sigma/\omega_E''}$ of the integrand in Eq. (A.6) in the complex s-plane. To be definite, we assume that s_1 is *initially* placed above and s_2 below the r-contour in the x-plane (see Fig. 16). The standard theory of residues establishes that integral (A.6) is equal to the residue at s_1 with the positive sign or to the residue at s_2 with the negative sign, which, in fact, yields the same result:

$$\mathcal{J}(\sigma) = +\frac{2\pi i}{[\omega_E'']^2 s_1^3} = -\frac{2\pi i}{[\omega_E'']^2 s_2^3}. \tag{A.7}$$

The first form of the $\mathcal{J}$ corresponds to shifting the r-contour upwards. This then wraps around the s_1 pole, making a small contour that detours the pole counterclockwise. The second form corresponds to shifting the r-contour downwards; it yields a small contour that detours the s_2 pole clockwise and, hence, gives the minus sign in the second line of Eq. (A.7).

Let us imagine that σ makes one turn around the $\sigma = 0$ point in the complex σ-plane; i.e., $\arg\sigma$ increases by 2π. Then, the s_1 pole (with the small contour attached) moves to the lower half of the s-plane and takes the place of the s_2 pole, while the s_2 pole takes the place of s_1 in the upper half-plane. Note that this oper-

ation makes the detour direction opposite to the previous case: the wrapped contour now detours the upper pole clockwise and the lower pole counterclockwise. Consequently, the value of $\mathcal{J}(\sigma)$ reverses its sign. The function $\mathcal{J}(\sigma)$ is single-valued on the Riemann surface produced from two σ-planes, which are linked together in such a way that $\arg\sigma$ spans over an interval of 4π.

An alternative treatment requires a branch cut to be drawn from $\sigma = 0$ to complex infinity and introduces two branches of $\mathcal{J}(\sigma)$ corresponding to two leaves of the Riemann surface. The second branch of $\mathcal{J}(\sigma)$ differs from Eq. (A.7) by the sign. The branch cut prohibits $\arg\sigma$ to be changed by 2π or more. The argument of σ experiences a jump of 2π when σ crosses the branch cut. As the jump reverses the sign of $\mathcal{J}(\sigma)$, the two branches $\pm\mathcal{J}(\sigma)$ must be linked on the opposite parts of the branch cut to emulate a continuous behavior of $\mathcal{J}(\sigma)$ on the Riemann surface.

The explicit choice of the branch cut geometry is a matter of convenience. Usually, it is convenient that the branch cut goes to the left in the shortest way, i.e., along the Rex axis. Figures 18 and 19 show the s-plane (which is in fact a small neighborhood of the $x = r_0$ point in the x-plane) and the σ-plane (i.e., a small neighborhood of the $p = -i\omega_E(r_0)$ point in the p-plane) with a branch cut and integration contour for the case $\omega_E'' < 0$. The position of the poles $s_{1,2}$ for a real and positive σ is also indicated in Fig. 16d.

As is shown in Fig. 19, the branch cut initially goes up along the Imσ axis. A transformation of the r-contour brings the branch cut to the desired position along the left half of the Rex axis. Such a choice of the branch cut means that $\arg\sigma \in (-\pi, \pi)$. This condition selects the "physical" sheet of the Riemann surface.

The transformed inversion contour goes along the two parts of the branch cut without crossing it. Therefore, one does not need to worry about how to link the two branches of the Laplace transform. The target branch (A.7) is fixed by the condition that the pole s_1 is placed above the transformed r-contour provided that σ belongs to the physical sheet; i.e.,

$$s_1 = i\left|\frac{2\sigma}{\omega_E''}\right|^{1/2}\exp\left\{-i\frac{\pi}{4}\mathrm{sgn}[\omega_E''] + i\frac{1}{2}\arg\sigma\right\}. \quad \text{(A.8)}$$

Hence,

$$\mathcal{J}(\sigma) = \frac{\pi\exp\{-i\pi\,\mathrm{sgn}[\omega_E'']/4\}}{\sqrt{|2\omega_E''|}\,\sigma^{3/2}}. \quad \text{(A.9)}$$

Inserting Eq. (A.9) into Eq. (A.5) yields

$$\phi_1(r,t) = \frac{\pi r h(r_0)}{\sqrt{|2\omega_E''|}\,r_0^3}H(r_0 - r)e^{-i\pi\,\mathrm{sgn}[\omega_E'']/4}\Phi, \quad \text{(A.10)}$$

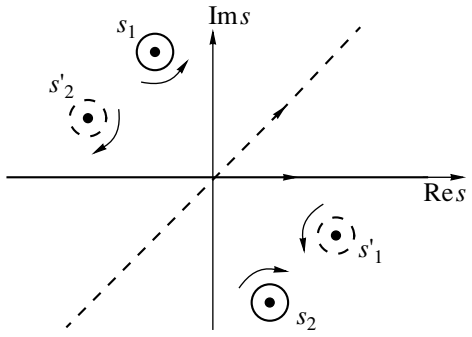

Fig. 18. Contour of integration in the complex s-plane ($s = x - r_0$). The original contour goes along the Res axis. The transformed contour (dashed line) is shown for the case $\omega_E'' < 0$ and moves at 45°. The contour wraps around the pole s_1 or s_2 if it shifts upward or downward, respectively. The arrows indicate the detour direction of the wrapped contours. Making one turn in the σ-plane exchanges s_1 with s_2, which reverses the detour direction and, hence, the sign of the Laplace transform (A.5).

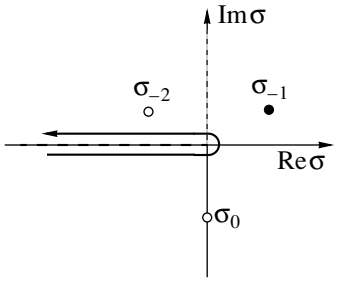

Fig. 19. Original (dotted line) and transformed (dashed line) branch cut in the σ-plane ($\sigma = p + i\omega_E(r_0)$) for the case $\omega_E'' < 0$. The inversion contour (solid line) wraps around the transformed branch cut and poles of the Laplace transform in Eq. (B.2). The poles σ_0 and σ_{-2} exist if $\beta > 0$ and the pole σ_{-1} exists if $\beta < 0$.

where

$$\Phi = \int_{Br}\frac{dp}{2\pi i}e^{pt}\left\{\frac{p + i\omega_E(r)}{[p + i\omega_E(r_0)]^{3/2}}\right\}. \quad \text{(A.11)}$$

Rearranging the integrand function in Eq. (A.11) and integrating by parts yields

$$\Phi = \int_{Br}\frac{dp}{2\pi i}e^{pt}\left\{\frac{i[\omega_E(r) - \omega_E(r_0)]}{[p + i\omega_E(r_0)]^{3/2}} + \frac{1}{[p + i\omega_E(r_0)]^{1/2}}\right\}$$

$$= \int_{Br}\frac{dp}{2\pi i}e^{pt}\left\{2t\frac{i[\omega_E(r) - \omega_E(r_0)]}{[p + i\omega_E(r_0)]^{1/2}} + \frac{1}{[p + i\omega_E(r_0)]^{1/2}}\right\}.$$

It is possible to neglect the second term in the brackets because we are interested in the behavior at $t \longrightarrow \infty$. Writing explicit limits for the inversion contour, we readily recognize that the remaining integral can be expressed through the Euler's Γ function as

$$\Phi = \frac{1}{\pi}[\omega_E(r) - \omega_E(r_0)]te^{-i\omega_E(r_0)t} \times \left\{ \int_{-\infty}^{0} \frac{dpe^{pt}}{-i|p|^{1/2}} + \int_{0}^{-\infty} \frac{dpe^{pt}}{+i|p|^{1/2}} \right\}$$

$$= \frac{1}{\pi}[\omega_E(r) - \omega_E(r_0)]te^{-i\omega_E(r_0)t}\{2i\Gamma(1/2)t^{-1/2}\}.$$

Inserting this result into Eq. (A.10) yields Eq. (11).

APPENDIX B

EXPONENTIAL SMITH–ROSENBLUTH INSTABILITY

Here, we invert the Laplace transform (8a) for the case treated in Section 4. Inserting Eq. (19) into Eq. (7a) and following the method of Appendix A, Eq. (8a) can be cast into the form

$$\phi_1(r, t) = \frac{\pi r h(r_0)}{\sqrt{|2\omega_E''|}r_0^3} H(r_0 - r)e^{-i\pi \operatorname{sgn}[\omega_E'']/4}\Phi, \quad \text{(B.1)}$$

where

$$\Phi = \int_{Br} \frac{dp}{2\pi i} e^{pt} \frac{p + i\omega_E(r)}{[p + i\omega_E(r_0)]^{3/2} + q}, \qquad q = \frac{\pi e^{-i\pi \operatorname{sgn}[\omega_E'']/4}}{|2\omega_E''|^{1/2}\beta r_0^3}, \quad \text{(B.2)}$$

and the inversion contour *Br* wraps around the branch cut $p + i\omega_E(r_0) \in (-\infty, 0]$ and the poles of the integrand function. Making the substitution $p = \sigma + i\omega_E(r_0)$ and neglecting σ in the numerator of the integrand function in Eq. (B.2), we obtain

$$\Phi = i[\omega_E(r) - \omega_E(r_0)]e^{-i\omega_E(r_0)t} \int_{Br} \frac{d\sigma}{2\pi i} \frac{e^{\sigma t}}{\sigma^{3/2} + q}. \quad \text{(B.3)}$$

To find the poles of Eq. (B.3), we introduce the notation $\sigma_n = i\gamma_0 e^{-2\pi i n/3}$, where n is an integer, and

$$\gamma_0 = \sqrt[3]{\frac{\pi^2}{2\beta^2 r_0^6 \omega_E''}}.$$

As is shown in Section 4, there are two poles σ_0 and $\sigma_{\pm 2}$ if $\beta > 0$ and a single pole $\sigma_{\pm 1}$ if $\beta < 0$. Here, the sign in the subscript corresponds to the sign of ω_E''. The contribution of any of the poles σ_n is given by

$$\Phi_n = \frac{2i}{3|\gamma_0|^{1/2}}[\omega_E(r) - \omega_E(r_0)] \times \exp\{-i\omega_E(r_0)t + \sigma_n t + i\pi n/3 - i\pi \operatorname{sgn}[\omega_E'']/4\}.$$

An exponentially growing term $\Phi_{\pm 1}$ appears if $\beta < 0$.

The contribution Φ_{cut} of the inversion contour wrapped around the branch cut $\sigma \in (-\infty, 0]$ can be evaluated as follows. For small times, $t < T$, one can neglect q in the denominator of Eqs. (B.2) and (B.3). This leads to Eq. (A.11), treated in Appendix A; as a result, we obtain

$$\Phi_{\text{cut}} = \frac{2i}{\sqrt{\pi}}[\omega_E(r) - \omega_E(r_0)]t^{1/2}e^{-i\omega_E(r_0)t}. \quad \text{(B.4)}$$

For larger times, $t > T$, we can expand the integrand function in Eq. (B.3) in the small ratio $\sigma^{3/2}/q$:

$$\Phi_{\text{cut}} = i[\omega_E(r) - \omega_E(r_0)]e^{-i\omega_E(r_0)t} \times \int_{Br} \frac{d\sigma}{2\pi i} \frac{e^{\sigma t}}{q}\left[1 - \frac{\sigma^{3/2}}{q}\right]. \quad \text{(B.5)}$$

Integrating the first term in brackets over a closed inversion contour yields zero. The remaining term decays as $t^{-5/2}$,

$$\Phi_{\text{cut}} = -\frac{3i}{4\sqrt{\pi}q^2}[\omega_E(r) - \omega_E(r_0)]t^{-5/2}e^{-i\omega_E(r_0)t}. \quad \text{(B.6)}$$

In conclusion, we note that $\Phi_{\text{cut}} \sim \Phi_n$ at $t \sim T$.

REFERENCES

1. J. H. Malmberg and J. S. deGrassie, Phys. Rev. Lett. **35**, 577 (1975).
2. T. M. O'Neil and C. F. Driscoll, Phys. Fluids **22**, 266 (1979).
3. S. A. Prasad and T. M. O'Neil, Phys. Fluids **22**, 278 (1979).
4. T. M. O'Neil, Phys. Fluids **23**, 2216 (1980).
5. T. M. O'Neil and D. H. E. Dubin, Phys. Plasmas **5**, 2163 (1998).
6. D. H. E. Dubin and T. M. O'Neil, Rev. Mod. Phys. **71**, 87 (1999).
7. I. Kotelnikov, R. Pozzoli, and M. Rome, Phys. Plasmas **7**, 4396 (2000).
8. R. C. Davidson, *Theory of Nonneutral Plasmas* (Benjamin, New York, 1974).
9. R. C. Davidson, *Physics of Nonneutral Plasmas* (Addison-Wesley, Redwood City, 1990).
10. R. H. Levy, Phys. Fluids **8**, 1288 (1965).
11. G. Rosenthal, G. Dimonte, and A. Y. Wong, Phys. Fluids **30**, 3257 (1987).

12. J. W. S. Rayieigh, Proc. London Math. Soc. **11**, 57 (1880).
13. R. J. Briggs, J. D. Dougherty, and R. H. Levy, Phys. Fluids **13**, 421 (1970).
14. A. V. Timofeev, in *Reviews of Plasma Physics*, Ed. by B. B. Kadomtsev (Énergoatomizdat, Moscow, 1989; Consultants Bureau, New York, 1992), Vol. 17.
15. N. R. Corngold, Phys. Plasmas **2**, 620 (1995).
16. R. L. Spencer and S. N. Rasband, Phys. Plasmas **4**, 53 (1997).
17. R. H. Levy, Phys. Fluids **11**, 920 (1968).
18. K. M. Case, Phys. Fluids **3**, 143 (1960).
19. L. A. Dikiĭ, Dokl. Akad. Nauk SSSR **135**, 1068 (1960) [Sov. Phys. Dokl. **5**, 1179 (1960)].
20. A. V. Timofeev, Plasma Phys. **10**, 235 (1968).
21. C. F. Driscoll, Phys. Rev. Lett. **64**, 645 (1990).
22. R. A. Smith and M. N. Rosenbluth, Phys. Rev. Lett. **64**, 649 (1990).
23. S. N. Rasband, R. L. Spencer, and R. R. Vanfleet, Phys. Fluids B **5**, 669 (1993).
24. S. N. Rasband, Phys. Plasmas **3**, 94 (1996).
25. R. A. Smith, Phys. Fluids B **4**, 287 (1992).
26. J. M. Finn, D. del-Castillo-Negrete, and D. C. Barnes, Phys. Plasmas **6**, 3744 (1999).
27. A. A. Kabantsev and C. F. Driscoll, in *Proceedings of the III Conference on Non-Neutral Plasma Physics, Princeton, 1999*, Ed. by J. J. Bollinger, R. L. Spencer, and R. C. Davidson (American Inst. of Physics, New York, 1999), p. 208; AIP Conf. Proc. **498**, 208 (1999).
28. G. G. M. Coppa, A. D'Angola, G. L. Delzanno, and G. Lapenta, Phys. Plasmas **8**, 1133 (2001).
29. T. J. Hilsabeck and T. M. O'Neil, Phys. Plasmas **8**, 407 (2001).
30. S. A. Prasad and J. H. Malmberg, Phys. Fluids **29**, 2196 (1986).
31. K. S. Fine, Phys. Fluids B **4**, 3981 (1992).
32. K. S. Fine, C. F. Driscoll, and J. H. Malmberg, Phys. Fluids **4**, 3981 (1992).
33. D. A. Schecter, D. H. Dubin, A. C. Cass, *et al.*, Phys. Fluids **12**, 2397 (2000).

Plasma Physics Reports, Vol. 28, No. 2, 2002, pp. 158–165. Translated from Fizika Plazmy, Vol. 28, No. 2, 2002, pp. 180–187.

WALL PLASMA

Model of the Near-Wall Conductivity in the Vicinity of a Macroscopically Inhomogeneous, Mirror-Reflecting Surface

A. N. Kozlov

Keldysh Institute of Applied Mathematics, Russian Academy of Sciences, Miusskaya pl. 4, Moscow, 125047 Russia
e-mail: kozlov@kiam.ru

Received June 21, 2001; in final form, September 27, 2001

Abstract—A study is made of the interaction of the electron component of a low-density plasma with a macroscopically inhomogeneous, mirror-reflecting surface in mutually orthogonal electric and magnetic fields. The collisionless kinetic equation is solved analytically in the $(2R + 3V)$-dimensional space. A nontrivial structure of the nascent near-wall currents is revealed, and their two-dimensional distribution is analyzed in detail. From the standpoint of practical applications, attention is focused on the near-wall conductivity in a stationary plasma thruster. The results obtained agree with the available experimental data. Moreover, the investigations described here provide a basis for the study of the possibility of tailoring the insulator in the channel for the purpose of suppressing anomalous erosion and ensuring the required operating period of plasma thrusters. © *2002 MAIK "Nauka/Interperiodica".*

1. INTRODUCTION

This paper is aimed at investigating the interaction of the electron component of a low-density plasma with a macroscopically inhomogeneous surface in mutually orthogonal electric and magnetic fields (Fig. 1). The Debye sheath at the surface—an intrinsic property of most plasma devices—is assumed to be sufficiently thin in comparison with the dimensions of macroinhomogeneities. On the other hand, the potential jump across the Debye sheath ensures a mirror reflection of the plasma electrons under consideration. Such a formulation of the problem is fairly general. Below, the problem will be reduced to that of investigating the near-wall conductivity (NWC) at a macroscopically inhomogeneous (rippled) insulator surface in a stationary plasma thruster (SPT).

The concept of NWC was first introduced by Morozov [1] in the context of developing the theory of physical processes in an SPT [2, 3]. Later, the NWC effect was revealed and thoroughly analyzed in the experiments of [4, 5]. The theory of the processes occurring in an SPT was generalized by Morozov and Savel'ev in their review [6].

The NWC is one of the most important factors in ensuring the normal operation of an SPT. In studying the situation under discussion, attention has been focused on the origin and structure of the near-wall currents stemming from the surface macro-inhomogeneities [7]. A general approach to investigating the relevant phenomena is described in [3, 6]. Note that, under certain circumstances, the NWC is particularly affected by such effects as multiple reflections of the electrons from the surface and their trapping in the surface macro-inhomogeneities. However, the results obtained in the present paper show that even a single reflection from a mirror-reflecting rippled surface can produce near-wall currents with a pronounced nontrivial structure and that this process is dominated by singly reflected electrons for a wide range of parameters of the problem.

It should be noted that, in this study, the effects of the possible screening of the rippled surface from a certain electron group and, accordingly, the appearance of

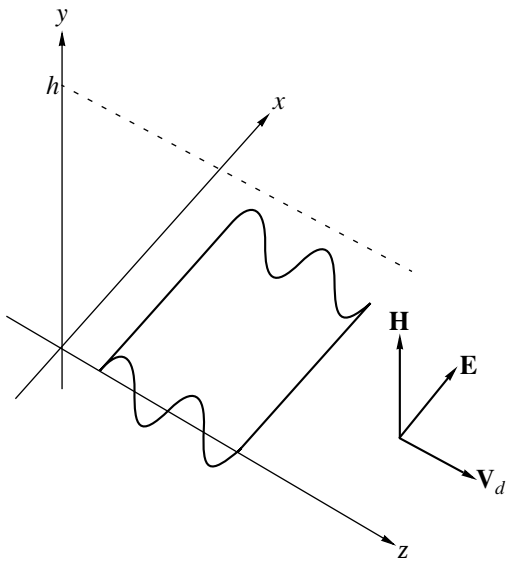

Fig. 1. Geometry of the problem.

1063-780X/02/2802-0158$22.00 © 2002 MAIK "Nauka/Interperiodica"

a shadow region are neglected. These effects require separate consideration.

The NWC, like neoclassical transport across a magnetic field, is associated with a reduction in electron drifts in crossed **E** and **H** fields due to collisions with heavy particles. The only difference is that, in the case of NWC, in which electron scatterings in the region near the wall are unimportant, the reduction in electron drifts is due to collisions of electrons with the wall, which thus plays the role of superheavy particles. Depending on the roughness of the surface, its geometry, and the Debye sheath thickness, electron drifts can be reduced either by diffusive scattering or by mirror reflections from particular surface sites. Of course, the NWC differs in origin and magnitude from both the plasma conductivity across the magnetic field, $\sigma^B \sim 1/H$ (which was introduced by David Bohm when analyzing experimental data), and from the classical electron conductivity, $\sigma_\perp \sim 1/H^2$.

The investigations described here are based on the analytic solution of the collisionless kinetic equation for plasma electrons in $(2R + 3V)$-dimensional space. The solution obtained describes, in particular, the NWC associated with a mirror reflection of the electrons from surface macroinhomogeneities and applies to the case in which the Debye sheath thickness is much smaller than both the characteristic inhomogeneity scale length and the thickness of the layer in which the near-wall current flows.

Macroinhomogeneities in insulator surfaces may result from anomalous erosion during long-term operation of the existing SPTs. However, the insulator can also be tailored artificially in order to ensure the desired level of the NWC in next-generation plasma thrusters and to provide the required operating period. Regardless of the properties of the insulator material, such artificial tailoring will make it possible to radically lower the rate of anomalous wall erosion, which limits the operating period of the thruster. The results obtained raise the hope of overcoming the problem. At present, SPTs are being successfully developed and are more advanced in comparison with, e.g., coaxial plasma accelerators [8–10]. Over the past few decades, SPTs have been used to correct for satellite orbits, and, in the near future, they are planned to be used as the mid-flight engines for possible long-duration space flights.

2. FORMULATION OF THE PROBLEM

We specify a mirror-reflecting rippled surface in such a way that its projection onto, e.g., the (y, z) plane is a sinusoid $Y_1(z) = A\sin(k_p z)$, where the quantity k_p determines the ripple period of the surface, $\lambda_p = 2\pi/k_p$, and A is the ripple amplitude. Figure 1 shows the geometry of the problem in the (x, y, z) coordinates. The model to be constructed possesses plane symmetry rather than axial symmetry, as is the case with existing SPTs. However, this circumstance is not of fundamental importance for the effects under investigation. Let the plasma occupy the region in the form of a strip $Y_1(z) \le y \le h$, and let the mutually orthogonal electric and magnetic fields be directed in such a way that $\mathbf{E} = (E, 0, 0)$ and $\mathbf{H} = (0, H, 0)$, where E and H are assumed to be constants.

A specific electromagnetic field strength can be chosen to fit the available experimental data, according to which the magnetic field strength is about $H \approx 100$–300 Oe and the length of the discharge gap is about $L \approx 2$–3 cm. In this case, the electron and ion gyroradii, R_e and R_i, satisfy the inequalities $R_e \ll L \ll R_i$. The potential difference across the discharge gap is about $U_p \approx 250$ V. Since the plasma configuration in the channel of an SPT is on the whole stable, the distribution of the electric field, which is directed along the system axis (the x-axis in Fig. 1), is also stable. According to the general pattern of the processes occurring in an SPT, the magnetized electrons in crossed (**E**, **H**) fields move in spirals around the magnetic field lines. On the whole, the electron cloud drifts in the azimuthal direction (along the z-axis in Fig. 1) with the velocity $\mathbf{V}_d = c\mathbf{E} \times \mathbf{H}/H^2$. The electron plasma component is transparent to the ions, whose gyroradii are much larger than the length L of the discharge gap. For the plasma to be quasineutral, the characteristic particle density should be equal in order of magnitude to $n \approx 10^{11}$ cm^{-3}.

In the kinetic model developed here, the most important point is that, according to the experimental data, the self-consistent field is negligible.

The plasma density is assumed to be sufficiently low, so that the electron dynamics is described by the following collisionless kinetic equation for the electron distribution function (EDF) $f(t, \mathbf{R}, \mathbf{V})$:

$$\frac{\partial f}{\partial t} + \mathbf{V} \cdot \frac{\partial f}{\partial \mathbf{R}} + \frac{\mathbf{F}}{m} \cdot \frac{\partial f}{\partial \mathbf{V}} = 0, \tag{1}$$

where

$$\mathbf{F} = -e\left(\mathbf{E} + \frac{1}{c}\mathbf{V} \times \mathbf{H}\right) = -e\left(E - \frac{V_z}{c}H, 0, \frac{V_x}{c}H\right).$$

The characteristics of the linear equation (1) satisfy the equations

$$\frac{dx}{dt} = V_x, \quad \frac{dV_x}{dt} = -\frac{eF}{m} + \omega V_z,$$
$$\frac{dy}{dt} = V_y, \quad \frac{dV_y}{dt} = 0, \quad \omega = \frac{eH}{mc}, \tag{2}$$
$$\frac{dz}{dt} = V_z, \quad \frac{dV_z}{dt} = -\omega V_x.$$

Integration of Eqs. (2) yields the following relationships describing the electron trajectories:

$$V_x = V_{x0}\cos\omega t + (V_{z0} - V_d)\sin\omega t,$$

$$x = x_0 + \frac{V_{x0}}{\omega}\sin\omega t + \frac{V_{z0} - V_d}{\omega}(1 - \cos\omega t),$$
$$V_y = V_{y0},$$
$$y = y_0 + V_{y0}t, \quad (3)$$
$$V_z = V_{z0}\cos\omega t - V_{x0}\sin\omega t + V_d(1 - \cos\omega t),$$
$$z = z_0 + \frac{V_{z0}}{\omega}\sin\omega t - \frac{V_{x0}}{\omega}(1 - \cos\omega t) + V_d t - \frac{V_d}{\omega}\sin\omega t,$$

where $V_d = cE/H$ is the electron drift velocity in crossed electric and magnetic fields.

In the case at hand, the trajectories of both the incident and reflected electrons are trochoids. Along the trajectories, which are characteristics of Eq. (1), the EDF is constant. Now, we take into account the above formulas in order to determine the EDF and generated electron current.

3. SOLUTION OF THE KINETIC EQUATION

The solution of the general kinetic equation (1) is based on the method of characteristics and the corresponding boundary condition for the EDF at the mirror-reflecting surface.

In order to determine the EDF over the entire region under consideration, it is necessary, first of all, to specify the distribution function of the electrons entering this region at the boundary $y = h$. It is natural to assume that the distribution function of the incident electrons, $f^- = f(y = h, V_y < 0)$, is known. One of the integrals of Eq. (1) is a Maxwellian distribution function shifted by the magnitude of the drift velocity V_d along the V_z-axis in velocity space (Fig. 1). This Maxwellian function can be taken as the distribution function f^- required for our problem:

$$f^- = C\exp\{-\beta[V_x^2 + V_y^2 + (V_z - V_d)^2]\}, \quad (4)$$

where $\beta = \frac{m}{2T}$ and $C = n\left(\frac{m}{2\pi T}\right)^{3/2}$ is a normalizing constant.

Since function (4) is an integral of Eq. (1), it is independent of the spatial coordinates everywhere, in particular, at the mirror-reflecting surface $y = Y_1(z)$. Consequently, electrons with the velocities $V_y \le 0$, which are incident on the surface, do not contribute to the sought-for near-wall current density $j_x = -e\iiint V_x f\, d\mathbf{V}$ $(e > 0)$ because the distribution function is even in V_x. We can thus conclude that, in a sense, the current j_x and, accordingly, the NWC stem exclusively from the effect of the mirror-reflecting surface. The possible deviation of the EDF at $y = h$ from a Maxwellian function has essentially no impact on the method developed here and may be the subject of ongoing investigations.

Taking into account the fact that the distribution function (4) is time-independent, we restrict ourselves to considering a steady-state problem, in which case the time dependence can be eliminated with the help of one of the relationships (3).

The boundary condition at the mirror-reflecting surface $y = Y_1(z)$ can be imposed in accordance with the standard assumption familiar in the theory of kinetic equations [11–14]: the distribution functions of the incident and reflected electrons with opposite signs of the normal velocity component V_n are the same.

As a result, the boundary condition that relates the distribution functions of the incident (f^-) and reflected (f^+) electrons at the surface $y = Y_1(z)$ can be written as

$$f^-(V_x, V_n, V_\tau) = f^+(V_x, -V_n, V_\tau). \quad (5)$$

The electrons moving along complicated trajectories can undergo multiple reflections from a macroscopically inhomogeneous (in the case at hand, rippled) mirror-reflecting surface. However, in our analysis, we use the single-reflection approximation [15] (its applicability range will be discussed in the next section).

In velocity space, we switch from the components (V_x, V_y, V_z) to the components (V_x, V_n, V_τ) using the following relationships, which are valid at the mirror-reflecting surface $y = Y_1(z)$:

$$\mathbf{V}_n = \frac{1}{a}(\mathbf{V}_y - Y_1'(z)\mathbf{V}_z), \quad \mathbf{V}_\tau = \frac{1}{a}(\mathbf{V}_z + Y_1'(z)\mathbf{V}_y), \quad (6)$$

where $a = \sqrt{1 + (Y_1'(z))^2}$ and $Y_1'(z) = dY_1/dz$.

Recall that, according to the geometry of the problem, the drift velocity is equal to $\mathbf{V}_d = V_d\mathbf{i}$, where $\mathbf{i}$ is a unit vector along the z-axis. In this case, using the transformations inverse to transformations (6), we can represent the distribution function (4) of the incident electrons in the form

$$f^- = C\exp\left\{-\frac{\beta}{a^2}[a^2\mathbf{V}_x^2 + (a\mathbf{V}_n + \mathbf{V}_d Y_1'(z))^2 + (a\mathbf{V}_\tau - \mathbf{V}_d)^2]\right\}.$$

From the mirror reflection condition (5) and transformations (6) in velocity space (V_x, V_y, V_z), we obtain the distribution function near the mirror-reflecting surface after a single reflection:

$$f_1^+ = C\exp\{-\beta[V_x^2 + V_y^2 + (V_z - V_1)^2]\}\exp(-\beta B_1), \quad (7)$$

where

$$V_1 = V_d\delta, \quad \delta = \frac{2}{a^2} - 1, \quad B_1 = \frac{4V_d^2}{a^4}(Y_1'(z))^2.$$

We can see that the distribution function of the reflected electrons depends on V_d rather than on the drift velocity V_1. Since the distribution function (7) is no longer an integral of Eq. (1), its shape and values will change with increasing distance from the mirror-reflecting surface, thereby determining the structure of the generated electron current.

Egorov *et al.* [5] suggested that the interaction of electrons with an inhomogeneous surface may change the electron drift velocity. This is clearly illustrated by formula (7).

The time dependence can be eliminated using one of the relationships (3), namely, $y = y_0 + V_{y0}t$, where $y_0 = Y_1(z)$ at $t = 0$. This relationship gives

$$t = \frac{y - Y_1(z)}{V_y}. \quad (8)$$

We assume that, in relationships (3), V_{x0}, V_{y0}, and V_{z0} are the components of the velocities of the electrons that start simultaneously from any point in the mirror-reflecting surface at the time $t = 0$. At $y = Y_1(z)$; we replace V_x, V_y, and V_z in formula (7) by V_{x0}, V_{y0}, and V_{z0}, respectively. According to relationships (3), the inverse transformation of the form $V_x \Rightarrow V_{x0}$ leads to the relationships

$$\begin{aligned} V_{x0} &= V_x\cos\omega t - (V_z - V_d)\sin\omega t, \\ V_{y0} &= V_y, \\ V_{z0} &= V_z\cos\omega t + V_x\sin\omega t + V_d(1 - \cos\omega t). \end{aligned} \quad (9)$$

In expression (7), we replace V_x, V_y, and V_z by V_{x0}, V_{y0}, and V_{z0}, respectively, and substitute relationships (8) and (9) into the resulting expression. As a result, we arrive at the distribution function of the reflected electrons for arbitrary values of y and z:

$$\begin{aligned} f_1^+ &= C\exp\langle -\beta\{[V_x + (V_d - V_1)\sin\theta]^2 \\ &+ V_y^2 + [V_z + (V_d - V_1)\cos\theta - V_d]^2 + B_1\}\rangle, \end{aligned} \quad (10)$$

where $\theta = \dfrac{y - Y_1(z)}{|V_y|}\omega$.

Let us solve for the x-component of the electron current density, $j_x = -e\int\limits_{V_x=-\infty}^{0}\int V_x f^- d\mathbf{V} - e\int\limits_{V_x=0}^{\infty}\int V_x f_1^+ d\mathbf{V}$. For $V_y < 0$, the function f^- does not contribute to the current density j_x, because it is even in V_x. Thus, we only need to substitute the function f_1^+ (10). Then, we perform integration to obtain

$$j_x(y, z) = enV_d G\left(\frac{y - Y_1(z)}{R_e}\right)(1 - \delta)\exp(-\beta B_1), \quad (11)$$

where $G(x) = \dfrac{1}{\sqrt{\pi}}\int_0^\infty \exp(-\xi^2)\sin\dfrac{x}{\xi}d\xi$, $R_e = \dfrac{V_T}{\omega}$, and $V_T = \sqrt{\dfrac{2T}{m}}$.

4. APPLICABILITY RANGE OF THE SINGLE-REFLECTION APPROXIMATION

We introduce the mirror-reflection operator $\hat{F}$ in such a way that it transforms the distribution function of the incident electrons to the distribution function of the reflected electrons in accordance with the above-described procedure. The single-reflection approximation ($\hat{F}f^- = f_1^+$) implies that all of the reflected electrons (whose density is n_I) pass through the boundary $y = h$ and move off to infinity. Using expression (10), we can easily find that the density of these electrons is equal to $n_\mathrm{I} = \iiint_{V_y=0}^{\infty} f_1^+ d\mathbf{V} = \dfrac{1}{2}n\exp(-\beta B_1)$. However, in reality, only part of the electrons moves off to infinity after one reflection, while another (smaller) part returns to the rippled surface. Denoting the distribution functions of these two electron groups by $f_{1,\infty}$ and $f_{1,CT}^{\mathrm{from}}$, respectively, we can write $\hat{F}f^- = f_{1,\infty} + f_{1,CT}^{\mathrm{from}}$.

According to relationship (8), the operation of changing the sign of V_y transforms the distribution function $f_{1,CT}^{\mathrm{from}}$ of singly reflected electrons that move away from the mirror-reflecting surface to the distribution function of singly reflected electrons that reverse the direction of their motion and return to the surface: $f_{1,CT}^{\mathrm{from}} \Rightarrow f_{1,CT}^{\mathrm{on}}$. Applying the mirror-reflection operation again, we can see that part of the doubly reflected electrons moves off to infinity. Denoting the distribution function of these electrons by $f_{2,\infty}$, we can write $\hat{F}f_{1,CT}^{\mathrm{on}} = f_{2,\infty} + f_{2,CT}^{\mathrm{from}}$. In the next approximation, it is natural to assume that $f_{2,CT}^{\mathrm{from}} = 0$, in which case we have $f_{2,\infty} = \hat{F}(\hat{F}f^- - f_{1,\infty})$, where $\hat{F}f_{1,\infty} = f_{1,\infty}$, and, accordingly, $f_{1,\infty} + f_{2,\infty} = \hat{F}^2 f^-$. Applying the mirror-reflection operation again, we obtain $\hat{F}^2 f^- = C\exp\{-\beta[V_x^2 + V_y^2 + (V_z - V_2)^2] - \beta B_1(1 + \delta^2)\}$, where $V_2 = V_d\delta^2$. Then, we can readily estimate the density of the doubly reflected electrons that move off to infinity: $n_\mathrm{II} = \iiint_{V_y=0}^{\infty}(f_{1,\infty} + f_{2,\infty})d\mathbf{V} = \dfrac{1}{2}n\exp(-\beta B_1(1 + \delta^2))$. At

the points on the rippled surface at which $Y_1' \approx 0$, the densities of the reflected electrons are nearly the same regardless of the approximation used, $n_{\rm I} \approx n_{\rm II} \approx n/2$, by virtue of the relationship $B_1 \sim (Y_1')^2$. Accordingly, the density of the doubly reflected electrons that move off to infinity, $\tilde{n}_2$, is negligible. At other points on the rippled surface, specifically, those at which $Y_1' \neq 0$, the density of such electrons in the approximation at hand should also be much lower than the density of the singly reflected electrons that move off to infinity, $\tilde{n}_1 \approx n_{\rm I}$. Since $\tilde{n}_2/\tilde{n}_1 \approx |n_{\rm I} - n_{\rm II}|/n_{\rm I} = 1 - \exp(-\beta B_1 \delta^2)$, inequality $\tilde{n}_2/\tilde{n}_1 \ll 1$ implies that

$$\beta B_1 \delta^2 \ll 1 \quad \text{or} \quad 4(V_d/V_T)^2 Q(Y_1'(z)) \ll 1, \qquad (12)$$

where $Q(\xi) = \xi^2(1 - \xi^2)^2/(1 + \xi^2)^4$ and $Y_1'(z) = \frac{2\pi A}{\lambda_p}\cos(k_p z)$ for the rippled surface under consideration. Elementary calculations show that $Q(\xi) \leq 0.06$ for arbitrary values of ξ. Consequently, inequality (12) holds for a broad range of A and λ_p values under the condition

$$\frac{V_d}{V_T} \leq 1. \qquad (13)$$

Hence, the single-reflection approximation is applicable to mirror-reflecting surfaces that are rippled in a fairly arbitrary manner, provided that the plasma electron temperature is sufficiently high ($V_T \geq V_d$). This conclusion agrees with the available experimental data, according to which the electron temperature is about several tens of electronvolts.

5. MAIN RESULTS

One of the main results obtained in this paper is that the onset of the near-wall current (in the case at hand, this is the current j_x) stems precisely from the surface macro-inhomogeneities. From formula (11), which was derived in the single-reflection approximation, we can see that, over the entire region adjacent to the unrippled ($A = 0$) surface, the electron current is identically zero ($j_x \equiv 0$). The second important result is that the near-wall current possesses a nontrivial structure. We should, first of all, note that the analytic solution of the above kinetic problem in two-dimensional configuration space implies that the integral in $G(x)$ in expression (11) should be calculated at each point in this space. A possible structure of the distribution of the current density j_x normalized to enV_d is depicted in Fig. 2. Shown here are isolines of the current density, whose direction is perpendicular to the plane of the figure and which was calculated for $A/\lambda_p = 0.3$, $R_L/\lambda_p = 0.3$, $h/\lambda_p = 3$, and $V_d/V_T = 0.5$. In this case, the gyroradius R_e of an electron moving in crossed electric and magnetic fields is equal to the amplitude A of the sinusoidal ripples in the mirror-reflecting surface. The upper boundary $y = h$ corresponds to the condition $h \gg A$. Recall that, at this boundary, the incident electrons are assumed to obey the initial Maxwellian distribution function (4) with an argument shifted along the V_z-axis in velocity space.

From Fig. 2 and formula (11), we can see that the obvious requirements for the solution and, accordingly, for the current density j_x are satisfied. The structure of the current density distribution is symmetric about the z-axis. At the mirror-reflecting surface $y = Y_1(z)$, the current density is identically zero, $j_x \equiv 0$, and, at sufficiently long distances from the surface, we have $j_x \longrightarrow 0$.

According to Fig. 2, the near-wall current is primarily localized in layers with a thickness on the order of R_e, which are separated by layers in which $Y_1'(z) \approx 0$ and the current vanishes. One can also see that, in the direction of the transverse y-coordinate, the current density distribution is oscillatory in nature, as is the case in the experiments of [4]. In the islands in the region $y \approx (0.2\text{–}0.4)h$, the current j_x flows in the direction opposite to that of the current near the mirror-reflecting surface but is much less in magnitude. This result also agrees with the available experimental data, according to which the current density experiences damped oscillations. The fact that some of the isolines in Fig. 2 are not smooth is associated with the inaccuracies of the numerical algorithm used to calculate the integral in $G(x)$ in expression (11) at each point in the (y, z) plane.

Varying the parameters of the problem made it possible to reveal a number of regular features in the behavior of the electron current in the approximation of single reflection of electrons from a macroscopically inhomogeneous, mirror-reflecting surface. In particular, when the amplitude A of the sinusoidal ripples in the surface is sufficiently small ($Ak_p < 1$, $V_d/V_T \leq 1$), formula (11) gives the following dependence of the maximum near-wall current on the parameters of the problem:

$$\frac{j_x^{\max}}{enV_d} \sim \left(\frac{A}{\lambda_p}\right)^2 \exp\left[-16\pi^2\left(\frac{V_d}{V_T}\right)^2\left(\frac{A}{\lambda_p}\right)^2\right]. \qquad (14)$$

Otherwise, for a large amplitude such that $Ak_p > 1$ and $V_d/V_T \leq 1$, we obtain

$$\frac{j_x^{\max}}{enV_d} \sim \exp\left[-\frac{1}{\pi^2}\left(\frac{V_d}{V_T}\right)^2\left(\frac{\lambda_p}{A}\right)^2\right]. \qquad (15)$$

In fact, a comprehensive calculation of the two-dimensional current density distribution showed that, in accordance with the above relationships, the current near the mirror-reflecting surface increases with increasing the ripple amplitude A of the surface. In this case, the overall pattern of the two-dimensional current

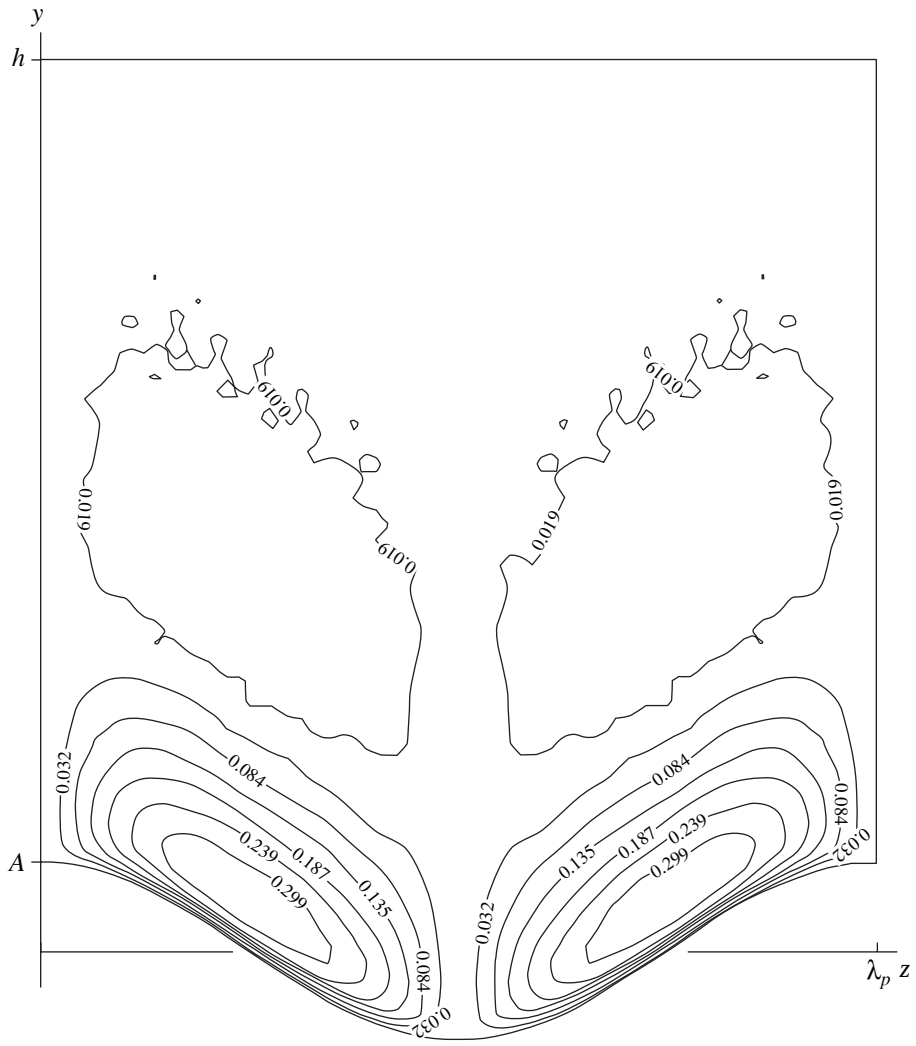

Fig. 2. Distribution of the electron current density $j_x(y, z)$ for $V_d/V_T = 0.5$.

density distribution does not change qualitatively. As the electron thermal velocity V_T increases, the current also increases, in which case the current structure remains essentially the same, provided that $V_d < V_T$.

The spatial distribution of the near-wall current changes markedly at a sufficiently large value of the ratio V_d/V_T, in particular, at temperatures lower than those prevailing in experiments. The current structure shown in Fig. 3 was calculated for $V_d/V_T = 2$, the remaining parameters being the same as those adopted above. In accordance with the indicated dependence of the current on the velocity ratio, the current magnitude in Fig. 3 is much lower than that in Fig. 2. In addition, the current in Fig. 3 is distributed in such a way that it tends to form its own wavelength λ_C in the direction of the electron drift (along the *z*-axis). In Fig. 2, this wavelength is approximately equal to $2\lambda_C \approx \lambda_p/2$, while, in Fig. 3, it is about $\lambda_C \approx \lambda_p/6$. A further increase in the velocity ratio V_d/V_T causes the current to decrease and be localized in layers where $Y_1' \approx 0$. Such a behavior of the near-wall current at $V_T < V_d$ agrees with the available experimental data. In the experiments of [5], the NWC was observed to decrease with temperature. For $V_T < V_d$, the single-reflection approximation can be used to treat each particular set of parameter values of the problem (including the set in Fig. 3) only under the more general applicability condition (12), which can be satisfied even when inequality (13) fails to hold. If this more general condition is violated, the only way to refine the results obtained in the single-reflection approximation is to develop the theory of NWC at macroscopically inhomogeneous surfaces with allowance for multiple reflections.

In addition to what was said above, note that varying the parameters that determine the two-dimensional current density distribution made it possible to reveal one more regular feature: the smaller the electron gyroradius R_e, the smaller the thickness h_{NWC} of the layer of

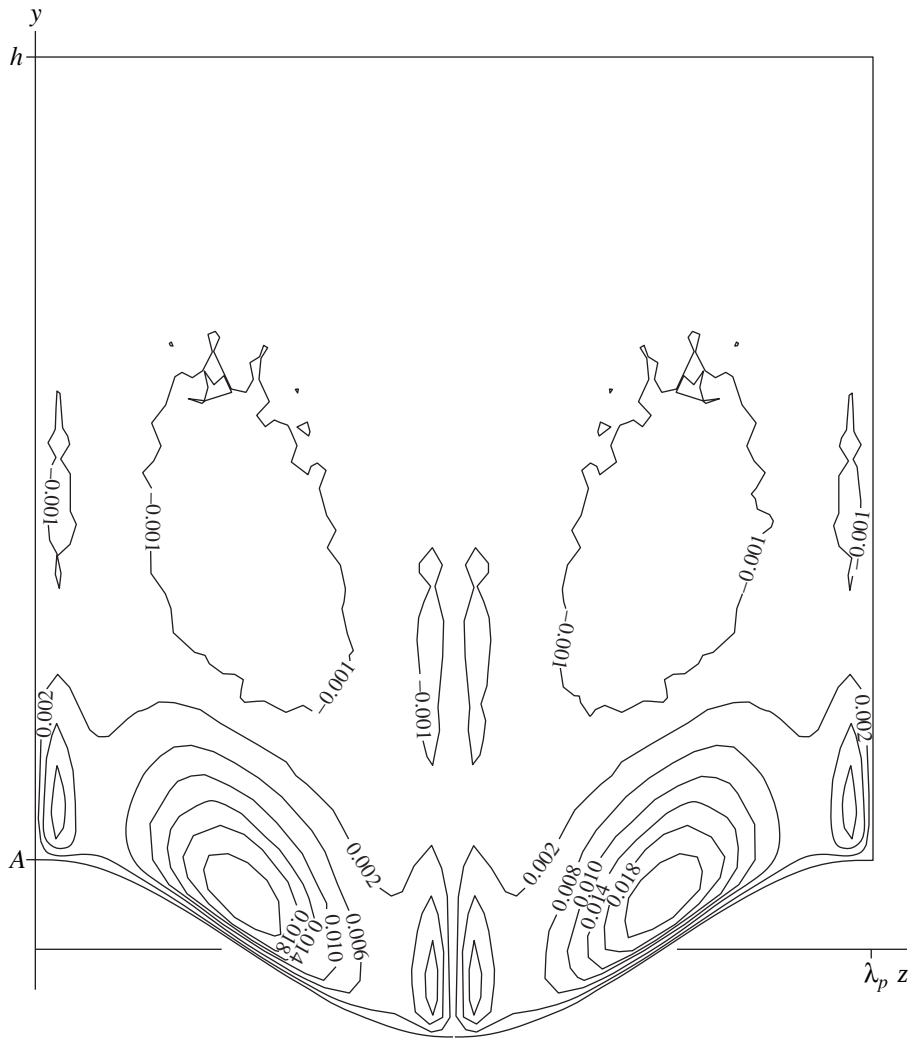

Fig. 3. Distribution of the electron current density for $V_d/V_T = 2$.

nonzero NWC. This conclusion can be written as $h_{\mathrm{NWC}} \approx R_e$, which agrees with the experimental results of [4].

Let us estimate the near-wall electron current I under the operating conditions typical of existing SPTs, e.g., for the current density distribution shown in Fig. 2. Let the characteristic strengths of the electric and magnetic fields be E = 100 V/cm and H = 100 Oe. In such fields, the electron drift velocity is equal to $V_d = 10^8$ cm/s and the electron thermal velocity is $V_T = 2V_d = 2 \times 10^8$ cm/s, which corresponds to an electron temperature of about $T \approx 10$ eV and an electron gyroradius $R_e = V_T/\omega = 4 \times 10^{-2}$ cm. For the current density distribution in Fig. 2, the ripple period of the mirror-reflecting surface is equal to $\lambda_p = (10/3)R_e = 0.133$ cm. For the characteristic radius R = 3 cm of the insulator surface, it is easy to find that the number of ripples is equal to $N = 2\pi R/\lambda_p \approx 140$. The electron current per ripple is calculated from the formula $i_1 = enV_d\tilde{i}_1$, where the dimensionless integral $\tilde{i}_1 = \int\int j_x(y,z)d\mathbf{S}$ of the electron current density (11) over the surface shown in Fig. 2 is approximately equal to $\tilde{i}_1 \approx 0.3A(\lambda_p/2) = 8 \times 10^{-4}$. In this case, the total near-wall electron current can be estimated as $I \approx N\, i_1 \approx 0.18$ A, which is in reasonable agreement with the available experimental data [6].

6. CONCLUSIONS

The collisionless kinetic equation for the electron plasma component near a macroscopically inhomogeneous, mirror-reflecting surface in mutually orthogonal electric and magnetic fields has been solved analytically in $(2R + 3V)$-dimensional space. The near-wall currents associated with the corresponding change in the drift velocity of the reflected electrons are found to possess a nontrivial structure, which stems precisely from the macroinhomogeneities of the mirror-reflecting surface. An analytic model for investigating the

structure of the generated currents has been developed on the basis of the single-reflection approximation. A detailed analysis made it possible to reveal the main features of the near-wall current density distribution. The characteristic magnitudes of the near-wall currents under different conditions are described by formulas (11), (14), and (15).

The results obtained provide a better insight into the causes of the onset and behavior of near-wall currents, even though the model developed here (like any other analytic model) makes it possible to investigate the subject primarily at a qualitative level and does not allow a detailed comparison with the experiment. Nevertheless, the above analysis of the NWC near macroscopically inhomogeneous (rippled) insulator surfaces in SPTs shows that the results obtained may find practical applications, primarily because the normal operating conditions of plasma thrusters are ensured precisely by the near-wall currents.

Another purpose of this work is to stimulate further theoretical and experiment investigations of such an important phenomenon as NWC, which has been studied very little up to now.

ACKNOWLEDGMENTS

I am grateful to A.I. Morozov for inspiring this study and to K.V. Brushlinskiĭ and V.V. Savel'ev for their interest in this paper and fruitful discussions. This work was supported in part by the Russian Foundation for Basic Research, project nos. 00-01-00395 and 99-07-90443.

REFERENCES

1. A. I. Morozov, Prikl. Mekh. Tekh. Fiz., No. 3, 19 (1968).
2. A. I. Morozov, in *Plasma Accelerators*, Ed. by L. A. Artsimovich (Mashinostroenie, Moscow, 1973), p. 5.
3. A. I. Morozov, *Physical Principles of Space Electrojet Engines* (Atomizdat, Moscow, 1978).
4. A. I. Bugrova and A. I. Morozov, in *Ionic Injectors and Plasma Accelerators*, Ed. by A. I. Morozov and N. N. Semashko (Énergoatomizdat, Moscow, 1990), p. 42.
5. V. V. Egorov, V. Kim, A. A. Semenov, and I. I. Shkarbman, in *Ionic Injectors and Plasma Accelerators*, Ed. by A. I. Morozov and N. N. Semashko (Énergoatomizdat, Moscow, 1990), p. 56.
6. A. I. Morozov and V. V. Savelyev, in *Reviews of Plasma Physics*, Ed. by B. B. Kadomtsev and V. D. Shafranov (Consultants Bureau, New York, 2000), Vol. 21, p. 203.
7. *Encyclopedia of Low Temperature Plasma*, Ed. by V. E. Fortov (Nauka, Moscow, 2000), Vol. III, p. 456.
8. A. I. Morozov, Fiz. Plazmy **16**, 131 (1990) [Sov. J. Plasma Phys. **16**, 69 (1990)].
9. K. V. Brushlinskiĭ, A. M. Zaborov, A. N. Kozlov, *et al.*, Fiz. Plazmy **16**, 147 (1990) [Sov. J. Plasma Phys. **16**, 79 (1990)].
10. A. N. Kozlov, Fiz. Plazmy **18**, 714 (1992) [Sov. J. Plasma Phys. **18**, 369 (1992)].
11. Yu. P. Raizer, *Gas Discharge Physics* (Nauka, Moscow, 1987; Springer-Verlag, Berlin, 1991).
12. C. Cercignani, *Mathematical Methods in Kinetic Theory* (Plenum, New York, 1969; Mir, Moscow, 1973).
13. M. V. Maslennikov, *Asymptotic Model of Particle Transport Phenomena* (Nauka, Moscow, 1989).
14. V. V. Vedenyapin, Dokl. Akad. Nauk SSSR **323**, 1004 (1992).
15. A. N. Kozlov, Preprint No. 29 (Keldysh Institute of Applied Mathematics, Russian Academy of Sciences, Moscow, 2001).

Translated by I. Kalabalyk

Plasma Physics Reports, Vol. 28, No. 2, 2002, pp. 166–168. Translated from Fizika Plazmy, Vol. 28, No. 2, 2002, pp. 188–190.

BRIEF COMMUNICATIONS

Structure of Global Tokamak Scalings

Yu. N. Dnestrovskij

Institute of Nuclear Fusion, Russian Research Centre Kurchatov Institute, pl. Kurchatova 1, Moscow, 123182 Russia

Received April 26, 2001; in final form, August 26, 2001

Abstract—In empirical tokamak scalings, not all of the standard engineering parameters are independent. Thus, the larger the tokamak, the higher the required plasma current and input power. Also, by using higher magnetic fields, it is possible to raise the plasma density. Instead of the plasma density, plasma current, and input power, it is proposed to use such combinations of engineering parameters whose values are essentially the same for different tokamaks. With this approach, the number of free scaling parameters can be reduced from six to three, thereby improving the reliability of the scaling. *© 2002 MAIK "Nauka/Interperiodica".*

1. There is a certain amount of disagreement between the global ITER scalings for the energy confinement time τ_E, which were constructed from a common database created by summarizing experimental data from various machines, and particular experiments in some tokamaks. The most familiar of these are T-10 experiments on determining the dependence of τ_E on the plasma density n and also JET and DIII-D experiments on determining the dependence of τ_E on the dimensionless parameter β.

In my opinion, the reason for the disagreement with these and other experiments lies in the disparity between the engineering plasma parameters

$$n, P, B, a, I, A, \tag{1}$$

which are used to construct the dimensional energy confinement time scaling

$$\tau_E = f n^{c_1} P^{c_2} B^{c_3} a^{c_4} I^{c_5} A^{c_6}. \tag{2}$$

The function $f = f(k, \delta, \ldots)$, which depends on dimensionless parameters, will not be considered here. In scaling (2), not all of the engineering parameters (1) are independent. The quantities

$$J_1 = nR/B, \quad J_2 = P/(aR), \quad J_5 = I/a^2 \tag{3}$$

are essentially the same in different devices and thus can be regarded as being quasi-invariant with respect to them. However, quantities (3) may vary widely in a particular tokamak. More precisely, shots with the same quasi-invariants can be realized in different tokamaks, whereas the parameters B, a, and A are essentially fixed for a given machine. Note that quantities (3), as well as engineering parameters (1), are dimensional.

The disparity of parameters (1) and the possibility of constructing quasi-invariants (3) suggest that the most adequate form of global scaling can be the following:

$$\tau_E = f_1 J_1^{d_1} J_2^{d_2} B^{d_3} a^{d_4} J_5^{d_5} A^{d_6}. \tag{4}$$

Not all of the quasi-invariants (3) should enter scaling (4); their number may be reduced. Thus, it might be convenient to omit the quasi-invariant J_1, which contains the plasma density. In this case, the scaling can be written as

$$\tau_E = f_1 n^{g_1} J_2^{g_2} B^{g_3} a^{g_4} J_5^{g_5} A^{g_6}. \tag{5}$$

For brevity, we will call scalings (4) and (5) subscalings. Different tokamak discharges can be referred to as similar discharges with respect to subscaling (4) or (5) if they have the same quasi-invariants included in this scaling. Similar discharges conform to subscalings with a smaller number of unknown parameters (power indexes). Thus, subscaling (4) contains three unknown power indexes (d_3, d_4, d_6) and, in subscaling (5), there are four unknown indexes.

The problem of constructing subscalings with the help of a large database, such that it includes the parameters of many shots from various tokamaks, can be formulated in two different ways. First, one may try to determine all six of the power indexes in subscalings (4) and (5). However, it should be kept in mind that this approach somewhat decreases the reliability of determining the power indexes of the quasi-invariants, because quasi-invariants differ only slightly between usual discharge modes peculiar to tokamaks. Consequently, in order to determine the desired power indexes reliably, it is necessary to use a database that contains enough information on "unusual" discharges, for which the values of quasi-invariants differ markedly.

The second approach is to select a class of similar shots from the general database and to construct a subscaling based on this class. Although this approach reduces the number of unknown parameters, it nevertheless yields subscalings that are valid only for a class of similar shots with the chosen values of quasi-invariants. In principle, the discrepancy between subscalings constructed from different classes should not be too

1063-780X/02/2802-0166$22.00

large, but it depends on how many unusual shots are in the selected classes.

With subscalings of the form of (4) or (5), the problem of modeling future tokamaks (e.g., the ITER device) by using the data from existing machines can be reformulated as follows. It is necessary to choose the parameters of the reference shot for a projected device and to determine the relevant values of quasi-invariants (3). Then, the problem of modeling reduces to carrying out experiments with discharges similar to the reference shot on existing tokamaks with different values of the parameters B, a, and A (or n, B, a, and A) and constructing subscalings of the form of (4) or (5) on the basis of the experimental data obtained.

2. As examples, let us consider subscalings that follow from the known ITER scalings constructed from the most complete database. First, we express the quantities n, P, I, and R in terms of quasi-invariants (3),

$$n = J_1 B/R, \quad P = J_2 aR, \quad I = J_5 a^2, \quad R = aA \tag{6}$$

and insert them into scaling (2). As a result, we arrive at subscaling (4) with

$$\begin{gathered} d_1 = c_1, \quad d_2 = c_2, \quad d_3 = c_1 + c_3, \\ d_4 = -c_1 + 2c_2 + c_4 + 2c_5, \\ d_5 = c_5, \quad d_6 = -c_1 + c_2 + c_6. \end{gathered} \tag{7}$$

Analogously, substituting expressions (6) for P, I, and R into scaling (2) yields subscaling (5) with

$$\begin{gathered} g_1 = c_1, \quad g_2 = c_2, \quad g_3 = c_3, \\ g_4 = 2c_2 + c_4 + 2c_5, \\ g_5 = c_5, \quad g_6 + c_2 + c_6. \end{gathered} \tag{8}$$

Let us derive subscalings for the L- and ELMy H-modes.

(i) In scaling (2) for the energy confinement time $\tau_{E,\,\mathrm{th}}^{\mathrm{L}}$ in the L-mode [1], the power indexes are equal to

$$c_1 = 0.4, \quad c_2 = -0.73, \quad c_3 = 0.03,$$
$$c_4 = 1.83, \quad c_5 = 0.96, \quad c_6 = 1.89.$$

Using relationships (7), we obtain the values

$$d_1 = 0.4, \quad d_2 = -0.73, \quad d_3 = 0.43,$$
$$d_4 = 1.89, \quad d_5 = 0.96, \quad d_6 = 0.76,$$

which yield

$$\tau_{E,\,\mathrm{th}}^{\mathrm{L}} = f_1 J_1^{0.4} J_2^{-0.73} B^{0.43} a^{1.89} J_5^{0.96} A^{0.76}. \tag{9}$$

Using relationships (8), we arrive at a subscaling with two quasi-invariants:

$$\tau_{E,\,\mathrm{th}}^{\mathrm{L}} = f_1 n^{0.4} J_2^{-0.73} B^{0.03} a^{2.29} J_5^{0.96} A^{1.16}. \tag{10}$$

(ii) In the IPB98(y, 2) scaling (2) for the energy confinement time $\tau_{E,\,\mathrm{th}}^{\mathrm{ELMy}}$ in the ELMy H-mode [1], the power indexes are equal to

$$c_1 = 0.41, \quad c_2 = -0.69, \quad c_3 = 0.15,$$
$$c_4 = 1.97, \quad c_5 = 0.93, \quad c_6 = 1.39.$$

Using these power indexes, we can readily obtain subscalings analogous to (9) and (10):

$$\tau_{E,\,\mathrm{th}}^{\mathrm{ELMy}} = f_1 J_1^{0.41} J_2^{-0.69} B^{0.56} a^{2.04} J_5^{0.93} A^{0.29}, \tag{11}$$

$$\tau_{E,\,\mathrm{th}}^{\mathrm{ELMy}} = f_1 n^{0.41} J_2^{-0.69} B^{0.15} a^{2.45} J_5^{0.93} A^{0.7}. \tag{12}$$

Since the quasi-invariants differ insignificantly between these modes, the dependence of the energy confinement time on the geometric dimensions of the device is of primary importance. This dependence is especially pronounced in subscalings (9) and (11), which contain three quasi-invariants. It is well known that $\tau_E \sim a^2$ for purely diffusive losses and $\tau_E \sim a$ for purely convective ones. In subscaling (9) for the L-mode, we have $d_4 = 1.89 < 2$. This indicates that convective losses play a significant role in the L-mode. In subscaling (11) for the H-mode, we have $d_4 = 2.04 > 2$, in which case the transport barrier that improves H-mode confinement completely prevents convective losses.

3. Now, we consider how the ITER-FEAT discharges can be modeled in existing tokamaks.

As a reference shot, we choose a planned ITER discharge with the parameters

$$R/a = 6.2\ \text{m}/2\ \text{m}, \quad B = 5.3\ \text{T}, \quad I = 15\ \text{MA},$$
$$P = 87\ \text{MW}, \quad n = 10^{20}\ \text{m}^{-3},$$

where P is the difference between the input power (including the α-particle power) and the radiation power. The quasi-invariants for this shot are equal to

$$J_1 = 11.7, \quad J_2 = 7, \quad J_5 = 3.75.$$

Let us analyze the possibility of modeling the reference shot in the JET tokamak with the parameters R/a = 3 m/1.1 m and B = 2.5 T. The parameters of a similar discharge in JET can be found from expressions (6): $n = 9.7 \times 10^{19}$ m^{-3}, P = 25 MW, and I = 4.4 MA. In pellet injection experiments in JET [2], the plasma density amounted to 9×10^{19} m^{-3}. The required power P = 25 MW and the required current I = 4.4 MA are also achievable in this tokamak. Hence, JET is a possible candidate for modeling discharges that are similar to the reference shot in terms of the above three quasi-invariants.

As for the possibility of modeling the reference ITER shot on the projected T-15M tokamak with the parameters R/a = 1.55 m/0.5 m and B = 2.0 T, the situation is different. The parameters of T-15M discharges similar to the reference shot should be as follows: $n = 15 \times 10^{19}$ m^{-3}, P = 5.3 MW, and I = 0.94 MA. We can

see that the required plasma density is unlikely to be achievable in T-15M, because, at a current of about $I \sim 1$ MA, Greenwald's formula for the maximum density gives $n_{Gr} = 13 \times 10^{19}$ m^{-3}.

4. If a subscaling of the form of (4) or (5) has been constructed, it might be expedient to express it in terms of the dimensionless parameters

$$\rho^*, \beta, \nu^*, d^*, q, A, \tag{13}$$

which were described in my earlier paper [3]. In order to analyze the difficulties arising in this way, we write out the following expressions for the quasi-invariants using the corresponding formulas of [3] and omitting the asterisk from parameters (13):

$$J_1 = nR/B = \beta^{0.5} A/d,$$
$$J_2 = P/(aR) = d^6 \beta^3 \nu/(q\rho^6 A^{3.5} \tau_E), \tag{14}$$
$$J_5 = I/a^2 = \beta^{2.5} d^9 \nu^2/(\rho^6 q^3 A^6).$$

Note that, in place of J_5, one can use the quasi-invariant q, which is better suited for an approach based on the dimensionless variables.

With allowance for the quasineutrality condition [4], the dimensionless scaling can be written as

$$B\tau_E = f\rho^{\alpha_1} \nu^{*\alpha_2} \beta^{\alpha_3} q^{\alpha_4} A^{\alpha_5}, \tag{15}$$

i.e, there are five independent parameters. However, since the parameter q is a quasi-invariant in the spirit of this article, scaling (15), in fact, contains four independent parameters. However, it is highly unlikely that the number of independent parameters can be further reduced with the help of quasi-invariants (14). The reason for this is the complicated dependence of these quasi-invariants on d, q, and τ_E. Of course, one may try to find quasi-invariants that depend on the dimensionless parameters in a simpler way than those used here. However, it is not *a priori* obvious that such quasi-invariants exist.

5. In conclusion, let us summarize the main results obtained in this paper. The disparity in the six main parameters entering the dimensional scalings for the energy confinement time of a tokamak plasma makes it possible to construct parameter combinations (quasi-invariants) that differ only slightly between different tokamaks. With these quasi-invariants, the number of independent parameters in the dimensional scaling can be reduced to three. As for the dimensionless scalings, they contain five main independent parameters by virtue of the quasineutrality condition. However, since one of the independent parameters, namely, q, is a quasi-invariant, the dimensionless scalings actually contain four independent parameters. It would hardly be possible to further reduce the number of independent parameters in dimensionless scalings.

REFERENCES

1. ITER Physics Basis, Nucl. Fusion, No. 11 (1999).
2. J. Ongena, in *Proceedings of the 28th EPS Conference on Controlled Fusion and Plasma Physics, Madejra, Portugal, 2001*, Invited Report.
3. Yu. N. Dnestrovskij, Fiz. Plazmy **25**, 115 (1999) [Plasma Phys. Rep. **25**, 97 (1999)].
4. B. B. Kadomtsev, Fiz. Plazmy **1**, 531 (1975) [Sov. J. Plasma Phys. **1**, 295 (1975)].

Translated by I. Kalabalyk

Plasma Physics Reports, Vol. 28, No. 2, 2002, pp. 169–170. Translated from Fizika Plazmy, Vol. 28, No. 2, 2002, pp. 191–192.

OBITUARY

In Memory of Vladimir Vladimirovich Alikaev (October 23, 1932–September 12, 2001)

Vladimir Vladimirovich Alikaev, an eminent Russian scientist and head of the Department of RF and Microwave Plasma Heating at the Nuclear Fusion Institute of the Russian Research Centre Kurchatov Institute, passed away on September 12, 2001 after an extended illness in his 69th year.

Alikaev was born October 23, 1932. After graduating from the Physics Department of Moscow State University in 1956, he began to work at the Kurchatov Institute in the laboratory headed by V.M. Glagolev. From the very beginning, his interests were related to both problems of the interaction of high-frequency fields with plasmas and plasma diagnostics. His first experimental works were aimed at studying the propagation of electromagnetic waves in a magnetized plasma and the related plasma instabilities. He was one of the first scientists in the Soviet Union to create a microwave interferometer for measuring the plasma density and successfully apply it to experimental investigations.

Alikaev's first works already showed him to be a competent experimentalist who was able to formulate an idea of the experiment and obtain reliable scientific results. He combined the talents of an eminently qualified physicist and an excellent engineer in the fields of electronics and plasma diagnostics. His exceptional abilities were recognized by Academician L.A. Artsimovich, who assigned Alikaev to the Research Institute of Radiophysics at Gorki (now, Nizhni Novgorod) in 1970. His mission there was to become acquainted with new high-power millimeter-wavelength microwave oscillators (gyrotrons), developed under the supervision of Academician Gaponov-Grekhov. Since then, a fruitful collaboration between Moscow and Nizhni Novgorod scientists on the development of the methods of electron cyclotron resonance (ECR) plasma heating and the improvement of gyrotrons has taken place.

In order to understand Alikaev's contribution to this field of research, we recall that, at the beginning of controlled fusion research, attention was primarily focused on direct RF heating of the plasma ion component. Alikaev was one of the first to recognize the importance of auxiliary heating (independent of ohmic heating) of the plasma electron component in tokamaks with the aim of investigating how the plasma thermal insulation depends on the experimental conditions. He put much effort into the implementation of this idea.

The pioneering attempts of using gyrotrons encountered many difficulties, which were overcome, first of all, owing to Alikaev. Experiments carried out under his leadership in the TM-3 and T-10 tokamaks demonstrated that it was in fact possible to use gyrotrons in controlled fusion experiments. At present, these high-power millimeter-wavelength oscillators are widely used in controlled fusion research. However, gyrotrons have another important application: they can be used to generate electric current in plasmas in order to both maintain plasma equilibrium and modify the current density profile with the aim of stabilizing dangerous helical perturbations in tokamaks. The ECR current drive became the main problem with which Alikaev was occupied for the last decade. A gyrotron complex for plasma heating and long-duration current drive is one of the main components in the ITER project. Alikaev contributed greatly to the development of continuously operating 170-GHz 1-MW gyrotrons, which are necessary for ITER.

1063-780X/02/2802-0169$22.00 © 2002 MAIK "Nauka/Interperiodica"

The great contributions of Alikaev to the development of methods for plasma heating did not go unrewarded. In 1983, he and his colleagues were awarded the State Prize.

Works by Alikaev have received world-wide recognition. It is fair to say that he is the founder of the practical implementation of ECR plasma heating and noninductive current drive in tokamaks.

Vladimir Vladimirovich Alikaev was a purposeful scientist; an excellent organizer; and an extremely reliable, modest, friendly, and attentive man. His memory will always remain in the hearts of all those who were lucky enough to know him and work with him and those with whom he generously shared his experience and knowledge.

Yu. I. Arsen'ev, V. A. Belyakov, A. A. Borshchegovskiĭ, E. P. Velikhov, A. V. Gaponov-Grekhov, V. A. Glukhikh, V. E. Golant, L. G. Golubchikov, G. G. Denisov, A. S. Dochenkov, Yu. N. Dnestrovskij, G. A. Eliseev, V. I. Il'in, V. M. Korzhavin, V. I. Kurbatov, A. G. Litvak, V. S. Mukhovatov, V. E. Myasnikov, G. E. Notkin, V. V. Parail, I. A. Popov, K. A. Razumova, I. N. Roĭ, I. M. Roĭfe, N. N. Semashko, A. A. Skovoroda, V. P. Smirnov, Yu. A. Sokolov, V. S. Strelkov, E. M. Taĭ, G. N. Tilinin, A. S. Trubnikov, O. G. Filatov, V. A. Flyagin, N. S. Cheverev, and V. D. Shafranov

Plasma Physics Reports, Vol. 28, No. 2, 2002, pp. 83–93. Translated from Fizika Plazmy, Vol. 28, No. 2, 2002, pp. 99–109.

TOKAMAKS

Transport Barrier as a Bifurcation of the Equilibrium of a Tokamak Plasma

V. I. Ilgisonis and Yu. I. Pozdnyakov

Institute of Nuclear Fusion, Russian Research Centre Kurchatov Institute, pl. Kurchatova 1, Moscow, Russia

Received August 23, 2001

Abstract—The phenomenon of the internal transport barrier in a tokamak plasma is interpreted as a bifurcation of the plasma equilibrium. An expression describing the change in the plasma pressure due to the buildup of the barrier is derived as a functional dependent on the parameters of the original plasma equilibrium and the plasma rotation velocity within the barrier. This expression is applied to a circular cross section tokamak, specifically, the T-10 device. © *2002 MAIK "Nauka/Interperiodica".*

1. INTRODUCTION

The progress achieved during the last 15 years in magnetic fusion research is mainly associated with the so-called improved confinement regimes of tokamak operation, among which we should, first of all, mention the H-mode and its modifications and regimes with internal transport barriers (ITBs). Beginning with a paper by Wagner [1], improved confinement regimes have been actively studied in experiments, so that, at present, they are attainable in virtually all existing tokamaks. The characteristic feature of these regimes is the appearance of a fairly narrow (localized in the minor radius) layer within which the main plasma parameters (the temperature T and/or density n) change sharply. This layer, which is referred to as a "barrier zone," can occur either at the edge of the plasma column [an external transport barrier (ETB), typical of the H-mode] or inside the hot plasma region (an ITB; see, e.g., Fig. 1 [2]). Although the physical mechanisms for the buildup of internal and external barriers are likely to be very similar, we will restrict ourselves to analyzing ITBs and will not consider the possible role of atomic processes, which should be taken into account in the analysis of peripheral effects.

An intrinsic property of transport barriers that has been definitely established is the generation of a fairly strong radial electric field in the barrier zone, resulting in observable macroscopic plasma rotation (see Fig. 2, borrowed from the paper by Synakowski [3]).

The term "transport barrier" may be illustrated by the following simple considerations. It is usually assumed that transport fluxes are linearly related to the temperature and/or density gradients. Consequently, if these gradients become large in a certain zone, then the conservation of transport fluxes indicates a sharp reduction in the corresponding transport coefficients in this zone. This is what is meant by the term transport barrier. Among the various theoretical speculations, the following concept [4] is now considered to be the dominant one: tokamak transport is anomalous, and the sheared plasma rotation under the action of the electric field in the barrier zone leads to the decoupling of the perturbation modes, thereby lowering the level of plasma turbulence and, accordingly, reducing the transport coefficients. In this paper, we will not discuss the transport mechanism in the barrier zone. Note only that the basic assumption regarding the linear dependence of transport fluxes on the gradients of the main physical parameters is not self-evident. On the other hand, the appearance of an ITB as a narrow layer with large gradients of the plasma parameters has clearly been established in experiments; moreover, the ITBs exist for a long period of time. The latter indicates that a plasma configuration with an ITB should be in an MHD equilibrium; otherwise, fast MHD processes would destroy the configuration on a time scale of about several Alfvén times. Here, the term "MHD equilibrium" is used in a generalized sense, i.e., with allowance for possible macroscopic plasma rotation.

An important property of the equilibrium of a plasma with an ITB can be revealed by analyzing the buildup of the barrier, because the scenarios for the development of transport barriers in different tokamaks are very similar. After a tokamak discharge has been initiated, the plasma evolves into a steady (equilibrium) state. Then, the plasma is exposed to an external local action (e.g., external heating) and, under certain conditions, makes a fairly rapid transition to a new equilibrium state with an ITB. The plasma can be affected in different ways, specifically, by neutral beam injection, pellet injection, RF heating, and even ECR heating. To a certain extent, the parameters of the new equilibrium state depend on the way in which the plasma is affected (the physical meaning of this dependence will be clarified below). However, a more important point is that the above transition is not possible for any arbitrary initial state. It is, in particular, for this reason that, despite the 50-year history of magnetic fusion research, improved

1063-780X/02/2802-0083$22.00

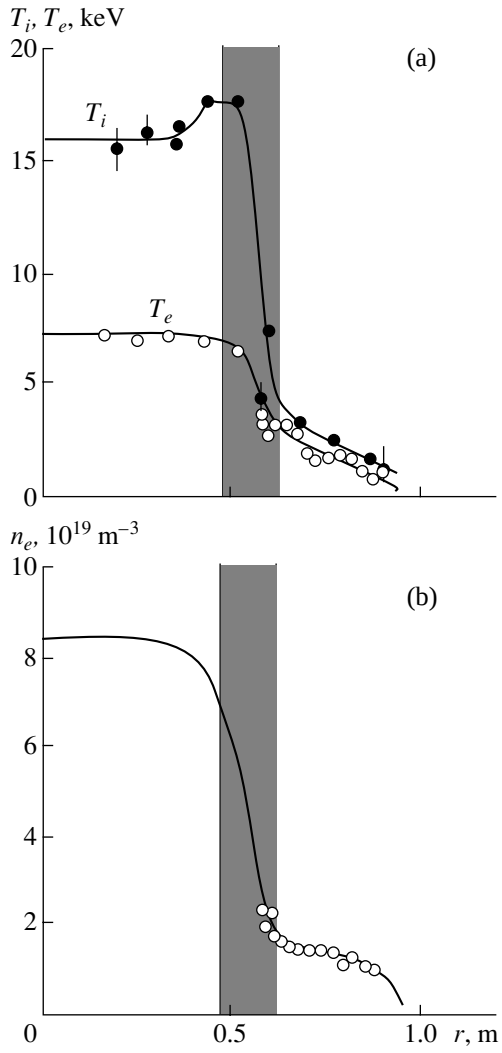

Fig. 1. Radial profiles of (a) the ion and electron temperatures and (b) electron density in JT-60. The barrier zone is hatched.

confinement regimes have been discovered only recently. The intensity of the external action that causes the plasma to undergo a transition to a new state with an ITB should, as a rule, exceed a certain threshold level, which is determined by the initial plasma state and by the external action itself. This situation is very similar to the classical example of the bifurcation of the equilibrium of a weight on an resilient rod with fixed ends (Fig. 3), in which case there are only two possible equilibrium states (while the intermediate equilibrium states are absent) and the transition from one equilibrium state to another can only be triggered by an external action that is strong enough to deform (bend) the rod.

It should be noted that, although the idea of interpreting the formation of transport barriers as a bifurcation of plasma equilibrium is generally not accepted, this assumption is rather straightforward and has already been discussed in the literature. However, the question of which of the many physical quantities characterizing the plasma equilibrium undergo the bifurcation remains open. Undoubtedly, sharp variations of the electric potential in the barrier zones have a direct relationship to the phenomenon of transport barriers. That is why, beginning with papers [5, 6], attempts were made to describe L–H transitions in the context of the bifurcation of the radial electric field (and, accordingly, the plasma rotation velocity). In turn, Hinton [7] explained the L–H transition in terms of the energy lifetime, taking into account the specific dependence of the turbulent thermal diffusivity on the shear of the poloidal rotation velocity, which was assumed to be neoclassical. It seems, however, that the logical approaches of these three papers are not quite adequate for explaining the ITB phenomenon. First, it is well known that, in the hot plasma core, the poloidal plasma rotation should be fairly rapidly damped by neoclassical viscous effects. Second, recent T-10 experiments on the formation of

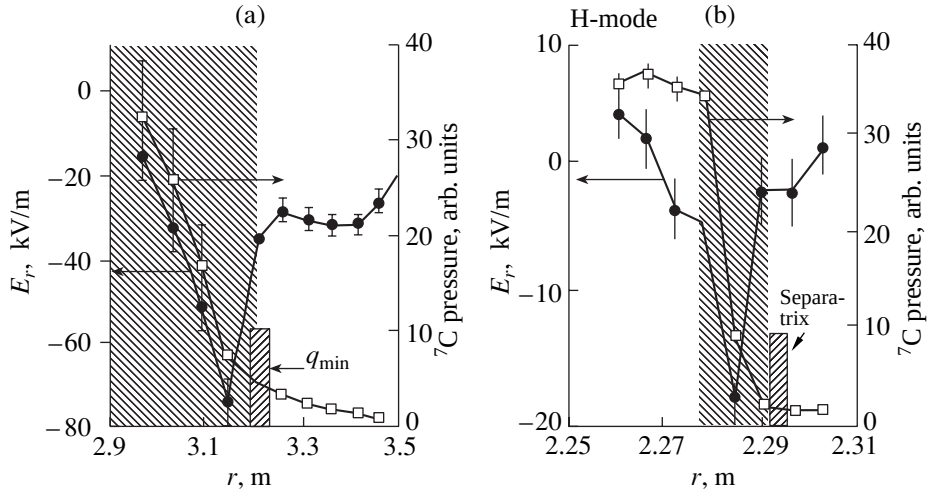

Fig. 2. Radial profiles of the radial electric field E_r and carbon pressure within (a) an ITB in TFTR and (b) an ETB in DIII-D.

ITBs by ECR heating [8] showed that, *after* the ITB has been formed and, accordingly, a characteristic bend has appeared in the temperature profile in the barrier zone (Fig. 4a), the radial electric field (and, accordingly, the plasma rotation velocity) again decreases (Fig. 4b, curve *3*). However, under these conditions, the shape of the temperature profile shows that the barrier continues to exist.

The foregoing allows us to draw the following conclusion: it is the thermodynamic functions (in the cited T-10 experiments, it is the plasma temperature, because the plasma density remains unchanged during ECR heating) that bifurcate during the transition to an improved confinement regime, while the plasma rotation generally acts as a trigger for this transition (an analogue of the bending deformation in the example shown in Fig. 3). In order for the plasma to undergo a transition to a new equilibrium state, the plasma should start to rotate; in MHD theory, the plasma rotation reflects an imbalance in the forces within the barrier zone under the external action. However, the specific functional dependence of the rotation velocity on the main plasma parameters seems to be of little significance. To pursue the analogy with the above mechanical system, we must specify the reference parameters that are conserved during the transition (these parameters are analogues of the fixed ends of the rod and its constant length in the example shown in Fig. 3). Here, we assume that the role of the reference parameters is played by the magnetic configuration or, more precisely, by the structure of the magnetic surfaces. At present, there is no experimental evidence that the buildup of the transport barrier leads to a more or less distinct restructuring of the magnetic configuration, so, in our analysis, it is assumed to be unchanged. (As will be shown in Section 3, we require only the invariance of some integral characteristics of the magnetic surfaces, while the surfaces themselves can be locally deformed.)

Our paper is organized as follows. Section 2 presents an abbreviated derivation of the equilibrium MHD equations for a steadily moving plasma. In Section 3, a general expression for the change in the plasma pressure at the inner boundary of the barrier zone is obtained under the assumption that the structure of the magnetic surfaces remains unchanged during the transition to a state with an ITB. In Section 4, a particular version of the general expression is deduced for a circular cross section tokamak and is tested against the data from T-10 experiments. In the conclusion, we summarize the main results obtained in this study.

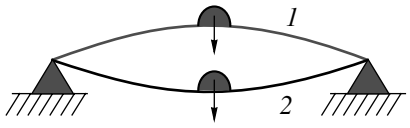

Fig. 3. Classical example of the bifurcation of the equilibrium of a weight on an elastic nonstretchable rod with fixed ends.

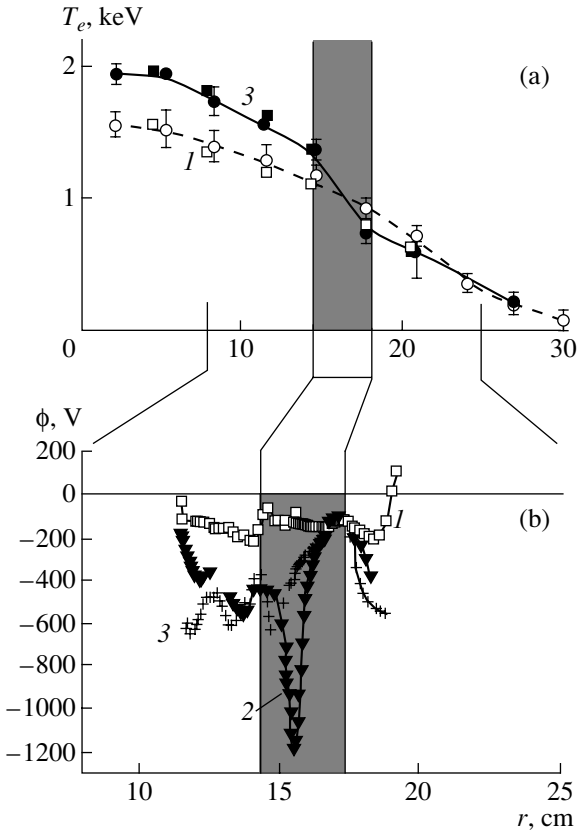

Fig. 4. Radial profiles of (a) the electron temperature and (b) plasma potential within an ITB in T-10: (*1*) before the barrier formation, (*2*) during the buildup of the barrier, and (*3*) after the formation of the barrier.

2. EQUILIBRIUM EQUATIONS

Here, we outline the derivation of MHD equilibrium equations for a rotating plasma. In a steady state, the ideal one-fluid MHD equations have the following form (for simplicity, we normalize the magnetic field by multiplying it by the factor $1/(2\sqrt{\pi})$):

$$\rho(\mathbf{v}\cdot\nabla)\mathbf{v} + \nabla p + \mathbf{B}\times[\nabla\times\mathbf{B}] = 0, \quad (1)$$

$$\nabla\cdot\mathbf{B} = 0, \quad (2)$$

$$\nabla\cdot(\rho\mathbf{v}) = 0, \quad (3)$$

$$\nabla\times[\mathbf{v}\times\mathbf{B}] = 0. \quad (4)$$

Equations (1)–(4) should be supplemented with the equation for the plasma pressure; this will be done below.

It is natural to describe an axisymmetric tokamak configuration in cylindrical coordinates $\{r, z, \zeta\}$ such that $(\partial/\partial\zeta) \longrightarrow 0$, where ζ is the toroidal angle. As usual, we consider a tokamak magnetic configuration with nested magnetic surfaces $\psi(r, z) = \text{const}$ defined by $\mathbf{B} \cdot \nabla\psi = 0$, in which case the tokamak magnetic field satisfying Eq. (2) has the form

$$\mathbf{B} = \mathbf{B}_p + \mathbf{B}_t = \nabla\psi \times \nabla\zeta + F(r, z)\nabla\zeta. \quad (5)$$

Accordingly, the current density and the square of the magnetic field are equal to

$$\nabla \times \mathbf{B} = -\Delta^*\psi\nabla\zeta + \nabla F \times \nabla\zeta,$$

$$B^2 = \frac{|\nabla\psi|^2}{r^2} + \frac{F^2}{r^2}.$$

Here and below, the subscripts p and t refer to the poloidal and toroidal components of the quantities and

$$\Delta^*(\ldots) = r^2\nabla \cdot \left(\frac{\nabla(\ldots)}{r^2}\right),$$

where ψ is the poloidal magnetic field flux and F is the poloidal current through the central hole of the toroidal magnetic surface with a given value of ψ. Below, we will see that, unlike in the case of static equilibrium, the poloidal current F is not necessarily a function of the magnetic surface.

The general expression for the plasma rotation velocity can be obtained from Eq. (3) in an analogous way [as in Eq. (5) for the magnetic field, we can discard in Eq. (3) possible δ-shaped solutions localized in the vicinity of the rational magnetic surfaces, which is justified by the assumption that the velocity field is sufficiently smooth]:

$$\mathbf{v} = \frac{\kappa}{\rho}[\nabla\psi \times \nabla\zeta] + \nu r^2\nabla\zeta, \quad (6)$$

where $\kappa = \kappa(\psi)$ and ν is the angular frequency of the toroidal plasma rotation. The poloidal rotation velocity is determined by the quantity κ:

$$v_p = \frac{\kappa}{\rho}B_p = \sqrt{\frac{\kappa^2}{\rho}}c_{Ap},$$

where c_{Ap} is the absolute value of the Alfvén speed in terms of the poloidal magnetic field; in other words, the quantity κ determines the Mach number $M_A = \kappa/\sqrt{\rho} = v_p/c_{Ap}$. Under the usual assumption $v < c_A$, the dimensionless parameter κ^2/ρ is smaller than unity. Integrating Eq. (4) gives the relationship

$$\mathbf{v} \times \mathbf{B} = c\nabla\phi, \quad (7)$$

where the quantity ϕ has the meaning of the electric field potential (in which case we can readily see that $\phi = \phi(\psi)$ and c is the speed of light. We introduce the quantity $\omega = -c\phi'$ (here and below, the prime denotes the derivative with respect to ψ) and take into account relationship (7) in order to rewrite the plasma rotation velocity (6) in the form

$$\mathbf{v} = \frac{\kappa}{\rho}\mathbf{B} + \omega r^2\nabla\zeta. \quad (8)$$

A comparison between expressions (6) and (8) yields

$$\nu = \left(\omega(\psi) + \frac{\kappa(\psi)}{\rho r^2}F\right). \quad (9)$$

Expression (8) implies that, in the absence of the electric field ($\omega = 0$), the plasma can only undergo a force-free rotation along the magnetic field lines; this rotation is described by the term proportional to $\sim\kappa$ in expression (8). From expression (9), we can see that, for $\kappa = 0$, the electric field determines only the toroidal rotation ($\nu|_{\kappa=0} = \omega$). Hence, in contrast to the widely held opinion based on the standard neoclassical theory, in ideal magnetohydrodynamics, the angular frequencies of the plasma rotation in both the poloidal and the toroidal directions cannot be uniquely determined by the electric field in a conventional MHD description of the plasma rotation in terms of the two flux-surface functions ω and κ.

The force balance equation in vector form (1) is equivalent to three scalar equations. The projection of Eq. (1) onto the direction of $[\nabla\zeta]$ gives the first equation, which characterizes the poloidal current,

$$F - \kappa\nu r^2 = I(\psi),$$

so that, with allowance for expression (9), we obtain

$$F = \frac{I + \kappa\omega r^2}{1 - \frac{\kappa^2}{\rho}}, \quad (10)$$

where $I(\psi)$ is a flux-surface function. For a purely toroidal ($\kappa = 0$) or a purely poloidal ($\nu = 0$) rotation, the poloidal current F is also a flux-surface function, $F = I(\psi)$, as in the case of static equilibrium. In particular, for a purely poloidal ($\nu \equiv 0$) rotation, expression (9) gives the following functional dependence of the plasma density:

$$\rho = \frac{f(\psi)}{r^2}.$$

Simple kinetic considerations show that, in static (rotation-free) equilibrium, the plasma density is a flux-surface function. The same conclusion can also be drawn from the multifluid hydrodynamic model, which possesses a limiting transition to the one-fluid MHD model (see, e.g., [9]). That is why, in ideal MHD, a purely poloidal (without singularities and discontinuities) plasma rotation in a narrow plasma layer localized in the minor radius is physically impossible.

The projection of Eq. (1) onto the radial direction gives the second equation, which relates the plasma pressure to the plasma rotation parameters:

$$\left(\frac{\partial p}{\partial r}\right)_\psi + \rho\frac{\partial}{\partial r}\left(\frac{\kappa^2 B^2}{2\rho^2} - \frac{\omega^2 r^2}{2}\right)_\psi = 0. \qquad (11)$$

The third equation is an analogue of the Grad–Shafranov equation for the function ψ:

$$\left(1 - \frac{\kappa^2}{\rho}\right)\Delta^*\psi + r^2\left(\frac{\partial p}{\partial \psi}\right)_r + F\left(\frac{\partial F}{\partial \psi}\right)_r - \kappa\nabla\psi\cdot\nabla\frac{\kappa}{\rho} + \rho\frac{\partial}{\partial\psi}\left(\frac{\kappa^2}{2\rho^2}|\nabla\psi|^2\right)_r = 0. \qquad (12)$$

In the absence of poloidal rotation, $\kappa = 0$, Eq. (12) is similar in structure to the conventional Grad–Shafranov equation; the only difference is that, in Eq. (12), the role of the derivative of the plasma pressure with respect to ψ is played by the partial derivative $(\partial/\partial\psi)_r$.

Equations similar to Eqs. (10)–(12) have already been used in the literature. In particular, Hameiri [10] considered the adiabatic case mentioned below, and very similar equations were obtained by Tasso and Throumoulopolus [11]. Here, we again emphasize that Eq. (11) can be easily integrated in the following three cases.

(i) The plasma density is a flux-surface function, $\rho = \rho(\psi)$. This case describes a steady incompressible plasma flow with velocity (6). Introducing the plasma temperature through the relationship $T = p/\rho$, we obtain from Eq. (11) the following expression:

$$T = \frac{p(\psi, r)}{\rho} = T_0(\psi) - \frac{\kappa^2}{2\rho^2}B^2 + \frac{\omega^2 r^2}{2}, \qquad (13)$$

where the quantity T_0 is a flux-surface function, which has the meaning of the temperature of a rotation-free plasma.

(ii) The plasma temperature is a flux-surface function, $T = T(\psi)$. This case corresponds to a practically important situation of high thermal conductivity along the magnetic field. In this case, Eq. (11) yields the following implicit expression for the plasma density:

$$\rho(\psi, r) = \rho_0(\psi)\exp\left(\frac{\omega^2 r^2}{2T} - \frac{\kappa^2 B^2}{2\rho^2 T}\right),$$

where ρ_0 is a flux-surface function, which has the meaning of the density of a rotation-free plasma.

(iii) The plasma entropy is a flux-surface function, $S = S(\psi) \sim p/\rho^\gamma$, where γ is the adiabatic index. Introducing the specific enthalpy h, we arrive at the following relationships for the thermodynamic quantities:

$$\rho = \left(\frac{h}{\alpha S}\right)^{\alpha - 1}, \quad p = \left(\frac{h}{\alpha S^{\frac{\alpha-1}{\alpha}}}\right)^\alpha,$$

$$T = \frac{h}{\alpha} \quad \left(\alpha = \frac{\gamma}{\gamma - 1} > 1\right).$$

From Eq. (11), we obtain

$$h = H(\psi) - \frac{\kappa^2}{2\rho^2}B^2 + \frac{\omega(\psi)^2 r^2}{2},$$

where H is a function of only ψ and has the meaning of the enthalpy of a rotation-free plasma.

We can see that the equilibrium configuration is determined by five flux-surface functions: one of them, $I(\psi)$, characterizes the effective poloidal current; another two, $\omega(\psi)$ and $\kappa(\psi)$, determine the steady-state velocity field; and the remaining two—$\rho(\psi)$ and $T_0(\psi)$ in case (i), or $\rho_0(\psi)$ and $T(\psi)$ in case (ii), or $S(\psi)$ and $H(\psi)$ in case (iii)—describe the thermodynamic plasma state. In case (i), the plasma pressure p is explicitly determined by expression (13); in cases (ii) and (iii), the functional dependence of p is described by transcendental equations.

In the Introduction, we pointed out that, when the ITB is formed by RF or even microwave (ECR) heating (as is the case in, e.g., the cited T-10 experiments), the plasma density does not change during the transition to a new equilibrium state. Hence, the plasma that starts to evolve from the static state with $\rho = \rho(\psi)$ undergoes a transition to a new state corresponding to case (i). It is this case that will be the subject of further analysis.

3. PRESSURE JUMP ACROSS THE ITB ZONE

The concept under discussion implies the buildup of an ITB in a comparatively narrow layer localized in the ψ coordinate: $\psi_1 < \psi < \psi_2$, where ψ_1 and ψ_2 are the outer and inner boundaries of the barrier (see Fig. 5, which schematically illustrates the formulation of the problem). As a result of bifurcation, the pressure profile in the barrier zone changes substantially: in Fig. 5, the dashed curve, which refers to the initial equilibrium state (below, the quantities corresponding to this state will be marked by the subscript i), evolves into the solid curve. In the initial and final states, the pressure gradients are different only inside the barrier zone, in which the plasma rotates in the poloidal direction (see the dotted curve in Fig. 5).

Let us calculate the pressure jump Δp at the inner boundary $\psi = \psi_2$ of the barrier after the bifurcation. It turns out that this can be done by using only the integral consequences of the equilibrium equations rather than by solving these equations exactly.

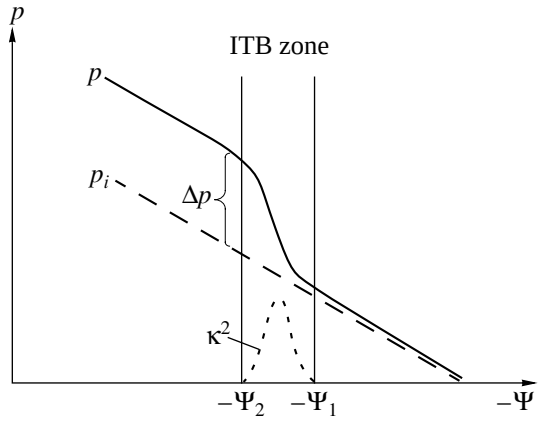

Fig. 5. Schematic representation of the barrier zone. The solid curve illustrates the change in the pressure profile after the development of the barrier, and the dashed curve refers to the initial pressure profile. The poloidal plasma rotation is localized in the barrier zone (the dotted curve).

We multiply the initial (before the bifurcation) static equilibrium equation

$$\Delta^*\psi + r^2 p_i' + F_i F_i' = 0 \tag{14}$$

by r^{-2} and integrate the resulting equation over the volume $V = V(\psi)$ of the toroidal region enclosed by the instantaneous flux surface $\psi = \text{const}$ with the cross-sectional area $S = S(\psi)$. As a result, we obtain

$$\oint_{S(\psi)} \frac{\nabla\psi}{r^2}\cdot d\mathbf{S} + \int_{\psi_0}^{\psi}\left(p_i' + \left(\frac{F_i^2}{2}\right)'\left\langle\frac{1}{r^2}\right\rangle\right)V'd\tilde{\psi} = 0, \tag{15}$$

where the angular brackets denote averaging over the toroidal flux surface $\psi = \text{const}$:

$$\langle f(\psi, r)\rangle = -\frac{1}{V'}\oint_{S(\psi)}\frac{f(\psi, r)dS}{|\nabla\psi|}. \tag{16}$$

The minus sign in formula (16) reflects the way in which the coordinate ψ is measured from the z-axis: at the magnetic axis, the quantity ψ is maximum and is equal to ψ_0 (this corresponds to $V' < 0$). With the poloidal magnetic field flux thus defined, we have $\langle f(\psi)\rangle = f(\psi)$ and

$$\int_{V(\psi)} f d\tilde{V} = \int_{\psi_0}^{\psi}\langle f\rangle V' d\tilde{\psi}.$$

On the other hand, by definition, we can write

$$\langle B_p^2\rangle = -\frac{1}{V'}\oint_{S(\psi)}\frac{|\nabla\psi|^2}{r^2}\frac{dS}{|\nabla\psi|} = -\frac{1}{V'}\oint_{S(\psi)}\frac{|\nabla\psi|}{r^2}dS. \tag{17}$$

Substituting this relationship into Eq. (15) yields the following expression for the derivative of the pressure:

$$\langle p_i\rangle' = p_i' = -\frac{1}{V'}(\langle B_p^2\rangle V')' - \frac{1}{2}(F_i^2)'\left\langle\frac{1}{r^2}\right\rangle. \tag{18}$$

Now, we apply the same procedure to calculate the derivative $\langle p\rangle'$ in the new equilibrium state (after the bifurcation). In the case $\rho = \rho(\psi)$, the Mach number $M_A = v_p/c_{Ap} = \kappa/\sqrt{\rho}$ is also a flux-surface function, and the new equilibrium state is described by Eq. (12), which now becomes

$$\begin{aligned}(1 - M_A^2)\Delta^*\psi + r^2\left(\frac{\partial p}{\partial\psi}\right)_r + F\left(\frac{\partial F}{\partial\psi}\right)_r \\ + M_A^2\left(\frac{\partial}{\partial\psi}\frac{|\nabla\psi|^2}{2}\right)_r = 0.\end{aligned} \tag{19}$$

Note that expression (13) makes it possible to relate the ψ-derivative of the averaged pressure, $\langle p\rangle'$, to the averaged partial derivative of the pressure, namely,

$$\begin{aligned}\left\langle\frac{\partial p}{\partial\psi}\right\rangle = \langle p\rangle' - \frac{\rho\omega^2}{2}\langle r^2\rangle' + \frac{M_A^2}{2}\langle B_p^2\rangle' \\ - \frac{M_A^2}{2}\left\langle\frac{\partial}{\partial\psi}B_p^2\right\rangle + \left(\frac{M_A^2}{2}\left\langle\frac{F^2}{r^2}\right\rangle\right)' - \left\langle\frac{\partial}{\partial\psi}\frac{F^2}{r^2}\right\rangle.\end{aligned} \tag{20}$$

We integrate Eq. (19) over the volume of the barrier zone. Taking into account the fact that, at the boundaries of the barrier, the plasma poloidal rotation velocity vanishes (Fig. 5) and, accordingly, $M_A|_{\psi = \psi_{1,2}} = 0$, we obtain

$$\begin{aligned}\oint_{S(\psi_1)}\frac{1}{V'}\frac{\nabla\psi\cdot d\mathbf{S}}{r^2} + \oint_{S(\psi_2)}\frac{1}{V'}\frac{\nabla\psi\cdot d\mathbf{S}}{r^2} \\ + \int_{\psi_1}^{\psi_2} d\psi\left(\frac{V''}{V'}(1 - M_A^2)\langle B_p^2\rangle - M_A^2\langle B_p^2\rangle'\right. \\ \left. + \left\langle\frac{\partial p}{\partial\psi}\right\rangle + \frac{M_A^2}{2}\left\langle\frac{\partial B_p^2}{\partial\psi}\right\rangle + \left\langle\frac{\partial}{\partial\psi}\frac{F^2}{2r^2}\right\rangle\right) = 0.\end{aligned} \tag{21}$$

Our conceptual assumption that the structure of the magnetic surface remains unchanged during the bifurcation is formalized as the conservation of the flux-surface functions $V = V_i$ and $\langle B_p^2\rangle = \langle B_{pi}^2\rangle$.

We insert Eq. (20) into Eq. (21) and combine the resulting equation with expressions (10), (17), and (18)

to obtain the following formula for the pressure jump at the inner boundary of the barrier:

$$\Delta p(\psi_2) = \int_{\psi_1}^{\psi_2} \frac{d}{d\psi}(\langle p\rangle - p_i)d\psi$$

$$= \int_{\psi_1}^{\psi_2}\left(\frac{\rho\omega^2}{2}\frac{\langle r^2\rangle'}{1-M_A^2} - \frac{M_A^2}{2}W' + \left[\frac{1}{2}\left\langle\frac{F_i^2 - F^2}{r^2}\right\rangle' \right.\right. \quad (22)$$

$$\left.\left. + \frac{1-M_A^2}{2}\left\langle\frac{1}{r^2}\right\rangle'\left(\left(\frac{I}{1-M_A^2}\right)^2 - F_i^2\right)\right]\right)d\psi = 0.$$

Here, following [12], we introduced the notation $W = \langle 2p_i + B_i^2\rangle$ and made use of the fact that, since there is no plasma rotation on the outside of the barrier zone, the pressures in the initial and final states are there the same, $\Delta p(\psi \le \psi_1) = 0$. The bifurcation gives rise to an ITB when $\Delta p(\psi_2) > 0$. Consequently, formula (22) implies that the presence of a magnetic well ($W'_\psi < 0$) in the initial state should favorably affect the buildup of the barrier. In the next section, we will analyze expression (22) in more detail for a tokamak with a relatively large aspect ratio and nearly circular cross sections of the magnetic surfaces.

4. CIRCULAR CROSS SECTION TOKAMAK

Let us apply expression (22) to a tokamak with a sufficiently large aspect ratio, $R/a_b \gg 1$ (where R and a_b are the major and minor radii of the tokamak). Magnetic surfaces with circular cross sections can be specified as [13]

$$\psi = \psi(a)\colon r \approx R + \Delta(a) - a\cos\theta, \quad z \approx a\sin\theta, \quad (23)$$

where the toroidal flux surface label a has the meaning of the characteristic minor radius of the flux surface, θ is the poloidal angle, and Δ is the shift of the center of the flux surface with respect to the magnetic axis. In the approximation at hand, we as usual assume that $\Delta(a) \sim a^2/R$. Having specified the geometric parameters, we can calculate the averaged quantities $\langle r^{\pm 2}\rangle$ in formula (22):

$$\langle r^2\rangle \approx R^2\left(1 + \frac{3}{2}\left(\frac{a}{R}\right)^2 + \frac{2\Delta}{R} + \frac{a}{R}\dot\Delta\right),$$
$$\left\langle\frac{1}{r^2}\right\rangle \approx \frac{1}{R^2}\left(1 - \frac{a}{R}\dot\Delta - 2\frac{\Delta}{R} + \frac{1}{2}\left(\frac{a}{R}\right)^2\right), \quad (24)$$

where a superior dot denotes the derivative with respect to a. In expressions (24), we neglect the terms on the order of $\sim(a_b/R)^3$ and higher but keep the second-order term in a_b/R (because these expressions contain no linear terms). Hence, in order of magnitude, we have

$$\langle r^2\rangle^{\cdot} \sim a, \quad \langle r^{-2}\rangle^{\cdot} \sim \frac{a}{R^4},$$

The signs of these quantities depend on the particular equilibrium conditions and, therefore, are not fully deterministic. Note that, as will be shown below, $\langle r^2\rangle^{\cdot} < 0$, and $\langle r^{-2}\rangle^{\cdot} > 0$ for "conventional" equilibrium states with customary parameter distributions. In the expression for the magnetic well, it is sufficient to retain only the lowest order terms in the expansion in powers of the inverse aspect ratio. Introducing the toroidal current J and the safety factor q through the relationships

$$J = -\frac{a}{R}\dot\psi,$$

$$q = \frac{F_i}{J}\frac{a^2}{R^2},$$

we can readily obtain the following expression for the magnetic well:

$$\dot W = F_i^2\left(\left\langle\frac{1}{r^2}\right\rangle^{\cdot} - \frac{2a}{q^2R^4}\right) \approx \frac{2F_i^2 a}{R^4}\left(1 - \frac{1}{q^2} + \beta_p - \frac{R}{a}s\dot\Delta\right), \quad (25)$$

where $\beta_p = -a^3\dot p J^{-2}$ is the so-called poloidal beta and $s = a\dot q/q$ is the shear. In deriving expression (25), we used the static equilibrium equation (14), which determines the derivatives $\dot J$ and $\ddot\Delta$ through two highest orders in the expansion in powers of a_b/R, namely,

$$J\dot J = -\frac{a^2}{R^2}F_i\dot F_i - a^2\dot p,$$
$$\ddot\Delta R \approx -1 - 2\beta_p + \frac{\dot\Delta R}{a}(2s-3). \quad (26)$$

In order to estimate the terms in the square brackets of expression (22), we turn to the virial theorem [14], which will be formulated and proved for an equilibrium state with a steady plasma flow in the Appendix. We start by noting that, according to our concept, the plasma pressure gradient outside the barrier zone does not change:

$$p(a \ge a_1) = p_i,$$
$$p(a \le a_2) = p_i + \Delta p. \quad (27)$$

Consequently, under the assumption that the magnetic surfaces remain unchanged, the quantity FF' also does not change:

$$F^2\big|_{a\le a_2} = I^2(a \le a_2) = F_i^2(a \le a_2) - c_2,$$
$$F^2\big|_{a\ge a_1} = I^2(a \ge a_1) = F_i^2(a \ge a_1) + c_1. \quad (28)$$

The ITB builds up when $c_{1,2} > 0$. The virial theorem relates the increment in pressure to the constants $c_{1,2}$. To see this, we use the formula

$$\int_{V_b}\left(3p + \frac{B^2}{2} + \rho v^2\right)dV = \oint\left\{\left(p + \frac{B^2}{2}\right)\mathbf{r}\cdot d\mathbf{S} + \rho(\mathbf{v}\cdot\mathbf{r})\mathbf{v}\cdot d\mathbf{S} - (\mathbf{B}\cdot\mathbf{r})\mathbf{B}\cdot d\mathbf{S}\right\}, \quad (29)$$

where $\mathbf{r}$ is the position vector drawn from the origin of the coordinates. The volume integral on the left-hand side is taken over the entire plasma volume V_b, first, for the initial equilibrium state and, then, for a state with a fully developed plasma rotation in the barrier zone. We take into account the relationships $\mathbf{v}\cdot d\mathbf{S} = 0$ and $\mathbf{B}\cdot d\mathbf{S} = 0$, which hold on the magnetic surfaces, and neglect the contribution of the barrier zone to the volume integral (this contribution is proportional to $\sim\Delta a/a_b$, where $\Delta a = a_1 - a_2$). As a result, we obtain

$$c_1 + c_2 = 6\Delta p R^2. \quad (30)$$

The relationship between the constants c_1 and c_2 can be found under the assumption that, during the bifurcation, the integral toroidal magnetic flux remains unchanged,

$$\int_{S_t(a_b)}\frac{F - F_i}{r}dS_t \approx 0, \quad (31)$$

because this flux is determined primarily by the currents flowing in the toroidal magnetic field coils rather than by the plasma currents, which merely redistribute the flux over the cross section (of area S_t) of the plasma column. Strictly speaking, the desired relationship between the constants c_1 and c_2 should be found by substituting into formula (31) expressions (28) and the specific dependence $F_i(a)$ characterizing the initial equilibrium state under consideration. This method requires numerical calculations. However, as will be seen below, there is no need to know the exact relationship when the magnetic flux changes relatively insignificantly, $|c_{1,2}/F_i^2| \ll 1$. To be specific, we estimate this relationship only roughly, assuming that the averaged toroidal field depends weakly on a, $\langle B_t\rangle = \langle F_1/r\rangle \approx$ const, in which case simple manipulations yield

$$\frac{c_2}{R^2} \approx 6\Delta p\left(1 - \frac{a_2^2}{a_b^2}\right), \qquad \frac{c_1}{R^2} \approx 6\Delta p\frac{a_2^2}{a_b^2}. \quad (32)$$

Here and below, we neglect the corrections proportional to $\sim\Delta a/a_{1,2}$ in comparison with the quantities of order unity (because the barrier zone is narrow). To calculate the pressure jump given by expression (22), we use the following linear interpolation formula for $I^2(a)$ in terms of a^2:

$$I^2(a \in [a_2, a_1]) \approx F_i^2(a) + c_1\frac{a^2 - a_2^2}{a_1^2 - a_2^2} + c_2\frac{a^2 - a_1^2}{a_1^2 - a_2^2},$$

which satisfies the boundary conditions (28) at $a = a_{1,2}$. Then, we find

$$\left(\frac{I}{1 - M_A^2}\right)^2 - F_i^2 = \frac{M_A^2(2 - M_A^2)}{(1 - M_A^2)^2}F_i^2 + \frac{6\Delta p R^2}{(1 - M_A^2)^2}\left(\frac{a^2 - a_1^2}{a_1^2 - a_2^2} + \frac{a_2^2}{a_b^2}\right).$$

In expression (22), we switch to integration over a to obtain

$$\Delta p\left(2 - 3R^2\int_{a_2}^{a_1}\frac{\langle r^{-2}\rangle^{\cdot}}{1 - M_A^2}\left(\frac{a^2 - a_1^2}{a_1^2 - a_2^2} + \frac{a_2^2}{a_b^2}\right)da\right) = \int_{a_2}^{a_1}da\left\{\frac{\rho\omega^2}{2}\frac{\langle r^2\rangle^{\cdot}}{1 - M_A^2} - \frac{M_A^2}{2}\dot{W} + \frac{F_i^2}{2}\left\langle\frac{1}{r^2}\right\rangle^{\cdot}\frac{M_A^2(2 - M_A^2)}{1 - M_A^2}\right\}. \quad (33)$$

The specific details of both the relationship between the constants $c_{1,2}$ and the approximate formula for $I^2(a \in [a_2, a_1])$ are associated with the integral term on the left-hand side of formula (33). This term is on the order of $\sim a\cdot\Delta a/R^2$ and, therefore, can be omitted. In order to estimate the integral on the right-hand side, note that, by virtue of expression (9), the quantities M_A and ω are related by

$$\omega = (1 - M_A^2)\langle v\rangle - \left\langle\frac{F}{r^2}\right\rangle\frac{\kappa}{\rho}.$$

In the absence of toroidal plasma rotation, we have $\langle v\rangle = 0$, so that

$$\omega \approx -\frac{\kappa}{\rho}F_i\left\langle\frac{1}{r^2}\right\rangle, \quad \rho\omega^2 \approx M_A^2F_i^2\left\langle\frac{1}{r^2}\right\rangle^2. \quad (34)$$

It is these conditions that are realized in the cited T-10 experiments with ECR plasma heating, which introduces no toroidal momentum in the plasma. Note that the difference of F_i from I in conditions (34) also yields

a correction on the order of $\sim \Delta p R^2/I^2 \ll 1$. This allows formula (33) to be reduced to

$$\Delta p \approx \frac{1}{2}\int_{a_2}^{a_1} \frac{M_A^2}{2} da \left\{ -\dot{W} + \frac{F_i^2}{1-M_A^2}\left(\langle r^2 \rangle \cdot \left\langle \frac{1}{r^2} \right\rangle^2 - \left\langle \frac{1}{r^2} \right\rangle^{\cdot} (2 - M_A^2) \right) \right\}. \quad (35)$$

In order to obtain a quantitative estimate for the pressure jump Δp in T-10, we substitute expressions (24) and (25) into formula (35) and replace the integrands by their characteristic values in the barrier zone, $f(a) \longrightarrow \bar{f}$ for $\forall f$. As a result, expression (35) simplifies to

$$\Delta p \approx \frac{\Delta a}{a_2} \overline{M_A^2} \frac{\overline{B_p^2}}{2} (1 + 2\overline{q^2}). \quad (36)$$

The characteristic feature of expression (36) is that it does not in fact contain the details of the particular equilibrium state that are associated with the parameters s, β_p, and $\dot{\Delta}$. This indicates that, if the auxiliary heating power is high enough for the plasma pressure to acquire pressure jump (36), the bifurcation actually occurs; otherwise, the new equilibrium state is not achieved.

Let us apply formula (36) to estimate the electron temperature jump observed in T-10 (assuming, as above, that the plasma density is unchanged). The quantity $\overline{M_A^2}$ can be calculated from expression (34), in which the quantity ω is determined by the measurable change in the electric potential, $\Delta\Phi$, in the barrier zone:

$$\omega^2 \approx \left(\frac{2c|\Delta\Phi|}{\Delta a} \right)^2 \frac{1}{B_p^2 R^2}.$$

Under the conditions prevailing in the T-10 tokamak ($B_t \approx 2.14$ T, $\Delta a \approx 2$ cm, $a_2 \approx 17$ cm, and $q \approx 2$), the electron temperature jump $\Delta T_e = \Delta p/n_e = m_p \Delta p/\rho$ is approximately equal to

$$\Delta T_e \approx 2\frac{1+2q^2}{a_2|\Delta a|} m_p \left(\frac{c\Delta\Phi}{B_t} \right)^2 \approx 200 \text{ eV}. \quad (37)$$

This order-of-magnitude estimate agrees reasonably well with the experiment (Fig. 4a). Note that the approximate formula (37) is unlikely to fit the experimental measurements exactly because of the fairly arbitrary estimates for the electric and poloidal magnetic fields within the barrier zone, so that the agreement to within a factor of 1 to 2 seems to be quite satisfactory. However, agreement between our estimates and the experiment is actually much better. The reason is that the upper temperature profile in Fig. 4a was calculated for a certain time *after* the formation of the barrier, i.e., when the electric field in the barrier zone has already dissipated (Fig. 4b), while formula (37) refers to the transient equilibrium state in which the electric field is at its *maximum*. As the electric field dissipates, the energy of the plasma rotation is converted into heat. Although this energy is lower than the plasma temperature, it is quite comparable to the temperature increment ΔT. The corresponding correction to the approximate formula (37) provides better agreement (to within 10%) with the cited T-10 experiments. It is important to note that, although the plasma stops rotating, it does not evolve back to the initial equilibrium state: after the bifurcation, the new equilibrium state is maintained, e.g., by continued ECR heating (as is the case in T-10).

5. CONCLUSION

The proposed concept of a transport barrier in a tokamak plasma as a bifurcation of an equilibrium plasma state makes it possible to obtain an expression for the plasma pressure jump resulting from the barrier formation. This expression can be tested against the experimental data, because, in expressions (22) and (33), all of the quantities characterizing both the initial equilibrium state and the final state with a fully developed barrier can be either measured directly or calculated relatively easily from the measurable parameters. It should be noted that, in light of the proposed concept, the nature of the physical processes that may affect the transport properties of a plasma with an ITB is unimportant, because all of the results were obtained only from the equilibrium conditions and their integral consequences.

One of the important statements of our work is the conclusion about the bifurcations of the thermodynamic functions describing the equilibrium gas-kinetic plasma pressure (e.g., the temperature and enthalpy) and the poloidal plasma current (the toroidal magnetic field). According to the analysis carried out in Section 4, a necessary condition for the buildup of the barrier is the change in the toroidal magnetic field over the entire plasma column (including the plasma edge). This change may be detected by magnetic measurements.

The theory developed here makes it possible to reveal an interesting feature of a circular cross section tokamak with auxiliary heating that does not perturb the plasma density (e.g., ECR heating). It was found [see expression (36)] that the details of a particular equilibrium state (e.g., the values of the shear and β_p in the barrier zone) are unimportant for determining a possible jump in the plasma pressure (or temperature). This feature explains why regimes with ITB are experimentally achievable both in discharges with positive shears and in those with negative shears. Note that situations with other heating methods for which $\langle \nu \rangle \neq 0$ (e.g., injection of the beams of fast atoms) are more complicated: the shear profile can have a significant impact on the value (and even the sign!) of the expected jump in the plasma pressure [see the term proportional to

$\sim\langle r^2\rangle^{\cdot}$ in formula (33)] and, moreover, the assumption that the plasma density profile is unchanged fails to hold. Such situations require a more detailed theoretical analysis.

From expressions (22) and (33), we can see that the toroidal plasma rotation ($\langle v\rangle \neq 0$) may play an important role in the buildup of "large" transport barriers (in which the temperature changes by an amount of about several initial plasma temperatures; see Fig. 1). However, even when the toroidal rotation velocity v_t is about the sound speed, this effect seems to be possible only for $M_A^2 \sim 1$ because of the corresponding denominator.

The above analysis still keeps the question of whether or not the barrier is localized in the vicinity of a rational magnetic surface to be open. In our opinion, the reason why ITBs are most likely to build up in the vicinity of the rational surfaces is the following: in the area of the magnetic islands or regions of stochastic magnetic field lines near these surfaces, it is easy to involve the plasma in macroscopic rotation by a slight force balance perturbation resulting from auxiliary heating and/or current drive; this rotation, in turn, can trigger the bifurcation of the equilibrium.

ACKNOWLEDGMENTS

We are grateful to K.A. Razumova for valuable stimulating discussions and to V.D. Shafranov for useful comments. We also thank G.N. Tilinin for his advice on outlining the distinguishing features of large transport barriers. This work was supported in part by the Russian Foundation for Basic Research, project no. 00-15-96526 (under the program "Leading Scientific Schools"). Yu.I. Pozdnyakov also acknowledges the support of INTAS, grant no. 99-00592.

APPENDIX

Virial Theorem for a Steady Plasma Flow

Following [14], note that, with allowance for Eq. (3), the equilibrium equation (1) can be written in divergent form:

$$\nabla \cdot \overleftrightarrow{\mathbf{T}} = 0, \tag{A.1}$$

where the tensor is given by its elements,

$$\overleftrightarrow{\mathbf{T}}\colon T^{ik} = \left(p + \frac{B^2}{2}\right)\left(\delta^{ik} - \frac{B^i B^k}{B^2}\right) + \left(p - \frac{B^2}{2}\right)\frac{B^i B^k}{B^2} + \rho v^i v^k. \tag{A.2}$$

Let $\mathbf{r}$ be the position vector drawn from the origin of the coordinates to the observation point in space. We integrate the identity

$$\nabla \cdot (\mathbf{r} \cdot \overleftrightarrow{\mathbf{T}}) = \underbrace{\overleftrightarrow{\mathbf{T}} : \overleftrightarrow{\mathbf{E}}}_{\mathrm{Sp}\overleftrightarrow{\mathbf{T}}} + \mathbf{r} \cdot \underbrace{(\nabla \cdot \overleftrightarrow{\mathbf{T}})}_{=0}, \tag{A.3}$$

over the plasma volume under consideration and, using Gauss's theorem, obtain

$$\int_V \mathrm{Sp}\overleftrightarrow{\mathbf{T}}\, dV = \oint_{\partial V} (\mathbf{r} \cdot \overleftrightarrow{\mathbf{T}}) \cdot d\mathbf{S}, \tag{A.4}$$

where $\overleftrightarrow{\mathbf{E}}$ is an identity tensor composed of the Kronecker indices δ_{ij} and the trace of the tensor is equal, by definition, to

$$\mathrm{Sp}\overleftrightarrow{\mathbf{T}} = T^{ij}\delta_{ij} = T^i_i.$$

Substituting (A.2) into (A.4) immediately yields the desired relationship (29).

The same result can be obtained without recourse to tensor analysis. We consider the integral of $(p + B^2/2)\mathbf{r}$ over the surface ∂V enclosing a plasma volume V:

$$\int_{\partial V}\left(p + \frac{B^2}{2}\right)\mathbf{r} \cdot d\mathbf{S} = \int_V \nabla \cdot \left(\left(p + \frac{B^2}{2}\right)\mathbf{r}\right) dV = \int_V \left\{3\left(p + \frac{B^2}{2}\right) + \mathbf{r} \cdot \nabla\left(p + \frac{B^2}{2}\right)\right\} dV. \tag{A.5}$$

The equilibrium equation gives

$$\nabla\left(p + \frac{B^2}{2}\right) = \nabla p + (\mathbf{B} \cdot \nabla)\mathbf{B} + \mathbf{B} \times \nabla \times \mathbf{B} = (\mathbf{B} \cdot \nabla)\mathbf{B} - \rho(\mathbf{v} \cdot \nabla)\mathbf{v},$$

so that we have

$$\mathbf{r} \cdot \nabla\left(p + \frac{B^2}{2}\right) = (\mathbf{B} \cdot \nabla)(\mathbf{B} \cdot \mathbf{r}) - (\rho\mathbf{v} \cdot \nabla)(\mathbf{v} \cdot \mathbf{r}) - B^2 + \rho v^2 = \rho v^2 - B^2 + \nabla \cdot ((\mathbf{B} \cdot \mathbf{r})\mathbf{B} - (\rho\mathbf{v} \cdot \mathbf{r})\mathbf{v}).$$

Taking into account relationships (A.5), we obtain

$$\int_{\partial V}\left(p + \frac{B^2}{2}\right)\mathbf{r} \cdot d\mathbf{S} = \int_V \left(3p + \frac{B^2}{2} + \rho v^2 + \nabla \cdot ((\mathbf{B} \cdot \mathbf{r})\mathbf{B} - (\rho\mathbf{v} \cdot \mathbf{r})\mathbf{v})\right) dV,$$

which yields

$$\int_V \left(3p + \frac{B^2}{2} + \rho v^2\right) dV$$

$$= \int_{\partial V} \left\{\left(p + \frac{B^2}{2}\right)\mathbf{r} \cdot d\mathbf{S} + \rho(\mathbf{v} \cdot \mathbf{r})\mathbf{v} \cdot d\mathbf{S} - (\mathbf{B} \cdot \mathbf{r})\mathbf{B} \cdot d\mathbf{S}\right\},$$

which was to be proved.

REFERENCES

1. F. Wagner, G. Becker, K. Behringer, *et al.*, Phys. Rev. Lett. **49**, 1408 (1982).
2. K. Tobita and the JT-60 Team, Plasma Phys. Controlled Fusion **40**, A333 (1998).
3. E. Synakowski, Plasma Phys. Controlled Fusion **40**, 581 (1998).
4. H. Biglari, P. Diamond, and P. Terry, Phys. Fluids B **2**, 1 (1990).
5. S.-I. Itoh and K. Itoh, Nucl. Fusion **29**, 1031 (1989).
6. K. Shaing and E. Crume, Jr., Phys. Rev. Lett. **63**, 2369 (1989).
7. F. Hinton, Phys. Fluids B **3**, 696 (1991).
8. V. V. Alikaev, A. A. Borshchegobskij, V. V. Chistyakov, *et al.*, in *Proceedings of the 27th EPS Conference on Controlled Fusion and Plasma Physics, Budapest, 2000*, ECA, Vol. 24B, p. 592; K. A. Razumova, Usp. Fiz. Nauk **171**, 329 (2001).
9. V. Ilgisonis, Plasma Phys. Controlled Fusion **43**, 1255 (2001).
10. E. Hameiri, Phys. Rev. A **27**, 1259 (1983).
11. H. Tasso and G. N. Throumoulopolus, Phys. Plasmas **5**, 2378 (1998).
12. V. D. Shafranov, Plasma Phys. **13**, 349 (1971).
13. L. E. Zakharov and V. D. Shafranov, in *Reviews of Plasma Physics*, Ed. by M. A. Leontovich and B. B. Kadomtsev (Énergoatomizdat, Moscow, 1982; Consultants Bureau, New York, 1987), Vol. 11.
14. V. D. Shafranov, in *Reviews of Plasma Physics*, Ed. by M. A. Leontovich (Gosatomizdat, Moscow, 1963; Consultants Bureau, New York, 1967), Vol. 2.

Translated by O. Khadin

Plasma Physics Reports, Vol. 28, No. 2, 2002, pp. 94–102. Translated from Fizika Plazmy, Vol. 28, No. 2, 2002, pp. 110–118.

TOKAMAKS

Ion Temperature Profiles along a Hydrogen Diagnostic Beam in a TORE SUPRA Tokamak Plasma

A. N. Romannikov*, Yu. V. Petrov, P. Platz***, W. R. Hess***, T. Hutter***, J. L. Farjon***, and P. Moreau*****

**Troitsk Institute for Innovation and Fusion Research, Troitsk, Moscow oblast, 142092 Russia*
***Prairie View A&M University, Prairie View, TX 77446, USA*
****Association Euratom-CEA sur la Fusion, Cadarache 13108, St. Paul Lez Durance, France*
Received June 25, 2001; in final form, August 28, 2001

Abstract—The active particle diagnostic technique is used to study the ion temperature at five spatial points along the path of a hydrogen diagnostic beam. The temperature of the main ion plasma component (deuterium ions) measured by this diagnostic technique along the beam path is compared with the temperature of carbon ions (C^{+5}). A study is made of the following characteristic features of the behavior of the ion temperature profiles T_i in various TORE SUPRA operating modes: the formation of flat and even hollow T_i profiles in ohmic discharges with $q \sim 3$ at the plasma edge, the change in T_i profiles in ergodic divertor discharges, and the difference between the temperature of the bulk ions measured by the active particle diagnostic technique and the temperature of C^{+5} ions in the plasma region $r/a > 0.5$. The features revealed are explained at a qualitative level.

1. INTRODUCTION

The main (and virtually only) method for investigating the energy distribution function $f(E)$ of hydrogen isotopes in tokamak plasmas is a particle diagnostic technique based on measurements of the energy spectra of charge-exchange neutrals [1]. The most informative version of this method is the so-called active particle diagnostic (APD) technique, which is based on the diagnostic beams (DBs) of atoms (usually, the beams of hydrogen isotopes) [2]. In the APD technique, the DB parameters are such that the beam has an insignificant impact on the distribution function $f(E)$ of the majority ions but makes it possible to localize charge-exchange neutral fluxes along the line of sight of a particle analyzer (PA), in which case the analyzer preferentially measures the fluxes from the region where the DB intersects its line of sight. Unfortunately, a diagnostic complex that includes a device capable of generating DBs adapted to particular experimental conditions as well as PAs is relatively difficult to create. That is why, in recent years, almost no experiments aimed at studying the main ion plasma component by the APD technique have been carried out in tokamaks. Because of this, of particular interest is a series of experiments with DBs (about 85 shots) that were conducted in the TORE SUPRA tokamak (a tokamak with superconducting windings and with a major radius of $R \sim 2.34$ m, a minor radius a of up to 0.8 m, a toroidal magnetic field B_t of up to 4 T, a plasma current I_p of up to 2 MA, and a mean plasma density $\langle n \rangle$ of up to 5×10^{19} m^{-3}) before it was shut down for upgrading. Moreover, these TORE SUPRA experiments with the APD technique are unique in that, in each shot, the distribution function of charge-exchange neutrals (and, accordingly, the ion temperature) was measured simultaneously at five spatial points along the DB path and, in most of the shots, DBs also served to measure the temperature of carbon ions (C^{+5}) at eight spatial points along the beam path by charge-exchange spectroscopy.

In this paper, the experimental data are described as follows.

In Section 2, we briefly describe the diagnostic complex used in experiments.

In Section 3, we investigate the main characteristic feature observed in experiments with an ohmically heated plasma, specifically, the flattening of the ion temperature profiles and even their deepening in the central plasma regions, in which case the profiles of the electron density n_e and electron temperature T_e in these regions behave in a conventional manner. We present an additional indirect confirmation that hollow ion temperature profiles T_1 are associated with the toroidal ion rotation in the central region of the TORE SUPRA plasma. We also explain the formation of hollow profiles at a qualitative level.

In Section 4, we present for the first time experimental findings providing evidence that an ergodic divertor (ED) [3] in TORE SUPRA affects the ion temperature in the central plasma regions.

In Section 5, we analyze the T_i profiles in the plasma regions $r/a > 0.5$ and arrive at the conclusion that, under the conditions prevailing in TORE SUPRA, the significant deviation of the profile of the temperature of car-

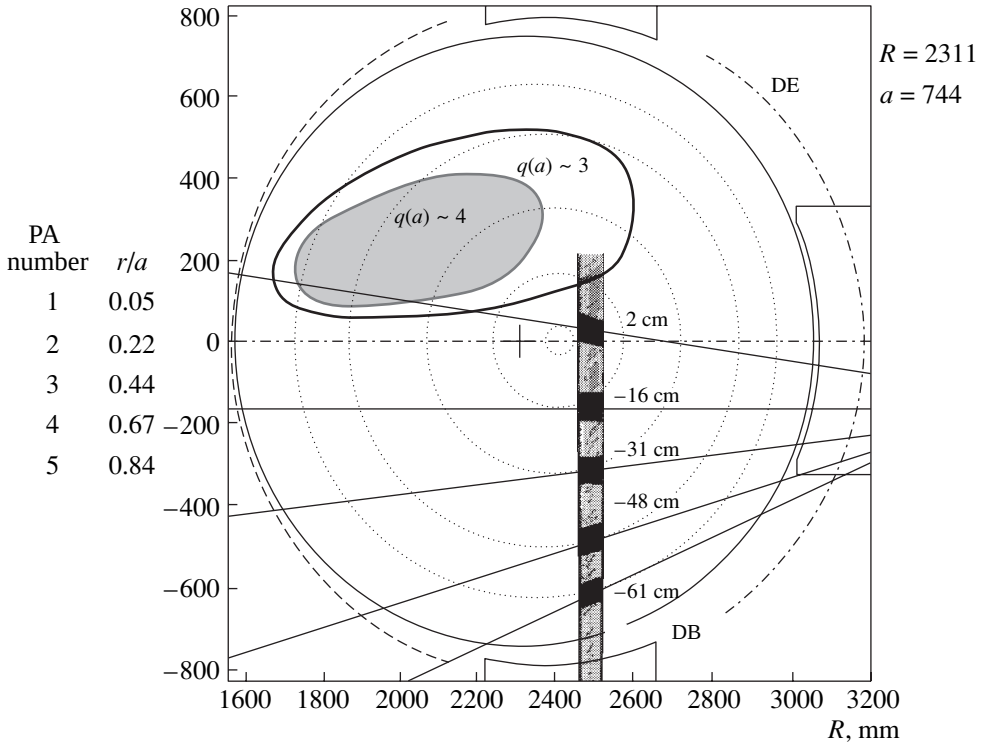

Fig. 1. DB path with respect to the magnetic surfaces (dotted circles) and the viewing chords of five PAs after the time $t = 6.01$ s from the beginning of shot no. 28099. The major and minor radii of the TORE SUPRA tokamak, R and a, are given in millimeters. As an example, two regions free of locally trapped ions, calculated for $q(a) \sim 3$ and 4, are shown in the upper part of the plasma column (in the lower part of the column, the corresponding regions, symmetric about the $z = 0$ plane, are not plotted).

bon ions from the deuterium temperature profile measured by the APD technique cannot be explained in a simple way.

In the conclusion, we summarize the observed characteristic features of the behavior of the energy distribution function $f(E)$ of the bulk ions in a TORE SUPRA plasma.

2. TORE SUPRA ION TEMPERATURE DIAGNOSTIC COMPLEX

In TORE SUPRA, the ion temperature is determined primarily from the energy spectra of charge-exchange H or D neutrals (the data presented here were obtained in experiments with deuterium beams) detected by six PAs of the **E** || **B** type [4]. Five analyzers are placed in the same toroidal cross section in which the DBs are injected (the coordinates along the beam path being 2 cm for PA1, –16 cm for PA2, –31 cm for PA3, –48 cm for PA4, and –61 cm for PA5). In order not to observe the region of locally trapped ions, the analyzers are oriented at an angle of about ~97° with respect to the direction of the toroidal magnetic field B_t at the center of the plasma column ($R = 2.5$ m). Figure 1 shows the lines of sight of the PAs with respect to the DB and the TORE SUPRA plasma. The sixth PA (the so-called tangential analyzer) is oriented at an angle of 38° to the direction of B_t in the equatorial plane, and its line of sight does not intersect the beam path. Each analyzer has 2×46 energy channels (in our experiments, the range of measured energies was 1–30 keV), which allows the simultaneous measurement of the distribution functions of H and D isotopes. The diameter of the observation region in the central plasma is about 7 cm. Along the lines of sight of PA1–PA5, the length of the region from which the charge-exchange neutrals are detected most efficiently is about 12–18 cm; this is the characteristic region of the DB neutrals (the beam plus the halo). Each energy spectrum of the beam neutrals is recorded during a time interval of about 150 ms.

A diagnostic neutral injector is located at the bottom vertical port (see, e.g., [5]). The injector produces hydrogen beams with an energy of about 45 keV (the beams consist of ~60% H, ~30% H_2, and ~10% H_3), a duration of up to 200 ms (in the experiments reported here), and a current of about 10 A. Thus, during the operation of the injector, the APD technique makes it possible to obtain the energy spectra of charge-exchange neutrals detected by PA1–PA5 at one point or even a pair of neighboring points of time. Figure 2 illustrates the representative energy spectra of charge-exchange neutrals recorded by PA1 and PA5 before (the lower spectrum) and during the beam injection (the two upper spectra). In the chosen discharge with ion cyclotron auxiliary heating (shot no. 27823), the mean ion

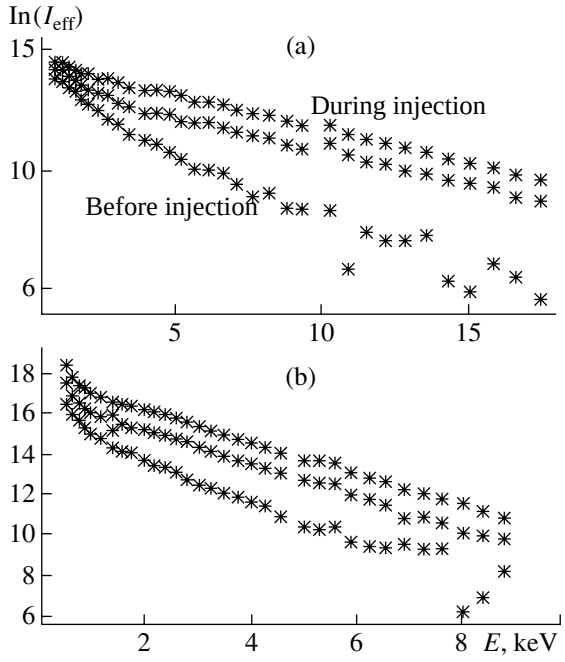

Fig. 2. Energy spectra of charge-exchange neutrals detected by (a) PA1 and (b) PA5 before (the lower spectrum in each figure) and during (the two upper spectra) beam injection after the time $t \sim 6.5$ s from the beginning of shot no. 27823 (I_{eff} is the ratio of the intensity of the neutral flux detected by the analyzer at a given energy to $E^{1/2}$).

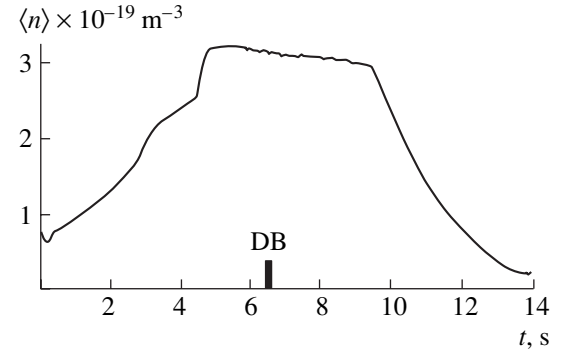

Fig. 3. Time evolution of the mean plasma density in shot no. 27823. The time at which the DB starts to be injected is indicated.

density was the highest ($\langle n \rangle \sim 3 \times 10^{19}$ m^{-3}) among the remaining discharges in the above experimental series with DBs. The time evolution of the central chord mean ion density during the discharge and the time at which the injector is switched on are illustrated in Fig. 3. Unfortunately, in this and some other discharges, the energy spectra recorded by PA3 were distorted because of technical problems. That is why the figures presented below contain no points obtained from PA3 during certain discharges. The spectra in Fig. 2 show that, even against the background of high ion density, the active signal associated with a DB is pronounced and is almost Maxwellian in shape in the energy range above $3T_i$. In all experiments with the neutral beam–based APD technique, the statistical deviation of the energy spectra from the straight line from which the deuterium ion temperature T_i was calculated (using up to 20 points in the energy range between $3T_i$ and $8T_i$) was, as a rule, smaller than 5%. The energy resolution in the channels of the analyzers provided measurements of the ion temperature with a relative accuracy of 10–15% [4]. The ion temperatures were calculated from the experimentally measured profiles of the electron temperature and Z_{eff} with allowance for the actual distortions of the energy spectra of the neutrals that originated in the DB region and propagated against the background of the plasma ions before reaching a PA. This procedure of determining the ion temperatures was applied to all of the discharges analyzed below.

The TORE SUPRA spectral diagnostic complex makes it possible to record the emission spectra produced by light impurities from eight viewing chords [5]. The spectral diagnostic complex is installed at the same port as a system of PAs, thereby providing the possibility of applying the methods of charge-exchange recombination spectroscopy (CXRS) to DBs. The eight viewing chords intersect the DB path at nearly equidistant points in the interval between $z = -12$ cm and $z = -58$ cm. In half of the TORE SUPRA experiments with DBs, the CXRS method was used to measure the Doppler broadening of the C^{+5} line ($n = 8 \longrightarrow 7$ at $\lambda = 5290.7$ nm). Our estimates show that, to a good accuracy, the carbon ion temperature calculated from the Doppler broadening of the C^{+5} lines in the TORE SUPRA steady-state operating modes coincides with the temperature of the thermal ions of the main ion plasma component. The spatial resolution of the CXRS method is determined by the DB dimension along the viewing chord (~15 cm). The temporal resolution (the time required to record one emission spectrum) is about 100 ms, which is long enough to obtain the energy spectrum at two points of time during the injection of a DB. All the results on the C^{+5} ion temperature that will be analyzed below were measured with a relative accuracy no worse than 10%. The comparative measurements of the ion temperature in the central plasma regions ($r/a < 0.25$) by the APD technique and CXRS method yielded essentially the same results (when corrected for a measurement error), except for the measurements in several discharges with lower hybrid heating.

Together with these two diagnostic methods, the central ion temperature and the toroidal rotation velocity of heavy impurity ions (Cr^{+22}, Fe^{+24}) were measured by a Bragg spectrometer recording X-ray helium-like lines of impurities [6]. The Bragg spectrometer is mounted at the tangential port, operates independently of the DBs, and makes it possible to measure the ion temperature throughout the discharge in a region with a

diameter of about 10 cm where the electron temperature is maximum. In experiments with DBs, the spectrometer operated for about 15 discharges. It was found that the temperature of Cr^{+22} ions was close to the temperature of D ions (the difference being smaller than 10%) measured with PA1 by the APD technique (the temperatures were measured at the same instant in neighboring spatial regions).

The electron temperature profiles used in our work were measured by Thomson scattering. The electron density profiles were measured by five vertically oriented microwave interferometers and also from Thomson scattering (as implied by the standard TORE SUPRA diagnostics). The results of measurements during each discharge were corrected for the position of the plasma column with respect to the DB. In essentially all of the discharges, the position of the plasma column corresponded to that shown in Fig. 1.

The parameters of the discharges to be analyzed below are listed in the table, in which the shots are numbered in order of their appearance in the paper. The duration of each of the discharges was about 12 s. The table illustrates ohmic discharges, discharges with ion-cyclotron auxiliary heating, and ohmic discharges with an ED.

3. CHARACTERISTIC FEATURES OF THE $T_i(z)$ PROFILES IN DIFFERENT OHMIC-HEATING REGIMES

About 40% of the experiments were carried out with ohmic discharges in a wide range of plasma currents (from 0.5 to 1.5 MA), edge safety factors $q(a)$ (from 3 to 11), and mean electron densities (from 0.7×10^{19} to 3.8×10^{19} m^{-3}). The maximum ion temperatures along the beam path varied from about 1 keV at low plasma currents to about 1.5 keV at high plasma currents. The experiments showed that, along with the expected profiles $T_i(z)$, which are peaked about the $z = 0$ plane (Fig. 4b), a fairly large number of discharges were characterized by flat and even hollow profiles $T_i(z)$ both for D and C^{+5} ions (Fig. 4a), in which case the radial profiles $T_e(r)$ and $n_e(r)$ in the central plasma regions were found to have a conventional shape. Figures 5a and 5b show the ratio T_i(PA1, +2 cm)/T_i(PA2, –16 cm) versus $\langle n \rangle$ and $q(a)$, respectively. We can see that there are not only discharges with T_i(PA1, +2 cm)/T_i(PA2,

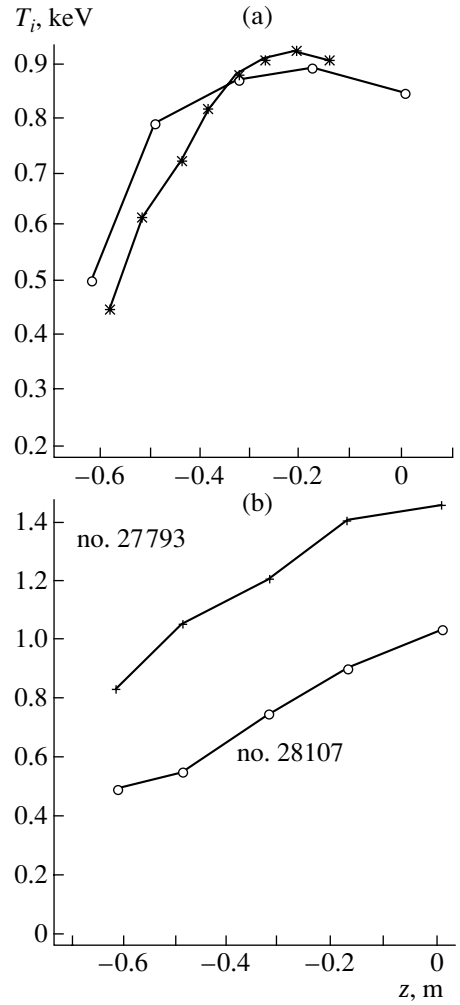

Fig. 4. (a) $T_i(z)$ profiles for deuterium (circles) and C^{+5} (asterisks) ions at $\langle n \rangle$ = ~1.2 and I_p = 0.75 in shot no. 28318. (b) $T_i(z)$ profiles along the DB path for deuterium ions at $\langle n \rangle \sim 2$ and I_p = 0.5 in shot nos. 27793 and 28107. The mean ion density $\langle n \rangle$ and plasma current I_p are given in units of 10^{19} m^{-3} and MA, respectively.

Table

Shot number	$\langle n \rangle \times 10^{-19}$, cm^{-3}	I_p, MA	B_t, T	Regimes
27823	3.2	1.6	3.8	ICRH
28318	1.2	0.75	1.6	Ohmic heating + ED
27793	2.6	1.4	3.8	Ohmic heating
28107	2.0	0.5	3.8	Ohmic heating
27905	2.0	1.5	3.2	Ohmic heating + ED
25737	2.0	1.0	3.9	Ohmic heating
28315	1.2	0.75	1.6	Ohmic heating + ED
28320	1.2	0.75	1.6	Ohmic heating + ED

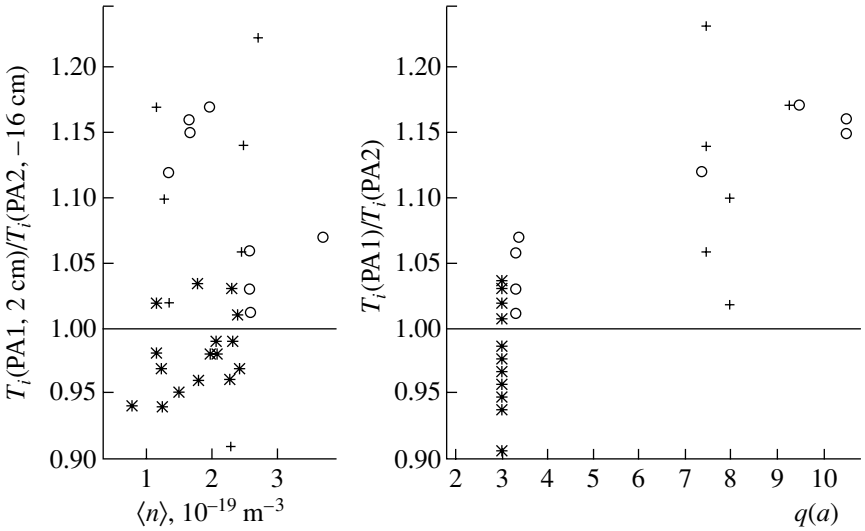

Fig. 5. Ratio of the deuterium temperature at the point +2 cm (measurements by PA1) to that at the point –16 cm (measurements by PA2) along the DB path vs. (a) the mean electron density and (b) the safety factor $q(a)$ at the boundary of the plasma column. The asterisks refer to deuterium discharges with an ED, the circles illustrate ohmic deuterium discharges, and the crosses correspond to ohmic helium discharges, in which the detected deuterium is an impurity species.

–16 cm) > 1 (centrally peaked ion temperature profiles) but also discharges for which this ratio is smaller than unity (hollow profiles).

Indirect evidence for the formation of hollow ion temperature profiles in such discharges is provided from measurements of the toroidal plasma rotation velocity V_{tor} (the positive direction of the toroidal rotation coincides with the direction of the plasma current) by the passive particle diagnostic technique with the help of a tangential PA [7]. A method analogous to that described in [7] was used to measure the toroidal rotation velocity in the steady-state phase (which lasts approximately from the fourth to the eighth second) of shot nos. 27905 and 25737; the mean toroidal rotation velocity was measured in the region ~(0.1–0.35)r/a at the given moderate plasma densities. In discharges with hollow ion temperature profiles, the velocity V_{tor} was found to be close to zero (shot no. 27905 with ED) and even to be slightly positive (about +10 km/s), in contrast to shot no. 25737 (from the series of experiments carried out in [7]), in which V_{tor} was about –40 km/s. The velocity was measured with an accuracy of ±20 km/s. According to [7], the role of the governing mechanism for the generation of the radial electric field in TORE SUPRA is played by significant ripples in the toroidal magnetic field B_t, in which case the velocity V_{tor} is described by the expression (see formula (9) in [7])

$$V_{\text{tor}} \approx c\frac{k}{eB_p}\frac{dT_i}{dr}, \qquad (1)$$

where B_p is the poloidal magnetic field and the coefficient k is about 3.5. Obviously, for discharges with hollow T_i profiles, the toroidal rotation velocity might be expected to be positive in regions where the derivative of T_i is increasing, as is the case in experiments. However, such a behavior of V_{tor} was also observed in discharges with $q(a) \sim 3$ but without an ED. Moreover, in experiments in which the ED was switched on (or off) nearly in the middle of the discharge, measurements by the particle diagnostic technique and by a Bragg spectrometer (in TORE SUPRA, this spectrometer is capable of measuring only the variations in the toroidal rotation velocity) revealed no significant change in V_{tor} (to within experimental error).

Since the ion temperature profiles were observed to become flat or hollow in all discharges with an ED [3], we made an attempt to explain the formation of such profiles as being due to the effect of the divertor operation. However, the data from experiments with an ED and the results of numerical calculations show that, at the same electron densities, the divertor does not change the radial profile of the electron temperature in the central plasma regions. The influence of the divertor on the magnetic configuration in the plasma core is also insignificant: near the plasma axis, the divertor-induced perturbation in the relative ripple amplitude of B_t (~0.003) is about 0.0001, the impact of the divertor on the poloidal magnetic field being negligible. That is why the divertor cannot be responsible for the formation of hollow radial profiles of T_i in the plasma.

Additional indirect evidence that the shape of the radial ion temperature profiles is not influenced by the ED operation is provided by Fig. 6. The shape of the deuterium temperature profile in the central region is insensitive to the decrease in the current flowing in the divertor from the nominal value 2.2 kA to 0.5 kA

(in which case the effect of the divertor on the plasma diminishes in the same proportion).

We believe that the most likely cause of the flattening or even deepening of the ion temperature profiles is associated with the dependence shown in Fig. 5b (the number of experimental points in Fig. 5b differs from that in Fig. 5a because some points coincide). The change in $q(a)$ results in a substantial change in the plasma magnetic configuration, thereby changing the behavior of the locally trapped ions. For the TORE SUPRA discharges illustrated in Fig. 5b, we calculated the regions of the locally unrippled magnetic field for different $q(a)$ values (in which case the relative ripple amplitude of the magnetic field at the plasma boundary is about 7% and, in the region where the beam intersects the $z = 0$ plane, it is about 0.3–0.4%). The calculations were carried out using the method described in [8]. The $q(r)$ profile was approximated by a parabola chosen so as to fit the q values measured experimentally at the plasma edge and plasma center. The unrippled magnetic field regions calculated for two different $q(a)$ values are shown schematically in Fig. 1 (in which the corresponding symmetric regions in the lower part of the plasma column are not plotted). In TORE SUPRA, the gradient drift of the ions is directed from bottom to top. From Fig. 1, we can see that, for $q(a) \sim 3$, sufficiently energetic ions trapped in local magnetic wells in the inner region enclosed by the magnetic surface with a radius of about $r \sim 15$ cm will drift upward, thereby inevitably leaving this inner region and accumulating in the region of the unrippled magnetic field. The only way that the ions can return to the inner region is to be trapped in magnetic wells in the lower part of the plasma column. However, in the lower part, ions will also appear in the unrippled magnetic field region. As a result, the core region will act as a heat sink, while the magnetic surface with a radius of $r \sim 15$ cm will play the role of a heat source, thereby leading to the formation of hollow ion temperature profiles in the steady-state phase of the discharge. In TORE SUPRA, the governing factor for the formation of such profiles is a marked relative ripple amplitude (about 0.003) of the toroidal magnetic field at the plasma center. In momentum space, the fraction of the locally trapped ions that are entrained in the upward drift in such a toroidal magnetic field is about 0.1. Among these ions, all D ions with an energy of about 7 keV and higher (for the characteristic parameter values $B_t = 3$ T and $n(0) = 5 \times 10^{19}$ m^{-3}) [9] will enter the unrippled magnetic field region and reach the magnetic surface with a radius of $r \sim 15$ cm. For sufficiently large $q(a)$ values, the unrippled magnetic field regions no longer overlap with the central plasma region. In this case, the only possible effect is a slight distortion of the tails of the distribution function $f(E)$ [9] at different magnetic surfaces without appreciable heating of any particular magnetic surface.

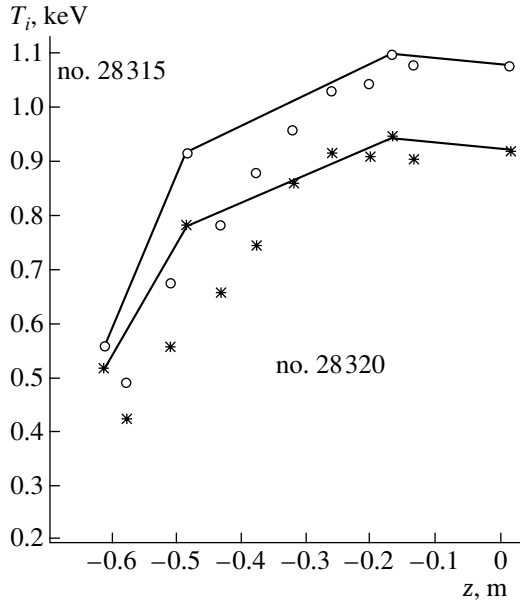

Fig. 6. $T_i(z)$ profiles for deuterium (points connected by line segments) and C^{+5} (unconnected points) ions in two identical discharges but with different currents in the ED: $I_{ed} = 0.55$ in shot no. 28315 (circles) and $I_{ed} = 2.2$ in shot no. 28320 (asterisks) (the current I_{ed} in the divertor is measured in kA). The toroidal magnetic field is $B_t = 1.6$ T, the plasma current is $I_p = 0.75$ MA, and the mean ion density is $\langle n \rangle = 1.2 \times 10^{19}$ m^{-3}.

4. EFFECT OF ED ON THE ION TEMPERATURE IN THE CENTRAL PLASMA REGIONS

Following [3], let us briefly discuss how the ED affects the TORE SUPRA plasma. The divertor gives rise to a region of ergodized magnetic field around the magnetic surface with $q(r) \sim 3$. When the edge q value is about 3 at the nominal current in the divertor, the plasma boundary is observed as if it were displaced at the magnetic surface with $r/a \sim 0.8$. However, for the electron plasma component, this effect cannot be treated merely as a decrease in the minor radius of the plasma. The divertor acts as a kind of barrier that cuts off the plasma edge but does not diminish the electron temperature and density in the plasma core. Prior to the experiments presented here, the effect of an ED on the core ions was experimentally investigated only by passive particle diagnostics [10]. These investigations revealed no significant impact of an ED on the ion temperature T_i.

Our experiments show that an ED may influence the ion plasma component. We found that the divertor does not substantially change the shape of the $T_i(z)$ profile along the DB path but decreases the central ion temperature by about 15%. This decrease was observed not only in the temperature of D ions measured by the APD technique but also in the temperature of C^{+5} ions measured by the CXRS method. Figure 6 illustrates two

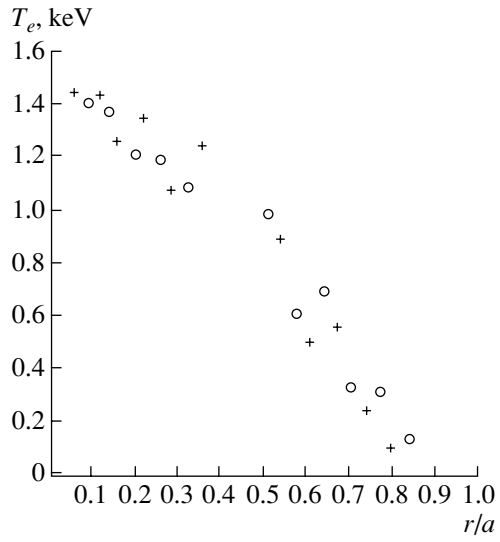

Fig. 7. Electron temperature measured by Thomson scattering in shot nos. 28315 (circles) and 28320 (crosses) vs. dimensionless minor radius.

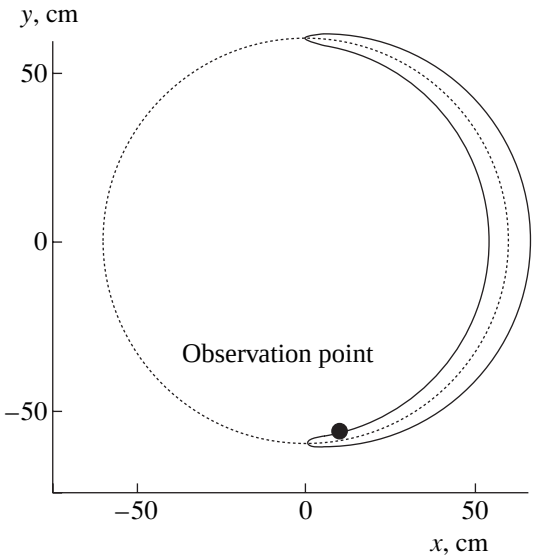

Fig. 8. Banana orbit of a 5-keV deuterium ion at the magnetic surface with a radius of $r \sim 60$ cm in a TORE SUPRA discharge with a toroidal magnetic field of 3 T and a plasma current of 0.65 MA. Indicated in the banana orbit is the observation point from which a charge-exchange neutral can reach the PA5 analyzer.

discharges with the same electron density, toroidal magnetic field B_t, and plasma current I_p, the profiles of the electron temperature in the central region also being practically the same (Fig. 7). The discharges differed only in the current flowing in an ED. Recall that, at the nominal current in the divertor, the effective minor radius of the plasma column decreased to $0.8r/a$ [3]. Since the effective minor radius increases almost linearly with the current in the divertor (provided the current is below the nominal value), we can expect that, for shot no. 28315, this radius is about $\sim 0.95r/a$. Let us estimate how the change in the central ion temperature $T_i(0)$ depends on the change in the minor radius, neglecting all the remaining factors that may affect this dependence. Under the assumption that the plasma electrons act as a heat source for the ions, the desired estimate can be obtained from the heat balance relation for the ion plasma component:

$$\frac{\chi(T_{i1})}{\chi(T_{i2})}\frac{T_{i1}}{T_{i2}}\left(\frac{a_2}{a_1}\right)^2 \approx \frac{T_e - T_{i1}}{T_e - T_{i2}}, \qquad (2)$$

where $\chi(T_i)$ is the ion thermal diffusivity. Ascribing to the diffusivity $\chi(T_i)$ the simple dependence $\sim 1/T_i^{1/2}$ and using Figs. 6 and 7 and formula (2), we can estimate the expected central temperature value T_{i1} for the effective minor radius $\sim 0.95a/r$ from the known central temperature $T_{i2} \sim 0.92$ keV for the effective minor radius $\sim 0.8a/r$ (in both cases, the electron temperature T_e is the same and is approximately equal to 1.5 keV). As a result, we obtain $T_{i1} \sim 1.08$ keV, which is close to the experimentally measured temperature (Fig. 6). We can thus conclude that the effect of the ED operation on the plasma ions consists merely in a reduction of the effective minor radius for the radial ion temperature profile.

5. PLASMA ION TEMPERATURE IN THE REGIONS $r/a > 0.5$

From Figs. 3b and 6, one can see that, in these regions, the temperature of the D ions measured with PA4 and PA5 by the APD technique is higher than the temperature of C^{+5} ions by about 20%. An analogous situation was observed in all experiments with DBs. We failed to reveal how this temperature difference changes depending on the plasma parameters. Note only that this difference was found to be minimum (about 10%) in discharges with ion cyclotron auxiliary heating, in which the mean electron density and central ion temperature were about $\sim 3 \times 10^{19}$ m^{-3} and about 3 keV, respectively (these values are approximately close to those in the discharge illustrated in Fig. 2). The effect of the broadening of the radial profile of the ion temperature measured by a particle diagnostic technique is often observed in experiments (see, e.g., [11]). In all particle diagnostic methods, the ion temperature is calculated from the tails of the ion energy distribution function. Consequently, it may be expected that, if the function $f(E)$ deviates from a Maxwellian distribution function (MDF), then the temperature of C^{+5} ions (in the CXRS method, the measured spectral line width is associated primarily with the thermal ions of the main ion plasma component) will differ from the calculated temperature of D ions. In the TORE SUPRA tokamak, there may be two possible causes for the deviation of the ion energy spectrum measured by the APD tech-

nique from being Maxwellian (these causes were already studied in the literature, see, e.g., [9, 12]). The first cause is associated with the position of the observation point in the banana orbit of an ion in the actual experimental geometry: it is this point from which a charge-exchange D neutral can reach the PA. Figure 8 shows the observation point for a 5-keV D ion detected by PA5 (the ion energy is chosen from the central spectral region, from which the ion temperature is calculated). We can see that, unlike in [12], the observation point lies in the inner circuit of the banana orbit. In the case at hand, this indicates that, in the energy range of about 5 keV, measurements of the ion temperature by detecting the ions that come from this observation point give the ion temperature at a magnetic surface whose minor radius is larger than the distance from the observation point to the plasma axis by about 5 cm [12]. In reality, the characteristic features of the method used to calculate T_i from the energy spectra of charge-exchange neutrals [10] are such that the resulting ion temperature is even lower. Consequently, the expected distortion of the MDF should lead to a lower temperature of D ions in comparison with C^{+5} ions. However, in actual experiments, the opposite situation occurs. Carrying out calculations with allowance for a marked toroidal plasma rotation [7] reduces the above difference from ~5 cm to ~4.5 cm, which is, nevertheless, too large to resolve the problem in question. Moreover, in earlier TORE SUPRA experiments with passive particle diagnostics, the temperature of D ions measured by PA4 in discharges with a reversed plasma current (the remaining parameters being fixed) was found to be the same (it has been established experimentally that, in discharges with a moderate electron density, passive and active particle diagnostics yielded practically equal ion temperatures). This contradicts the predictions of our analysis, according to which the temperature of D ions calculated from their energy spectra is expected to be substantially higher.

The second possible cause for the above temperature difference may be associated with the large ripple amplitude of the toroidal magnetic field in TORE SUPRA. The exact calculation of the maximum possible number of fast ions that can occur at different magnetic surfaces and can be detected by PA4 and PA5 after they have undergone charge exchange is a very complicated task and is to be the subject of our further studies. However, we believe that the experimental results under discussion can hardly be interpreted as manifestations of the locally trapped ions. The main reasons for this are twofold. First, the analyzers were oriented in such a way that their viewing chords do not intersect the corresponding regions of local magnetic wells. The experimental data obtained in [8] show that, for the ions to be trapped in a local magnetic well along the viewing chord of PA4, the ratio of their longitudinal velocity to their transverse velocity should be smaller than 0.03; in turn, PA4 can detect ions for which this ratio is about 0.11. In energy space, the corresponding zones are well separated. For PA5, these zones are closer to one another but still do not overlap. Hence, the detectable ions move along banana orbits and can be described using the above approach, which is based on Fig. 8. Second, in accordance with [9], we can expect that the maximum possible number of ions at a given magnetic surface will be achieved, in particular, at the expense of retrapping ions that were trapped at neighboring surfaces (in this case, the retrapped ions all have physically reasonable longitudinal and transverse momenta and thus fill the entire momentum space). For a relative ripple amplitude of about 1% near PA4 and PA5, the number of such retrapped ions can be fairly large. However, unlike in [9], the ripple amplitude in TORE SUPRA varies strongly in the vertical direction. To be specific, let us illustrate how the relative ripple amplitude changes along the DB path in a discharge with $q(a) \sim 4$. It decreases from ~7% at $z = -75$ cm to ~1.5% at $z = -60$ cm (PA5). Further, it continues to decrease to 0.9% at $z = -50$ cm (PA4) and to 0.1% at $z = -15$ cm (PA2). Then, it starts increasing to 0.4% at $z = 0$ cm (PA1). The variation in the relative ripple amplitude in the upper part of the plasma column is a mirror image of that just described.

Let us consider a magnetic surface associated with AH4. In our experiments, this analyzer measured ions with mean energies of about 6–7 keV. For the characteristic experimental plasma parameters, the result is that, for the ions trapped in local magnetic wells at inner magnetic surfaces to become untrapped in the upper half-plane, they should travel a distance of about 15 cm (with allowance for the variation in the ripple amplitude) and, analogously, for the ions trapped at outer magnetic surfaces to become untrapped in the lower half-plane, they should travel a distance of about 25 cm. That is why, in regions far from the local magnetic wells, the distortion of the MDF at a chosen magnetic surface is more likely to reflect the losses of ions with energies of about 6–7 keV in the energy spectrum (with allowance for the ion escape from the chosen surface outward in the upper half-plane and inward in the lower half-plane). As a result, the temperature of D ions measured by the APD technique should be lower than the temperature of the thermal ions of the main ion plasma component. Hence, we believe that neither the methodical consideration nor the above qualitative physical analysis can explain the difference in the ion temperatures measured by two diagnostic techniques in the region $r/a > 0.5$ (the temperature of deuterium ions is always measured to be higher than the temperature of carbon ions).

6. CONCLUSIONS

Our experimental investigations of the $T_i(z)$ profiles along the DB path in various TORE SUPRA operating modes allow us to draw the following conclusions.

(i) Measurements of the ion temperature in the central plasma regions by three different diagnostic tech-

niques (the APD, CXRS, and Bragg methods) yield the same results (to within the experimental error).

(ii) The TORE SUPRA tokamak can operate in ohmic modes with hollow ion temperature profiles and conventional electron temperature profiles. A possible cause of these operating modes, which occurs when $q(a) \sim 3$, is associated with locally trapped ions and regions of locally unrippled magnetic field in the cross section of the plasma column. The toroidal ion rotation velocity in the plasma core was measured to be close to zero and even positive, in agreement with the theoretical model proposed in [7] (in TORE SUPRA, the formation of the radial electric field and the onset of the toroidal ion velocity V_{tor} is associated with the ripples in the toroidal magnetic field B_t). Since, in some tokamaks, the ripple amplitude in the central plasma regions is always significant, the radial ion temperature profiles $T_i(r)$ may become hollow during discharges with small q values. The study of such operating modes can also be of interest from the standpoint of the possible evolution of a discharge to a state in which the toroidal ion rotation velocity V_{tor} (and, accordingly, the radial electric field [7]) may have opposite directions at neighboring magnetic surfaces in the plasma core [formula (2)].

(iii) In our experiments, the effect of the ED on the ion temperature T_i in the central regions has been measured for the first time. As the current in the divertor increases, the central ion temperature T_i decreases, the shape of the $T_i(z)$ profile being unchanged. This behavior of the ion temperature can be explained as being due to the divertor-induced reduction of the effective minor radius for the radial ion temperature profile.

(iv) In the plasma region $r/a > 0.5$, the ion temperatures measured by two diagnostic techniques differ by about 20%. The temperature of the thermal ions measured from the Doppler broadening of the C^{+5} line by the CXRS method is lower than the temperature of D ions measured by the APD technique. As a result, in the energy range from $3T_i$ to $8T_i$, the MDF is observed to be distorted in such a way that it reflects a significant increase in the fraction of these ions above the Maxwellian background level. A qualitative analysis carried out with allowance for such factors as the influence of locally trapped ions and the position of the observation region in the banana orbit fails to explain the results obtained. Moreover, the analysis shows that these factors should produce the opposite result.

It is well known that a similar strong distortion of the MDF in the thermal energy range plays a governing role in the transport processes of the majority ions in tokamak plasmas. The results from the above supplementary methods for measuring the ion temperature T_i provide a clearer insight into the problems associated with ion confinement. In recent years, particle diagnostic methods for ion measurements in the thermal energy range have been largely abandoned in favor of the spectral methods for measuring the emission from impurity ions. However, this preference leads to a significant loss of information about the ion component of the tokamak plasma.

ACKNOWLEDGMENTS

We are grateful to M. Becoulet for fruitful discussions of the effect of an ergodic divertor on the TORE SUPRA plasma.

REFERENCES

1. M. P. Petrov, Fiz. Plazmy **2**, 371 (1976) [Sov. J. Plasma Phys. **2**, 201 (1976)].
2. A. I. Kislyakov and L. I. Krupnik, Fiz. Plazmy **7**, 866 (1981) [Sov. J. Plasma Phys. **7**, 478 (1981)].
3. A. Grosman, Plasma Phys. Controlled Fusion **41**, A185 (1999).
4. T. Hutter, V. Basiuk, A. Becoulet, *et al.*, in *Proceedings of the 21st EPS Conference on Controlled Fusion and Plasma Physics, 1994*, Vol. 18B, Part II, p. 956.
5. W. R. Hess, W. Mandl, J. L. Farjon, *et al.*, in *Proceedings of the 24th EPS Conference on Controlled Fusion and Plasma Physics, 1997*, Vol. 21A, Part I, p. 189.
6. P. Platz, Y. Margerit, J.-F. Artaud, *et al.*, Rev. Sci. Instrum. **70**, 308 (1999).
7. A. Romannikov, C. Bourdell, J. Bucalossi, *et al.*, Nucl. Fusion **40**, 319 (2000).
8. V. Basiuk, A. Becoulet, T. Hutter, *et al.*, Fusion Technol. **26**, 222 (1994).
9. A. V. Gurevich and Ya. S. Dimant, in *Reviews of Plasma Physics*, Ed. by B. B. Kadomtsev (Énergoizdat, Moscow, 1987; Consultants Bureau, New York, 1990), Vol. 16.
10. W. R. Hess, C. DeMichelis, M. Mattioli, *et al.*, Plasma Phys. Controlled Fusion **37**, 951 (1995).
11. V. S. Zaveryaev, A. B. Izvozchikov, S. E. Lysenko, and M. P. Petrov, Fiz. Plazmy **4**, 1205 (1978) [Sov. J. Plasma Phys. **4**, 671 (1978)].
12. Yu. V. Gott and E. I. Yurchenko, Dokl. Akad. Nauk SSSR **260**, 1352 (1981) [Sov. Phys. Dokl. **26**, 995 (1981)].

Translated by G. Shepekina